

# Chapter 9

# Parameter Estimation II

## 9.1 Introduction

In Chapter 8, we focused on maximum likelihood estimation and the bounds on achievable performance. We found that the stochastic maximum likelihood estimator achieved the Cramér-Rao bound but it required a significant amount of computation to find the estimate. We introduced several other estimators. Some of the estimators provided good performance but, in general, still required a significant amount of computation. In this chapter we focus our attention on estimators that are computationally simpler, but may provide acceptable performance in many problems of interest.

In Section 9.2, we discuss several estimators that we refer to as quadratic estimators because they compute a quadratic form as a function of  $\psi$  and choose the  $D$  largest peaks as  $\hat{\psi}$ .

In Section 9.3, we develop a family of subspace algorithms. The most prominent of these algorithms is the MUSIC (Multiple Signal Classification) algorithm invented by Schmidt [Sch79] and Bienvenu and Kopp [BK80]. It is widely used because of its performance capability, and various versions and modifications of the MUSIC algorithm have been extensively studied.

In Section 9.4, we discuss linear prediction (LP) algorithms briefly. These algorithms grew out of the work by Burg [Bur67] on maximum entropy estimators and modified forward-backward linear prediction estimators due to Tufts and Kumaresan [TK82]. We do not develop this area in detail.

In Sections 9.2 and 9.3, we utilize simulation to study the performance of the various estimators. In Section 9.5, we consider the asymptotic regime and derive expressions for the probability of resolution, the bias, and the variance. We then combine these results to obtain an analytic expression for

the mean-square error.

Many of the algorithms developed in this chapter suffer significant performance degradation (or fail to work) when the incoming plane waves are correlated or coherent. In Section 9.6, we study one technique, spatial smoothing (SS), for solving this problem.

In Section 9.7, we develop beampulse algorithms. In these algorithms we preprocess the incoming signal with a matrix that, in essence, creates a set of beams. We then utilize these beam outputs to find the DOAs. We show that, in many environments, we can obtain estimators with equivalent variance and an improved probability of resolution with significantly less computational complexity.

In Section 9.8, we study the sensitivity of the various algorithms to perturbations in the array or the noise environment.

In Section 9.9, we consider planar arrays. Most of the algorithms developed in this chapter are applicable to arbitrary array geometries. However, some of the particularly efficient techniques, such as algorithms that find the roots of a polynomial, do not extend easily.

In Section 9.10, we summarize the results of the chapter and indicate several topics that we have omitted. In Table 9.1, we show the structure of the chapter.

## 9.2 Quadratic Algorithms

### 9.2.1 Introduction

In this section we discuss several algorithms that we refer to as quadratic algorithms because each of them computes one or more quadratic forms. We should note that several of the algorithms that we develop in Sections 9.3 and 9.4 also compute quadratic forms. However, the logic leading to their structure is different. One should view the quadratic algorithm term as a convenient descriptor rather than a precise definition.

The basic estimators of interest are listed in Table 9.2. In each algorithm, we vary  $\mathbf{v}(\psi)$  over the *a priori* range of the sources in  $\psi$ -space, plot the value of the indicated function, and select the  $D$  largest values as the estimates of  $\psi_1, \psi_2, \dots, \psi_D$ . We assume that  $D$  is known or has been estimated. All of these algorithms are valid for an arbitrary array geometry. For 2-D estimation, the scalar  $\psi$  is replaced by the vector  $\psi$ , whose components are  $\psi_x$  and  $\psi_y$ .

Table 9.1 Structure of Chapter 9

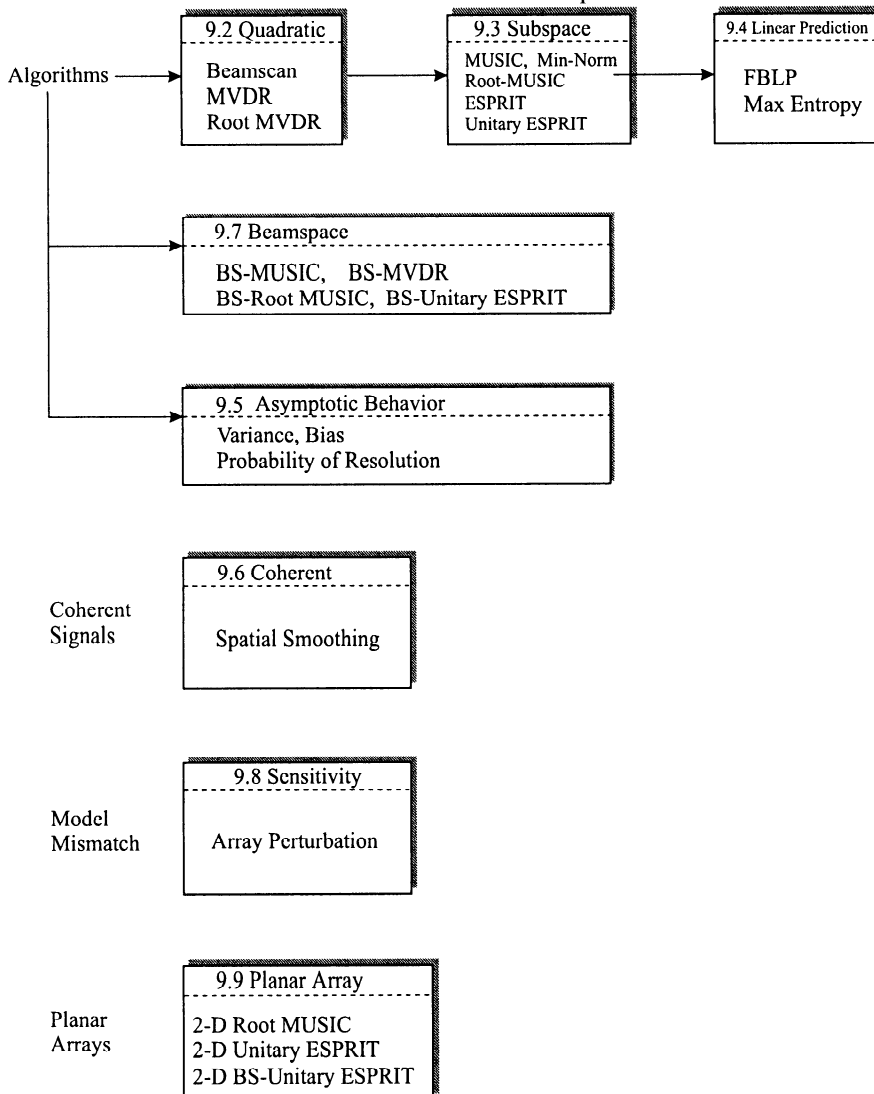


Table 9.2: Quadratic Algorithms

1. Beamscale	$\mathbf{v}^H(\psi) \mathbf{C}_x \mathbf{v}(\psi)$
2. Weighted beamscale	$\mathbf{v}^H(\psi) \mathbf{C}_{x,w} \mathbf{v}(\psi)$
3. MVDR	$\frac{1}{\mathbf{v}^H(\psi) \mathbf{C}_x^{-1} \mathbf{v}(\psi)}$

For linear, equally-spaced arrays, we develop a polynomial version of the algorithm where the roots correspond to  $\hat{\psi}_1, \hat{\psi}_2, \dots, \hat{\psi}_D$ . These rooting algorithms are computationally simpler and more accurate.

In Sections 9.2.2 and 9.2.3, we develop the algorithms and give a graphical indication of their performance. In Section 9.2.4, we develop the rooting version of the algorithms. In Section 9.2.5, we present a detailed comparison of the performance of the various algorithms based on simulation and compare their performance to the Cramér-Rao bound derived in Chapter 8. In Section 9.2.6, we summarize our results.

The results in this section are similar to those in Barabell et al. [BCD<sup>+</sup>84],<sup>1</sup> which analyzed the algorithms listed in Table 9.1 along with the MUSIC algorithm (Section 9.3). Their report considers uncorrelated signals and contains extensive simulations for various combinations of  $SNR$ ,  $\Delta\psi$ , and  $K$ .

### 9.2.2 Beamscale Algorithms

The beamscale algorithm forms a conventional beam, scans it over the appropriate region of  $\psi$ -space, and plots the magnitude squared of the output. If the  $k$ th snapshot vector in the frequency domain is

$$\mathbf{X}_k = \left[ \begin{array}{c|c|c|c} X_k(1) & X_k(2) & \cdots & X_k(N) \end{array} \right]^T, \quad (9.1)$$

then, for  $K$  snapshots,

$$\widehat{P}_B(\psi) = \frac{1}{K} \sum_{k=1}^K \left| \mathbf{v}^H(\psi) \mathbf{X}_k \right|^2, \quad -\pi \leq \psi \leq \pi. \quad (9.2)$$

We have omitted the  $\frac{1}{N}$  scaling factor in the weight vector of the conventional beam pattern to be consistent with the majority of the literature. This

---

<sup>1</sup>This reference is a Lincoln Laboratory report that has a distribution restriction but appears to be well-known in the community.

estimator is referred to as the Bartlett beamformer. The expression in (9.2) can be rewritten as,

$$\widehat{P}_B(\psi) = \mathbf{v}^H(\psi) \left\{ \frac{1}{K} \sum_{k=1}^K \mathbf{X}_k \mathbf{X}_k^H \right\} \mathbf{v}(\psi). \quad (9.3)$$

The term in the braces is the sample spectral matrix. Thus (9.3) can be rewritten as

$$\widehat{P}_B(\psi) = \mathbf{v}^H(\psi) \mathbf{C}_x \mathbf{v}(\psi), \quad (9.4)$$

where  $\mathbf{C}_x$  is the sample spectral matrix. Notice that  $\widehat{P}_B(\psi)$  is providing an estimate of the spatial spectrum. Its performance has been studied in detail in the context of both temporal and spatial spectrum estimation (e.g., [Kay88], or [Mar87]). If the array is a standard linear array, we would compute  $\widehat{P}_B(\psi)$  by using an FFT in (9.2).

In our application, we select the  $D$  peaks of  $\widehat{P}_B(\psi)$  and designate them as  $\hat{\psi}_i, i = 1, 2, \dots, D$ . We assume that the number of signals,  $D$ , is known. Zhang [Zha95b] has studied the performance of the Bartlett beamformer.

The algorithm is scanning a conventional beam so the resolution cannot exceed the classical resolution we developed in Chapter 2. For an arbitrary array, if the ANSR and  $K$  are large enough, we will be able to resolve targets separated by the beamwidth of the array. For a standard  $N$ -element linear array, this will correspond to sources whose separation is greater than or equal to  $2/N$ .

There are various modification to the Bartlett estimator that are appropriate for various environments.

If we anticipate that there are weak targets in the sidelobe region of the conventional beam, we can use one of the weightings developed in Chapter 3 to reduce the sidelobes at the expense of broadening the main lobe and decreasing resolution. The resulting estimator is

$$\widehat{P}_{BW}(\psi) = \frac{1}{K} \sum_{k=a}^K \left| \mathbf{v}^H(\psi) \mathbf{w} \mathbf{X}_k \right|^2, \quad -\pi \leq \psi \leq \pi. \quad (9.5)$$

where

$$\mathbf{w} = \text{diag} \left[ \begin{array}{c|c|c|c} w(1) & w(2) & \cdots & w(N) \end{array} \right]. \quad (9.6)$$

Then,

$$\widehat{P}_{BW}(\psi) = \mathbf{v}^H(\psi) \mathbf{C}_{x,w} \mathbf{v}(\psi), \quad -\pi \leq \psi \leq \pi, \quad (9.7)$$

where

$$\mathbf{C}_{\mathbf{x},w} = \mathbf{w} \mathbf{C}_{\mathbf{x}} \mathbf{w}^H. \quad (9.8)$$

For a conjugate symmetric array, we can improve the performance for a modest number of snapshots by using FB averaging, as discussed in Section 7.2.3. In this case the estimator is

$$\widehat{P}_{B,fb}(\psi) = \frac{1}{2K} \sum_{k=1}^K \left| \mathbf{v}^H(\psi) [\mathbf{X}_k + \mathbf{J} \mathbf{X}_k^*] \right|^2, \quad -\pi \leq \psi \leq \pi, \quad (9.9)$$

where  $\mathbf{J}$  is the exchange matrix. The expression for  $\widehat{P}_{B,fb}(\psi)$  can be rewritten as

$$\widehat{P}_{B,fb}(\psi) = \mathbf{v}^H(\psi) \mathbf{C}_{\mathbf{x},fb} \mathbf{v}(\psi), \quad (9.10)$$

where

$$\mathbf{C}_{\mathbf{x},fb} = \frac{1}{2K} \sum_{k=1}^K \left( \mathbf{X}_k \mathbf{X}_k^H + \mathbf{J} \mathbf{X}_k^* \mathbf{X}_k^T \mathbf{J} \right). \quad (9.11)$$

The behavior of these estimators is discussed in Problems 9.2.1 through 9.2.3.

### 9.2.3 MVDR (Capon) Algorithm

The MVDR algorithm was discussed in the context of waveform estimation in Section 6.2.1. To use these results in the parameter estimation context, we use the weighting in (6.71) with  $\mathbf{C}_{\mathbf{x}}$ , the sample spectral matrix, replacing  $\mathbf{S}_{\mathbf{x}}$ . Then,<sup>2</sup>

$$\begin{aligned} \widehat{P}_{mvdr}(\psi) &= \frac{1}{K} \sum_{k=1}^K \left| \mathbf{w}_{mvdr}^H \mathbf{X}_k \right|^2, \quad -\pi \leq \psi \leq \pi \\ &= \frac{1}{K} \sum_{k=1}^K \left| \frac{\mathbf{v}^H(\psi) \mathbf{C}_{\mathbf{x}}^{-1}}{\mathbf{v}^H(\psi) \mathbf{C}_{\mathbf{x}}^{-1} \mathbf{v}(\psi)} \mathbf{X}_k \right|^2, \quad -\pi \leq \psi \leq \pi. \end{aligned} \quad (9.12)$$

This reduces to

$$\widehat{P}_{mvdr}(\psi) = \frac{1}{\mathbf{v}^H(\psi) \mathbf{C}_{\mathbf{x}}^{-1} \mathbf{v}(\psi)}, \quad -\pi \leq \psi \leq \pi. \quad (9.13)$$

---

<sup>2</sup>In the notation of Chapter 6, we should call this the MPDR algorithm. The MVDR terminology is so widely used in the parameter estimation literature that we will use it.

This estimator is due to Capon [Cap69], and its behavior was discussed in by Lacoss [Lac71]. We plot  $\widehat{P}_{mvdr}(\psi)$  and find its  $D$  peaks. These values correspond to the  $D$  wavenumber estimates:  $\hat{\psi}_1, \hat{\psi}_2, \dots, \hat{\psi}_D$ .

As in the case of the Bartlett beamformer, the MVDR algorithm also provides a spatial spectral estimate that does not rely on any underlying signal model. We focus our attention on its performance as a DOA estimator.

Frequently we plot the inverse of  $\widehat{P}_{mvdr}(\psi)$  and find the  $D$  minima of function. We refer to the inverse as the null spectrum,

$$\widehat{Q}_{mvdr}(\psi) = \mathbf{v}^H(\psi) \mathbf{C}_{\mathbf{x}}^{-1} \mathbf{v}(\psi), \quad -\pi \leq \psi \leq \pi. \quad (9.14)$$

If  $\mathbf{v}(\psi)$  is conjugate symmetric, we can improve performance and reduce computation by FB averaging of the data. Then (9.13) becomes

$$\widehat{P}_{mvdr,fb}(\psi) = \frac{1}{\mathbf{v}^H(\psi) \mathbf{C}_{\mathbf{x},fb}^{-1} \mathbf{v}(\psi)}, \quad -\pi \leq \psi \leq \pi, \quad (9.15)$$

where  $\mathbf{C}_{\mathbf{x},FB}$  is given by (9.11). The null spectrum in (9.14) becomes,

$$\widehat{Q}_{mvdr,fb}(\psi) = \mathbf{v}^H(\psi) \mathbf{C}_{\mathbf{x},fb}^{-1} \mathbf{v}(\psi), \quad -\pi \leq \psi \leq \pi. \quad (9.16)$$

We consider a simple example to show its behavior for a large number of snapshots.

### Example 9.2.1

We consider a standard 10-element linear array. There are two sources located at  $u = \pm 0.0433$ . This corresponds to a separation of  $\Delta\psi_R$ . The sources are uncorrelated and their strength is 20 dB above the white sensor noise. We process 1,000 snapshots.

The results for a typical trial are shown in Figure 9.1(a) for the Bartlett algorithm (9.2) and the MVDR algorithm.<sup>3</sup> We see that the MVDR algorithm exhibits two distinct peaks at the location of the two sources. It is important to point out that that case corresponds to high  $SNR$  and a large number of snapshots. It does indicate that the MVDR algorithm appears to have a resolution capability in this environment. Although there are two peaks in the spectrum, the dip between the peaks is very small, so we would anticipate that the signals might not be resolved on other trials. This behavior is due to the close spacing between the signals. In Figure 9.1(b), we show the results from a typical trial when the spacing is doubled so that  $\Delta u = 0.1732$ . Now the dip between the peaks is significant.

These plots provide an indication of behavior, but they do not tell how well the MVDR algorithm works in terms of estimation accuracy or its behavior for lower  $SNR$  or fewer snapshots. Later we investigate its behavior in terms of estimation accuracy and resolvability as a function of source  $SNR$ , separation, and the number of snapshots ( $K$ ).

We return to the MVDR algorithm in Section 9.2.4 and study its behavior as a function of  $SNR$ , source separation, and number of snapshots. We now look at a root version of the MVDR algorithm that is applicable to standard linear arrays.

---

<sup>3</sup>Gabriel [Gab80] has similar plots.

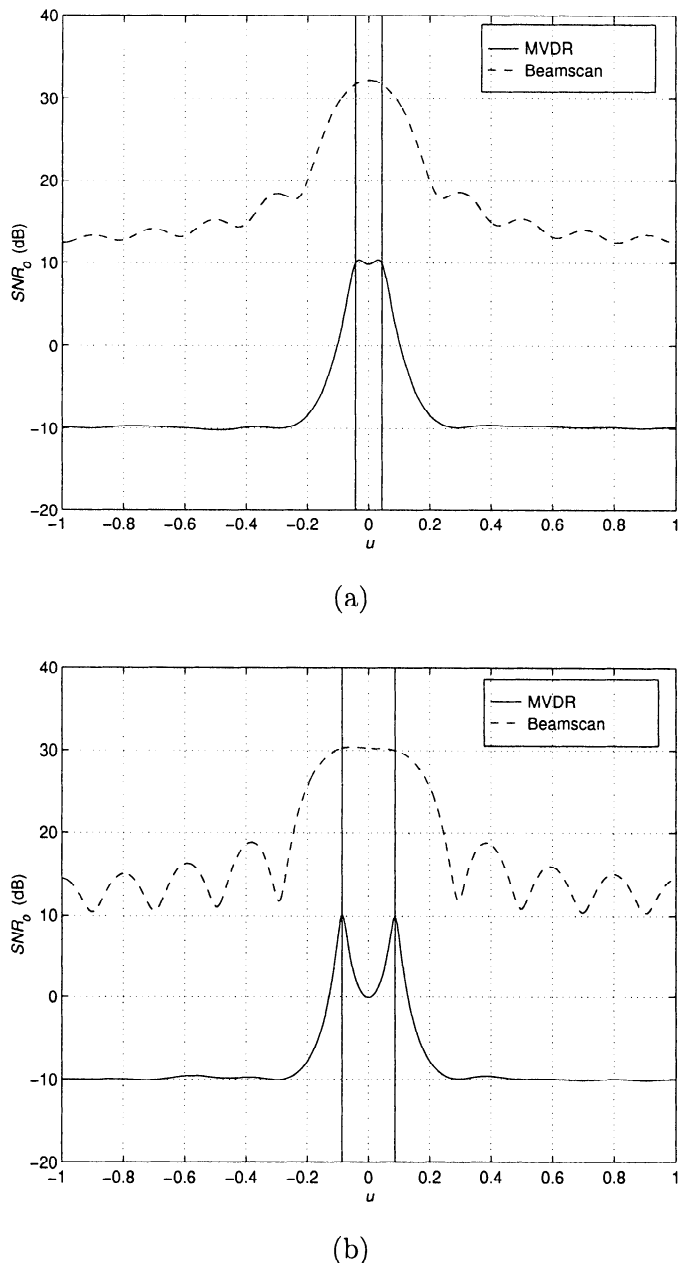


Figure 9.1 Performance of beamscan and MVDR algorithms: standard 10-element linear array,  $\rho = 0$ ,  $SNR = 20$  dB,  $K = 1,000$ : (a)  $u = \pm 0.0433$ ; (b)  $u = \pm 0.0866$ .

### 9.2.4 Root Versions of Quadratic Algorithms

In this section we consider a standard  $N$ -element linear array. For this case we can derive an alternative version of the quadratic algorithms that is computationally simpler and more accurate.<sup>4</sup>

The null spectrum of the MVDR algorithm can be written as a quadratic form,

$$\hat{Q}(\psi) = \mathbf{v}^H(\psi) \mathbf{G} \mathbf{v}(\psi), \quad (9.17)$$

where  $\mathbf{G}$  is a Hermitian matrix. Finding the peaks of  $P(\psi)$  is equivalent to finding the minimum (or nulls) of  $\hat{Q}(\psi)$ . We want to find a polynomial whose roots correspond to the minimum of  $\hat{Q}(\psi)$ .

We recall that we can write

$$\mathbf{v}(\psi) = [1 \ e^{j\psi} \ \dots \ e^{j(N-1)\psi}]^T, \quad (9.18)$$

where we have put the first element at the origin to simplify notation. Letting

$$z = e^{j\psi}, \quad (9.19)$$

we can write (9.17) as

$$\hat{Q}_z(z) = \sum_{m=0}^{N-1} \sum_{n=0}^{N-1} z^{-m} g_{mn} z^n = \sum_{m=0}^{N-1} \sum_{n=0}^{N-1} g_{mn} z^{n-m}, \quad (9.20)$$

where  $g_{mn}$  is the  $mn$ th element of  $\mathbf{G}$ . Now define  $k = n - m$  and write  $\hat{Q}_z(z)$  as

$$\hat{Q}_z(z) = \sum_{k=-(N-1)}^{N-1} q_k z^k, \quad (9.21)$$

where

$$q_k = \begin{cases} \sum_{n=0}^{k+N-1} g_{n-k,n}, & k = -(N-1), \dots, -1, 0, \\ \sum_{n=k}^{N-1} g_{n-k,n}, & k = 1, 2, \dots, N-1. \end{cases} \quad (9.22)$$

The Hermitian property of  $\mathbf{G}$  implies that the coefficients of  $\hat{Q}_z(z)$  are conjugate symmetric,

$$q_{-k} = q_k^*. \quad (9.23)$$

---

<sup>4</sup>The use of rooting algorithm is due to Barabell [Bar83] (see also [BCD<sup>+</sup>84])

The null spectrum can also be written as,

$$\widehat{Q}_z(z) = \sum_{k=-(N-1)}^{N-1} q_k^* z^{-k}. \quad (9.24)$$

and

$$\widehat{Q}(\psi) = \widehat{Q}_z(z) \Big|_{z=e^{j\psi}} \quad (9.25)$$

The nulls of  $\widehat{Q}(\psi)$  are due to the roots of  $\widehat{Q}_z(z)$  that lie near the unit circle. Due to the conjugate symmetry, if  $z_d$  is a root of  $\widehat{Q}_z(z)$ , then so is  $1/z_d^*$ .

$\widehat{Q}_z(z)$  can be factored,

$$\widehat{Q}_z(z) = H(z) H^* \left( \frac{1}{z^*} \right), \quad (9.26)$$

where  $H(z)$  is the FIR filter that would generate a spectrum  $\widehat{Q}_z(z)$ .

Half of the roots of  $\widehat{Q}_z(z)$  will lie inside the unit circle. The rooting algorithm constructs  $\widehat{Q}_z(z)$  using the appropriate  $\mathbf{G}$  ( $\mathbf{C}_x^{-1}$  for MVDR), and computes the  $D$  roots inside and closest to the unit circle. Then,

$$\hat{\psi}_d = \frac{\arg \hat{z}_d}{\pi}, \quad d = 1, 2, \dots, D. \quad (9.27)$$

The estimate of the root  $\hat{z}_d$  has a radial and angular error. Only the angular error affects  $\hat{\psi}_d$ . In many cases of interest, this angular component is smaller than the estimate of null location obtained from the null spectrum. We analyze this behavior in detail in Section 9.5.

In Section 9.3, we encounter algorithms in which

$$\mathbf{G} = \hat{\mathbf{U}}_N \hat{\mathbf{U}}_N^H. \quad (9.28)$$

In that case we take advantage of this decomposition and construct  $\widehat{Q}_z(z)$  in a different manner.

### 9.2.5 Performance of MVDR Algorithms

In this section we investigate the behavior of the MVDR and root MVDR algorithms as a function of the array  $SNR$  and the number of snapshots. There are a number of papers in the literature that analyze the performance of MVDR. The paper by Vaidyanathan and Buckley [VB95] contains several results of interest and summarizes some of the previous work. They derive

an expression for the asymptotic ( $K \rightarrow \infty$ ) bias, the additional bias due to finite data, and the standard deviation. They also studied the effects of array perturbations. The reader is referred to this reference for a discussion of these analytic results.

We restrict our discussion at this point to two uncorrelated signals impinging on the array. The array is a standard 10-element linear array, so we use  $\mathbf{C}_{\mathbf{x},fb}$ .

### Example 9.2.2

We use a standard 10-element linear array and assume there are two uncorrelated signals impinging on the array from  $\pm \Delta\psi/2$ . We assume  $\Delta\psi = \Delta\psi_R$ . We simulate the performance of the algorithms for various  $SNR$  and number of snapshots. We measure the probability that the algorithm can resolve the two signals in the following manner. If the algorithm produces two distinct solutions inside the main lobe and  $|\hat{\psi}_i - \psi_i| \leq \Delta\psi/2$ , we say that the signals are resolved. In this example, we use the sample covariance matrix  $\mathbf{C}_{\mathbf{x},fb}$ . We consider the spectral MVDR and root MVDR algorithms.

In Figure 9.2 we plot the probability of resolution versus  $ASNR$ . In Figure 9.3, we plot the normalized RMSE versus  $ASNR$ . In Figure 9.4, we plot the normalized RMSE versus  $K$ , the number of snapshots.

The threshold of root MVDR occurs at an  $ASNR$  of about 15 dB for  $K = 100$ . Above threshold, the RMSE is very close to the CRB. The threshold of spectral MVDR is harder to specify. The dramatic increase in RMSE occurs at about 22 dB, but the RMSE does not approach the CRB until the  $ASNR = 40$  dB. In Figure 9.4, we see that root MVDR is very close to CRB as  $K \rightarrow \infty$  but spectral MVDR is not.<sup>5</sup> An analysis of this behavior if contained in [Lac71].

In Figures 9.5, 9.6, and 9.7, we show the behavior of the two algorithms as a function of signal separation for various values of  $ASNR$ . In each case, there is a critical value of  $\Delta u$  for the root MVDR and spectral MVDR algorithms (which are different). If  $\Delta u$  is larger than the critical value, then the MVDR algorithms are very close to the CRB.

### 9.2.6 Summary

In this section, we have observed that root MVDR performs reasonably well above threshold, but the threshold is significantly higher than the ML algorithms for closely spaced signals. Spectral MVDR has an even higher threshold.

In the problems, we develop two other quadratic algorithms, AAR and TNA, which exhibit somewhat better performance than MVDR but do not appear to be used in practice. We also discuss diagonal loading in the problems and see that it improves the performance in the low sample support case.

---

<sup>5</sup>The result in Figure 9.4 appears to exhibit different behavior than the example in [VB95]. The reason is that their signal separation is about  $2\Delta_R$  instead of  $\Delta_R$ .

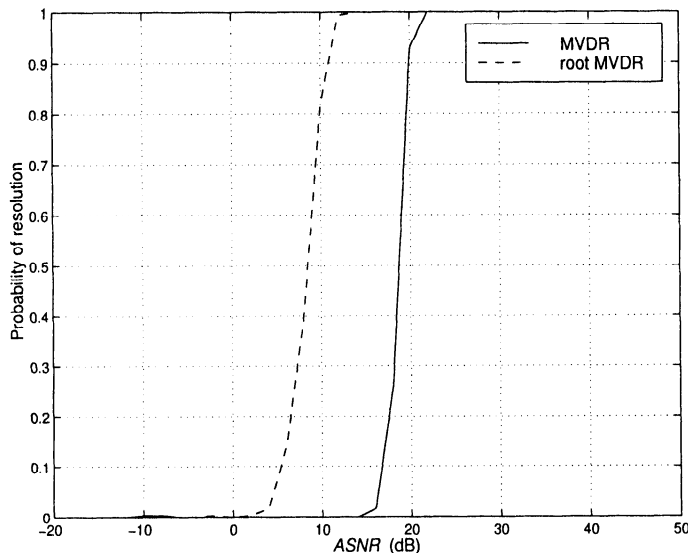


Figure 9.2 MVDR-FB algorithms: probability of resolution versus  $ASNR$ :  $N = 10$ ,  $K = 100$ ,  $\Delta\psi = \Delta\psi_R$ , 300 trials.

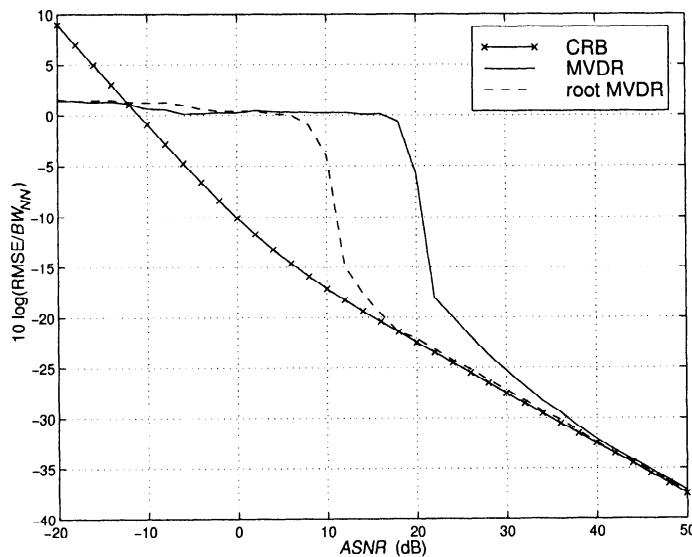


Figure 9.3 MVDR-FB algorithms: normalized RMSE versus  $ASNR$ :  $N = 10$ ,  $K = 100$ ,  $\Delta\psi = \Delta\psi_R$ , 300 trials.

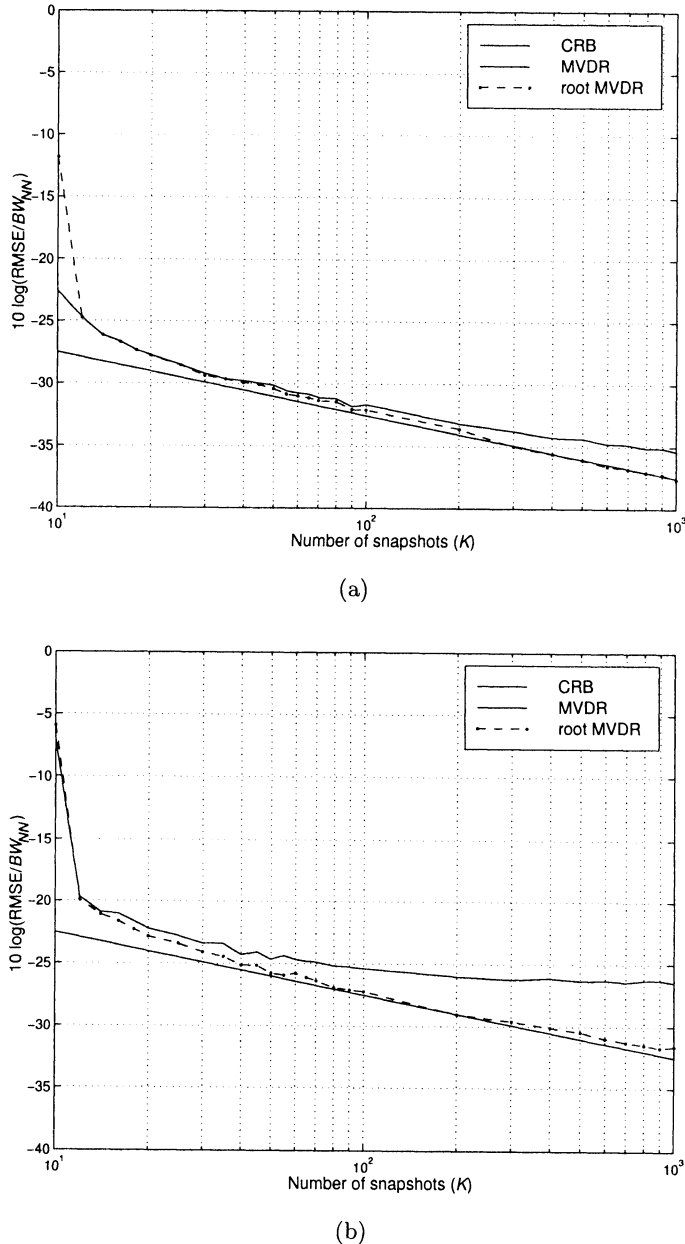
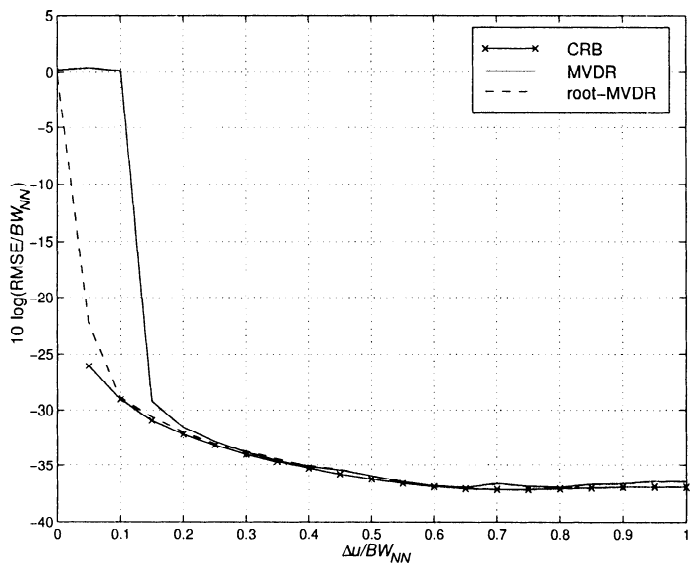
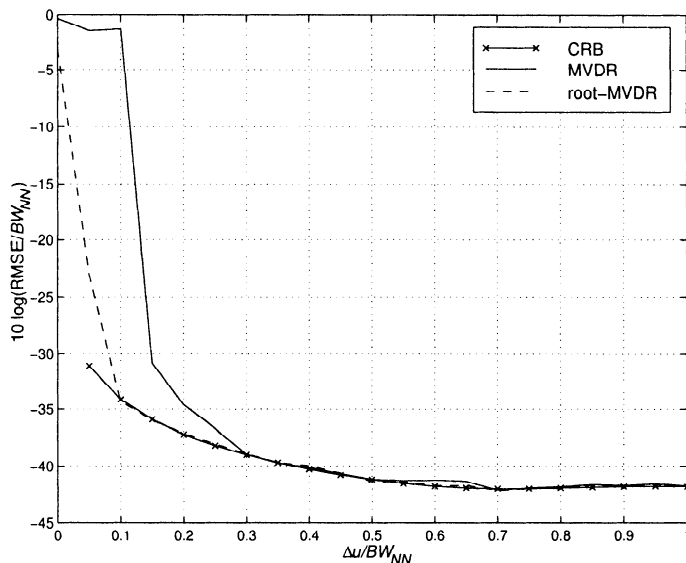


Figure 9.4 MVDR-FB algorithms: normalized RMSE versus  $K$ :  $N = 10, K = 100, \Delta\psi = \Delta\psi_R$ , 200 trials: (a)  $\text{ANSR} = 40 \text{ dB}$ ; (b)  $\text{ANSR} = 30 \text{ dB}$ .

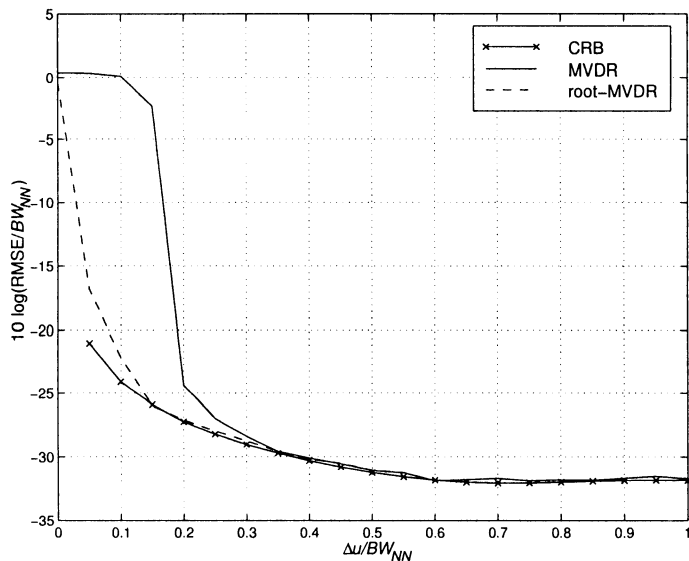


(a)

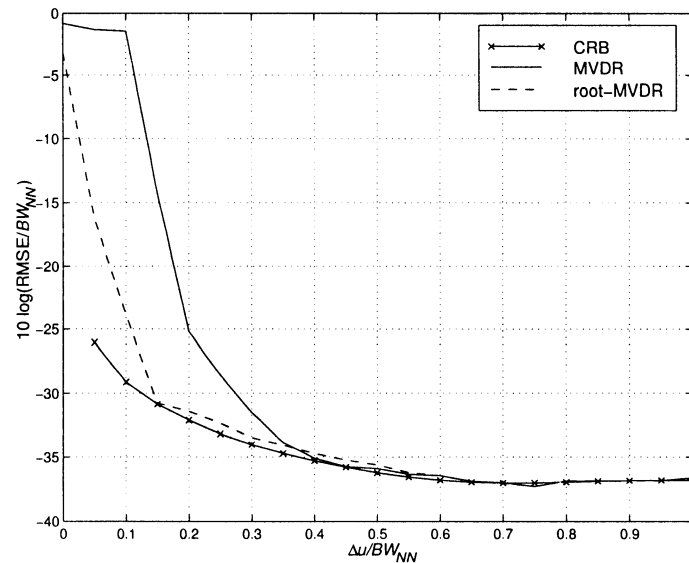


(b)

Figure 9.5 MVDR-FB algorithms: normalized RMSE versus  $\Delta u/BW_{NN}$ :  
 $N = 10$ ,  $ASNR = 40$  dB, 300 trials: (a)  $K = 100$ ; (b)  $K = 1,000$ .

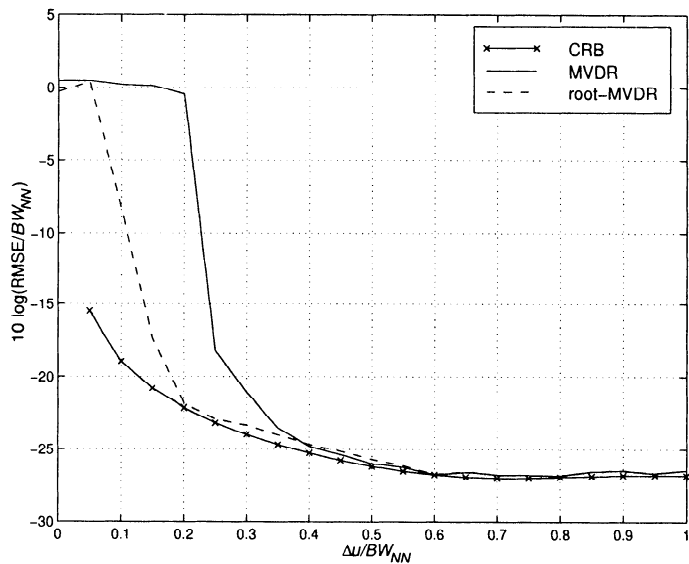


(a)

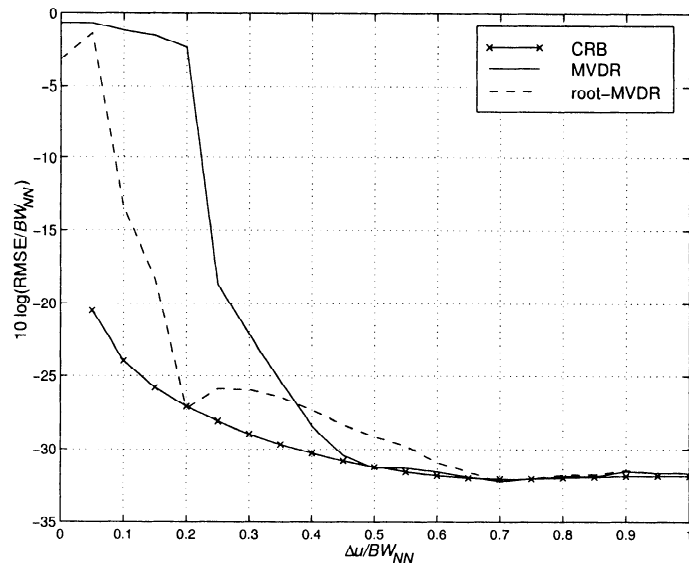


(b)

Figure 9.6 MVDR-FB algorithms: normalized RMSE versus  $\Delta u / BW_{NN}$ :  
 $N = 10$ ,  $ASNR = 30$  dB, 300 trials: (a)  $K = 100$ ; (b)  $K = 1,000$ .



(a)



(b)

Figure 9.7 MVDR-FB algorithms: normalized RMSE versus  $\Delta u / BW_{NN}$ :  
 $N = 10$ ,  $ASNR = 20$  dB, 300 trials: (a)  $K = 100$ ; (b)  $K = 1,000$ .

Although neither the Bartlett beamformer nor spectral MVDR are efficient parameter estimators, they can play a useful role as a preliminary processor to indicate the number of plane waves impinging on the array, their approximate location, and their approximate signal power. If two plane waves are closely spaced, the algorithms will think they are single plane waves and underestimate the number of signals. The more sophisticated algorithms such as AIC or MDL can correct the underestimation. The more sophisticated parameter estimation algorithms that we develop can improve the estimation accuracy.

In the next section we explore algorithms that exploit the orthogonality between the signal and noise subspaces.

## 9.3 Subspace Algorithms

### 9.3.1 Introduction

In our discussion of optimum beamformers in Chapter 6, we saw that whenever the received waveform consisted of  $D$  plane-wave signals plus uncorrelated noise, we could immediately reduce the problem from an  $N$ -dimensional problem to a  $D$ -dimensional problem. This reduction was accomplished by generating  $D$  sufficient statistics that defined a signal subspace. Once the signal subspace was created, all further processing was done in that subspace. We were able to generate the signal subspace exactly because we knew the angles of arrival of the  $D$  signals. A similar result held for correlated noise, assuming that we knew the spectral matrix of the noise.

In the parameter estimation problem, the  $D$  angles of arrival are unknown. We want to utilize the received data to estimate the signal subspace and utilize this information to estimate the angles of arrival.

We can utilize either the narrowband snapshot model in either the frequency domain or the time domain. In the frequency-domain snapshot model,

$$\mathbf{S}_x = \mathbf{V}(\psi) \mathbf{S}_f \mathbf{V}^H(\psi) + \sigma_w^2 \mathbf{I}, \quad (9.29)$$

where

$$\mathbf{V}(\psi) = \left[ \begin{array}{c|c|c|c} \mathbf{v}(\psi_1) & \mathbf{v}(\psi_2) & \cdots & \mathbf{v}(\psi_D) \end{array} \right]. \quad (9.30)$$

We assume that  $D$  is known. We want to estimate  $\psi_1, \psi_2, \dots, \psi_D$ .

The spectral matrix can be written in terms of its eigenvalues and eigenvectors as

$$\mathbf{S}_x = \sum_{i=1}^N \lambda_i \Phi_i \Phi_i^H, \quad (9.31)$$

or

$$\mathbf{S}_x = \Phi_i \Lambda \Phi_i^H, \quad (9.32)$$

where  $\Lambda = \text{diag}[\lambda_1, \lambda_2, \dots, \lambda_N]$ .

We assume the eigenvalues are in order of decreasing size. Since there are  $D$  signals,

$$\lambda_1 \geq \lambda_2 \geq \dots \geq \lambda_D > \lambda_{D+1} = \dots = \sigma_w^2. \quad (9.33)$$

We refer to the first  $D$  eigenvalues,

$$\lambda_i, \quad i = 1, 2, \dots, D, \quad (9.34)$$

as the signal-subspace eigenvalues and

$$\Phi_i, \quad i = 1, 2, \dots, D, \quad (9.35)$$

as the signal-subspace eigenvectors. Note that there is still a noise component in the signal subspace. The remaining eigenvectors define a noise subspace that does not contain any signal component.

We define these subspaces,

$$\mathbf{U}_S \triangleq \left[ \Phi_1 \mid \Phi_2 \mid \dots \mid \Phi_D \right], \quad (9.36)$$

as an  $N \times D$  matrix and

$$\mathbf{U}_N \triangleq \left[ \Phi_{D+1} \mid \Phi_{D+2} \mid \dots \mid \Phi_N \right], \quad (9.37)$$

as an  $N \times (N - D)$  matrix. Then

$$\left\| \mathbf{v}_i^H \mathbf{U}_S \right\|^2 = \sum_{j=1}^D \left| \mathbf{v}_i^H \Phi_j \right|^2 = N^{\frac{1}{2}}, \quad i = 1, 2, \dots, D, \quad (9.38)$$

and

$$\left\| \mathbf{v}_i^H \mathbf{U}_N \right\|^2 = 0, \quad i = 1, 2, \dots, D. \quad (9.39)$$

The theory of subspace processing follows directly from (9.39). We find a set of vectors that span  $\mathbf{U}_N$ . Project  $\mathbf{v}(\psi)$  onto  $\mathbf{U}_N$  for all allowable

values of  $\psi$ . The  $D$  values of  $\psi$  where the projection is zero are the desired  $\psi_1, \psi_2, \dots, \psi_D$ .

In practice, we do not know the eigenvalues and eigenvectors and must estimate them from the data. We denote the estimated spectral matrix by  $\hat{\mathbf{S}}_{\mathbf{x}}$ . It could be the sample spectral matrix  $\mathbf{C}_{\mathbf{x}}$  or, if appropriate,  $\mathbf{C}_{\mathbf{x},fb}$  as defined in (9.11).

Then, we can expand  $\hat{\mathbf{S}}_{\mathbf{x}}$ ,

$$\hat{\mathbf{S}}_{\mathbf{x}} = \sum_{i=1}^N \hat{\lambda}_i \hat{\Phi}_i \hat{\Phi}_i^H, \quad (9.40)$$

$$\hat{\mathbf{U}}_S \triangleq \left[ \begin{array}{c|c|c|c} \hat{\Phi}_1 & \hat{\Phi}_2 & \cdots & \hat{\Phi}_D \end{array} \right], \quad (9.41)$$

and

$$\hat{\mathbf{U}}_N \triangleq \left[ \begin{array}{c|c|c|c} \hat{\Phi}_{D+1} & \hat{\Phi}_{D+2} & \cdots & \hat{\Phi}_N \end{array} \right]. \quad (9.42)$$

We developed the statistics of  $\hat{\lambda}_i$  and  $\hat{\Phi}_i$  in Section 5.7.

For finite  $K$ ,  $\hat{\mathbf{U}}_S \neq \mathbf{U}_S$  and  $\hat{\mathbf{U}}_N \neq \mathbf{U}_N$ . Therefore, different choices of vectors in the estimated noise subspace will lead to different performances of the estimators. We discuss various algorithms and their performance.

The common steps are:

- (i) Use  $\hat{\mathbf{S}}_{\mathbf{x}}$  to determine  $\hat{\mathbf{U}}_N$  and  $\hat{\mathbf{U}}_S$ . In some algorithms, we also need the eigenvalues. Note that this assumes we have already estimated  $D$  using one of the techniques that was developed in Section 7.9.
- (ii) Compute a function  $\hat{Q}(\psi)$  called the null spectrum by projecting  $\mathbf{v}(\psi)$  on a particular set of vectors in  $\hat{\mathbf{U}}_N$ . Choose the  $D$  minima of  $\hat{Q}(\psi)$ . The corresponding values of  $\psi$  are the  $\hat{\psi}_i$ ,  $i = 1, 2, \dots, D$ .

Note that  $\hat{Q}(\psi)$  is a one-dimensional function so that we are no longer searching over a  $D$ -dimensional space to find  $\psi$ .

In most cases, we will use the singular value decomposition developed in Section 5.8 to compute the eigenvalues and eigenvectors directly from the data.

In Sections 9.3.2 and 9.3.3, we discuss two subspace algorithms: MUSIC and Min-Norm. In Section 9.3.3, we compare their performance. In Section 9.3.4, we derive a different type of subspace algorithm, ESPRIT, and compare its performance to that of MUSIC and Min-Norm. In Section 9.3.5, we summarize our results.

### 9.3.2 MUSIC

The first algorithm of interest is called MUSIC (Multiple Signal Classification), and was invented by Schmidt ([Sch79], [Sch81], [Sch83], [Sch86], and [SF86]) and independently by Bienvenu and Kopp [BK80], [BK83].

In Section 9.3.2.1, we develop the spectral MUSIC algorithm. In Section 9.3.2.2, we develop the root version of the MUSIC algorithm, which is applicable to standard linear arrays.

#### 9.3.2.1 Spectral MUSIC

In this case,  $\hat{Q}(\psi)$  is expressed in terms of the eigenvectors of the noise subspace

$$\hat{Q}_{MU}(\psi) = \mathbf{v}^H(\psi) \left( \sum_{i=D+1}^N \hat{\Phi}_i \hat{\Phi}_i^H \right) \mathbf{v}(\psi), \quad (9.43)$$

which can also be written as

$$\hat{Q}_{MU}(\psi) = \mathbf{v}^H(\psi) \hat{\mathbf{U}}_N \hat{\mathbf{U}}_N^H \mathbf{v}(\psi). \quad (9.44)$$

Thus, MUSIC is using a uniform weighting of the norms of the projections of  $\mathbf{v}(\psi)$  onto the estimated eigenvectors. Equivalently, in terms of the eigenvectors of the signal subspace,

$$\hat{Q}_{MU}(\psi) = \mathbf{v}^H(\psi) [\mathbf{I} - \hat{\mathbf{U}}_S \hat{\mathbf{U}}_S^H] \mathbf{v}(\psi). \quad (9.45)$$

The steps in the algorithm are:

- (1) We compute either  $\hat{\mathbf{U}}_S$  or  $\hat{\mathbf{U}}_N$  using the SVD procedure in Section 7.2.6. The choice will depend on the size of  $D$ , the number of signals compared to  $N$ , and the number of sensors. In most cases, we use  $\hat{\mathbf{U}}_S$ .
- (2) We plot  $\hat{Q}_{MU}(\psi)$  by varying  $\mathbf{v}(\psi)$  over  $-\pi \leq \psi \leq \pi$  and choose the  $D$  minima.

In order to implement MUSIC, we need enough snapshots to get a reasonable estimate of  $\hat{\mathbf{S}}_x$  and we have to know the array manifold  $\mathbf{v}(\psi)$ . Note that spectral MUSIC is applicable to arbitrary array geometry and its extension to  $\psi = [\psi_x \psi_y]^T$  is straightforward.

For standard linear arrays, the root MUSIC algorithm is applicable.

### 9.3.2.2 Root MUSIC

For a standard linear array, we can use a polynomial representation. The array manifold polynomial vector is defined as

$$\mathbf{v}_z(z) = \begin{bmatrix} 1 & z & \cdots & z^{N-1} \end{bmatrix}^T, \quad (9.46)$$

which is the array manifold vector, with a phase shift, evaluated at  $z = \exp(j\psi)$ ,

$$[\mathbf{v}_z(z)]_{z=e^{j\psi}} = e^{j(\frac{N-1}{2})\psi} \mathbf{v}(\psi). \quad (9.47)$$

Then, (9.44) can be written as

$$\begin{aligned} \hat{Q}_{MU,z}(z) &= \mathbf{v}_z^T \left( \frac{1}{z} \right) \hat{\mathbf{U}}_N \hat{\mathbf{U}}_N^H \mathbf{v}_z(z) \\ &= \mathbf{v}_z^T \left( \frac{1}{z} \right) \left[ 1 - \hat{\mathbf{U}}_S \hat{\mathbf{U}}_S^H \right] \mathbf{v}_z(z). \end{aligned} \quad (9.48)$$

If the eigendecomposition corresponded to the true spectral matrix, then the exact MUSIC spectrum could be obtained by evaluating  $\hat{Q}_{MU,z}(z)$  on the unit circle,

$$\hat{Q}_{MU,z}(z)|_{z=e^{j\psi}} = \hat{Q}_{MU}(\psi), \quad (9.49)$$

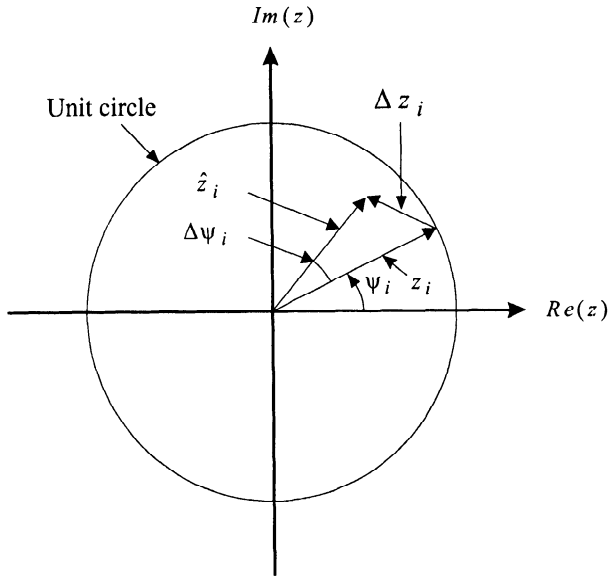
and the  $D$  roots would correspond to the location in  $\psi$ -space of the  $D$  signals. In practice, we compute the roots of  $\hat{Q}_{MU,z}(z)$  and choose the  $D$  roots that are inside the unit circle and closest to the unit circle.

We denote these roots by  $\hat{z}_i, i = 1, 2, \dots, D$ . Then

$$\hat{\psi}_i = \frac{\arg \hat{z}_i}{\pi}, \quad i = 1, 2, \dots, D. \quad (9.50)$$

Since we are using an estimated covariance matrix, there will be errors in the location of roots. The effect of this error is shown in Figure 9.8. We observe that the radial component of the error  $\Delta z_i$  will not affect  $\hat{\psi}_i$ . However, it would distort the MUSIC spectrum. Thus, we would expect that spectral MUSIC will have less resolution capability than root MUSIC. We investigate this behavior analytically in the asymptotic region in Section 9.5.

For a standard linear array, the performance can be improved by using FB averaging of the data, as in (9.11), to obtain  $\mathbf{C}_{\mathbf{x},fb}$ . The corresponding

Figure 9.8 Behavior of roots in  $z$ -plane.

subspace decomposition is

$$\begin{aligned}\hat{\mathbf{S}}_{\mathbf{x},fb} \triangleq \mathbf{C}_{\mathbf{x},fb} &= \sum_{i=1}^N \hat{\lambda}_{i,fb} \hat{\Phi}_{i,fb} \hat{\Phi}_{i,fb}^H \\ &= \hat{\mathbf{U}}_{S,fb} \hat{\Lambda}_{S,fb} \hat{\mathbf{U}}_{S,fb}^H + \hat{\mathbf{U}}_{N,fb} \hat{\Lambda}_{N,fb} \hat{\mathbf{U}}_{N,fb}^H.\end{aligned}\quad (9.51)$$

Then, the FB root MUSIC polynomial can be written as

$$\begin{aligned}\hat{\mathbf{Q}}_{MU,fb,z}(z) &= \mathbf{v}_z^T \left( \frac{1}{z} \right) \hat{\mathbf{U}}_{N,fb} \hat{\mathbf{U}}_{N,fb}^H \mathbf{v}_z(z) \\ &= \mathbf{v}_z^T \left( \frac{1}{z} \right) \left[ 1 - \hat{\mathbf{U}}_{S,fb} \hat{\mathbf{U}}_{S,fb}^H \right] \mathbf{v}_z(z).\end{aligned}\quad (9.52)$$

We find the roots of  $\hat{\mathbf{Q}}_{MU,fb,z}(z)$  and proceed as in the forward-only root MUSIC algorithm.

### 9.3.2.3 Unitary root MUSIC

The forward-backward root MUSIC algorithm can be implemented with real computation by using a unitary transformation. This approach is due to Pesavento et al. [PGH00] and our discussion follows that reference.

We define a real-valued sample spectral matrix,

$$\mathbf{C}_{\mathbf{x},Re} = \mathbf{Q}^H \mathbf{C}_{\mathbf{x},fb} \mathbf{Q}, \quad (9.53)$$

where  $\mathbf{Q}$  can be any unitary, column conjugate symmetric matrix. In the text, we will always use the sparse matrices introduced in (7.58) and (7.59),

$$\mathbf{Q} = \frac{1}{\sqrt{2}} \begin{bmatrix} \mathbf{I} & j\mathbf{I} \\ \mathbf{J} & -j\mathbf{J} \end{bmatrix}, \quad (9.54)$$

for  $N$  even, and

$$\mathbf{Q} = \frac{1}{\sqrt{2}} \begin{bmatrix} \mathbf{I} & \mathbf{0} & j\mathbf{I} \\ \mathbf{0}^T & \sqrt{2} & \mathbf{0}^T \\ \mathbf{J} & \mathbf{0} & -j\mathbf{J} \end{bmatrix}, \quad (9.55)$$

for  $N$  odd.

Note that

$$\mathbf{C}_{\mathbf{x},Re} = \frac{1}{2} [\mathbf{Q}^H \mathbf{C}_{\mathbf{x}} \mathbf{Q} + \mathbf{Q}^H \mathbf{J} \mathbf{C}_{\mathbf{x}}^* \mathbf{J} \mathbf{Q}]. \quad (9.56)$$

Using

$$\mathbf{J} \mathbf{Q}^* = \mathbf{Q}, \quad (9.57)$$

(9.56) can be written as

$$\begin{aligned} \mathbf{C}_{\mathbf{x},Re} &= \frac{1}{2} [\mathbf{Q}^H \mathbf{C}_{\mathbf{x}} \mathbf{Q} + [\mathbf{Q}^*]^H \mathbf{C}_{\mathbf{x}}^* \mathbf{Q}^*] \\ &= Re [\mathbf{Q}^H \mathbf{C}_{\mathbf{x}} \mathbf{Q}]. \end{aligned} \quad (9.58)$$

We denote the eigenvalues and eigenvectors of  $\mathbf{C}_{\mathbf{x},Re}$  by  $\hat{\lambda}_{i,Re}$  and  $\hat{\phi}_{i,Re}$ , respectively. They satisfy the characteristic equation,

$$\mathbf{C}_{\mathbf{x},Re} \hat{\phi}_{Re} = \hat{\lambda}_{Re} \hat{\phi}_{Re}. \quad (9.59)$$

The eigenvalues and eigenvectors of  $\hat{\mathbf{C}}_{\mathbf{x},fb}$  are denoted by  $\hat{\lambda}_{i,fb}$  and  $\hat{\phi}_{i,fb}$ , respectively. They satisfy the characteristic equation,

$$\mathbf{C}_{\mathbf{x},fb} \hat{\phi}_{fb} = \hat{\lambda}_{fb} \hat{\phi}_{fb}. \quad (9.60)$$

Pre-multiplying (9.60) by  $\mathbf{Q}^H$  gives

$$\mathbf{Q}^H \mathbf{C}_{\mathbf{x},fb} \hat{\phi}_{fb} = \mathbf{Q}^H \mathbf{C}_{\mathbf{x},fb} \mathbf{Q} \mathbf{Q}^H \hat{\phi}_{fb} = \hat{\lambda}_{fb} \mathbf{C}_{\mathbf{x},Re} \mathbf{Q}^H \hat{\phi}_{fb}, \quad (9.61)$$

which is (9.59) with

$$\hat{\phi}_{Re} = \mathbf{Q}^H \hat{\phi}_{fb}, \quad (9.62)$$

and

$$\hat{\lambda}_{Re} = \hat{\lambda}_{fb}. \quad (9.63)$$

The subspace decomposition of the real matrix  $\mathbf{C}_{x,Re}$  can be written as

$$\mathbf{C}_{x,Re} = \hat{\mathbf{U}}_{S,Re} \hat{\Lambda}_{S,Re} \hat{\mathbf{U}}_{S,Re}^H + \hat{\mathbf{U}}_{N,Re} \hat{\Lambda}_{N,Re} \hat{\mathbf{U}}_{N,Re}^H, \quad (9.64)$$

and corresponds to the subspace decomposition in (9.51) through the relation in (9.62) and (9.63). The FB MUSIC polynomial in (9.52) can be written as

$$\begin{aligned} \hat{Q}_{MU,fb,z}(z) &= \mathbf{v}_z^T \left( \frac{1}{z} \right) \mathbf{Q} \mathbf{Q}^H \hat{\mathbf{U}}_{N,fb} \hat{\mathbf{U}}_{N,fb}^H \mathbf{v}_z(z) \\ &= \mathbf{v}_z^T \left( \frac{1}{z} \right) \mathbf{Q} \hat{\mathbf{U}}_{N,Re} \hat{\mathbf{U}}_{N,Re}^H \mathbf{Q}^H \mathbf{v}_z(z) \\ &= \tilde{\mathbf{v}}_z^T \left( \frac{1}{z} \right) \hat{\mathbf{U}}_{N,Re} \hat{\mathbf{U}}_{N,Re}^H \tilde{\mathbf{v}}_z(z) \\ &\triangleq \hat{Q}_{MU,U,z}(z), \end{aligned} \quad (9.65)$$

where the array manifold polynomial is

$$\tilde{\mathbf{v}}_z(z) \triangleq \mathbf{Q}^H \mathbf{v}_z(z). \quad (9.66)$$

The steps in unitary root MUSIC can be summarized:

1. Compute the real sample spectral matrix  $\mathbf{C}_{x,Re}$  using (9.58),
2. Perform the eigendecomposition in (9.64),
3. Compute  $\hat{Q}_{MU,U,z}(z)$  using (9.65) and (9.66),
4. Find the roots of  $\hat{Q}_{MU,U,z}(z)$  and choose the  $D$  roots that are inside the unit circle and closest to the unit circle. Denote these roots as  $\hat{z}_i, i = 1, \dots, D$ ,
5. The estimates are

$$\hat{\psi}_i = \arg \hat{z}_i, \quad i = 1, \dots, D. \quad (9.67)$$

The advantage of unitary root MUSIC is that it has the same performance as FB root MUSIC. It provides a significant reduction in computational complexity. In order to achieve this reduction, an efficient polynomial root-finding algorithm must be used.<sup>6</sup> The Lang-Frenzel algorithm ([LF94]) is used in our examples.

Pesavento et al. [PGH00] have derived closed-form expressions for the large sample mean-square estimation error of unitary root MUSIC.

Before we do any examples of the MUSIC algorithm, we derive a second subspace algorithm.

### 9.3.3 Minimum-Norm Algorithm

A second algorithm of interest is called the Min-Norm algorithm. It was first developed by Reddi [Red79]. The minimum-norm property and a better motivation for the algorithm was presented by Kumaresan and Tufts [KT83]. Our derivation follows this latter reference.

The signal subspace is spanned by the columns of  $\mathbf{V}$  (see (9.2)). We define a vector

$$\mathbf{d} = \begin{bmatrix} d_1 & d_2 & \cdots & d_N \end{bmatrix}^T \quad (9.68)$$

that has the property that,

$$\mathbf{v}^H(\psi_i) \mathbf{d} = 0, \quad i = 1, 2, \dots, D, \quad (9.69)$$

or equivalently,

$$\Phi_i^H \mathbf{d} = 0, \quad i = 1, 2, \dots, D. \quad (9.70)$$

Then, the polynomial,

$$D(z) = \sum_{k=1}^N d_k z^{-(k-1)} \quad (9.71)$$

has zeros at

$$z_k = \exp(j\psi_k), \quad i = 1, 2, \dots, D. \quad (9.72)$$

As we discussed in Section 9.3.1, the  $N - D$  noise eigenvectors all have this property (i.e., satisfy (9.69) and (9.70)) and span the noise subspace.<sup>7</sup> The MUSIC algorithm utilizes all of the noise subspace eigenvectors. In the Min-Norm algorithm, Kumaresen and Tufts propose to use a single vector

---

<sup>6</sup>This suggestion was due to A. Gershmann (private communication). The unitary root MUSIC examples were done by D. Bray using a slightly improved version of the LF algorithm.

<sup>7</sup>This use of this property was first proposed by Pisarenko ([Pis72], [Pis73]).

$\mathbf{d}$  in the noise subspace. They hypothesize that the estimate of  $\psi_k$  will be more accurate and that the  $N - D$  “noise” zeros will tend to be uniformly distributed within the unit circle and will be less likely to generate false sources.

We want to find  $\mathbf{d}$  as a linear combination of the  $N - D$  noise eigenvectors. Then, if  $\mathbf{S}_x$  were known exactly,  $D(z)$  will have its zeros at  $\psi_1, \psi_2, \dots, \psi_D$ .

We require that  $d_1$  equal unity and minimize

$$Q \triangleq \sum_{k=1}^N |d_k|^2, \quad d_1 = 1. \quad (9.73)$$

It is useful to discuss why this particular choice of  $\mathbf{d}$  is logical (e.g., Kumaresen [Kum83]). We factor  $D(z)$  into two polynomials,

$$D(z) = D_1(z) D_2(z), \quad (9.74)$$

where

$$D_1(z) = \sum_{k=1}^D a_k z^{-(k-1)}, \quad a_1 = 1, \quad (9.75)$$

has the signal zeros, and

$$D_2(z) = \sum_{k=1}^{N-D} b_k z^{-(k-1)}, \quad b_1 = 1, \quad (9.76)$$

has the noise zeros. Minimizing  $Q$  is the same as minimizing

$$\int_{-\pi}^{\pi} |D(e^{j\psi})|^2 d\psi. \quad (9.77)$$

This is equivalent to minimizing  $D_2(z)$  given  $D_1(z)$ . Using the analogy to linear prediction [Mak75], Kumaresen [Kum83] shows that the zeros of  $\hat{D}_2(z)$  always has zeros inside the unit circle that are independent of the zeros of  $\hat{D}_1(z)$  and they are approximately uniformly distributed in the sectors where the  $D$  signal zeros are absent.

We now find  $D(z)$  in terms of the estimated signal or noise eigenvectors. First, partition  $\mathbf{d}$ ,

$$\mathbf{d} = \begin{bmatrix} 1 \\ \mathbf{d}' \end{bmatrix}. \quad (9.78)$$

Next, we partition the signal subspace matrix  $\widehat{\mathbf{U}}_S$  as

$$\widehat{\mathbf{U}}_S = \begin{bmatrix} \mathbf{g}^T \\ \widehat{\mathbf{U}}'_S \end{bmatrix}, \quad (9.79)$$

where  $\mathbf{g}$  has the first elements of each of the signal eigenvectors. We partition the noise subspace matrix  $\widehat{\mathbf{U}}_N$  as

$$\widehat{\mathbf{U}}_N = \begin{bmatrix} \mathbf{c}^T \\ \widehat{\mathbf{U}}'_N \end{bmatrix}, \quad (9.80)$$

where  $\mathbf{c}$  has the first elements of each of the noise eigenvectors. From (9.70),  $\mathbf{d}$  will be orthogonal to the columns of  $\widehat{\mathbf{U}}_S$ ,

$$\widehat{\mathbf{U}}_S^H \mathbf{d} = 0. \quad (9.81)$$

Substituting (9.78) and (9.79) into (9.81) gives

$$[\widehat{\mathbf{U}}'_S]^H \mathbf{d}' = -\mathbf{g}^*. \quad (9.82)$$

Now, minimizing  $\mathbf{d}'$  subject to the constraint in (9.82). This is a familiar minimization subject to linear constraint. The minimum-norm value of  $\mathbf{d}'$  is

$$\mathbf{d}' = -\widehat{\mathbf{U}}'_S \left( [\widehat{\mathbf{U}}'_S]^H \widehat{\mathbf{U}}'_S \right)^{-1} \mathbf{g}^*. \quad (9.83)$$

From the definition in (9.79), we observe that

$$[\widehat{\mathbf{U}}'_S]^H \widehat{\mathbf{U}}'_S = \mathbf{I} - \mathbf{g}^* \mathbf{g}^T. \quad (9.84)$$

Using the matrix inversion lemma,

$$\left( [\widehat{\mathbf{U}}'_S]^H \widehat{\mathbf{U}}'_S \right)^{-1} = \mathbf{I} + \frac{\mathbf{g}^* \mathbf{g}^T}{1 - \mathbf{g}^T \mathbf{g}^*}. \quad (9.85)$$

Substituting (9.85) into (9.83) gives

$$\mathbf{d}' = -\frac{\widehat{\mathbf{U}}'_S \mathbf{g}^*}{1 - \mathbf{g}^T \mathbf{g}}, \quad (9.86)$$

or

$$\mathbf{d} = \begin{bmatrix} 1 \\ \frac{\widehat{\mathbf{U}}'_S \mathbf{g}^*}{1 - \mathbf{g}^T \mathbf{g}} \end{bmatrix}. \quad (9.87)$$

We can also express  $\mathbf{d}$  in terms of the noise eigenvectors.

Since

$$\widehat{\mathbf{U}} \widehat{\mathbf{U}}^H = \mathbf{I}, \quad (9.88)$$

$$\left[ \begin{array}{c|c} \widehat{\mathbf{U}}_S & \widehat{\mathbf{U}}_N \end{array} \right] \left[ \begin{array}{c} \widehat{\mathbf{U}}_S^H \\ \widehat{\mathbf{U}}_N^H \end{array} \right] = \mathbf{I}, \quad (9.89)$$

and

$$\left[ \begin{array}{c|c} \mathbf{g}^T & \mathbf{c}^T \\ \hline \widehat{\mathbf{U}}_S' & \widehat{\mathbf{U}}_N' \end{array} \right] \left[ \begin{array}{c|c} \mathbf{g}^* & [\widehat{\mathbf{U}}_S']^H \\ \hline \mathbf{c}^* & [\widehat{\mathbf{U}}_N']^H \end{array} \right] = \mathbf{I}. \quad (9.90)$$

Thus,

$$\mathbf{d} = \begin{bmatrix} 1 \\ \hline \frac{\widehat{\mathbf{U}}_N' \mathbf{c}^*}{\mathbf{c}^H \mathbf{c}} \end{bmatrix}. \quad (9.91)$$

We observe that we can also write

$$\mathbf{d} = \widehat{\mathbf{U}}_N \frac{\mathbf{c}^*}{|\mathbf{c}|^2}. \quad (9.92)$$

If we define

$$\mathbf{w}^{\frac{1}{2}} = \frac{\mathbf{c}^*}{|\mathbf{c}|^2}, \quad (9.93)$$

then

$$\mathbf{d} = \widehat{\mathbf{U}}_N \mathbf{w}^{\frac{1}{2}}. \quad (9.94)$$

Then the Min-Norm null spectra can be written as

$$Q_{MN}(\psi) \triangleq \left| \mathbf{v}^H(\psi) \mathbf{d} \right|^2 \triangleq \mathbf{v}^H(\psi) \widehat{\mathbf{U}}_N \mathbf{W} \widehat{\mathbf{U}}_N^H \mathbf{v}(\psi), \quad (9.95)$$

where

$$\mathbf{W} = \mathbf{w}^{\frac{1}{2}} \mathbf{w}^{\frac{H}{2}} \quad (9.96)$$

and interpreted as a weighted eigenspace algorithm. It is sometimes referred to in the literature as a weighted MUSIC algorithm. Comparisons of MUSIC and Min-Norm are contained Xu and Kaveh [XK96] and Kaveh and Bassias [KB90].

The Min-Norm null spectra can also be written in terms of signal subspace eigenvectors,

$$Q_{MN}(\psi) \triangleq |\mathbf{v}^H(\psi)\mathbf{d}|^2 = \mathbf{v}^H(\psi)\widehat{\mathbf{U}}_S\mathbf{W}_S\widehat{\mathbf{U}}_S^H\mathbf{v}(\psi), \quad (9.97)$$

where

$$\mathbf{d} = \widehat{\mathbf{U}}_S \frac{\mathbf{g}^*}{1 - \mathbf{g}^H \mathbf{g}}, \quad (9.98)$$

and

$$\mathbf{w}^{\frac{1}{2}} = \frac{\mathbf{g}^*}{1 - \mathbf{g}^H \mathbf{g}}. \quad (9.99)$$

For root Min-Norm we calculate  $\mathbf{d}$  using (9.92) and then form the polynomial

$$D(z) = 1 + d_1 z^{-1} + \cdots + d_N z^{-N}, \quad (9.100)$$

and compute the roots of  $D(z)$ . We choose the  $D$  roots that are closest to the unit circle in the  $z$ -plane. It turns out that the difference in performance between spectral Min-Norm and root Min-Norm is not as great as the difference between spectral MUSIC and root MUSIC (e.g., [RH89b]).

We now consider the same models as in Examples 9.2.3 and 9.2.5, and use the MUSIC and Min-Norm algorithms to estimate the directions of arrival in  $\psi$ -space.

#### Example 9.3.1 (continuation)

Consider a standard 10-element linear array and assume there are two uncorrelated plane-wave signals impinging on the array from  $\pm\Delta\psi/2$ . Assume  $\Delta\psi = \Delta\psi_R$ . We simulate the four algorithms derived above: MUSIC, root MUSIC, Min-Norm, and root Min-Norm. We use  $\mathbf{C}_{x,f_b}$ .

In Figure 9.9, we show the probability of resolution versus  $ASNR$  for  $K = 100$  ( $10N$ ). In Figure 9.10, we show the normalized RMSE versus  $ASNR$ . We see that spectral Min-Norm has better resolution behavior than spectral MUSIC. However, root MUSIC has better resolution behavior than root Min-Norm. The threshold of root MUSIC occurs when the  $ASNR = 7-8$  dB. Above threshold, MUSIC and root MUSIC approach the CRB. (In Section 9.5, we show that the ratio of the MUSIC variance to the CRB is  $(1+ASNR^{-1})$  for large  $K$  and  $ASNR$ .) However, the Min-Norm RMSE remains about 2.5 dB above the bound.

In Figure 9.11, we plot the normalized RMSE versus  $K$  for an  $ASNR = 20$  dB. Spectral Min-Norm has better threshold performance than spectral MUSIC, but it remains about 2.5 dB above the CRB. For this  $ASNR$ , both root algorithms are above threshold for  $K = 10$  ( $K = N$ ). Root MUSIC approaches the CRB bound, while root Min-Norm remains 1.9 dB above it.

#### Example 9.3.2 (continuation)

We consider the same model as in Example 9.3.1 except  $\rho = 0.95$ . In Figure 9.12, we show the probability of resolution versus  $ASNR$ , and in Figure 9.13, we plot the normalized

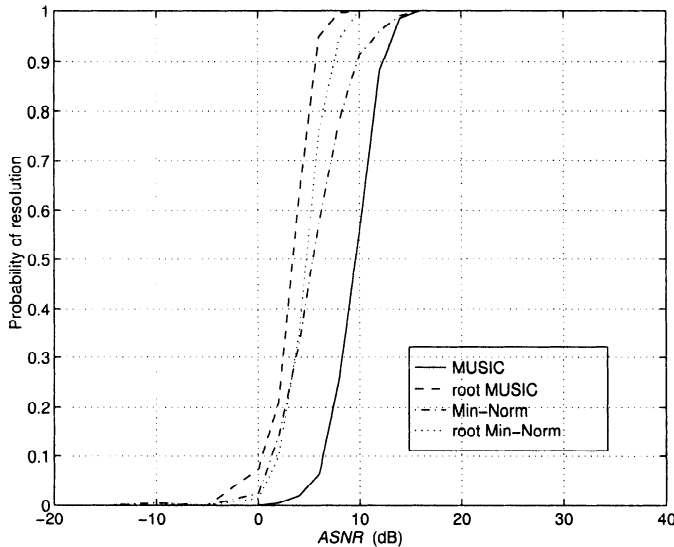


Figure 9.9 MUSIC and Min-Norm algorithms: probability of resolution versus  $ASNR$ ;  $N = 10$ ,  $\Delta\psi = \Delta\psi_R$ ,  $\rho = 0$ ,  $K = 100, 200$  trials.

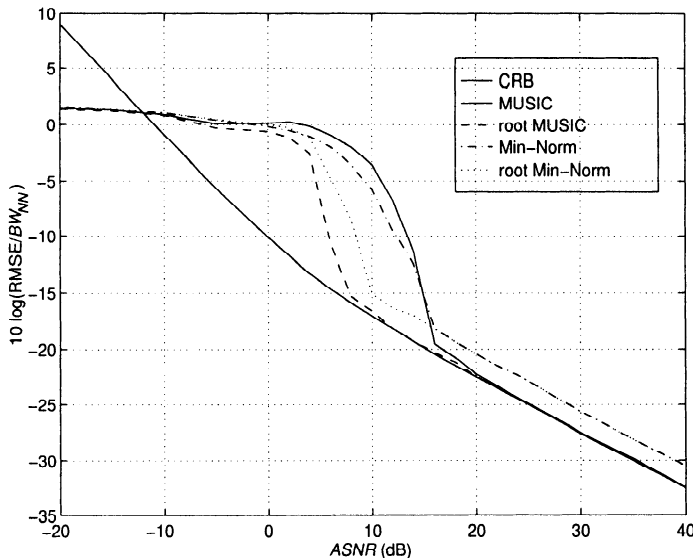


Figure 9.10 MUSIC and Min-Norm algorithms: normalized RMSE versus  $ASNR$ ;  $N = 10$ ,  $\Delta\psi = \Delta\psi_R$ ,  $\rho = 0$ ,  $K = 100, 200$  trials.

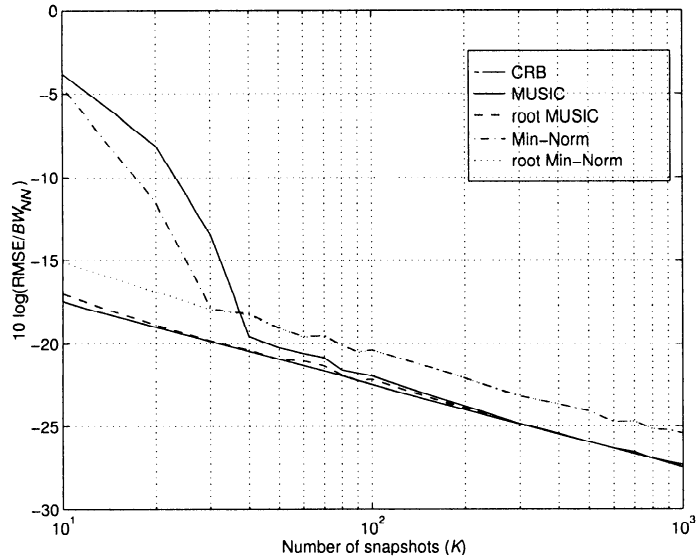


Figure 9.11 MUSIC and Min-Norm algorithms: normalized RMSE versus  $K : N = 10$ ,  $ASNR = 20$  dB,  $\Delta\psi = \Delta\psi_R$ ,  $\rho = 0$ , 200 trials.

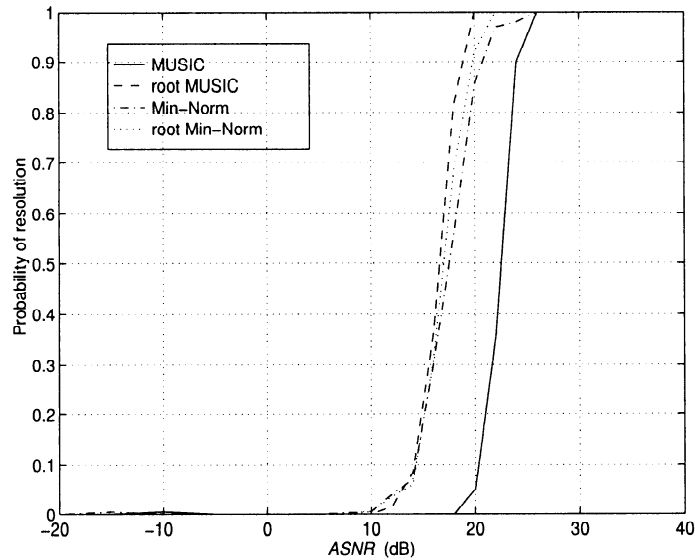


Figure 9.12 MUSIC and Min-Norm algorithms: probability of resolution versus  $ASNR$ ;  $N = 10$ ,  $\Delta\psi = \Delta\psi_R$ ,  $\rho = 0.95$ ,  $K = 100$ , 200 trials.

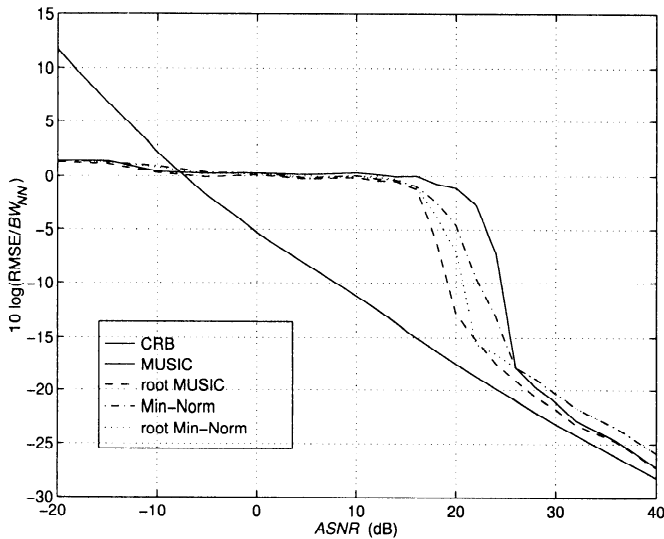


Figure 9.13 MUSIC and Min-Norm algorithms: normalized RMSE versus  $ASNR$ ;  $N = 10$ ,  $\Delta\psi = \Delta\psi_R$ ,  $\rho = 0.95$ ,  $K = 100$ , 200 trials.

RMSE versus  $ASNR$ . The results are similar to those in Example 9.3.1, except the curves are shifted to the right by about 15 dB.

#### Example 9.3.3

Consider the same model as in Example 9.3.1 except  $\Delta\psi = 2.0BW_{NN}$ . The normalized RMSE is shown in Figure 9.14.

#### 9.3.4 ESPRIT

In this section we discuss a subspace algorithm referred to as **ESPRIT** for “Estimation of Signal Parameter via Rotational Invariance Techniques”. It was derived by Roy and is described in detail in his doctoral dissertation [Roy87], as well as several other publications ([RK89], [RPK86], [PRK86], [OK90], [RK87], and [OVK91]).

One version of ESPRIT (least squares) is identical to the Toeplitz approximation method (TAM) used earlier by Kung et al. [KLF86] for direction finding (e.g., Mayrargue [May88] and Rao and Hari [RH89a]).

There are several versions of ESPRIT. In the text, we discuss three versions. In Section 9.3.4.1, we discuss LS (least squares) and TLS (total least squares) ESPRIT. In Section 9.3.4.2, we discuss unitary ESPRIT. In Sec-

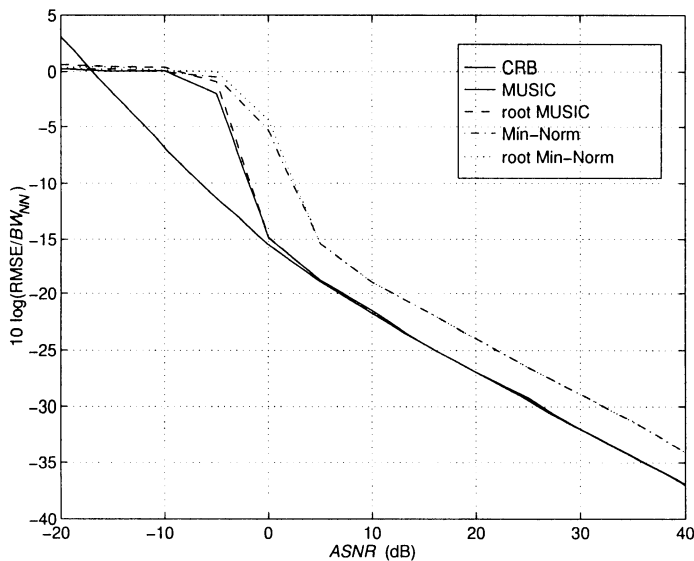


Figure 9.14 MUSIC and Min-Norm algorithms: normalized RMSE versus ASNR;  $N = 10$ ,  $\Delta\psi = 2BW_{NN}$ ,  $\rho = 0$ ,  $K = 100$ , 200 trials.

tion 9.3.4.3, we summarize our ESPRIT results and discuss some related algorithms.

### 9.3.4.1 LS and TLS ESPRIT

In this section, we develop the ESPRIT algorithm in the context of a uniform linear array. Our discussion follows Ottersten et al. [OVK91].

We consider the standard  $N$ -element linear array. In Figure 9.15, we show a 10-element array. The first step in the ESPRIT algorithm is to choose two identical subarrays. The number of elements in the subarrays is denoted by  $N_s$  and  $N_s \geq D + 1$  where  $D$  is the number of signals. We assume that the first element in the original array is the first element in the first subarray and that the  $(d_s + 1)$ th element in the original array is the first element in the second subarray. The parameter  $d_s$  denotes the distance between the subarrays measured in  $\Delta p$  units ( $\Delta p$  is interelement spacing). The first set of subarrays in Figure 9.15 shows the case of two overlapping subarrays with  $d_s = 1$ . The second set of subarrays in Figure 9.15 shows the case of two overlapping subarrays with  $d_s = 3$ . The third set of subarrays in Figure 9.15 shows the case of two non-overlapping subarrays with  $d_s = 5$ . In Figure 9.16, the case of two non-overlapping subarrays with  $d_s = 1$  is

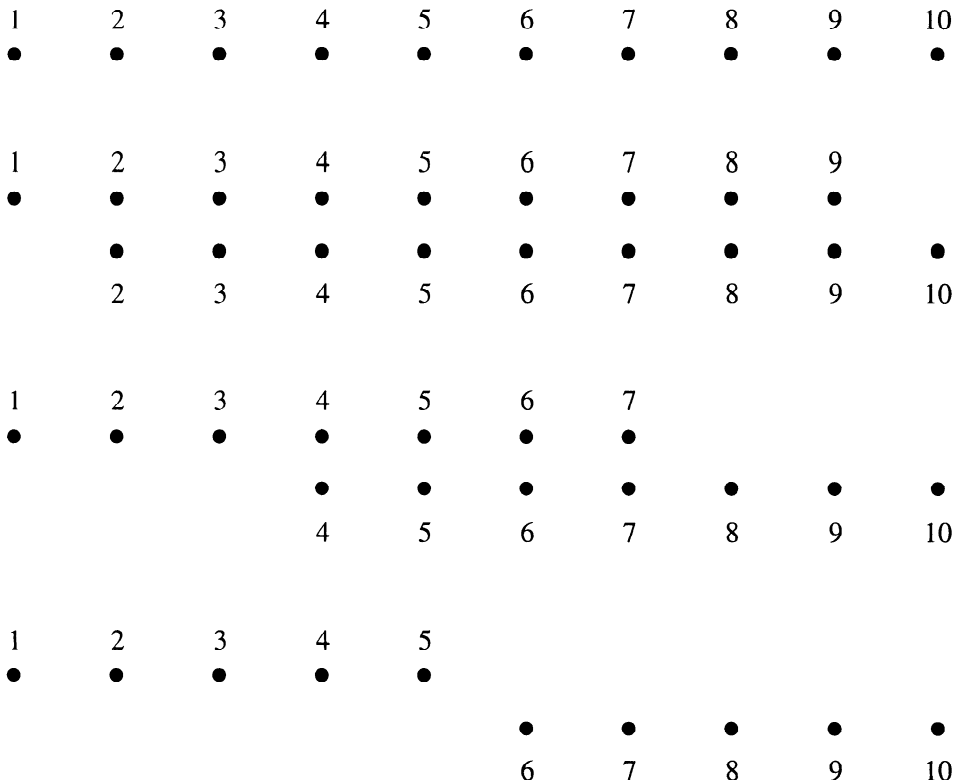


Figure 9.15 Subarrays for ESPRIT algorithm.

shown. In this case, the element spacing in the subarrays is  $\lambda$  so we would anticipate ambiguity problems.

We can specify the subarrays by use of a selection matrix  $\mathbf{J}_s$ . We begin by defining the non-zero component, which we denote by  $\tilde{\mathbf{J}}_s$ . For the first set of subarrays in Figure 9.15,  $\tilde{\mathbf{J}}_s$  is a  $9 \times 9$  identity matrix. For the second set of subarrays in Figure 9.15,  $\tilde{\mathbf{J}}_s$  is a  $7 \times 7$  identity matrix. For the third set of subarrays in Figure 9.15,  $\tilde{\mathbf{J}}_s$  is a  $5 \times 5$  identity matrix. For the general case corresponding to Figure 9.15,  $\tilde{\mathbf{J}}_s$  is an  $N_s \times N_s$  identity matrix where  $N_s$  is the length of the subarray.

We now define the  $N_s \times N$  selection matrices for the subarrays in Figure 9.15 ,

$$\mathbf{J}_{s1} \triangleq \left[ \begin{array}{c|c} \tilde{\mathbf{J}}_s & \mathbf{0}_{N_s \times d_s} \end{array} \right], \quad (9.101)$$

and,

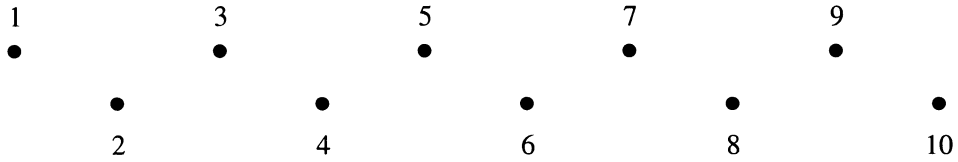


Figure 9.16 Subarray for ESPRIT algorithm.

$$\mathbf{J}_{s2} \triangleq \left[ \mathbf{0}_{N_s \times d_s} \mid \tilde{\mathbf{J}}_s \right]. \quad (9.102)$$

For the subarray choice in Figure 9.16,  $\mathbf{J}_s$  is a  $5 \times 9$  matrix,

$$\mathbf{J}_s = \begin{bmatrix} 1 & 0 & 0 & \cdots & & 0 \\ 0 & 0 & 1 & 0 & \cdots & 0 \\ 0 & 0 & 0 & 0 & 1 & \cdots 0 \\ \vdots & \vdots & \vdots & \vdots & \ddots & \cdots \vdots \\ 0 & \cdots & & & & 1 \end{bmatrix}. \quad (9.103)$$

If we denote the array manifold matrix of the total array as  $\mathbf{V}$  and the array manifold matrix of the  $i$ th subarray ( $i = 1, 2$ ) as  $\mathbf{V}_i$ , then

$$\mathbf{V}_1 = \mathbf{J}_{s1}\mathbf{V}, \quad (9.104)$$

and

$$\mathbf{V}_2 = \mathbf{J}_{s2}\mathbf{V}. \quad (9.105)$$

The ESPRIT algorithm exploits the shift invariance property of the array, which implies

$$\mathbf{V}_2 = \mathbf{V}_1\Phi, \quad (9.106)$$

where

$$\Phi \triangleq \text{diag} \left[ e^{jds\psi_1}, e^{jds\psi_2}, \dots, e^{jds\psi_D} \right], \quad (9.107)$$

for the subarrays in Figure 9.15. The  $\psi_i, i = 1, 2, \dots, D$  are the wavenumbers of the  $D$  signals in  $\psi$ -space. The source spectral matrix and the steering matrix are assumed to have full rank  $D$ . This restriction does not allow fully correlated signals. For the subarrays in Figure 9.16, each exponent is multiplied by 2. The ESPRIT algorithm will find an estimate of  $\Phi$  and use that estimate to estimate  $\psi_1, \dots, \psi_D$ .

The columns of  $\mathbf{V}$  span the signal subspace, therefore, we have the relationship

$$\mathbf{U}_s = \mathbf{V}\mathbf{T}, \quad (9.108)$$

where  $\mathbf{T}$  is a non-singular  $D \times D$  matrix. This relationship says that the signal subspace eigenvectors are linear combinations of the array manifold vectors of the  $D$  sources.

Selecting subarray signal subspaces gives

$$\mathbf{U}_{s1} \triangleq \mathbf{J}_{s1}\mathbf{U}_s = \mathbf{J}_{s1}\mathbf{V}\mathbf{T} = \mathbf{V}_1\mathbf{T}, \quad (9.109)$$

and

$$\mathbf{U}_{s2} \triangleq \mathbf{J}_{s2}\mathbf{U}_s = \mathbf{J}_{s2}\mathbf{V}\mathbf{T} = \mathbf{V}_2\mathbf{T}. \quad (9.110)$$

The relation

$$\mathbf{U}_{s1} = \mathbf{V}_1\mathbf{T} \quad (9.111)$$

implies

$$\mathbf{V}_1 = \mathbf{U}_{s1}\mathbf{T}^{-1}. \quad (9.112)$$

Similarly,

$$\mathbf{U}_{s2} = \mathbf{V}_2\mathbf{T} = \mathbf{V}_1\Phi\mathbf{T} \quad (9.113)$$

implies

$$\mathbf{U}_{s2} = \mathbf{U}_{s1}\mathbf{T}^{-1}\Phi\mathbf{T}. \quad (9.114)$$

We define

$$\Psi = \mathbf{T}^{-1}\Phi\mathbf{T}. \quad (9.115)$$

Note that the eigenvalues of  $\Psi$  are the elements of  $\Phi$ . Thus, if we obtain an estimate of  $\Psi$  and compute its eigenvalues, we can obtain an estimate of  $\psi_1, \dots, \psi_D$ .

The equivalent relationship to  $\mathbf{V}_2 = \mathbf{V}_1\Phi$  in terms of signal subspace eigenvectors is

$$\mathbf{U}_{s1}\Psi = \mathbf{U}_{s2}. \quad (9.116)$$

Since  $N_s$  is greater than  $D$ , this is an overdetermined set of equations. In practice, we have estimates for  $\mathbf{U}_{s2}$  and  $\mathbf{U}_{s1}$

$$\hat{\mathbf{U}}_{s1} = \mathbf{J}_{s1}\hat{\mathbf{U}}_s, \quad (9.117)$$

and

$$\hat{\mathbf{U}}_{s2} = \mathbf{J}_{s2}\hat{\mathbf{U}}_s. \quad (9.118)$$

Then (9.116) is replaced by

$$\hat{\mathbf{U}}_{s1}\hat{\Psi} = \hat{\mathbf{U}}_{s2}. \quad (9.119)$$

If we solve (9.119) using a least squares approach, then we minimize the difference between  $\hat{\mathbf{U}}_{s2}$  and  $\hat{\mathbf{U}}_{s1}\hat{\Psi}$ ,

$$\begin{aligned}\hat{\Psi}_{LS} &= \arg \min_{\Psi} \left\{ \left\| \hat{\mathbf{U}}_{s2} - \hat{\mathbf{U}}_{s1}\Psi \right\|_F \right\} \\ &= \arg \min_{\Psi} \left\{ \text{tr} \left\{ \left[ \hat{\mathbf{U}}_{s2} - \hat{\mathbf{U}}_{s1}\Psi \right]^H \left[ \hat{\mathbf{U}}_{s2} - \hat{\mathbf{U}}_{s1}\Psi \right] \right\} \right\} \quad (9.120)\end{aligned}$$

The result is

$$\hat{\Psi}_{LS} = [\hat{\mathbf{U}}_{s1}^H \hat{\mathbf{U}}_{s1}]^{-1} \hat{\mathbf{U}}_{s1}^H \hat{\mathbf{U}}_{s2}. \quad (9.121)$$

The steps in the LS-ESPRIT algorithm can be summarized:

1. Perform the eigendecomposition on  $\mathbf{C}_x$  to obtain  $\hat{\mathbf{U}}_s$ ,
2. Find  $\hat{\mathbf{U}}_{s1}$  and  $\hat{\mathbf{U}}_{s2}$  by using (9.109) and (9.110),
3. Find  $\hat{\Psi}_{LS}$  using (9.121),
4. Find the eigenvalues of  $\hat{\Psi}_{LS}$  denoted by  $\hat{\lambda}_1, \hat{\lambda}_2, \dots, \hat{\lambda}_D$ ,
5. Find the estimates in  $\psi$ -space by using  $\hat{\psi}_i = \frac{1}{d_s}(\arg \hat{\lambda}_i), i = 1, \dots, D$ .

Golub and Van Loan (Section 12.3 of [GVL83] and [GVL80]) suggest that a total least squares (TLS) criterion is more appropriate because both  $\hat{\mathbf{U}}_{s1}$  and  $\hat{\mathbf{U}}_{s2}$  are estimates containing errors.

If the TLS formulation is used

$$\hat{\Psi}_{TLS} = -\mathbf{V}_{12}\mathbf{V}_{22}^{-1}, \quad (9.122)$$

where  $\mathbf{V}_{12}$  and  $\mathbf{V}_{22}$  are  $D \times D$  matrices defined by the eigendecomposition of the  $2D \times 2D$  matrix

$$\tilde{\mathbf{C}} \triangleq \begin{bmatrix} \hat{\mathbf{U}}_{s1}^H \\ \hat{\mathbf{U}}_{s2}^H \end{bmatrix} \begin{bmatrix} \hat{\mathbf{U}}_{s1} & \hat{\mathbf{U}}_{s2} \end{bmatrix} = \begin{bmatrix} \mathbf{V}_{11} & \mathbf{V}_{12} \\ \mathbf{V}_{21} & \mathbf{V}_{22} \end{bmatrix} \mathbf{\Lambda}_E \begin{bmatrix} \mathbf{V}_{11}^H & \mathbf{V}_{21}^H \\ \mathbf{V}_{12}^H & \mathbf{V}_{22}^H \end{bmatrix}, \quad (9.123)$$

with

$$\mathbf{\Lambda}_E = \text{diag} [\lambda_{E_1}, \lambda_{E_2}, \dots, \lambda_{E_{2D}}], \quad (9.124)$$

where the eigenvalues are ordered,

$$\lambda_{E_1} \geq \lambda_{E_2} \geq \dots \geq \lambda_{E_{2D}}. \quad (9.125)$$

The TLS-ESPRIT algorithm uses  $\Psi_{TLS}$  from (9.122) in steps 4 and 5 of the LS-ESPRIT algorithm to find  $\hat{\lambda}_i, i = 1, \dots, D$ . We normally use the

TLS-ESPRIT algorithm for the examples in the text. One can show that LS ESPRIT and TLS ESPRIT have the same asymptotic ( $K \rightarrow \infty$ ) variance (e.g., RH89a). However, TLS ESPRIT generally has better threshold behavior.

We can now summarize the steps in the TLS-ESPRIT algorithm:

1. Perform the eigendecomposition on  $\mathbf{C}_x$  to obtain  $\hat{\mathbf{U}}_s$ ,
2. Find  $\hat{\mathbf{U}}_{s1}$  and  $\hat{\mathbf{U}}_{s2}$  by using (9.109) and (9.110),
3. Perform the  $2D \times 2D$  eigendecomposition in (9.123) and use (9.122) to obtain  $\hat{\Psi}_{TLS}$ ,
4. Find the eigenvalues of  $\hat{\Psi}_{TLS}$ , denoted by  $\hat{\lambda}_1, \hat{\lambda}_2, \dots, \hat{\lambda}_D$ ,
5. Find the estimates in  $\psi$ -space by using,

$$\hat{\psi}_i = \arg \hat{\lambda}_i, i = 1, 2, \dots, D. \quad (9.126)$$

We will do several examples to illustrate ESPRIT performance in typical scenarios. Before doing the examples, there is an issue of interest.

The issue is the choice of  $d_s$  for the overlapping subarrays shown in Figure 9.15. We can rewrite the angle of the  $i$ th term in (9.107) as

$$d_s \pi \sin \bar{\theta}_i = d_s \pi u_i, \quad (9.127)$$

where  $\bar{\theta}_i$  is the angle of the  $i$ th plane-wave signal to broadside. If  $d_s = 1$ , then we can determine  $u_i$  unambiguously for

$$-1 \leq u_i \leq 1, \quad (9.128)$$

or

$$-\frac{\pi}{2} \leq \theta_i \leq \frac{\pi}{2}. \quad (9.129)$$

However, for  $d_s > 1$ , the unambiguous range decreases to

$$-\frac{1}{d_s} \leq u_i \leq \frac{1}{d_s}. \quad (9.130)$$

For example, for the last set of subarrays in Figure 9.15, we would need to know the *a priori* location of the  $u_i$  in the range,

$$-0.2 \leq u_i \leq 0.2, \quad (9.131)$$

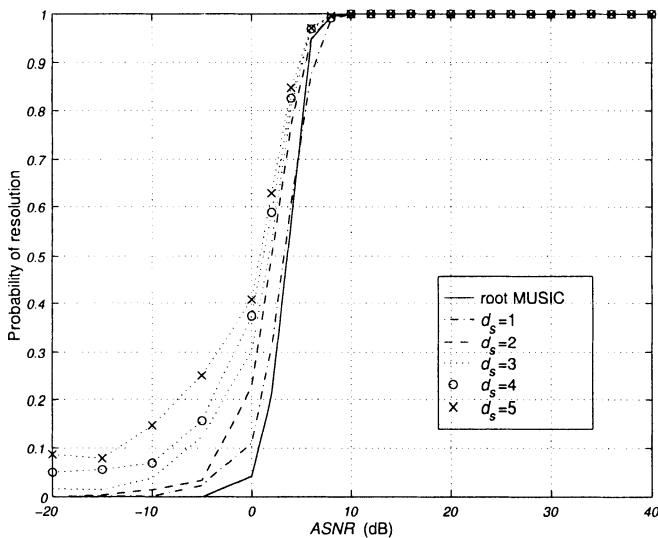


Figure 9.17 TLS-ESPRIT algorithm: probability of resolution versus  $ASNR$ ;  $N = 10, \rho = 0, K = 100, 500$  trials.

which corresponds to the  $BW_{NN}$  of the conventional beam pattern. Thus, in order to use  $d_s > 1$ , we either need *a priori* knowledge of the sector of  $u$ -space where the signals are located or we have to do some preprocessing to determine the sector. The limitations for unambiguous location follow directly from our classical array discussion in Chapter 2, because we can think of the ESPRIT algorithm as operating on a 2-element array where each element consists of an identical subarray.

We consider several examples to illustrate the performance of the ESPRIT algorithm.

#### Example 9.3.4 (continuation, Example 9.3.1)

Consider the same model as in Example 9.3.1. We have a standard 10-element linear array with two equal-power uncorrelated plane waves impinging on the array from  $\pm\Delta\psi/2$ , where  $\Delta\psi = \Delta\psi_R$ .

In Figure 9.17, we show the probability of resolution versus  $ASNR$  for TLS-ESPRIT and various subarrays. We see that, for  $d_s = 1$ , TLS-ESPRIT has slightly better resolution performance than root MUSIC. The resolution performance improves as  $d_s$  increases. However, for  $d_s > 1$ , the model assumes prior knowledge of the range of  $\psi$  (see (9.130)).

The normalized RMSE is shown in Figure 9.18. Note that, as the  $ASNR$  approaches zero, the RMSE approaches the variance of a random variable that is uniform over the *a priori* range ( $Var(u) = 1/3d_s^2$ ). Above threshold, the RMSE is parallel to, but above, the CRB. For  $d_s = 1$ , the RMSE is about 1 dB above the bound.

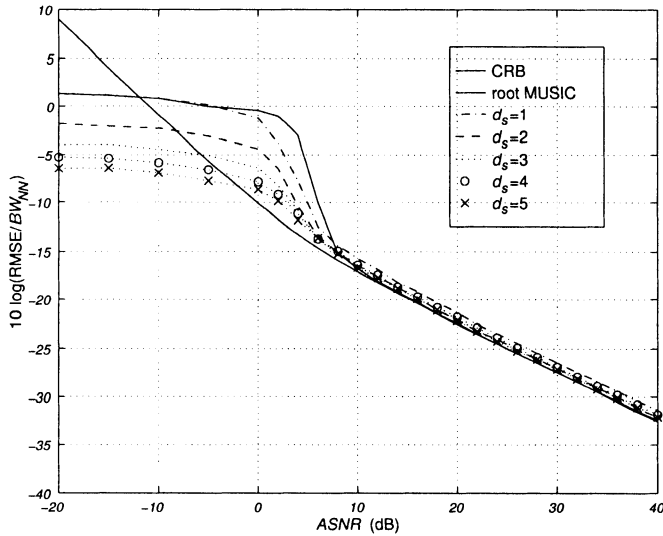


Figure 9.18 TLS-ESPRIT algorithm:  $N = 10, \rho = 0, K = 100, 500$  trials; normalized RMSE versus  $ASNR$ .

**Example 9.3.5** (continuation)

Consider the same model as in Example 9.3.4 except  $\rho = 0.95$ . The probability of resolution versus  $ASNR$  is shown in Figure 9.19. The normalized RMSE versus  $ASNR$  is shown in Figure 9.20. The results are similar to the  $\rho = 0$  case, but are shifted to the right by about 15 dB.

One can improve the performance of the ESPRIT algorithm by a technique referred to as row weighting. This technique is described in [OVK91]. The basic idea is to weight the rows of  $\widehat{\mathbf{U}}_s$  by modifying the identity matrix component of the selection matrix  $\mathbf{J}_s$ ,

$$\tilde{\mathbf{J}}_s^{(m_s)} \triangleq \text{diag} \left[ 1, \sqrt{2}, \sqrt{3}, \dots, \sqrt{w}, \sqrt{w}, \sqrt{w}, \dots, \sqrt{3}, \sqrt{2}, 1 \right], \quad (9.132)$$

where

$$w = \min \{m_s, N - m_s - d_s + 1\}. \quad (9.133)$$

The parameter  $m_s$  determines where the increase in weighting stops. In most cases,  $m_s$  is chosen as large as possible. We show the results with a simple example.

**Example 9.3.6** (continuation)

Consider the same model as in Example 9.3.4 and assume  $d_s = 1$ . In Figure 9.21, we show the probability of resolution versus  $ASNR$  for various  $m_s$ . In Figure 9.22, we

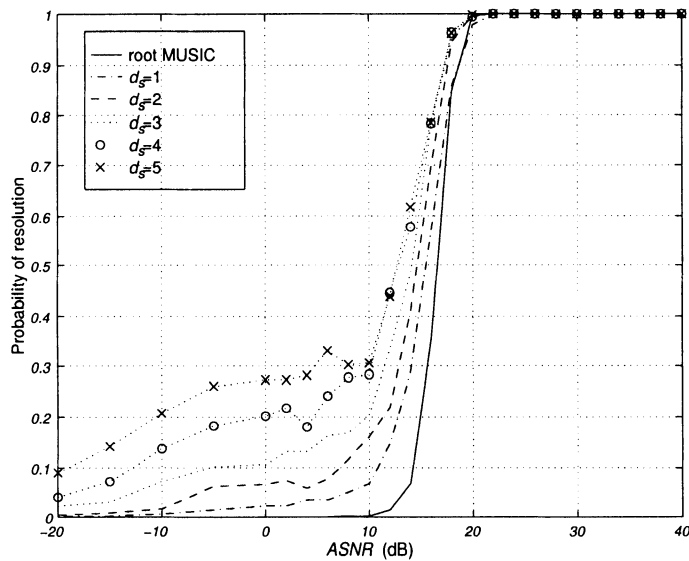


Figure 9.19 TLS-ESPRIT algorithm:  $N = 10, \rho = 0.95, K = 100$ , 500 trials, probability of resolution versus  $ASNR$ .

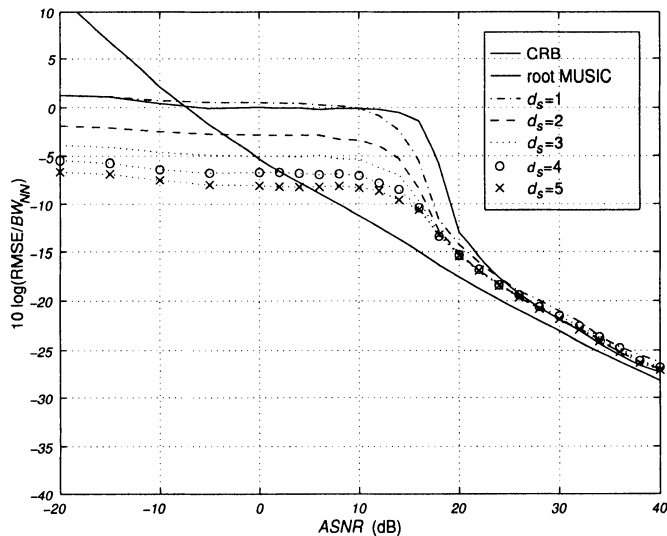


Figure 9.20 TLS-ESPRIT algorithm:  $N = 10, \rho = 0.95, K = 100$ , 500 trials; normalized RMSE versus  $ASNR$ .

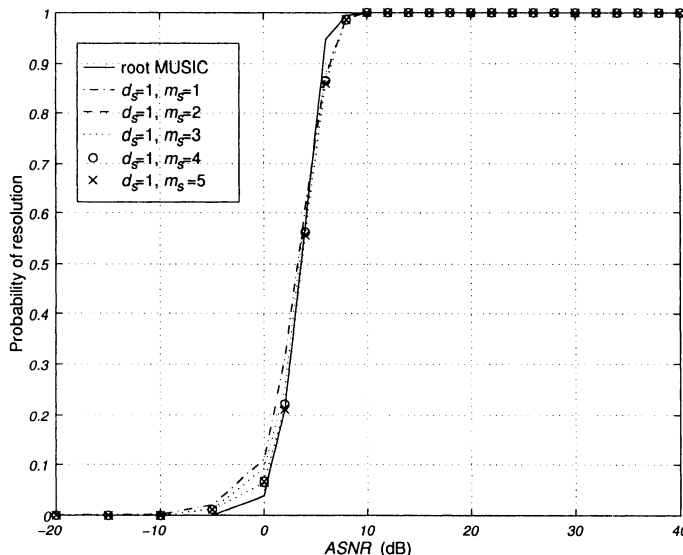


Figure 9.21 TLS-ESPRIT algorithm with row weighting:  $N = 10, \rho = 0, K = 100$ , 500 trials, probability of resolution versus  $ASNR$ , various  $m_s$ .

show the normalized RMSE. We see that there is a useful improvement in the RMSE for  $m_s = 3, 4$ , or  $5$ . The normalized RMSE is about 0.2 dB above the CRB.

In most applications of LS-ESPRIT and TLS-ESPRIT, row weighting will be used. Stoica and Viberg [SV95] discuss the asymptotic equivalence of weighted LS-ESPRIT and TLS-ESPRIT.

The TLS-ESPRIT algorithm applies to arbitrary array geometries that exhibit the shift invariance property. For ULAs, one can develop an algorithm referred to as unitary ESPRIT that exploits the conjugate symmetry. We develop it in the next section.

#### 9.3.4.2 Unitary ESPRIT

We encountered unitary transformations in the context of adaptive beamforming in Chapter 7 and in the unitary root MUSIC discussion in Section 9.3.2.3. The original references on unitary ESPRIT are by Haardt and Nossek [HN95] and Haardt and Ali-Hackl [HAH94]. Zoltowski et al. [ZHM96] provide a concise discussion of unitary ESPRIT as background for their development of 2-D unitary ESPRIT. Our discussion follows Section III of [ZHM96]. Unitary ESPRIT is one method of accomplishing FB

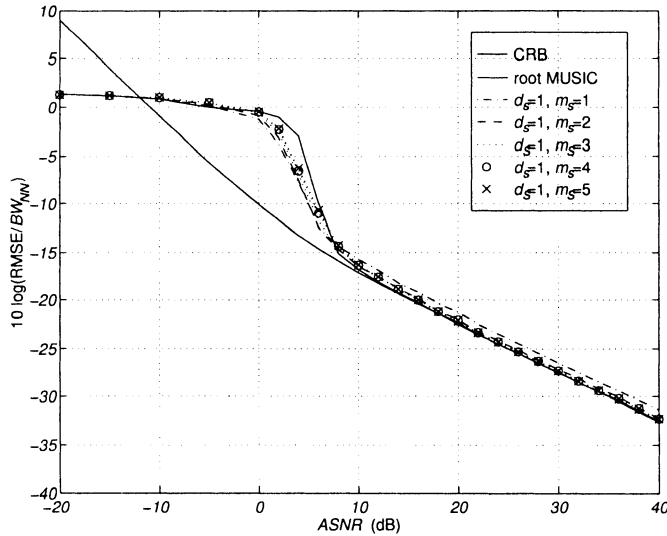


Figure 9.22 TLS-ESPRIT with row weighting, various  $m_s$ :  $N = 10, \rho = 0, K = 100, 500$  trials; normalized RMSE versus ASNR.

averaging with ESPRIT. Other references that discuss FB-ESPRIT or FB-TLS-ESPRIT include Roy [Roy87], Mou and Zhang [MZ91], Zoltowski and Stavrinides [ZS89], Rao and Hari [RH93], and Bachl [Bac95].

We start with the invariance relationship in element space. We assume  $d_s = 1$ , and therefore  $N_s = N - 1$ . The selection matrices are  $(N - 1) \times N$ ,

$$\mathbf{J}_{s1} \triangleq \begin{bmatrix} 1 & 0 & \cdots & 0 & 0 \\ 0 & 1 & \cdots & 0 & 0 \\ \vdots & \vdots & \ddots & \vdots & \vdots \\ 0 & 0 & \cdots & 1 & 0 \end{bmatrix}, \quad (9.134)$$

and

$$\mathbf{J}_{s2} \triangleq \begin{bmatrix} 0 & 1 & 0 & \cdots & 0 \\ 0 & 0 & 1 & \cdots & 0 \\ \vdots & \vdots & \vdots & \ddots & \vdots \\ 0 & 0 & 0 & \cdots & 1 \end{bmatrix}. \quad (9.135)$$

Then,

$$e^{j\psi} \mathbf{J}_{s1} \mathbf{v}(\psi) = \mathbf{J}_{s2} \mathbf{v}(\psi). \quad (9.136)$$

We can transform  $\mathbf{v}(\psi)$  into a real array manifold vector by using the unitary matrix  $\mathbf{Q}_N^H$ .

Recall from (9.54) and (9.55) that

$$\mathbf{Q}_{2K} = \frac{1}{\sqrt{2}} \begin{bmatrix} \mathbf{I}_K & j\mathbf{I}_K \\ \mathbf{J}_K & -j\mathbf{J}_K \end{bmatrix}, \quad (9.137)$$

$K = N/2$ , for  $N$  even, and

$$\mathbf{Q}_{2K+1} = \frac{1}{\sqrt{2}} \begin{bmatrix} \mathbf{I}_K & \mathbf{0} & j\mathbf{I}_K \\ \mathbf{0}^T & \sqrt{2} & \mathbf{0}^T \\ \mathbf{J}_K & \mathbf{0} & -j\mathbf{J}_K \end{bmatrix}, \quad (9.138)$$

where  $K = (N - 1)/2$ , for  $N$  odd.<sup>8</sup> The  $\mathbf{Q}_N$  matrices are unitary,

$$\mathbf{Q}_N^H \mathbf{Q}_N = \mathbf{Q}_N \mathbf{Q}_N^H = \mathbf{I}. \quad (9.139)$$

Premultiplying  $\mathbf{v}(\psi)$  by  $\mathbf{Q}_N^H$  gives a real array manifold vector,

$$\mathbf{v}_R(\psi) = \mathbf{Q}_N^H \mathbf{v}(\psi). \quad (9.140)$$

Because  $\mathbf{Q}_N$  is unitary, we can write (9.136) as

$$e^{j\psi} \mathbf{J}_{s1} \mathbf{Q}_N \mathbf{Q}_N^H \mathbf{v}(\psi) = \mathbf{J}_{s2} \mathbf{Q}_N \mathbf{Q}_N^H \mathbf{v}(\psi), \quad (9.141)$$

or, using (9.140),

$$e^{j\psi} \mathbf{J}_{s1} \mathbf{Q}_N \mathbf{v}_R(\psi) = \mathbf{J}_{s2} \mathbf{Q}_N \mathbf{v}_R(\psi). \quad (9.142)$$

Pre-multiplying by  $\mathbf{Q}_{N-1}^H$  gives,

$$e^{j\psi} \mathbf{Q}_{N-1}^H \mathbf{J}_{s1} \mathbf{Q}_N \mathbf{v}_R(\psi) = \mathbf{Q}_{N-1}^H \mathbf{J}_{s2} \mathbf{Q}_N \mathbf{v}_R(\psi). \quad (9.143)$$

Observing that

$$\mathbf{J}_{N-1} \mathbf{J}_{s2} \mathbf{J}_N = \mathbf{J}_{s1}, \quad (9.144)$$

and

$$\mathbf{J}_N \mathbf{Q}_N = \mathbf{Q}_N^*, \quad (9.145)$$

---

<sup>8</sup>There are two different  $\mathbf{J}$  matrices in this section. We have added a subscript (in capital letters) to the exchange matrix  $\mathbf{J}$  to denote its dimensionality. The selection matrices  $J_{s1}$  and  $J_{s2}$  have lowercase subscripts.

we can write

$$\begin{aligned}\mathbf{Q}_{N-1}^H \mathbf{J}_{s2} \mathbf{Q}_N &= \mathbf{Q}_{N-1}^H \mathbf{J}_{N-1} \mathbf{J}_{N-1} \mathbf{J}_{s2} \mathbf{J}_N \mathbf{J}_N \mathbf{Q}_N \\ &= \mathbf{Q}_{N-1}^T \mathbf{J}_{s1} \mathbf{Q}_N^* \\ &= (\mathbf{Q}_{N-1}^H \mathbf{J}_{s1} \mathbf{Q}_N)^*. \end{aligned} \quad (9.146)$$

We now define the real and imaginary parts of the left side of (9.146)

$$\mathbf{K}_1 \triangleq \operatorname{Re} \left\{ \mathbf{Q}_{N-1}^H \mathbf{J}_{s2} \mathbf{Q}_N \right\}, \quad (9.147)$$

and

$$\mathbf{K}_2 \triangleq \operatorname{Im} \left\{ \mathbf{Q}_{N-1}^H \mathbf{J}_{s2} \mathbf{Q}_N \right\}. \quad (9.148)$$

Using (9.147) and (9.148) in (9.143) and incorporating the result in (9.146) gives

$$e^{j\frac{\psi}{2}} (\mathbf{K}_1 - j\mathbf{K}_2) \mathbf{v}_R(\psi) = e^{-j\frac{\psi}{2}} (\mathbf{K}_1 + j\mathbf{K}_2) \mathbf{v}_R(\psi), \quad (9.149)$$

which can be written as,

$$\left( e^{j\frac{\psi}{2}} - e^{-j\frac{\psi}{2}} \right) \mathbf{K}_1 \mathbf{v}_R(\psi) = j \left( e^{j\frac{\psi}{2}} + e^{-j\frac{\psi}{2}} \right) \mathbf{K}_2 \mathbf{v}_R(\psi). \quad (9.150)$$

We now have the invariance relation,

$$\tan \left( \frac{\psi}{2} \right) \mathbf{K}_1 \mathbf{v}_R(\psi) = \mathbf{K}_2 \mathbf{v}_R(\psi), \quad (9.151)$$

which has only real-valued elements. Defining the array manifold matrix,

$$\mathbf{V}_R(\psi) = \begin{bmatrix} \mathbf{v}_R(\psi_1) & \mathbf{v}_R(\psi_2) & \cdots & \mathbf{v}_R(\psi_D) \end{bmatrix}, \quad (9.152)$$

we can write (9.151) as,

$$\mathbf{K}_1 \mathbf{V}_R(\psi) \boldsymbol{\Omega}_\psi = \mathbf{K}_2 \mathbf{V}_R(\psi), \quad (9.153)$$

where

$$\boldsymbol{\Omega}_\psi = \operatorname{diag} \left[ \tan \left( \frac{\psi_1}{2} \right), \dots, \tan \left( \frac{\psi_D}{2} \right) \right]. \quad (9.154)$$

The next step is to find the signal subspace eigenvectors corresponding to  $\mathbf{V}_R(\psi)$ . If we define  $\mathbf{X}$  as the  $N \times K$  data matrix and

$$\mathbf{Y} = \mathbf{Q}_N^H \mathbf{X}, \quad (9.155)$$

then the largest left singular vectors of

$$\mathbf{Y}_E = [Re\mathbf{Y}, Im\mathbf{Y}], \quad (9.156)$$

are the real signal subspace eigenvectors. We denote the real signal subspace by  $\hat{\mathbf{U}}_{RS}$ .

Alternatively, we can find the eigenvectors of

$$\hat{\mathbf{S}}_R = Re \left\{ \mathbf{Q}_N^H \hat{\mathbf{S}}_{\mathbf{x}} \mathbf{Q}_N \right\}, \quad (9.157)$$

corresponding to the  $D$  largest eigenvalues, and they will define  $\hat{\mathbf{U}}_{RS}$ .

The signal eigenvector matrix is related to  $\mathbf{V}_R(\psi)$  by the real-valued  $D \times D$  unknown matrix  $\mathbf{T}$ ,

$$\mathbf{U}_{RS} = \mathbf{V}_R \mathbf{T}, \quad (9.158)$$

or

$$\mathbf{V}_R = \mathbf{U}_{RS} \mathbf{T}^{-1}. \quad (9.159)$$

Substituting (9.159) into (9.153) gives,

$$\mathbf{K}_1 \mathbf{U}_{RS} \Psi = \mathbf{K}_2 \mathbf{U}_{RS}, \quad (9.160)$$

where

$$\Psi = \mathbf{T}^{-1} \Omega_{\psi} \mathbf{T}. \quad (9.161)$$

The eigenvalues of the  $D \times D$  solution  $\Psi$  to (9.160) correspond to  $\tan(\psi_i/2)$ . Substituting  $\hat{\mathbf{U}}_{RS}$  for  $\mathbf{U}_{RS}$  in (9.160) gives

$$\mathbf{K}_1 \hat{\mathbf{U}}_{RS} \hat{\Psi} = \mathbf{K}_2 \hat{\mathbf{U}}_{RS}. \quad (9.162)$$

The form of (9.162) is identical to that in (9.119). Thus, unitary LS-ESPRIT uses (9.121) with  $\hat{\mathbf{U}}_{s1}$  replaced by  $\mathbf{K}_1 \hat{\mathbf{U}}_{RS}$  and  $\hat{\mathbf{U}}_{s2}$  replaced by  $\mathbf{K}_2 \hat{\mathbf{U}}_{RS}$ ,

$$\hat{\Psi}_{ULS} = \left[ [\mathbf{K}_1 \hat{\mathbf{U}}_{RS}] [\mathbf{K}_1 \mathbf{U}_{RS}] \right]^{-1} \left[ \mathbf{K}_1 \hat{\mathbf{U}}_{RS} \right]^T \left[ \mathbf{K}_2 \hat{\mathbf{U}}_{RS} \right]. \quad (9.163)$$

For unitary TLS-ESPRIT, define

$$\tilde{\mathbf{C}} = [\mathbf{K}_1 \hat{\mathbf{U}}_{RS} \quad \mathbf{K}_2 \hat{\mathbf{U}}_{RS}]^T [\mathbf{K}_1 \hat{\mathbf{U}}_{RS} \quad \mathbf{K}_2 \hat{\mathbf{U}}_{RS}]. \quad (9.164)$$

The eigendecomposition of  $\tilde{\mathbf{C}}$  gives  $\mathbf{V}_{12}$  and  $\mathbf{V}_{22}$  (see (9.122)–(9.125)). Then,

$$\hat{\Psi}_{UTLS} = -\mathbf{V}_{12} \mathbf{V}_{22}^{-1}. \quad (9.165)$$

We summarize the steps for the unitary ESPRIT algorithms:

1. Find  $\hat{\mathbf{U}}_{RS}$  by either finding the eigenvectors with the largest eigenvalues of  $\text{Re} \left\{ \mathbf{Q}_N^H \hat{\mathbf{S}}_x \mathbf{Q}_N \right\}$  or by computing the largest left singular vectors of

$$\mathbf{Y}_E = \left[ \text{Re} \left[ \mathbf{Q}_N^H \mathbf{X} \right], \text{Im} \left[ \mathbf{Q}_N^H \mathbf{X} \right] \right], \quad (9.166)$$

2. Find either  $\hat{\Psi}_{ULS}$  from (9.163) or  $\hat{\Psi}_{UTLS}$  from (9.165),  
 3. Compute  $\hat{\omega}_i, i = 1, \dots, D$ , the eigenvalues of the real-valued matrix  $\hat{\Psi}_{ULS}$  or  $\hat{\Psi}_{UTLS}$ ,  
 4. Compute  $\hat{\psi}_i = 2\tan^{-1}(\hat{\omega}_i), i = 1, \dots, D$ .

We consider an example to illustrate the performance of unitary ESPRIT.

**Example 9.3.7** (continuation, Example 9.3.4)

Consider the same model as in Example 9.3.4. We have a standard 10-element linear array with two equal-power uncorrelated signals impinging on the array from  $\pm\Delta\psi/2$ , where  $\Delta\psi = \Delta\psi_R$ .

In Figure 9.23(a), we plot the probability of resolution versus  $ASNR$ . In Figure 9.23(b), we plot the normalized RMSE versus  $ASNR$ . In Figure 9.24, we show a plot of the roots for 100 trials. By imposing the conjugate symmetry constraint (recall the IQML discussion) the roots appear on the unit circle when we are above threshold. We see that the threshold performance is a little better than TLS-ESPRIT due to FB averaging. However there are significant computational savings.

In the next example, we consider weighted unitary ESPRIT.

**Example 9.3.8** (continuation)

Consider the same model as in Example 9.3.7. We use a weighted  $\mathbf{J}_{s1}$  matrix with

$$\mathbf{J}_{s1} = \begin{bmatrix} 1 & 0 & \cdots & & & 0 \\ 0 & \sqrt{2} & & & & \vdots \\ \vdots & & \sqrt{3} & & & \\ & & & \sqrt{m_s} & & \\ & & & & \ddots & \\ & & & & & \sqrt{m_s} \\ 0 & \cdots & & & & \ddots \\ & & & & & & 1 & 0 \end{bmatrix}, \quad (9.167)$$

where  $m_s \leq N/2$  and simulate  $m_s = 2, \dots, 5$ . In Figure 9.25, we plot the probability of resolution and the normalized RMSE versus  $ASNR$ . We see that, for  $m_s \geq 2$ , the RMSE essentially equals the CRB.

Gershman and Haardt [GH99] have developed a version of unitary ESPRIT that uses pseudonoise resampling to try and eliminate outlier estimates. It relies on earlier work by Gershman [Ger98], Gershman and Böhme

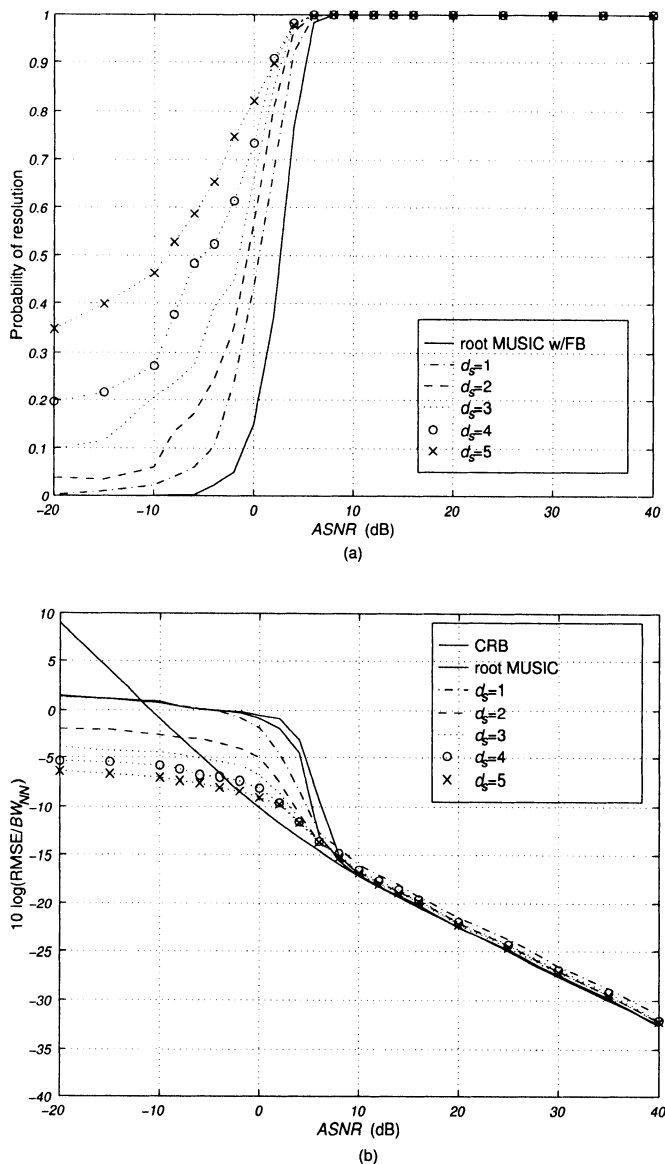


Figure 9.23 Unitary TLS-ESPRIT:  $N = 10, \rho = 0, d_s = 1, \dots, 5, K = 100$ , 500 trials: (a) probability of resolution versus  $ASNR$ ; (b) normalized RMSE versus  $ASNR$ .

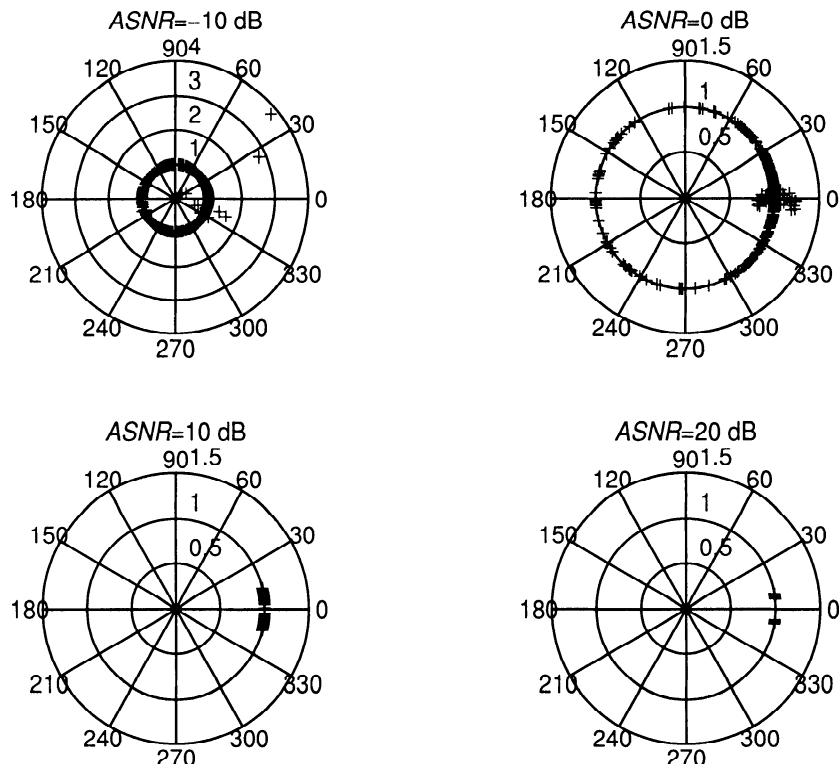


Figure 9.24 Unitary TLS-ESPRIT: location of estimates for various  $ASNR$ :  $K = 100, 200$  trials.

[GB97], [GB98], and Efron [Efr79]. The technique offers some performance improvement in the vicinity of the threshold. The reader is referred to these references for further discussion.

We have discussed unitary transformations in the context of root MUSIC and ESPRIT. Whenever FB averaging can be used, we can develop a unitary algorithm. Huarng and Yeh [HY91] developed a unitary version of spectral MUSIC. Gershman and Stoica [GS99] developed a unitary version of MODE (see [SJ97] also).

### 9.3.4.3 Summary of ESPRIT

In Section 9.3.4, we have developed LS-ESPRIT and TLS-ESPRIT and unitary ESPRIT and studied their performance. The LS- and TLS-ESPRIT algorithms with row weighting achieve an RMSE that is very close to the CRB

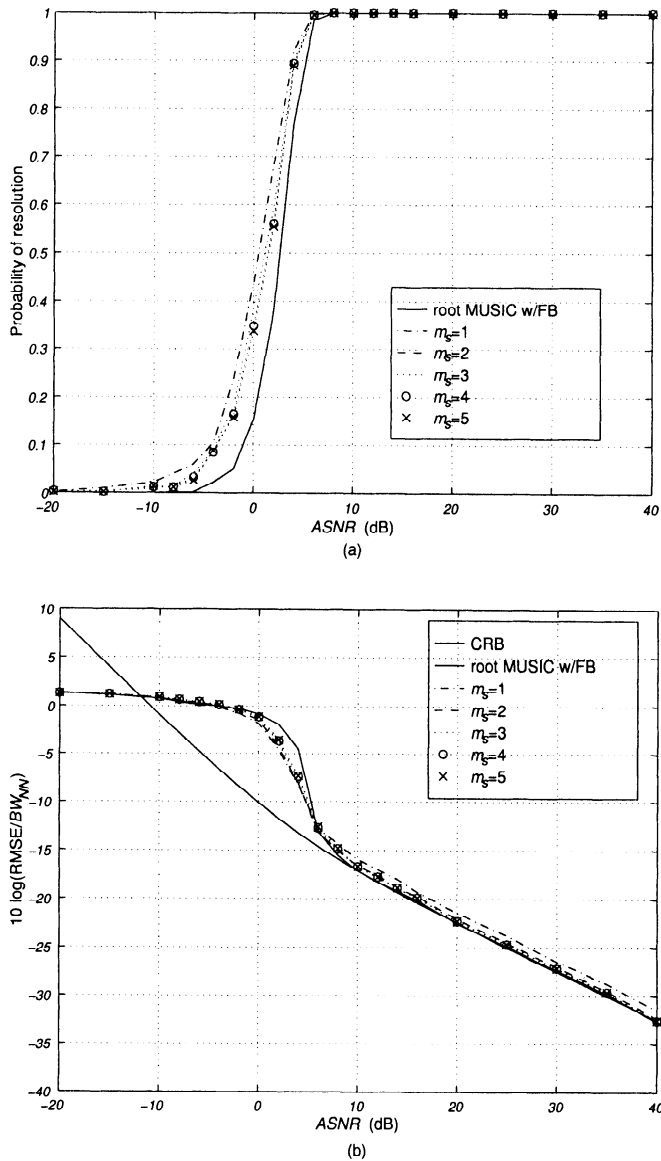


Figure 9.25 Unitary TLS-ESPRIT with row weighting,  $d_s = 1, m_s = 2, \dots, 5$ :  $N = 10, \rho = 0, K = 100, 500$  trials: (a) probability of resolution versus ASNR; (b) normalized RMSE versus ASNR.

for  $ASNR$ s above threshold. For SLAs, unitary ESPRIT using appropriate row weighting provides similar performance with reduced computation.

ESPRIT can also be used in a broader class of array geometries. The requirement is that the array exhibit a shift invariance property.

### 9.3.5 Algorithm Comparison

In Sections 8.7 and 9.3, we have developed a number of algorithms that are computationally feasible and have good performance for SLAs. Some of these algorithms can be adapted for other array geometries, but our current discussion will focus on SLAs.

Our examples up to this point suggest that the three algorithms that should receive further study are:

- (i) Unitary IMODE,
- (ii) Unitary root MUSIC,
- (iii) Unitary TLS-ESPRIT with  $d_s = 1, m_s = (N + 1)/2$  for  $N$  odd and  $m_s = N/2$  for  $N$  even.

We did not derive unitary IMODE in Chapter 8 because the issue of computational complexity was not emphasized. Unitary IMODE is derived in Gershmann and Stoica [GS99]. The derivation is summarized in Problem 9.3.30. We have used unitary IMODE in this comparison because we want to compare computational complexity.

Unitary IMODE is identical to FB-MODE, which is derived and analyzed in Stoica and Jansson [SJ97]. FB-IMODE is identical to standard IMODE except FB averaging is used to construct the estimate of the spectral matrix. As discussed in [GS99], FB-MODE (or unitary MODE) has better threshold performance for uncorrelated signals. We discuss the correlated signal case in Section 9.6.

We consider two examples to compare their performance. In this section, we consider uncorrelated signals. The correlated and coherent signals case is discussed in Section 9.6.

#### **Example 9.3.9** (continuation)

Consider a standard 10-element array. There are two uncorrelated equal-power plane-wave signals impinging on the array from  $\pm\Delta_R/2$ . We assume that the number of signals is known. The three algorithms are simulated. In Figure 9.26(a), the normalized RMSE is plotted versus  $ASNR$ . In Figure 9.26(b), the flop count for the three algorithms is plotted versus  $ASNR$ .

The unitary IMODE algorithm has the best threshold performance ( $ASNR=5$  dB). The threshold of unitary root MUSIC is slightly higher ( $ASNR = 6$  dB). The RMSE of

the unitary TLS-ESPRIT algorithm approaches the CRB in a more gradual manner. All of the algorithms are close to the CRB above threshold.

The unitary TLS-ESPRIT algorithm has the smallest flop count. Both unitary IMODE and unitary root MUSIC have a slightly higher flop count.

#### Example 9.3.10 (continuation)

Consider the same model as in Example 9.3.9, except the number of signals,  $D$ , is unknown. We use one of the detection algorithms developed in Section 7.8 to find  $\hat{D}$ . We then use  $\hat{D}$  in the three parameter estimation algorithms from Example 9.3.9.

It is important not to underestimate  $D$ , so we consider detection algorithms where  $P_M$  is close to zero for all  $ASNR$ s above the resolution threshold of the estimation algorithms ( $ASNR = 5$  dB in this example). In order to evaluate the performance, we assume that, if  $\hat{D} > D$ , that the RMSE of the  $D$  estimates that are closest to the true values are calculated and the other ( $\hat{D} - D$ ) estimates are ignored. The rationale for this approach is that a subsequent processing step will discard the extra estimates. We must also consider  $P_M$  in order to evaluate the algorithm's performance. Two detection algorithms are used:

- (i) AIC-FB
- (ii) MDL-FB

The results are shown in Figure 9.27. In Figure 9.27(a), the probability that  $\hat{D} \geq D$  is plotted. This curve is equal to  $1-P_M$ . In Figure 9.27(b), the normalized RMSE is plotted versus  $ASNR$  for the AIC-FB algorithm. In Figure 9.27(c), the normalized RMSE is plotted versus  $ASNR$  for the MDL-FB algorithm. In Figure 9.27(d), the normalized RMSE is plotted  $ASNR$  for the MDL-FB+1 algorithms.

For the AIC-FB detection algorithm, the threshold occurs at the same  $ASNR$  as in the known  $D$  case. Above the threshold, the IMODE algorithm and the unitary root MUSIC algorithm reach the CRB. The overestimation degrades the performance of the unitary TLS-ESPRIT algorithm and the RMSE is slightly above the CRB.

For the MDL-FB algorithm, the threshold occurs at an  $ASNR$  that is about 2.5 dB higher than the known  $D$  case. Above threshold, the probability that  $\hat{D} = D$  approaches one quickly, so the algorithms behave as in the known  $D$  case.

Based on this example and other cases developed in the problems, it appears that the best approach is to use AIC-FB as the detection algorithm. The combined detection and estimation problem should be analyzed (or simulated) for the scenario of interest to see the effect of unknown  $D$  on the estimation performance.

#### 9.3.6 Summary

In this section, we have developed several algorithms that provide good performance with reasonable computational complexity.

Three versions of the MUSIC algorithm were developed: spectral MUSIC, root MUSIC, and unitary root MUSIC. Spectral MUSIC is applicable to arbitrary arrays, but the threshold occurs at a higher  $ASNR$  than the ML algorithms. For uncorrelated signals and high  $ASNR$ , the RMSE of the spectral MUSIC algorithm is close to the CRB. The root MUSIC algorithm

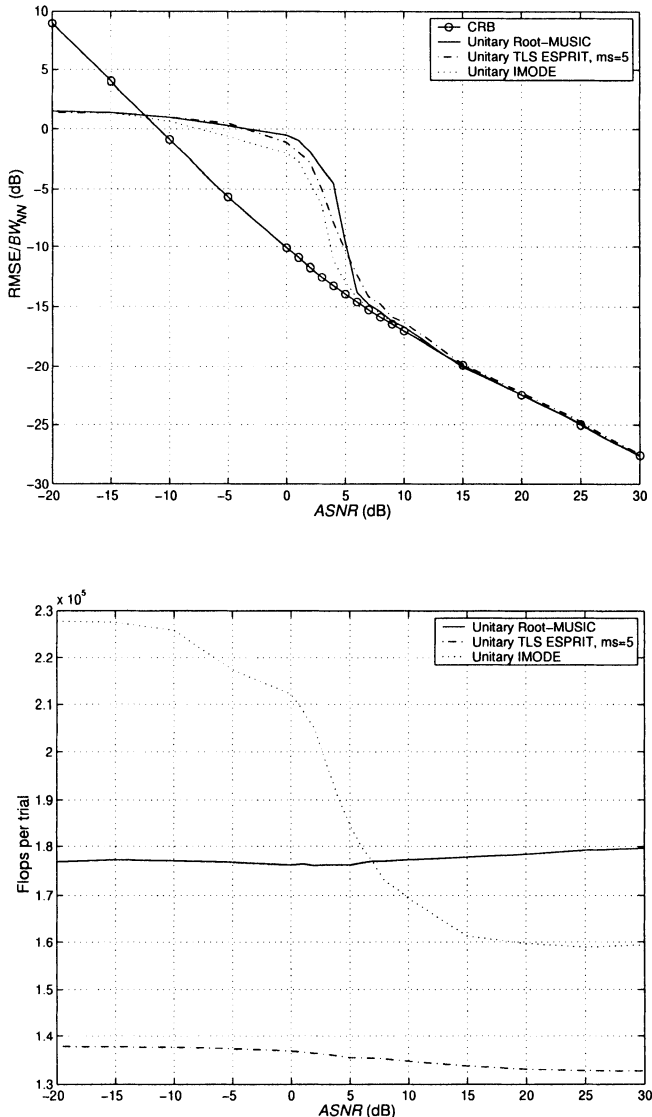
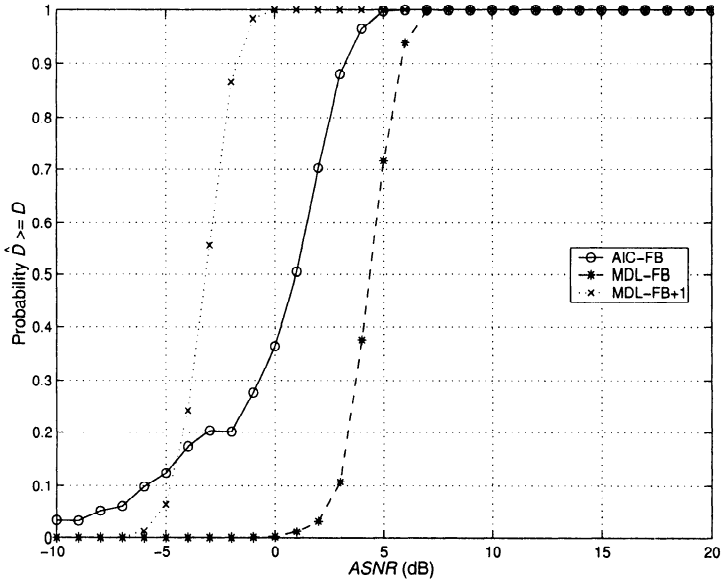
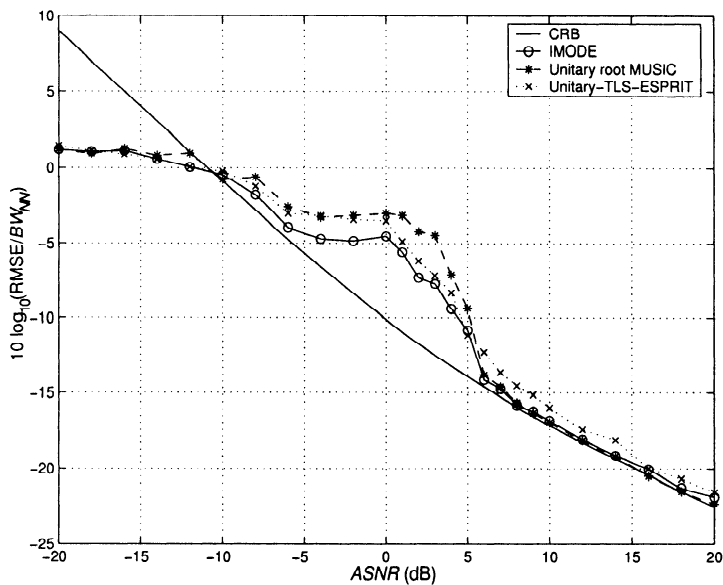


Figure 9.26 Performance of unitary IMODE, unitary root MUSIC, and unitary TLS-ESPRIT:  $N = 10$ ,  $K = 100$ , two uncorrelated plane-wave signals at  $\pm \Delta_R/2$ , 1,000 trials: (a) normalized RMSE versus  $ASNR$ ; (b) MATLAB® flop count versus  $ASNR$ .



(a)



(b)

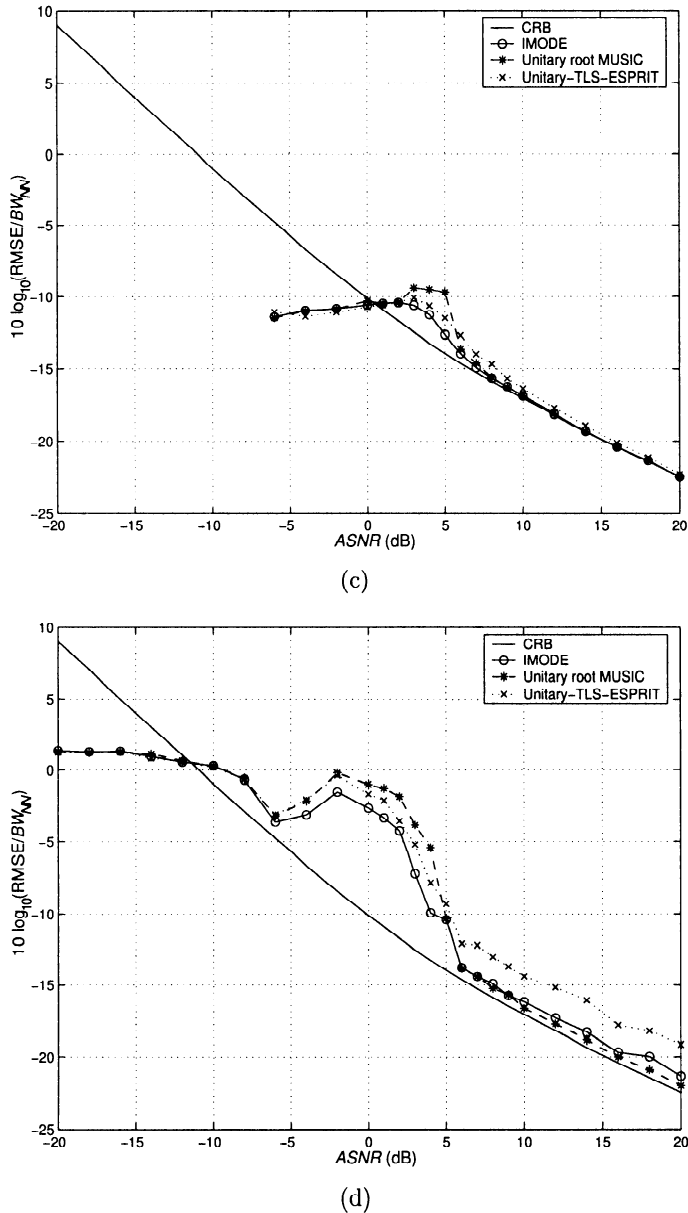


Figure 9.27 Performance of IMODE, unitary root MUSIC, and unitary TLS-ESPRIT:  $N = 10, K = 100$ , two uncorrelated plane-wave signals at  $\pm \Delta_R/2$ ,  $D$  is estimated using AIC-FB and MDL-FB algorithms, 1000 trials: (a)  $Pr(\hat{D} \geq D)$  versus ASNR; (b) normalized RMSE versus ASNR, AIC-FB detection. (c) RMSE versus ASNR, MDL-FB detection; (d) RMSE versus ASNR, MDL-FB+1 detection.

was applied to standard linear arrays. The threshold occurs at a lower  $ASNR$  than spectral MUSIC and the two algorithms have the same asymptotic performance. FB root MUSIC uses FB averaging of the sample spectral matrix and has better threshold performance. Unitary root MUSIC uses a unitary transformation that leads to an implementation using real computation and provides a significant reduction in computation. All of the MUSIC algorithms degrade in the presence of highly correlated signals and do not work in the presence of coherent signals.

Both LS- and TLS-ESPRIT were developed and the unitary versions of both algorithms were provided. All of our examples considered SLAs. TLS-ESPRIT has better threshold performance than LS-ESPRIT, with a slight increase in computational complexity. The two algorithms have the same asymptotic behavior. For uncorrelated signals, the row-weighted versions of ESPRIT were close to the CRB above threshold. The unitary versions of the algorithms provided a significant reduction in computational complexity and improved threshold performance.

In Section 9.3.5, we compared the performance of the unitary IMODE algorithm, the unitary root MUSIC algorithm, and the unitary TLS-ESPRIT algorithm with row weighting for uncorrelated signals. For the example considered, the three algorithms had similar performance and computational complexity. For uncorrelated signals, the unitary version of the algorithms should be used. The correlated signal case is considered in Section 9.6. The issue of unknown  $D$  was also discussed. The AIC-FB algorithm did not impact the threshold performance, but caused some degradation above threshold.

## 9.4 Linear Prediction

Linear prediction is widely used in a number of different applications, such as time-series analysis, spectral estimation, speech processing, radar and sonar signal processing, and geophysical signal processing. There are excellent discussions of it in a number of articles and books. (e.g., [Mak75], [Kay88], [Mar87], [PRLN92], or [Hay96]).

The application of linear prediction techniques to the DOA estimation problem in antenna arrays has been discussed by Schmidt [Sch81], Gabriel [Gab80], Tufts and Kumaresan [TK82], [KT83], Johnson and De Graaf [JD82]. We investigated these algorithms and considered both full-array linear prediction and subarray linear prediction. We found that, for estimating the DOAs of plane-wave signals the LP algorithms did not perform as well

as MUSIC and ESPRIT. The reader is referred to the above references for further discussion.

The comment does not imply that LP techniques would not be useful for spatial spectral estimation. These algorithms are the maximum entropy algorithms introduced by Burg (e.g., [Bur67] [Bur75]) and Van der Bos [VDB71]. We do not discuss the spatial spectral estimation problem.

## 9.5 Asymptotic Performance

Up to this point in our discussions we have relied on simulations to evaluate the performance of the various algorithms. We now want to derive some analytic comparisons.<sup>9</sup>

In this section we discuss the asymptotic performance of the various subspace algorithms. Asymptotic performance analysis studies the behavior of the algorithms as  $K$ , the number of snapshots, goes to infinity. One way to study the asymptotic performance is to use a series expansion and retain the appropriate first-order and second-order terms and neglect terms of  $O(K^{-1})$ . We then compare these asymptotic expressions to simulations to assess their accuracy for smaller values of  $K$ .

In Section 9.5.1, we discuss how the probability of resolution and the MSE are related. In Section 9.5.2, we analyze the resolution performance of some of the algorithms developed in Sections 9.2 and 9.3. In Section 9.5.3, we analyze the small error behavior of these algorithms. In Section 9.5.4, we summarize our results.

Most of the analyses are reasonably detailed. Our approach is to outline the steps in the analyses, give the key results, and illustrate them with examples.

### 9.5.1 Error Behavior

In this section, we discuss how the probability of resolution and the MSE are related. We use spectral MUSIC as an example, but the principles apply to any estimator. We first consider the resolution behavior. Our experimental results in Figures 9.9 and 9.10 showed that, for this particular example, we could divide the *ASNR* axis into the following regions (the endpoints are approximate at this point in the discussion):

---

<sup>9</sup>This section contains a number of detailed analytic expressions. Sections 9.5.2 and 9.5.3 can be omitted (or skimmed) at first reading without loss of continuity.

- (i)  $ASNR \geq 20$  dB; the RMSE is very close to the CRB for unbiased estimation.  $P_R$  is equal to unity.
- (ii)  $15 \text{ dB} \leq ASNR \leq 20$  dB; the RMSE increases slightly above the CRB. We find that this increase is due to a non-zero “local bias.”  $P_R$  is still equal to unity.
- (iii)  $10 \text{ dB} \leq ASNR \leq 15$  dB; the  $P_R$  decreases from unity to 0.5; the RMSE increases dramatically over this range (about 17 dB). We need to determine the cause of this increase. We refer to this as the upper threshold region.
- (iv)  $0 \text{ dB} \leq ASNR \leq 10$  dB; the  $P_R$  decreases from 0.5 to zero; the RMSE increases gradually. We refer to this as the lower threshold region.
- (v)  $ASNR \leq 0$  dB; the RMSE for each signal approaches the variance of a uniform random variable ( $1/3$  in  $u$ -space). We refer to this as the *a priori* region.

The behavior in regions 1 and 2 can be accurately described by a local error analysis, which we carry out in Section 9.5.3. In this section, we characterize the behavior in the region 3, the upper threshold region.

When the two sources are separated by much less than the beamwidth of the array, then a key issue in the threshold region is whether the null spectrum will exhibit one or two peaks in the region of the sources. This behavior is shown in Figure 9.28, where we show representative MUSIC spectra for four  $ASNR$ s. If we fix the number of snapshots and decrease the  $SNR$ , then the null spectrum proceeds from the representative shape in (a) to the shape in (d). Similarly, if we fix the  $SNR$  and decrease the number of snapshots, a similar progression occurs.

We see that there are three types of behavior:

- (i) In (a) and (b), the signals are resolved. In this region, we can assume the errors are small, and we analyze the bias and variance using an asymptotic analysis.
- (ii) In (c), the spectrum contains a single peak in the region of the two signals. We analyze when this transition to a single peak occurs. We refer to this as the resolution problem.
- (iii) In (d), the single peak due to the signals is no longer distinguishable and the estimator selects two peaks due to noise.

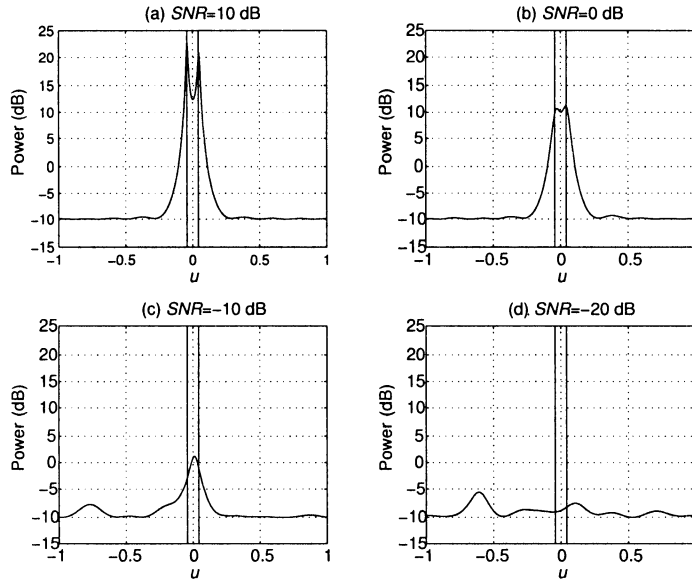


Figure 9.28 Behavior of a typical MUSIC spectrum: (a)  $ASNR = 20$  dB; (b)  $ASNR = 10$  dB; (c)  $ASNR = 0$  dB; and (d)  $ASNR = -10$  dB.

We first consider the probability of resolution,  $P_R$ . We would like to determine the probability that there are two peaks in the MUSIC spectrum in the “correct region.” We use the experimental criterion that the two signals are resolved if there are two peaks and

$$|\hat{\psi}_i - \psi_i| \leq \min \left\{ \frac{\Delta\psi}{2}, \frac{2\pi}{N} \right\}, \quad i = 1, 2. \quad (9.168)$$

In order to derive the  $P_R$  analytically, we denote the actual location of the sources by  $\psi_1$  and  $\psi_2$  and then define the midpoint,

$$\psi_m = \frac{\psi_1 + \psi_2}{2}. \quad (9.169)$$

One criterion of resolution is that

$$D(\psi_m) \geq D(\psi_i), \quad i = 1, 2, \quad (9.170)$$

where  $D(\psi) = (\hat{Q}_{MU}(\psi))^{-1}$ . If (9.170) is satisfied, then our estimator would not resolve the two signals. A second criterion is

$$D(\psi_m) \geq \frac{D(\psi_1) + D(\psi_2)}{2} = \bar{D}. \quad (9.171)$$

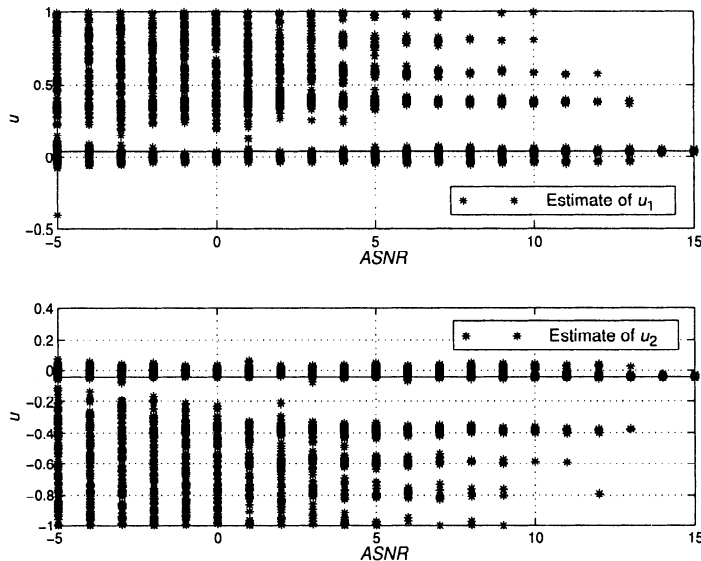


Figure 9.29 Spectral MUSIC estimates for various  $ASNR$ :  $N = 10, K = 100, \rho = 0, u_1 = 0.0433, u_2 = -0.0433$ , 200 trials.

Once again, if (9.171) is satisfied, then our estimator would not resolve the two signals. We would like to compute the probability of the events described by (9.170) and (9.171). Note that we are concerned with the *heights* of the spectrum, *not* the accuracy of location of the peaks.

Using (9.170), we can write,

$$P_R = Pr(D(\psi_m) < D(\psi_1) \text{ and } D(\psi_2)). \quad (9.172)$$

Similarly, using (9.171), we can write

$$P_R = Pr(D(\psi_m) < \bar{D}). \quad (9.173)$$

In order to understand the RMSE behavior, we examine the error behavior when the signals are not successfully resolved. In Figure 9.29 we show the location of the estimates for 200 trials at  $ASNR$ s going from 15 dB to  $-5$  dB. In Figure 9.30, we show the corresponding histograms. We now consider the behavior at each  $ASNR$  in the “upper threshold region.”

- (i)  $ASNR = 15$  dB: The signals are resolved on all trials and the estimates are clustered around the correct value.

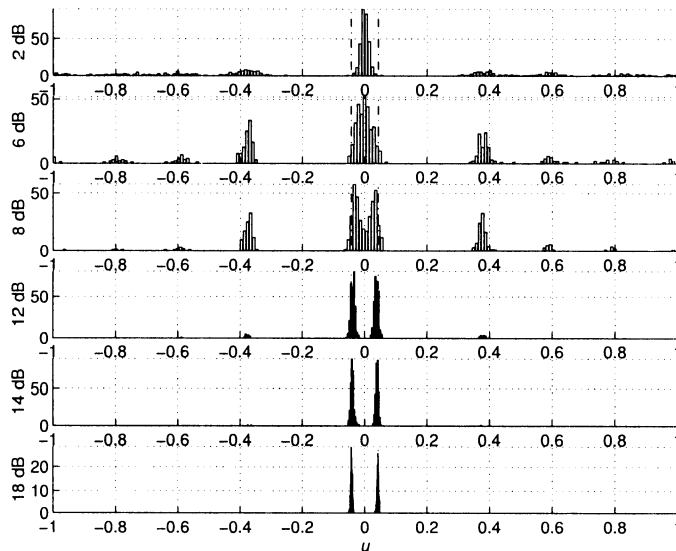


Figure 9.30 Histogram of spectral MUSIC estimates for *ASNRs* in upper threshold region:  $N = 10, K = 100, \rho = 0, u_1 = 0.0433, u_2 = -0.0433, 200$  trials.

- (ii)  $ASNR = 14$  dB: The signals are resolved on most trials. On several trials, the signals are not resolved. If signal 1 is assigned the peak, then  $\hat{u}_2 \simeq -0.374$ . If signal 2 is assigned the peak, then  $\hat{u}_1 \simeq 0.374$ .
- (iii)  $ASNR = 12$  dB and 13 dB: Similar behavior to 14 dB. More trials have unresolved signals. The outlying estimates are clustered around  $\pm 0.374$ .
- (iv)  $ASNR = 10$  dB and 11 dB: More trials have unresolved signals. The majority of the outlying estimates are at  $\pm 0.374$ , but some estimates appear around  $\pm 0.59$  and one estimate is at  $+0.81$ .

In order to understand this behavior we plot the MUSIC spectrum averaged over 500 trials at various *ASNR* in Figure 9.31. We see that there are sidelobes at  $\pm 0.37, \pm 0.59, \pm 0.80$ , and  $\pm 1.0$ . Note that, in a normal plot that is scaled to show the peaks, the sidelobe structure can easily be overlooked.

The importance of this observation is that the increase in RMSE is dominated by these sidelobe terms.

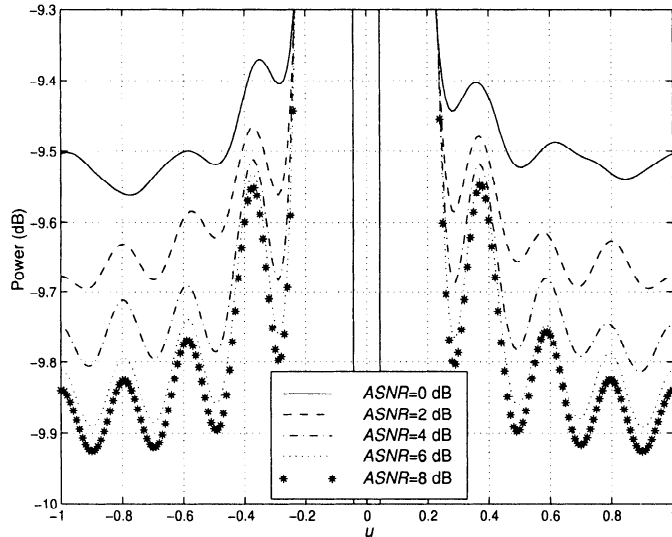


Figure 9.31 Plot of average of  $\mathbf{v}^H(\psi)\hat{\mathbf{U}}_S\hat{\mathbf{U}}_S^H\mathbf{v}(\psi)$  for various ASNR:  $N = 10, K = 100, \rho = 0, u_1 = 0.433, u_2 = -0.0433, 500$  trials.

We first consider the case when the second estimate is near the first sidelobe. Then, for this example, the MSE for signal 1 is,

$$\begin{aligned} MSE_1 &= P_R \{localMSE\} + \frac{1}{2}(1 - P_R) \{localMSE\} \\ &\quad + \frac{1}{2}(1 - P_R) \left\{ |u_{sl1} - u_1|^2 \right\}, \end{aligned} \quad (9.174)$$

and a similar expression for  $MSE_2$ .

We can rewrite the local MSE as

$$\{localMSE\} = \left\{ (local\ bias)^2 + local\ variance \right\}. \quad (9.175)$$

The reason for this decomposition is that analytic expressions for both terms on the right side of (9.175) are available in the literature. An analytic expression for  $P_R$  is also available, so we can create an analytic expression for the MSE behavior in the critical part of the upper threshold region using (9.174).

For the multiple-sidelobe case, we can write

$$MSE_1 = P_R \{localMSE\} + \frac{1}{2}(1 - P_R) \{localMSE\}$$

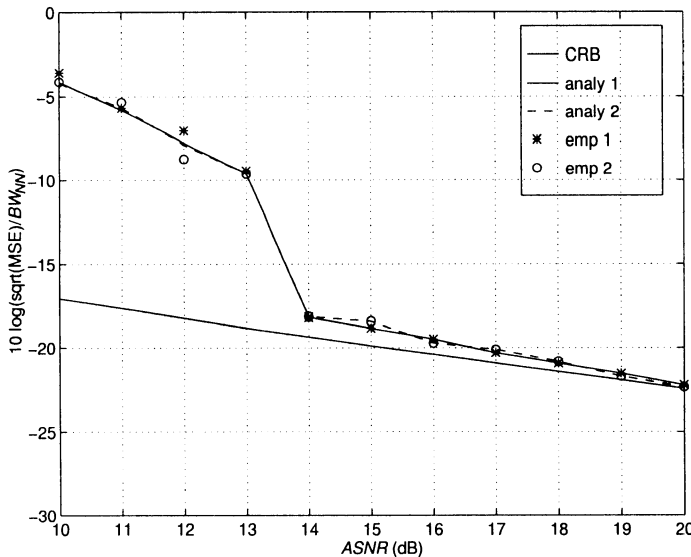


Figure 9.32 Comparison of “analytic” and empirical results: spectral MU-SIC,  $N = 10, K = 100, \rho = 0, u_1 = 0.0433, u_4 = -0.0433$ , 500 trials.

$$+ \frac{1}{2}(1 - P_R) \left\{ \sum_{k=1}^K p_{slk} |u_{slk} - u_1|^2 \right\}, \quad (9.176)$$

where  $p_{slk}$  is the conditional probability that the estimate is near the  $k$ th sidelobe, given the signals were not resolved.

In Figure 9.32, we show the MSE calculated using (9.174), (9.175), and (9.176). In those equations we use measured quantities. Later we show how well the analytic expressions can predict performance.

In Figure 9.33, we show the measured bias and standard deviation. We see that in the region just above the threshold point (in this case, 16 dB), the standard deviation is still essentially on the CRB, but the bias term increases the MSE by a small amount. In the upper threshold region, the variance is the dominant factor in the MSE.

In Figure 9.32, we see that there is a dramatic increase in the MSE in the 3-dB region from 16 dB to 13 dB. The empirical probability of resolution curve is shown in Figure 9.34. We see that  $P_R$  goes from about 0.965 to 1.0 in this region. Therefore, to predict the performance in the upper threshold region, we will need accurate expressions on the upper tail of the  $P_R$  probability density. In addition, we need a large number of trials to get good empirical results in this region.

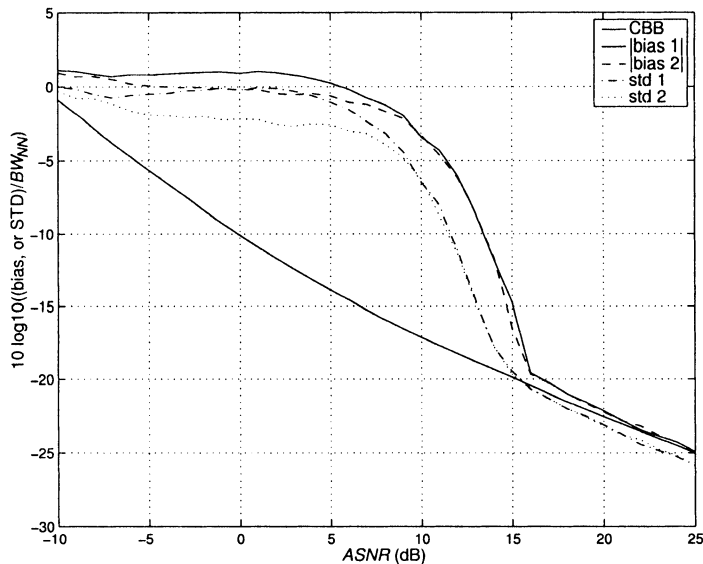


Figure 9.33 Bias and standard deviation versus  $ASNR$ : spectral MUSIC,  $N = 10, K = 100, \rho = 0, u_1 = 0.0433, u_2 = -0.0433$ , 2000 trials.

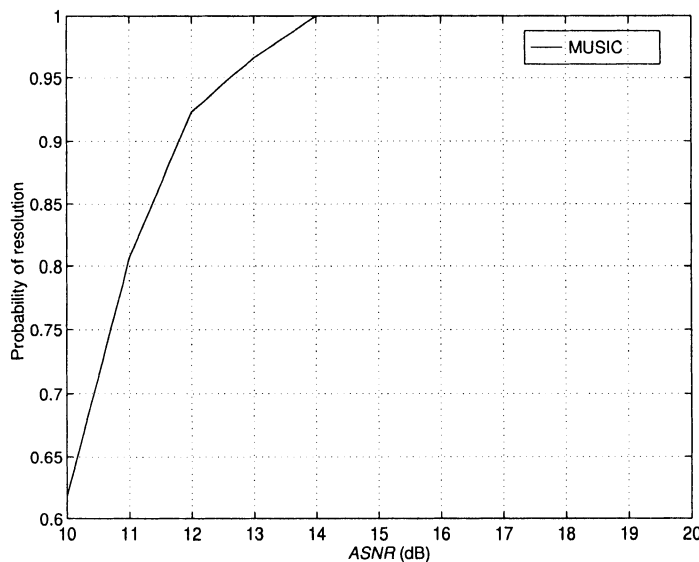


Figure 9.34 Empirical probability of resolution versus  $ASNR$ : spectral MU-SIC,  $N = 10, K = 100, \rho = 0, u_1 = 0.0433, u_2 = -0.0433$ , 500 trials.

### 9.5.2 Resolution of MUSIC and Min-Norm

In this section we study the resolution capability of MUSIC and Min-Norm. The first comprehensive study in this area was due to Kaveh and Barabell ([KB86]). Their analysis is also available in Sections 5.4–5.8 in the chapter by Kaveh and Wang in [Hay91]. Their analysis emphasizes the importance of the mean-value of the null spectrum  $\hat{Q}_{MN}(\psi)$  and justifies its importance by showing that the standard deviation is small. Other studies that utilized the mean of the spectrum include Jeffries and Farrier [JF85], Böhme [Böh83], and Sharman et al. [SDWK83]. In a much earlier paper Cox [Cox73] had analyzed the resolution behavior of various algorithms. Other resolution discussions include Marple [Mar77], Gabriel [Gab80], DeGraaf and Johnson [DJ85] and Johnson and DeGraaf [JD82].

A subsequent paper by Zhou et al. [ZHZ91] developed an expression based on the ensemble covariance matrix and compared their results to Kaveh and Barabell's work.

None of above analyses actually computed a probability of resolution (or an approximation to it). Lee and Wengrovitz [LW91] developed a comprehensive asymptotic statistical characterization of the null spectrum and then used a Gaussian approximation to compute the resolution probability. Zhang [Zha95a] derived the probability distribution without using the Gaussian approximation and got better results in the low *SNR* region.

In this section, we use the sample covariance matrix,

$$\hat{\mathbf{S}}_{\mathbf{x}} = \mathbf{C}_{\mathbf{x}} = \frac{1}{K} \sum_{k=1}^K \mathbf{X}(k) \mathbf{X}^H(k). \quad (9.177)$$

In other words, forward averaging only.

The initial part of our analysis follows Kaveh and Barabell ([KB86]). In order to analyze the asymptotic behavior of subspace methods we need the asymptotic statistics of the estimated eigenvalues and eigenvectors. The original work on asymptotic behavior is due to Anderson [And63]. It has been extended by Brillinger [Bri81], Gupta [Gup65], and Wilkinson [Wil65]. The estimated covariance matrix  $\hat{\mathbf{S}}_{\mathbf{x}}$  has a complex Wishart density whose elements are asymptotically jointly normal (see Section 7.2).

We define

$$\hat{\Phi}_i = \Phi_i + \boldsymbol{\eta}_i, \quad (9.178)$$

and

$$\hat{\lambda}_i = \lambda_i + \beta_i. \quad (9.179)$$

We assume that  $\hat{\Phi}_i$  is normalized. Then  $\boldsymbol{\eta}_i$  and  $\beta_i$  have the following asymptotic properties.

The estimated eigenvalues are asymptotically Gaussian and statically independent,

$$E[\beta_i] = 0, \quad (9.180)$$

$$E[\beta_i \beta_j] = \frac{\lambda_i^2}{K} \delta_{ij}, \quad (9.181)$$

where  $K$  is the number of snapshots.

The estimation error for the eigenvectors are asymptotically jointly Gaussian distributed with mean

$$E[\boldsymbol{\eta}_i] \simeq -\frac{\lambda_i}{2K} \sum_{\substack{k=1 \\ k \neq i}}^N \frac{\lambda_k}{(\lambda_i - \lambda_k)^2} \Phi_i \triangleq c_i \Phi_i, \quad (9.182)$$

and covariances

$$\begin{aligned} E[\boldsymbol{\eta}_i \boldsymbol{\eta}_j^H] &\simeq \frac{\lambda_i}{K} \sum_{\substack{k=1 \\ k \neq i}}^N \frac{\lambda_k}{(\lambda_k - \lambda_i)^2} \Phi_k \Phi_k^H \delta_{ij} \\ &= \frac{\lambda_i}{K} \left\{ \sum_{\substack{k=1 \\ k \neq i}}^D \frac{\lambda_k}{(\lambda_k - \lambda_i)^2} \Phi_k \Phi_k^H + \sum_{k=D+1}^{N-D} \frac{\sigma_n^2}{(\sigma_n^2 - \lambda_i)^2} \Phi_k \Phi_k^H \right\} \delta_{ij} \\ &\triangleq \mathbf{W}_i \delta_{ij}, \end{aligned} \quad (9.183)$$

and

$$E[\boldsymbol{\eta}_i \boldsymbol{\eta}_j^T] \cong -\frac{\lambda_i \lambda_j}{K (\lambda_i - \lambda_j)^2} \Phi_j \Phi_i^T (1 - \delta_{ij}) \triangleq \mathbf{V}_{ij}. \quad (9.184)$$

All of the approximations in (9.180)–(9.184) are of order  $O(K^{-1})$ . Note that (9.184) means that the  $\boldsymbol{\eta}_i$  are not joint complex Gaussian random variables.

Because of the normalization assumption, we can use (9.178) to obtain

$$\|\hat{\Phi}_i\|^2 = 1 + \Phi_i^H \boldsymbol{\eta}_i + \boldsymbol{\eta}_i^H \Phi_i + \boldsymbol{\eta}_i^H \boldsymbol{\eta}_i = 1. \quad (9.185)$$

Therefore,

$$2\operatorname{Re} [\Phi_i^H \eta_i] = -\eta_i^H \eta_i. \quad (9.186)$$

Taking the expectation of (9.186), using (9.182), and retaining terms of order  $K^{-1}$  gives

$$\begin{aligned} 2\operatorname{Re} [\Phi_i^H E[\eta_i]] &\cong -\frac{\lambda_i}{K} \sum_{\substack{k=1 \\ k \neq i}}^N \frac{\lambda_k}{(\lambda_i - \lambda_k)^2} \Phi_i^H \Phi_i \\ &= -\frac{\lambda_i}{K} \sum_{\substack{k=1 \\ k \neq i}}^N \frac{\lambda_k}{(\lambda_i - \lambda_k)^2}. \end{aligned} \quad (9.187)$$

We first consider the MUSIC algorithm.

### 9.5.2.1 MUSIC

The expected value of the null spectrum is obtained by substituting (9.178) in  $\hat{Q}_{MU}(\psi)$  in (9.43) and taking the expectation. Using (9.183) and (9.187), we obtain

$$\begin{aligned} E[\hat{Q}_{MU}(\psi)] &\simeq Q_{MU}(\psi) - \\ &\quad \mathbf{v}^H(\psi) \left[ \sum_{i=1}^D \sum_{\substack{j=1 \\ j \neq i}}^N \frac{\lambda_i \lambda_j}{K(\lambda_i - \lambda_j)^2} (\Phi_j \Phi_j^H - \Phi_i \Phi_i^H) \right] \mathbf{v}(\psi). \end{aligned} \quad (9.188)$$

At the correct DOAs,  $\psi_i, i = 1, 2, \dots, D$ ,  $Q_{MU}(\psi_i) = 0$ . Therefore, in the vicinity of the correct value, when  $D = 2$ , (9.188) reduces to

$$\begin{aligned} E[\hat{Q}_{MU}(\psi_k)] &\simeq \frac{\sigma_w^2}{K} \mathbf{v}^H(\psi_k) \left[ \frac{\lambda_1(N-2)}{(\lambda_1 - \sigma_w^2)^2} \Phi_1 \Phi_1^H + \frac{\lambda_2(N-2)}{(\lambda_2 - \sigma_w^2)^2} \Phi_2 \Phi_2^H \right] \mathbf{v}(\psi_k) \\ &= \frac{\sigma_w^2}{K}(N-2) \mathbf{v}^H(\psi_k) \left[ \frac{\lambda_1}{(\lambda_1^f)^2} \Phi_1 \Phi_1^H + \frac{\lambda_2}{(\lambda_2^f)^2} \Phi_2 \Phi_2^H \right] \mathbf{v}(\psi_k), \\ &\quad k = 1, 2, \end{aligned} \quad (9.189)$$

where the approximation is of  $O(K^{-1})$ .

For two equal-power uncorrelated sources, we use  $\lambda_i$  and  $\Phi$ , from Chapter 5 ((5.255) and (5.259)) in (9.189) to obtain

$$E \left[ \widehat{Q}_{MU}(\psi_k) \right] \simeq \frac{N-2}{K} \left[ \frac{1}{(ASNR)} + \frac{1}{(ASNR)^2 \Delta^2} \right], \quad k = 1, 2, \quad (9.190)$$

where

$$ASNR \triangleq \frac{N\sigma_s^2}{\sigma_w^2}, \quad (9.191)$$

is assumed to be much larger than one and

$$\Delta = \frac{N(\psi_1 - \psi_2)}{2\sqrt{3}}, \quad (9.192)$$

is a separation factor that is proportional to the normalized difference between the wavenumbers. Here we are normalizing with respect to the approximate HPBW ( $\sqrt{3}/N$ ) instead of  $BW_{NN}$  ( $4/N$ ) that we normally use. Most of the papers dealing with this topic use this normalization, so we will also use it in order to simplify comparisons with the literature.

It is difficult to obtain an expression of order  $K^{-2}$  for the variance ( $K^{-1}$  for the standard deviation). Based on reasonably extensive simulation results one can argue that the standard deviation is small compared to the mean. Therefore, we develop a resolution criterion based on  $E \left[ \widehat{Q}_{MU}(\psi) \right]$ .

Kaveh and Barabell [KB86] proposed that the resolution threshold be defined as the  $ASNR$  where

$$E \left[ \widehat{Q}_{MU}(\psi_1) \right] = E \left[ \widehat{Q}_{MU}(\psi_2) \right] = E \left[ \widehat{Q}_{MU}(\psi_m) \right] \quad (9.193)$$

where

$$\psi_m = \frac{\psi_1 + \psi_2}{2}. \quad (9.194)$$

Their logic was:

- (1) If the three variations were statistically independent, then the resolution probability would be 0.33 when (9.193) was satisfied.
- (2) If  $\widehat{Q}_{MU}(\psi_1)$  and  $\widehat{Q}_{MU}(\psi_2)$  were completely correlated, then the resolution probability would be 0.5.
- (3) The MUSIC  $P_R$  result is given in Figure 9.10 (this corresponds to Example 9.2.6 in Section 9.2). The curve is steep in the 0.33–0.50 range and the spread in  $ASNR$  is 1.2 dB between the ends of the range.

The threshold  $ASNR$  is denoted by  $ASNR_T$ . We find  $E[\hat{Q}_{MU}(\psi_m)]$  from (9.189) and  $E[\hat{Q}_{MU}(\psi_1)] (= E[\hat{Q}_{MU}(\psi_2)])$  from (9.190) and equate the two results. For  $N \gg 1$ ,  $\Delta \ll 1$ , and  $ASNR \gg 1$ , we have

$$ASNR_T \simeq \frac{1}{K} \left\{ \frac{20(N-2)}{\Delta^4} \left[ 1 + \sqrt{1 + \frac{K}{5(N-2)} \Delta^2} \right] \right\}. \quad (9.195)$$

For large  $N$ , the threshold  $ASNR$  is proportional to  $N$ . For a small number of snapshots ( $K \ll 5N/\Delta^2$ ),  $ASNR_T$  varies as  $1/\Delta^4 K$ . For a large number of snapshots ( $K \gg 5N/\Delta^2$ ),  $ASNR_T$  varies as  $1/\Delta^3 K^{1/2}$ .

This result (and extensions of it to other cases) has been widely used in the literature. However, if we examine the normalized MSE plot in Figure 9.11 and the probability of resolution plot in Figure 9.10, we see that the definition of resolution threshold (9.193) and the subsequent expressions may give misleading results. When  $P_R = 0.5$ , the MSE shown in Figure 9.11 has already increased dramatically above the CRB and is approaching the *a priori* variance.

A better definition of threshold is the point at which the actual MSE is 3 dB above the CRB. The MSE curve is steep in this region so the use of 3 dB (as contrasted to 2 or 4 dB) is not critical. From Figure 9.10, we see that this choice corresponds to  $P_R$  greater than 0.95. This is what we would expect because with probability  $(1 - P_R)$  we are adding a large MSE to a very small MSE (e.g., from Figure 9.10, the “local” MSE in  $u$ -space is 0.004 at an  $ASNR$  of 12 dB). Note that this point is about 4 dB higher than the  $P_R = 0.4$  value. This threshold definition requires us to examine the  $P_R$  curve in the 0.95–1.00 region.

In [LW91], Lee and Wengrovitz develop a comprehensive statistical characterization of the MUSIC spectrum using asymptotic properties. They find an expression for the joint probability density of  $\hat{\theta}_1$ ,  $\hat{\theta}_2$ , and  $\hat{\theta}_m$ . They compute the probability of the event,

$$\hat{Q}_{MU}(\psi_m) \geq \hat{Q}_{MU}(\psi_i), \quad i = 1, 2. \quad (9.196)$$

In their calculation, they approximate the joint density by a joint Gaussian density using a central limit theorem justification. Zhang [Zha95a] has done a detailed analysis that avoids the Gaussian assumption and obtains a better match between the analytic result and the simulation result in the low  $SNR$  region.

In Figure 9.35, we show an example of Zhang’s result for a standard 8-element array with uncorrelated equal power sources. We see that there is good agreement between the analyses and the simulation.

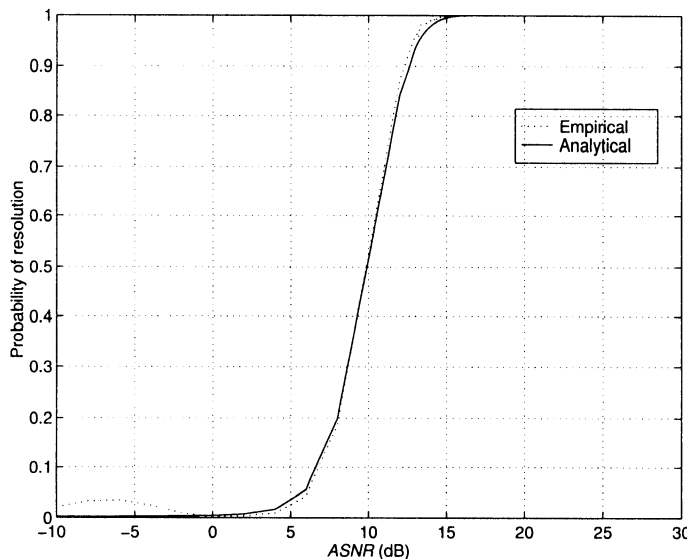


Figure 9.35 Comparison of analytic probability of resolution result and simulation result: 500 trials.

To determine the threshold  $P_R$  we can use the relationship

$$(1 - P_R) [\text{bias}_{1sl}]^2 = \text{MSE}_{loc}, \quad (9.197)$$

and solve for  $P_R$ .

We use the 3-dB criterion as a threshold definition. We use the result in (9.195) to compare various algorithms, but not as an absolute measure.

### 9.5.2.2 Min-Norm

A similar analysis can be carried out for the Min-Norm algorithm. Kaveh and Barabell (e.g., [KB86]) have done this analysis. The expression for the mean value analogous to (9.190) is

$$E[\hat{Q}_{MU}(\psi_k)] \simeq \frac{1}{\left(1 - \frac{4}{N}\right)K} \left[ \frac{1}{(ASNR)} + \frac{1}{(ASNR)^2 \Delta^2} \right] \quad (9.198)$$

(see (5.135) in Chapter 5 of [Hay91]). Comparing (9.190) and (9.198) we see that for large  $N$ , we might expect a lower Min-Norm threshold by a factor of  $N$ . This result is consistent with our simulations in Section 9.3 (see Figure 9.10 at the  $P_R = 0.5$  point).

### 9.5.2.3 Root MUSIC and root Min-Norm

In our simulations, we observed that root MUSIC and root Min-Norm had probability of resolution performance that was significantly better than the spectral versions. We now develop an asymptotic analysis to explain this behavior.<sup>10</sup>

An asymptotic analysis for root MUSIC was derived by Rao and Hari [RH89b]. They derive an expression for the MSE in the asymptotic regime. They approach the problem by first finding the MSE in the location of the zeros and then show how it translates into the MSE in the DOA. Their results retain terms of  $O(K^{-1})$  and assume the bias is zero. The key result is that the asymptotic MSE (which equals the variance) is the same as for spectral MUSIC. Thus, the advantage of root MUSIC is in improved threshold performance and computational simplicity rather than improved asymptotic performance. The reader is referred to [RH89b] for the detailed discussion of their analysis.

In Figure 9.36 we show the effect of an error in the root location on the estimate of the angle. We need to examine both  $E\{|\Delta z_i|^2\}$  and  $E\{|\Delta\psi_i|^2\}$ . In the root case, only  $\Delta\psi_i$  affects the DOA estimate. However, if  $\Delta z_i$  is large, it will cause the peaks in spectral MUSIC to be misplaced and degrade the probability of resolution performance.

Krim et al. [KFP92] carry out an asymptotic analysis of root MUSIC and root Min-Norm by using a series expansion of the projection operators. Their results are in a useful form for comparing the two algorithms.

For root Min-Norm, they show that for the  $m$ th root

$$\begin{aligned} \text{Var}[\Delta\psi_m] &= \text{Var}[\Delta r_m] \\ &= \frac{\sigma_w^2}{2K} \frac{(\mathbf{e}_1^T \mathbf{P}_{\mathbf{V}}^\perp \mathbf{e}_1)}{|(\mathbf{e}_1^T \mathbf{P}_{\mathbf{V}}^\perp \mathbf{d}_m)|^2} \sum_{i=1}^D \frac{\lambda_i}{(\lambda_i - \sigma_w^2)^2} |\Phi_i^H \mathbf{v}_i|^2, \end{aligned} \quad (9.199)$$

where

$$\mathbf{e}_1 = [1 \mid 0 \mid \cdots \mid 0]^T, \quad (9.200)$$

and the summation is familiar (see (9.214)) as

$$\mathbf{v}_i^H \mathbf{U}_P \mathbf{v}_i, \quad (9.201)$$

---

<sup>10</sup>This asymptotic analysis focuses on the mean and variance of the zero location. It only treats the probability of resolution qualitatively.

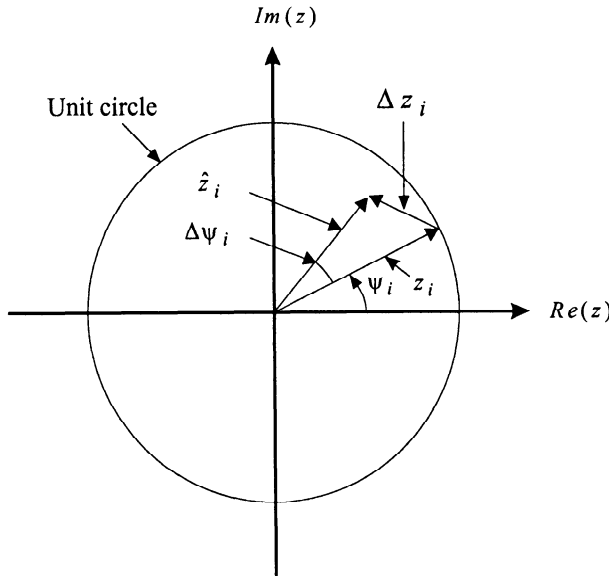


Figure 9.36 Effect of error in the root location on the estimate of  $\psi_i$ .

with  $\mathbf{U}_P$  defined in (9.216). Note that the radial component of the error and the angular (wavenumber) component of the error has the same variance. [KFP92] also show that both components have zero bias and are uncorrelated.

For root MUSIC, one can show that

$$E [\Delta\psi_m] = 0, \quad (9.202)$$

and

$$\begin{aligned} Var [\Delta\psi_m] &= \frac{\sigma^2}{2K (\mathbf{d}_m^H \mathbf{P}_{\mathbf{V}}^{-1} \mathbf{d}_m)} \sum_{i=1}^D \frac{\lambda_i}{(\lambda_i - \sigma_w^2)^2} |\Phi_i^H \mathbf{v}_m|^2 \\ &= \frac{\sigma_w^2}{2K} \frac{\mathbf{v}_m^H \mathbf{U}_P \mathbf{v}_m}{h(\psi_m)}. \end{aligned} \quad (9.203)$$

In Section 9.5.3 we find that spectral MUSIC has the same variance. Thus, spectral MUSIC and root MUSIC have the same asymptotic variance.

In addition, they show  $\Delta\psi_m$  and  $\Delta r_m$  are uncorrelated. However,

$$E [\Delta r_m] = -\sqrt{2(N - D) - \frac{3}{2}} \sqrt{Var (\Delta\psi_m)}, \quad (9.204)$$

and

$$\text{Var} [\Delta r_m] = \frac{\text{Var} (\Delta \psi_m)}{2}. \quad (9.205)$$

This bias in the radial component explains the loss of resolution in spectral MUSIC because it changes the shape of the spectral plot.

We will revisit the variance results for root MUSIC and root Min-Norm in Section 9.5.3.4.

#### 9.5.2.4 Summary

In this section we have included analytic expressions for the probability of resolution for MUSIC and Min-Norm. The analyses used the asymptotic properties of the eigenvectors and eigenvalues. The results were consistent with our simulations and indicated the following ordering in representative cases. In decreasing order of performance:

- (i) Root MUSIC,
- (ii) Root Min-Norm,
- (iii) Min-Norm,
- (iv) MUSIC,

for uncorrelated signals. Note that we did not prove that the above ordering always holds.

There are a large number of analyses of these cases and other cases in the literature. For the case of FB averaging Pillai and Kwon [PK89a] have derived similar results. Roy et al. [RPK86] and Roy and Kailath [RK87] have compared MUSIC and ESPRIT.

If the algorithm has successfully resolved the signals, then we want to analyze the bias and the variance of the estimates. We discuss this problem in the next section.

### 9.5.3 Small Error Behavior of Algorithms

In this section we analyze the error behavior of the various algorithms when the values of  $\text{SNR}$  and  $K$  are such that the algorithms are operating above threshold. In this case, the probability of resolution approaches unity.

In Section 9.5.3.1, we repeat the relevant CRBs from Chapter 8. In Section 9.5.3.2, we analyze the variance of spectral MUSIC. In Section 9.5.3.3, we analyze the bias of spectral MUSIC. In Section 9.5.3.4, we analyze weighted MUSIC, which includes Min-Norm as a special case. In Section

9.5.3.5, we analyze root MUSIC and root Min-Norm. In Section 9.5.3.6, we analyze ESPRIT.

### 9.5.3.1 Cramér-Rao bound

In our discussion we use both the stochastic (or unconditional) CRB and asymptotic conditional CRB as a basis of comparison for the various algorithms.

From (8.99), the unconditional CRB on the  $D \times 1$  DOA vector  $\psi$  is,

$$CRB(\psi) = \frac{\sigma_w^2}{2K} \left[ Re \left\{ \mathbf{H} \odot \left( \mathbf{S}_f \mathbf{V}^H \mathbf{S}_x^{-1} \mathbf{V} \mathbf{S}_f \right)^T \right\} \right]^{-1}, \quad (9.206)$$

where

$$\mathbf{H} = \mathbf{D}^H \mathbf{P}_V^\perp \mathbf{D}. \quad (9.207)$$

From (8.236), the asymptotic conditional Cramér-Rao bound is

$$C_{ACCR}(\psi) = \frac{\sigma_w^2}{2K} \left[ Re \left\{ \mathbf{H} \odot \mathbf{S}_f^T \right\} \right]^{-1}. \quad (9.208)$$

For the special case of uncorrelated sources,  $\mathbf{S}_f$  is a diagonal matrix,

$$\mathbf{S}_f = \text{diag} \left[ \begin{array}{cccc} \sigma_1^2 & \sigma_2^2 & \cdots & \sigma_D^2 \end{array} \right], \quad (9.209)$$

and the asymptotic conditional Cramér-Rao bound for the variance of the  $i$ th source, can be written as

$$C_{ACCR}(\psi_i) = [2KSNR_i h(\psi_i)]^{-1}, \quad (9.210)$$

where

$$h(\psi_i) = \mathbf{D}^H(\psi_i) \mathbf{P}_V^\perp \mathbf{D}(\psi_i). \quad (9.211)$$

### 9.5.3.2 Variance of spectral MUSIC

In this section we derive the asymptotic properties of the spectral MUSIC algorithm. Our discussion follows Stoica and Nehorai [SN89]. Their derivation is also available in their Chapters 7 and 8 of [Hay91]. An earlier discussion that derived the asymptotic relative efficiency for uncorrelated signals is contained in Porat and Friedlander [PF88]. Another early asymptotic analysis is contained in Sharman et al. [SDWK84].

The MUSIC null spectrum is

$$\hat{Q}_{MU}(\psi) = \mathbf{v}^H(\psi) \hat{\mathbf{U}}_N \hat{\mathbf{U}}_N^H \mathbf{v}(\psi), \quad (9.212)$$

in terms of the noise subspace, or

$$\hat{Q}_{MU}(\psi) = \mathbf{v}^H(\psi) \left[ \mathbf{I} - \hat{\mathbf{U}}_S \hat{\mathbf{U}}_S^H \right] \mathbf{v}(\psi), \quad (9.213)$$

in terms of the signal subspace.

The asymptotic behavior of the eigenvectors was given at the beginning of Section 9.5.2 (see (9.182)–(9.184)).

In addition, we need the statistics of the projections of  $\hat{\Phi}_i$ ,  $i = D + 1, \dots, N$  onto the column space of  $\mathbf{U}_S$ . Using (9.178) and (9.183) one can show that these projections are asymptotically jointly Gaussian with zero means and covariance matrices given by

$$\begin{aligned} E \left\{ \left( \mathbf{U}_S \mathbf{U}_S^H \hat{\Phi}_i \right) \left( \mathbf{U}_S \mathbf{U}_S^H \hat{\Phi}_j \right)^H \right\} &= \frac{\sigma_w^2}{K} \left[ \sum_{k=1}^D \frac{\lambda_k}{(\sigma_w^2 - \lambda_k)^2} \Phi_k \Phi_k^H \right] \delta_{ij} \\ &\triangleq \frac{\sigma_w^2}{K} \mathbf{U}_P \delta_{ij}, \quad i, j = D + 1, \dots, N, \end{aligned} \quad (9.214)$$

and

$$E \left\{ \left( \mathbf{U}_S \mathbf{U}_S^H \hat{\Phi}_i \right) \left( \mathbf{U}_S \mathbf{U}_S^H \hat{\Phi}_j \right)^T \right\} = \mathbf{0}, \quad i, j = D + 1, \dots, N. \quad (9.215)$$

The matrix  $\mathbf{U}_P$  can also be expressed as

$$\mathbf{U}_P = \mathbf{U}_S \Lambda_f^{-2} \Lambda_S \mathbf{U}_S^H, \quad (9.216)$$

where

$$\Lambda_f = \text{diag} \left[ \lambda_1 - \sigma_w^2, \quad \lambda_2 - \sigma_w^2, \quad \dots, \quad \lambda_D - \sigma_w^2 \right]. \quad (9.217)$$

With these statistics as background one can derive the asymptotic variance of the MUSIC estimator.

The derivation is due to Stoica and Nehorai [SN89] and relies on a technique used by Sharman et al. [SDWK83] in an earlier analysis of eigenspace methods. Another early analysis is contained in Jeffries and Farrier [JF85].

We start with the necessary condition of the derivative of  $\hat{Q}_{MU}(\psi)$ ,

$$\dot{\hat{Q}}_{MU}(\hat{\psi}) = 0, \quad (9.218)$$

where

$$\dot{\hat{Q}}_{MU}(\hat{\psi}) \triangleq \left. \frac{d\hat{Q}_{MU}(\psi)}{d\psi} \right|_{\psi=\hat{\psi}}. \quad (9.219)$$

We then expand  $\dot{\hat{Q}}_{MU}(\hat{\psi})$  in a Taylor series around  $\psi_i$  and retain the first-order terms. The reader is referred to [SN89] or Chapter 7 of [Hay91] for the detailed derivation.

The result is that the MUSIC estimation errors,

$$\psi_{e_i} \triangleq \hat{\psi}_i - \psi_i, \quad (9.220)$$

are asymptotically jointly Gaussian with zero means and correlation given by

$$E \left\{ \psi_{e_i} \psi_{e_j} \right\} = \frac{1}{2K} \frac{Re \left[ \mathbf{d}^H(\psi_j) \mathbf{U}_N \mathbf{U}_N^H \mathbf{d}(\psi_i) \cdot \mathbf{v}^H(\psi_i) \mathbf{U}_P \mathbf{v}(\psi_j) \right]}{h(\psi_i) h(\psi_j)}, \quad (9.221)$$

where  $\mathbf{d}(\psi)$  is the derivative of the array manifold vector,

$$\mathbf{d}(\psi) = \frac{d\mathbf{v}(\psi)}{d\psi}, \quad (9.222)$$

and

$$h(\psi) = \mathbf{d}^H(\psi) \mathbf{U}_N \mathbf{U}_N^H \mathbf{d}(\psi). \quad (9.223)$$

For the mean square of  $\psi_{e_i}$ , (9.221) reduces to

$$E \left\{ \psi_{e_i}^2 \right\} = \frac{1}{2K} \frac{\mathbf{v}^H(\psi_i) \mathbf{U}_P \mathbf{v}(\psi_i)}{h(\psi_i)}, \quad (9.224)$$

or

$$E \left\{ \psi_{e_i}^2 \right\} = \frac{\sigma_w^2}{2K} \left\{ \frac{\sum_{k=1}^D \frac{\lambda_k}{(\sigma_w^2 - \lambda_k)^2} |\mathbf{v}^H(\psi_i) \Phi_k|^2}{\sum_{k=D+1}^N |\mathbf{d}^H(\psi_i) \Phi_k|^2} \right\}. \quad (9.225)$$

We observe that the numerator will be large if one or more of the  $D$  largest eigenvalues are close to  $\sigma_w^2$ . The denominator in the numerator sum is just the eigenvalue of the source-signal matrix

$$\lambda_k^f = \lambda_k - \sigma_w^2 \quad (9.226)$$

This term will be small if:

- (i) There are two or more closely spaced signals;
- (ii) The signals are highly correlated;
- (iii) The signal-to-noise ratio is low.

(Recall our discussion of eigenvalues in Section 5.5.)

The denominator will be small when  $\mathbf{d}(\psi)$  is close to the column space of  $\mathbf{V}(\psi)$  (or equivalently  $\mathbf{U}_S$ ). In this case, the projection onto  $\mathbf{U}_N$  will be small. This results in a  $Q_{MU}(\psi)$  with a relatively flat minimum around  $\psi = \psi_i$ . If one or more of these conditions occur, then the variance of MUSIC estimator is large.

We now want to put (9.225) in a more convenient form.<sup>11</sup> We can rewrite (9.225) as<sup>12</sup>

$$Var_{MU}(\hat{\psi}_i) = \frac{\frac{\sigma_w^2}{2K} \left\{ \mathbf{v}^H(\psi_i) \left[ \mathbf{U}_S \boldsymbol{\Lambda}_f^{-1} \mathbf{U}_S^H + \sigma_w^2 \mathbf{U}_S \boldsymbol{\Lambda}_f^{-2} \mathbf{U}_S^H \right] \mathbf{v}(\psi_i) \right\}}{\mathbf{d}^H(\psi_i) \mathbf{U}_N \mathbf{U}_N^H \mathbf{d}(\psi_i)}, \quad (9.227)$$

where, from (9.217),

$$\boldsymbol{\Lambda}_f \triangleq \boldsymbol{\Lambda} - \sigma_w^2 \mathbf{I} \triangleq \begin{bmatrix} \lambda_1 & & 0 \\ & \ddots & \\ 0 & & \lambda_D \end{bmatrix} - \sigma_w^2 \mathbf{I}. \quad (9.228)$$

The spectral matrix  $\mathbf{S}_x$  is

$$\mathbf{S}_x = \mathbf{V} \mathbf{S}_f \mathbf{V}^H + \sigma_w^2 \mathbf{I} = \mathbf{U}_S \boldsymbol{\Lambda} \mathbf{U}_S^H + \sigma_w^2 \mathbf{U}_N \mathbf{U}_N^H = \mathbf{U}_S \boldsymbol{\Lambda}_f \mathbf{U}_S^H + \sigma_w^2 \mathbf{I}. \quad (9.229)$$

Thus,

$$\mathbf{V} \mathbf{S}_f \mathbf{V}^H = \mathbf{U}_S \boldsymbol{\Lambda}_f \mathbf{U}_S^H, \quad (9.230)$$

and

$$\mathbf{V} \mathbf{S}_f \mathbf{V}^H \mathbf{V} \mathbf{S}_f \mathbf{V}^H = \mathbf{U}_S \boldsymbol{\Lambda}_f^2 \mathbf{U}_S^H. \quad (9.231)$$

Therefore,

$$(\mathbf{U}_S^H \mathbf{V}) \mathbf{S}_f (\mathbf{V}^H \mathbf{U}_S) = \boldsymbol{\Lambda}_f, \quad (9.232)$$

and

---

<sup>11</sup>This derivation follows Section 7.7 of Stoica and Nehorai's chapter in [Hay91], which originally appeared in [SN89].

<sup>12</sup>In (9.227) we have assumed  $K$  is large enough that the bias can be neglected.

$$\left(\mathbf{U}_S^H \mathbf{V}\right) \mathbf{S}_f \left(\mathbf{V}^H \mathbf{V}\right) \mathbf{S}_f \left(\mathbf{V}^H \mathbf{U}_S\right) = \Lambda_f^2. \quad (9.233)$$

Since  $\mathbf{V}$  has full rank and the columns of  $\mathbf{V}$  lie in the column space of  $\mathbf{U}_S$ , the matrix  $\mathbf{U}_S^H \mathbf{V}$  is non-singular and

$$\mathbf{U}_S \mathbf{U}_S^H = \mathbf{V} \left(\mathbf{V}^H \mathbf{V}\right)^{-1} \mathbf{V}^H. \quad (9.234)$$

Inverting (9.232) and (9.233), we obtain

$$\left(\mathbf{V}^H \mathbf{U}_S\right) \Lambda_f^{-2} \left(\mathbf{U}_S \mathbf{V}\right) = \mathbf{S}_f^{-1} \left(\mathbf{V}^H \mathbf{V}\right)^{-1} \mathbf{S}_f^{-1}, \quad (9.235)$$

and

$$\left(\mathbf{V}^H \mathbf{U}_S\right) \Lambda_f^{-2} \left(\mathbf{U}_S \mathbf{V}\right) = \mathbf{S}_f^{-1} \left(\mathbf{V}^H \mathbf{V}\right)^{-1} \mathbf{S}_f^{-1}. \quad (9.236)$$

Using (9.235) and (9.236) in (9.227) gives

$$Var_{MU}(\hat{\psi}_i) = \frac{\sigma_w^2}{2K} \frac{\left\{ [\mathbf{S}_f^{-1}]_{ii} + \sigma_w^2 \left[ \mathbf{S}_f^{-1} \left(\mathbf{V}^H \mathbf{V}\right)^{-1} \mathbf{S}_f^{-1} \right]_{ii} \right\}}{\mathbf{d}^H(\psi_i) \left[ \mathbf{I} - \mathbf{V} \left(\mathbf{V}^H \mathbf{V}\right)^{-1} \mathbf{V}^H \right] \mathbf{d}(\psi_i)}, \quad (9.237)$$

or

$$Var_{MU}(\hat{\psi}_i) = \frac{\sigma_w^2}{2K} \frac{\left\{ [\mathbf{S}_f^{-1}]_{ii} + \sigma_w^2 \left[ \mathbf{S}_f^{-1} \left(\mathbf{V}^H \mathbf{V}\right)^{-1} \mathbf{S}_f^{-1} \right]_{ii} \right\}}{\mathbf{d}^H(\psi_i) \mathbf{P}_{\mathbf{V}}^\perp \mathbf{d}(\psi_i)}, \quad (9.238)$$

which is the desired result. Using (9.211), (9.238) can be written as

$$Var_{MU}(\hat{\psi}_i) = \frac{\sigma_w^2}{2K} \frac{\left\{ [\mathbf{S}_f^{-1}]_{ii} + \sigma_w^2 \left[ \mathbf{S}_f^{-1} \left(\mathbf{V}^H \mathbf{V}\right)^{-1} \mathbf{S}_f^{-1} \right]_{ii} \right\}}{h(\psi_i)}. \quad (9.239)$$

We observe that we can evaluate (9.237) or (9.238) directly from the original parameters of the model and eigenvector decomposition is not necessary. It is also in a form that is suitable to compare to the Cramér-Rao bound. For analytic simplicity, we use the asymptotic conditional CRB given by (9.208). However, our numerical examples will include the unconditional CRB. In the region of interest, the unconditional and conditional CRBs are essentially the same. In most of our examples, the threshold occurs before the two bounds separated. The results for uncorrelated signals are due to Porat and Friedlander [PF88].

We first consider the case of a single source. In this case, (9.208) reduces to

$$\begin{aligned} \text{Var}_{\text{ACCR}} [\hat{\psi}] &= \frac{\frac{\sigma_w^2}{\sigma_s^2}}{2Kh(\psi)} \left[ 1 + \frac{\sigma_w^2}{N\sigma_s^2} \right] \\ &= \frac{(1 + ASNR^{-1})}{2Kh(\psi) SNR}. \end{aligned} \quad (9.240)$$

Similarly, from (9.239),

$$\text{Var}_{\text{MU}} [\hat{\psi}] = \frac{\frac{\sigma_w^2}{\sigma_s^2}}{2Kh(\psi)} \left[ 1 + \frac{\sigma_w^2}{N\sigma_s^2} \right]. \quad (9.241)$$

Thus, for a single signal the asymptotic variance of MUSIC is identical to the CRB variance.

We now consider the case of  $D$  uncorrelated signals. For the case of uncorrelated signals,  $\mathbf{S}_F$  is a diagonal matrix whose  $i$ th element is  $\sigma_i^2$ , the power of the  $i$ th signal. In this case, (9.239) reduces to

$$\begin{aligned} \text{Var}_{\text{MU}} [\hat{\psi}_i] &= \frac{1}{2K \cdot SNR_i} \frac{\left\{ 1 + \frac{[(\mathbf{V}^H \mathbf{V})^{-1}]_{ii}}{SNR_i} \right\}}{h(\psi_i)} = \frac{1 + (N \cdot SNR_i)^{-1}}{2K \cdot SNR_i \cdot h(\psi_i)} \\ &= \frac{\left[ 1 + ASNR_i^{-1} \right]}{2Kh(\psi_i) SNR_i} \approx \frac{1}{2(K \cdot SNR_i)(N \cdot SNR_i)h(\psi_i)}, \end{aligned} \quad (9.242)$$

where the approximation is valid for  $ASNR_i \gg 1$ . The  $SNR$  for the  $i$ th signal is

$$SNR_i \triangleq \frac{\sigma_i^2}{\sigma_w^2}. \quad (9.243)$$

The asymptotic conditional CRB is

$$\text{Var}_{\text{ACCR}} (\hat{\psi}_i) = \frac{1}{2K \cdot SNR_i \cdot h(\psi_i)}. \quad (9.244)$$

Using (9.242) and (9.244), we have

$$\frac{\text{Var}_{\text{MU}} (\hat{\psi}_i)}{\text{Var}_{\text{ACCR}} (\hat{\psi}_i)} = 1 + ASNR_i^{-1}. \quad (9.245)$$

Therefore, as the  $ASNR_i$  increase, the variance of spectral MUSIC approaches the Cramér-Rao bound. In many cases (e.g., Figure 9.10), the  $ASNR$  required to be above the threshold is such that the ratio in (9.245) is close to one.

The last case of interest is  $D$  correlated signals. In this case, we use (9.239) with a non-diagonal  $\mathbf{S}_f$  and the CRB expression in (9.206). In the examples, we verify that, for correlated signals, the variance of MUSIC does not approach the Cramér-Rao bound. The results for correlated signals are due to Stoica and Nehorai [SN89].

Before considering several examples, we note that we can write the covariance matrix given by (9.221) compactly as

$$\begin{aligned} \mathbf{C}_{MU} = & \frac{\sigma_w^2}{2K} \left( \mathbf{D}^H \mathbf{P}_V^\perp \mathbf{D} \odot \mathbf{I} \right)^{-1} \\ & \times \left[ \operatorname{Re} \left\{ \mathbf{D}^H \mathbf{P}_V^\perp \mathbf{D} \odot \mathbf{S}_f^{-1} + \sigma_w^2 \left( \mathbf{S}_f \mathbf{V}^H \mathbf{V} \mathbf{S}_f \right)^{-1} \right\} \right] \\ & \times \left( \mathbf{D}^H \mathbf{P}_V^\perp \mathbf{D} \odot \mathbf{I} \right)^{-1}. \end{aligned} \quad (9.246)$$

and (9.239) is the diagonal element of (9.246). This expression can be rewritten as

$$\mathbf{C}_{MU} = \frac{\sigma_w^2}{2K} \left\{ [\mathbf{H} \odot \mathbf{I}]^{-1} \left[ \operatorname{Re} \left\{ \mathbf{H} \odot \mathbf{F}^T \right\} \right] [\mathbf{H} \odot \mathbf{I}]^{-1} \right\}, \quad (9.247)$$

where  $\mathbf{H}$  is defined in (9.192) and

$$\mathbf{F} \triangleq \mathbf{S}_f^{-1} + \sigma_w^2 \mathbf{S}_f^{-1} \left( \mathbf{V}^H \mathbf{V} \right)^{-1} \mathbf{S}_f^{-1}. \quad (9.248)$$

We now consider several examples to illustrate the asymptotic behavior of the MUSIC estimator. The examples consider the case of two signals of equal power and a linear uniform array. Then we can write

$$\mathbf{S}_f = \begin{bmatrix} 1 & \rho \\ \rho^* & 1 \end{bmatrix}, \quad (9.249)$$

where  $\rho$  is correlation coefficient and we have assumed  $\sigma_s^2 = 1$ . For two signals, the variance in wavenumber space will depend on

$$\Delta\psi = \psi_1 - \psi_2. \quad (9.250)$$

In the examples, we plot

$$EFF_{MU} = \frac{Var_{MU}(\hat{\psi}_i)}{Var_{CRB}(\hat{\psi}_i)}, \quad (9.251)$$

where the numerator is given by (9.239) and the denominator by (9.210). Note that we use the  $Var_{CRB}$  in our plot rather than  $Var_{ACCR}$ .

### Example 9.5.1

We consider a 10-element standard linear array and consider several values of  $SNR$  and  $\rho$ . The three values of  $ASNR$  are 10 dB, 20 dB, and 30 dB. We consider five values of  $\rho$ : 0, 0.5, 0.5  $\exp(-j\pi/2)$ , 0.9 and 0.9  $\exp(-j\pi/2)$ .

In the first set of figures, we plot the normalized  $Var_{MU}(\hat{\psi}_i)$  as given by (9.239) (normalized by  $BW_{NN}$ ). In Figure 9.37(a), we show the results for  $ASNR = 10$  dB. In Figure 9.37(b) we show the results for  $ASNR = 20$  dB. In Figure 9.37(c), we show the results for  $ASNR = 30$  dB.

In the second set of figures, Figure 9.38(a), 9.38(b), and 9.38(c), we plot the efficiency as given by (9.251) for the same cases as in Figure 9.37. These figures are similar to those in [SN89] except they use asymptotic CCRB.

We see that the efficiency that is higher for smaller  $\Delta\psi/BW_{NN}$ . Once the separation exceeds  $2BW_{NN}$ , the efficiency is reasonably constant,

$$EFF_{MU} = 1 - |\rho|^2, \quad (9.252)$$

for  $\Delta\psi > BW_{NN}$ .

### Example 9.5.2

In this example we plot the relative asymptotic efficiency of MUSIC versus the signal separation normalized by the  $BW_{NN}$  for  $N = 10$ , and  $SNR = 0$  and 20 dB. Figure 9.39 corresponds to  $\rho = 0.5$ , and Figure 9.40 corresponds to  $\rho = 0.9$ .

All of our examples have considered two signals. For large  $N$ , high  $SNR$ , and  $\Delta\psi \geq BW_{NN}$ , one can show that, for  $D$  signals,

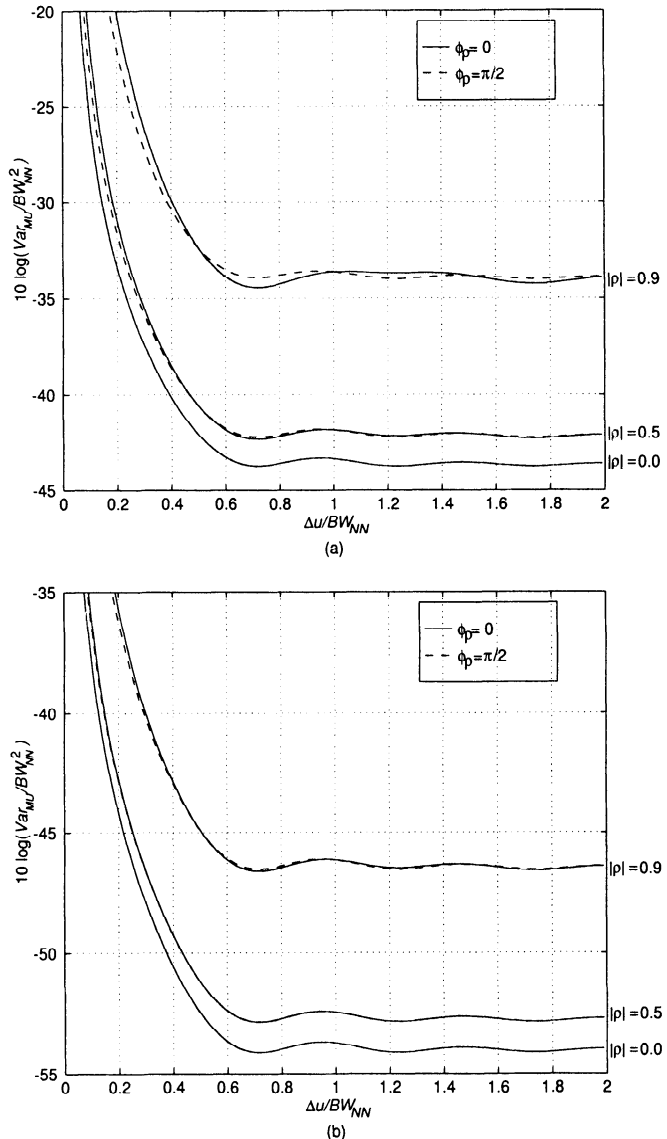
$$EFF_{MU} = \frac{[\mathbf{S}_f]_{ii}}{[\mathbf{S}_f^{-1}]_{ii}}, \quad (9.253)$$

(see [SN89]). Note that for  $D = 2$ , (9.253) reduces to

$$EFF_{MU} = 1 - |\rho|^2, \quad (9.254)$$

which is consistent with the results in Figures 9.38–9.40. For  $D \geq 2$ , as  $\mathbf{S}_f$  approaches a singular matrix, the efficiency of MUSIC approaches zero.

All of the asymptotic results for spectral MUSIC are valid for large  $K$  and used  $O(K^{-1})$  approximations. However, Xu and Buckley [XB92] pointed out that the treatment of bias term in the MUSIC derivation was a first-order approximation and that, as we moved closer to the transition region, a second-order approximation is more appropriate. In the next section we introduce their analysis.



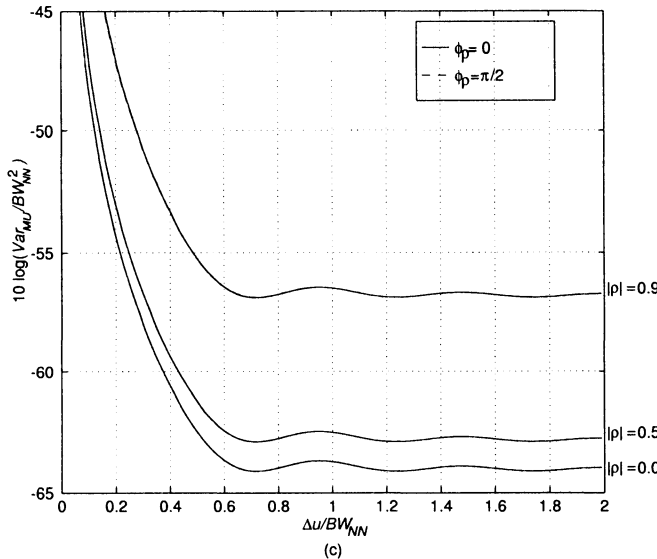


Figure 9.37 Asymptotic variance of spectral MUSIC versus  $\Delta u/BW_{NN}$ :  $N = 10$ ,  $|\rho| = 0, 0.5$  and  $0.9$ : (a)  $ASNR = 10$  dB; (b)  $ASNR = 20$  dB; and (c)  $ASNR = 30$  dB.

### 9.5.3.3 Bias analysis of MUSIC

A bias analysis of the MUSIC algorithm has been carried out by Xu and Buckley [XB92]. The bias of the MUSIC algorithm is a relevant performance issue when either the  $SNR$  or  $K$ , the number of snapshots is in a “medium” range so that the system is approaching the threshold.

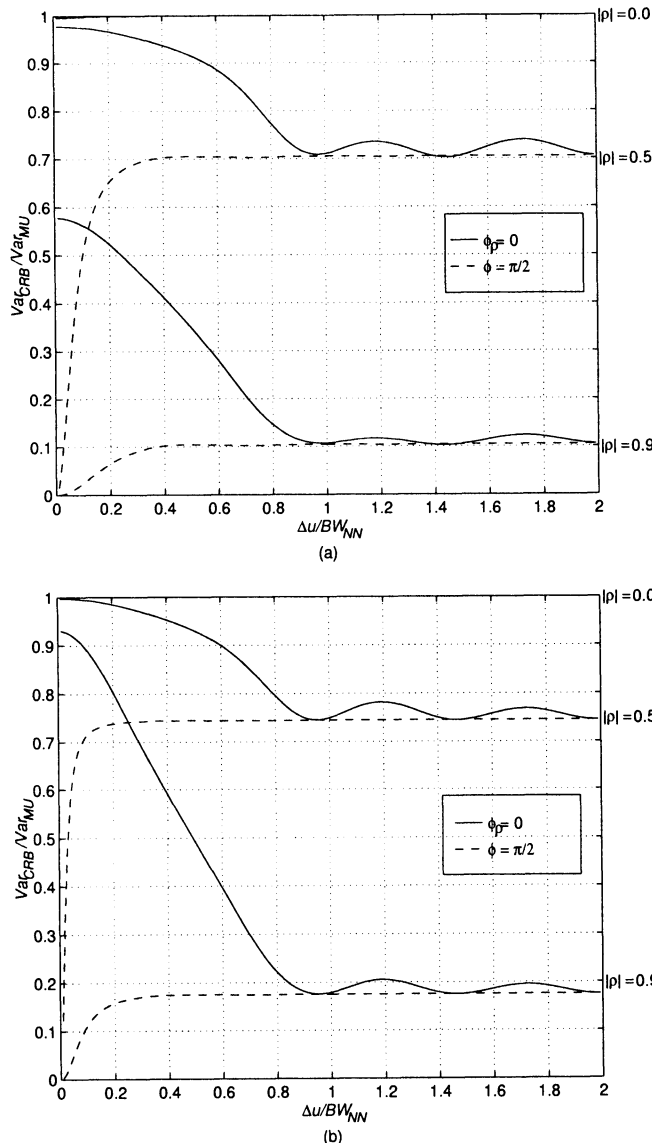
In [XB92], a bias analysis using a second-order Taylor series expansion of  $\dot{Q}_{MU}(\hat{\psi}_m, \hat{\mathbf{U}}_S)$  around  $(\psi_m, \mathbf{U}_S)$  is carried out.<sup>13</sup> The mid-point,  $\psi_m$ , is defined in (9.169). The result is

$$\begin{aligned} E(\Delta\psi_m) &\simeq -\frac{2\sigma_n^2}{K} \frac{\sum_{k=1}^D \frac{(N-D-1)\lambda_k}{(\lambda_k - \sigma_n^2)^2} \operatorname{Re} [\mathbf{d}^H(\psi_m) \Phi_k \Phi_k^H \mathbf{v}(\psi_m)]}{\ddot{Q}_{MU}(\psi_m, \mathbf{U}_S)} \\ &\quad - \frac{\ddot{Q}_{MU}(\psi_m, \mathbf{U}_S)}{6\dot{Q}_{MU}(\psi_m, \mathbf{U}_S)} \operatorname{Var}(\Delta\psi_m), \end{aligned} \quad (9.255)$$

where

$$\ddot{Q}_{MU}(\psi_m, \mathbf{U}_S) = 2\mathbf{d}^H(\psi_m) [\mathbf{I} - \mathbf{U}_S \mathbf{U}_S^H] \mathbf{d}(\psi_m), \quad (9.256)$$

<sup>13</sup>We have suppressed the overbar in  $\dot{Q}_{MU}(\hat{\psi}_m, \hat{\mathbf{U}}_S)$  to simplify the notation.



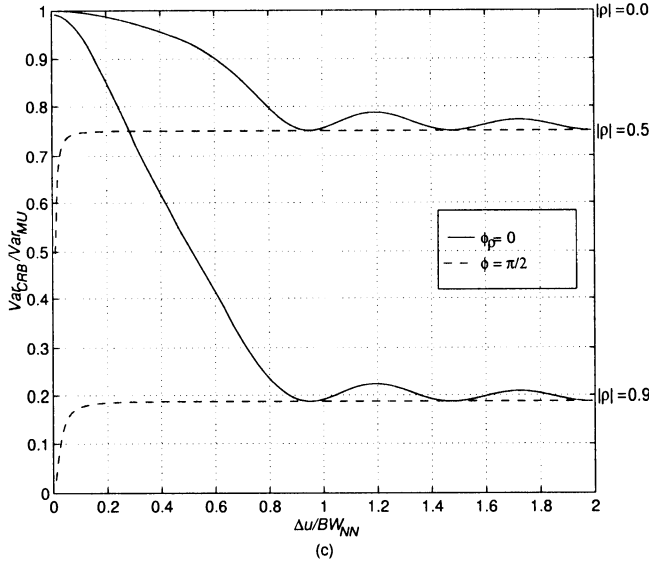


Figure 9.38 Asymptotic efficiency of spectral MUSIC algorithm versus  $\Delta u/BW_{NN}$ :  $N = 10$ ,  $|\rho| = 0, 0.5$ , and  $0.9$ : (a)  $ASNR = 10$  dB; (b)  $ASNR = 20$  dB; and (c)  $ASNR = 30$  dB.

and

$$\ddot{Q}_{MU}(\psi_m, \mathbf{U}_S) = 6Re \left\{ \dot{\mathbf{d}}^H(\psi_m) \left[ \mathbf{I} - \mathbf{U}_S \mathbf{U}_S^H \right] \mathbf{d}(\psi_m) \right\}. \quad (9.257)$$

The reader is referred to [XB92] for the details of the derivation and further discussion of the results.

#### 9.5.3.4 Weighted eigenspace algorithms

We have developed several weighted eigenspace (WES) algorithms in addition to MUSIC. These included Min-Norm (9.95). In this section, we provide the asymptotic variance for WES algorithms and show that their variance is greater than or equal to the asymptotic variance of MUSIC. The initial discussion follows [SN90] (see also Chapter 8 of [Hay91]).

Note that this result does not imply that the composite MSE performance of MUSIC is better than the other WES algorithms.

We use the spectral form for discussion. The WES algorithm constructs the null spectrum

$$\hat{Q}_{WES}(\psi) = \mathbf{v}^H(\psi) \hat{\mathbf{U}}_N \mathbf{W} \hat{\mathbf{U}}_N^H \mathbf{v}(\psi), \quad (9.258)$$

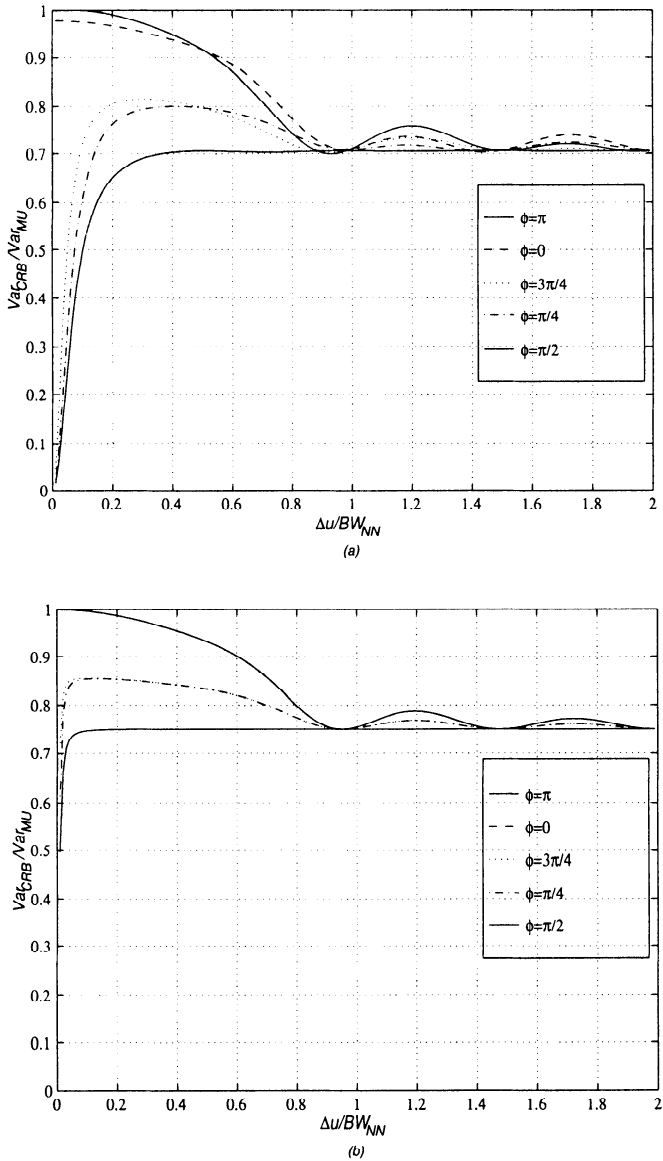


Figure 9.39 Asymptotic efficiency of spectral MUSIC for two equal-power signals as a function of  $\Delta u/BW_{NN}$ :  $|\rho| = 0.5$ , and  $N = 10$ : (a)  $SNR = 0$  dB; (b)  $SNR = 20$  dB.

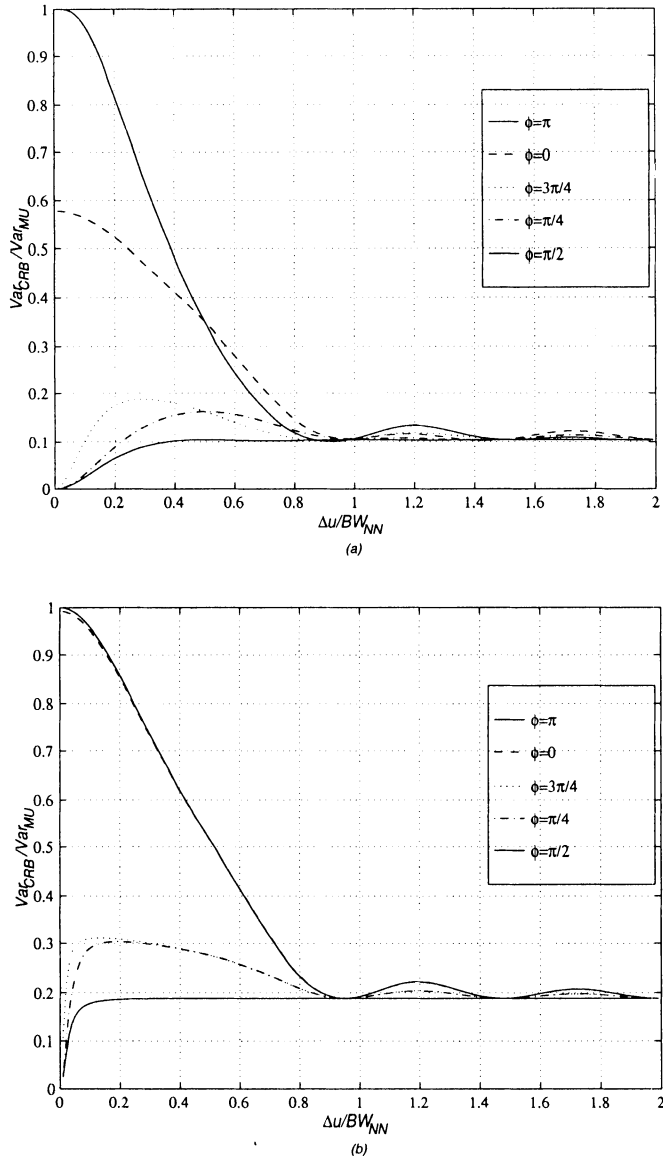


Figure 9.40 Asymptotic efficiency of spectral MUSIC for two equal-power signals as a function of  $\Delta u/BW_{NN}$ :  $\rho = 0.9$ , and  $N = 10$ : (a)  $SNR = 0$  dB; (b)  $SNR = 20$  dB.

where  $\mathbf{W}$  is a positive definite weighting matrix. We search over  $\psi$  to find the nulls.

One can show that the asymptotic covariance matrix is

$$\mathbf{C}_{WES} = \frac{\sigma_w^2}{2K} (\bar{\mathbf{H}} \odot \mathbf{I})^{-1} \cdot \text{Re} \left\{ \tilde{\mathbf{H}} \odot (\mathbf{V}^H \mathbf{U} \mathbf{V})^T \right\} \cdot (\bar{\mathbf{H}} \odot \mathbf{I})^{-1}, \quad (9.259)$$

where  $\mathbf{U}$  is defined implicitly by

$$\mathbf{V}^H \mathbf{U} \mathbf{V} = \mathbf{S}_f^{-1} + \sigma_w^2 \mathbf{S}_f^{-1} (\mathbf{V}^H \mathbf{V})^{-1} \mathbf{S}_f^{-1}, \quad (9.260)$$

and

$$\bar{\mathbf{H}} = \mathbf{D}^H \mathbf{U}_N \mathbf{W} \mathbf{U}_N^H \mathbf{D}, \quad (9.261)$$

$$\tilde{\mathbf{H}} = \mathbf{D}^H \mathbf{U}_N \mathbf{W}^2 \mathbf{U}_N^H \mathbf{D}, \quad (9.262)$$

(e.g., Appendix B of [SN90]). The elements of  $\mathbf{C}_{WES}$  can be written as

$$[\mathbf{C}_{WES}]_{ij} = \frac{\sigma_w^2}{2K} \frac{\text{Re} \left[ \tilde{\mathbf{H}}_{ij} (\mathbf{V}^H \mathbf{U} \mathbf{V})_{ji} \right]}{(\bar{\mathbf{H}} \odot \mathbf{I})_{ii} (\bar{\mathbf{H}} \odot \mathbf{I})_{jj}}. \quad (9.263)$$

The variances are given by (9.263) with  $i = j$ .

We can use the result in (9.259) for two purposes. First, we can compare the error variances for arbitrary  $\mathbf{W}$  to the case when  $\mathbf{W} = \mathbf{I}$ . Second, we can compare the error variances for other WES algorithms.

One can show that

$$\mathbf{C}_{WES} \odot \mathbf{I} \geq \mathbf{C}_{MU} \odot \mathbf{I}. \quad (9.264)$$

(e.g., Appendix C of [SN90]). Thus, if we are in the asymptotic regime, the best weighting is the identity matrix of conventional MUSIC. As pointed out in [SN90], the optimal weighting might be different for small- or medium-sized samples.

We consider a simple example to illustrate the asymptotic behavior of the algorithms.

### Example 9.5.3

We consider a 10-element standard linear array. We assume that there are two uncorrelated equal-power signals located at  $\pm \Delta\psi/2$  where  $\Delta\psi = \Delta\psi_R$ . In Figure 9.41, we plot  $[\mathbf{C}_{WES}]_{11}$  from (9.263) for MUSIC and Min-Norm. The unconditional CRB is shown for comparison.

We see that the simulated results and the analytic results are the same above 15 dB. MUSIC achieves the CRB, while Min-Norm is 1.9 dB above it.

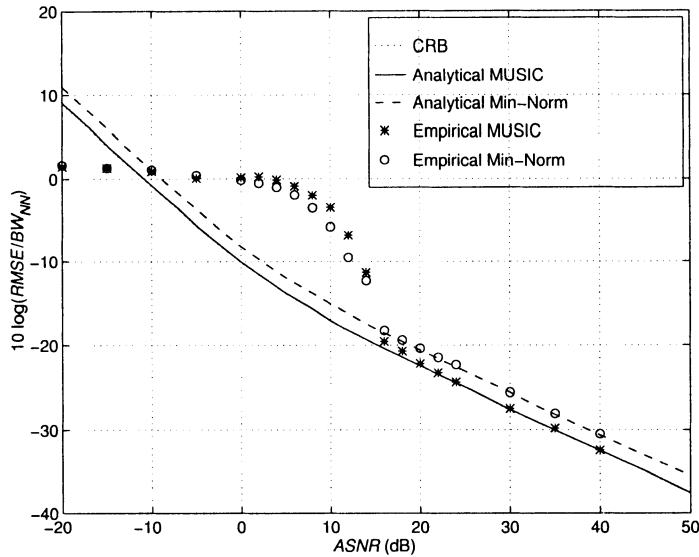


Figure 9.41 Asymptotic variance of MUSIC and Min-Norm algorithms versus  $ASNR : N = 10, K = 100, \rho = 0, \Delta u = 0.2165BW_{NN}$ .

### 9.5.3.5 Root MUSIC and root Min-Norm

In Section 9.5.2.3 we provided expressions for the mean and variance of the roots in root MUSIC and root Min-Norm. We repeat the results here for convenience.

For root Min-Norm, for the  $m$ th root,

$$\begin{aligned} Var[\Delta\psi_m] &= Var[\Delta r_m] \\ &= \frac{\sigma_w^2}{2K} \frac{(\mathbf{e}_1 \mathbf{P}_{\mathbf{V}}^\perp \mathbf{e}_1)}{|(\mathbf{e}_1^T \mathbf{P}_{\mathbf{V}}^\perp \mathbf{d}_m)|^2} \sum_{i=1}^D \frac{\lambda_i}{(\lambda_i - \sigma_w^2)^2} |\Phi_i^H \mathbf{v}_i|^2, \end{aligned} \quad (9.265)$$

where

$$\mathbf{e}_1 = [1 \mid 0 \mid \cdots \mid 0]^T, \quad (9.266)$$

and the summation is familiar (see (9.214)) as

$$\mathbf{v}_i^H \mathbf{U}_P \mathbf{v}_i, \quad (9.267)$$

with  $\mathbf{U}_P$  defined in (9.216). Note that the radial component of the error and the angular (wavenumber) component of the error has the same variance.

Krim et al. [KFP92] also show that both components have zero bias and are uncorrelated.

For root MUSIC, one can show that

$$E[\Delta\psi_m] = 0, \quad (9.268)$$

and

$$\begin{aligned} Var[\Delta\psi_m] &= \frac{\sigma_w^2}{2K(\mathbf{d}_m^H \mathbf{P}_V^\perp \mathbf{d}_m)} \sum_{i=1}^D \frac{\lambda_i}{(\lambda_i - \sigma_w^2)^2} |\Phi_i^H \mathbf{v}_m|^2 \\ &= \frac{\sigma_w^2}{2K} \frac{\mathbf{v}_m^H \mathbf{U}_P \mathbf{v}_m}{h(\psi_m)}, \end{aligned} \quad (9.269)$$

which is identical to (9.238), so root MUSIC and spectral MUSIC have the same asymptotic variance.

In addition, one can show that  $\Delta\psi_m$  and  $\Delta r_m$  are uncorrelated. However,

$$E[\Delta r_m] = -\sqrt{2(N-D) - \frac{3}{2}} \sqrt{Var(\Delta\psi_m)}, \quad (9.270)$$

and

$$Var[\Delta r_m] = \frac{Var(\Delta\psi_m)}{2}. \quad (9.271)$$

This bias in the radial component explains the loss of resolution in spectral MUSIC because it changes the shape of the spectral plot.

Using the result in (9.265) and (9.269), we can compare the performance of root MUSIC and root Min-Norm. The ratio of the two variances is

$$\gamma = \frac{Var_{RMU}\{\Delta\psi_m\}}{Var_{RMN}\{\Delta\psi_m\}} = \frac{|\mathbf{e}_1^T \mathbf{P}_V^\perp \mathbf{d}_m|^2}{(\mathbf{e}_1^T \mathbf{P}_V^\perp \mathbf{e}_1)(\mathbf{d}_m^H \mathbf{P}_V^\perp \mathbf{d}_m)}. \quad (9.272)$$

Using the Schwarz inequality on the numerator and remembering that  $\mathbf{P}_V^\perp \mathbf{P}_V^\perp$ , we have

$$|\mathbf{e}_1^T \mathbf{P}_V^\perp \mathbf{d}_m|^2 = |\mathbf{e}_1^T \mathbf{P}_V^\perp \mathbf{P}_V^\perp \mathbf{d}_m|^2 \leq |\mathbf{e}_1^T \mathbf{P}_V^\perp|^2 |\mathbf{P}_V^\perp \mathbf{d}_m|^2. \quad (9.273)$$

Thus,  $\gamma \leq 1$ . Note that  $\gamma$  is independent of the *SNR*. In addition, as  $N$  increases, the performance difference increases.

We consider an example to illustrate the behavior.

#### Example 9.5.4

Consider a 10-element standard linear array with two equal power uncorrelated sources separated by  $\Delta\psi_R$  impinging on the array. The results predicted by (9.265) and (9.269) are shown in Figure 9.42. For this scenario,  $\gamma = 1.9$  dB.

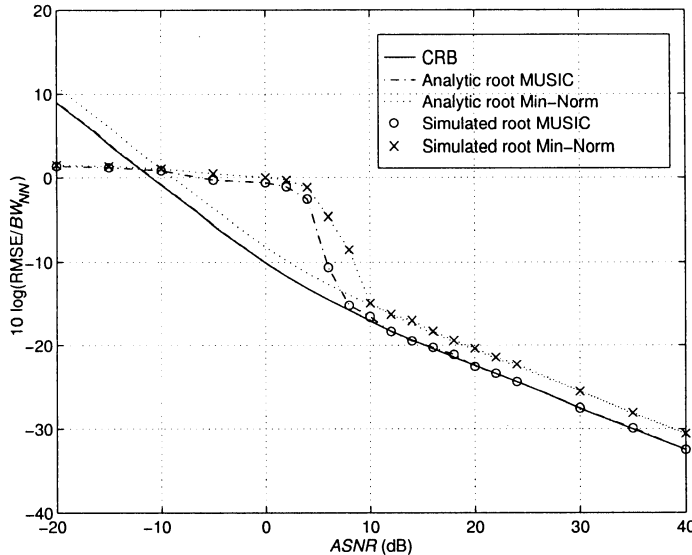


Figure 9.42 Theoretical and simulated RMSE for root MUSIC and root Min-Norm:  $N = 10, K = 100, \Delta\psi = \Delta\psi_R$ , 200 trials.

In addition, we show the results of the previous simulations. We see that the simulations are consistent with the analytic results.

The results in this section and Section 9.5.1 lead to two observations:

- (i) Root MUSIC has advantages over spectral MUSIC in terms of computational complexity and probability of resolution. The two versions of MUSIC have the same asymptotic MSE.
- (ii) The asymptotic variance of root Min-Norm is always greater than or equal to the variance of asymptotic root MUSIC. In many scenarios of interest, the difference is significant.

The asymptotic behavior of unitary root MUSIC is derived in Pesavento et al. [PGH00].

#### 9.5.3.6 Asymptotic behavior of ESPRIT

The ESPRIT algorithm was described in Section 9.4.3. A sequence of papers has analyzed the asymptotic performance. We briefly summarize the results of four of these references: Rao and Hari [RH89a], Stoica and Nehorai [SN91b], Ottersten et al. [OVK91], and Viberg and Ottersten [VO91]. Other

references that discuss the asymptotic behavior include Yuen and Friedlander [YF96b], Li et al. [LVT91], and Gavish and Weiss [GW93].

The first results are in [RH89a]. They consider the asymptotic behavior of ESPRIT, TLS-ESPRIT, and TAM (Toeplitz Approximation Method). They show:

- (a) TLS-ESPRIT and ESPRIT have the same asymptotic variance;
- (b) ESPRIT and TAM have the same statistical properties and the same MSE (without an asymptotic assumption).

They derive an asymptotic formula for the MSE using a first-order approximation.

Stoica and Nehorai [SN91b] derived results for the asymptotic variance. Their results are more general than [RH89a] and the expressions are in the same format as the MUSIC results in Section 9.5. Their analysis is for least squares ESPRIT, but [RH89a] showed the asymptotic variances are equal, so the results hold for the TLS-ESPRIT algorithm developed in Section 9.4.4.

We assume the subarrays contain  $N_s$  elements where  $D \leq N_s \leq N - 1$  and  $N_s = N - d_s$ . The subarray manifolds are given by

$$\mathbf{V}_y = \left[ \begin{array}{c|c} \mathbf{0} & \tilde{\mathbf{J}}_{N_s} \end{array} \right] \mathbf{V} = \left[ \begin{array}{c|c} \tilde{\mathbf{J}}_{N_s} & \mathbf{0} \end{array} \right] \mathbf{V} \Phi = \mathbf{V}_x \Phi, \quad (9.274)$$

where the various matrices were defined in (9.103)–(9.107). Then, using the same approach as in Section 9.5.3.2, we obtain<sup>14</sup>

$$E \left[ (\hat{\psi}_k - \psi_k) (\hat{\psi}_l - \psi_l) \right] = \frac{\sigma_w^2}{2Kd_s^2} Re \left[ e^{j(\psi_l - \psi_k)} (\mathbf{C}_l^H \mathbf{C}_k) (\mathbf{v}_k^H \mathbf{U}_P \mathbf{v}_l) \right], \quad (9.275)$$

where

$$\mathbf{C}_k = \left[ \left( \mathbf{V}_x^H \mathbf{V}_x \right)^{-1} \mathbf{V}_x^H \mathbf{F}_k \right]_k^{(r)}, \quad (9.276)$$

and  $[\mathbf{X}]_k^{(r)}$  denotes the  $k$ th row of  $\mathbf{X}$ . The  $\mathbf{F}_k$  matrix is

$$\mathbf{F}_k = \left[ \begin{array}{c|c} \mathbf{0} & \mathbf{I}_{N_s} \end{array} \right] - e^{j d_s \psi_k} \left[ \begin{array}{c|c} \mathbf{I}_{N_s} & \mathbf{0} \end{array} \right], \quad (9.277)$$

where  $\mathbf{I}_{N_s}$  is an  $N_s \times N_s$  identity matrix. As before,

$$\mathbf{U}_P = \mathbf{U}_S \boldsymbol{\Lambda}_f^{-2} \boldsymbol{\Lambda}_S \mathbf{U}_S^H, \quad (9.278)$$

---

<sup>14</sup>The result in (9.275) is given in [SN91b]. The  $\theta_k$  in their notation corresponds to  $d_s \psi_k$  in our notation.

and

$$\mathbf{v}_k^H \mathbf{U}_P \mathbf{v}_l = \left[ \mathbf{S}_{\mathbf{f}}^{-1} \right]_{kl} + \sigma_w^2 \left[ \mathbf{S}_{\mathbf{f}}^{-1} \left( \mathbf{V}_{\mathbf{x}}^H \mathbf{V}_{\mathbf{x}} \right)^{-1} \mathbf{S}_{\mathbf{f}}^{-1} \right]_{kl}. \quad (9.279)$$

We consider two simple examples to illustrate the result. Before doing that, it is useful to compare the asymptotic variance of ESPRIT to the asymptotic variance of MUSIC. We can write the ratio of the variance as

$$\gamma_k = \frac{\text{Var}_{\text{ES}}(\hat{\psi}_k)}{\text{Var}_{\text{MUSIC}}(\hat{\psi}_k)}. \quad (9.280)$$

The numerator is given by (9.275) with  $k = l$ , and the denominator is given by (9.238). Cancelling common terms, we have

$$\gamma_k = \left( \mathbf{C}_k^H \mathbf{C}_k \right) \left( \mathbf{d}_k^H \mathbf{U}_N \mathbf{U}_N^H \mathbf{d}_k \right), \quad k = 1, 2, \dots, D. \quad (9.281)$$

In Appendix B of [SN91b], the Schwarz inequality is used to show that  $\gamma_k \geq 1$ . Note that the ratio does not depend on  $\sigma_w^2$  or  $\mathbf{S}_{\mathbf{f}}$ .

We now illustrate the behavior with two examples.

#### Example 9.5.5<sup>15</sup>

Consider a single source at wavenumber  $\psi$  impinging on a ULA with  $N$  sensors. Assume that  $N_s = N - 1$  and that row weighting is not used.

From (9.276),

$$\begin{aligned} \mathbf{C}^H &= \frac{1}{N-1} \left[ \begin{array}{c|c|c|c|c} 1 & e^{-j\psi} & \cdots & e^{-j(N-2)\psi} \\ \hline \mathbf{0} & \mathbf{I}_{N-1} & & & \end{array} \right] \\ &\quad \cdot \left( \left[ \begin{array}{c|c} \mathbf{0} & \mathbf{I}_{N-1} \end{array} \right] - e^{j\psi} \left[ \begin{array}{c|c} \mathbf{I}_{N-1} & \mathbf{0} \end{array} \right] \right) \\ &= \frac{1}{N-1} \left[ \begin{array}{c|c|c|c|c} e^{j\psi} & 0 & \cdots & 0 & e^{-j(N-2)\psi} \end{array} \right]. \end{aligned} \quad (9.282)$$

Then

$$\mathbf{C}^H \mathbf{C} = \frac{2}{(N-1)^2}. \quad (9.283)$$

We evaluated the asymptotic variance of MUSIC in Example 9.5.1. For a linear array, we have

$$\mathbf{v} = \left[ \begin{array}{c|c|c|c} 1 & e^{j\psi} & \cdots & e^{j(N-1)\psi} \end{array} \right]^T, \quad (9.284)$$

$$\mathbf{d} = \left[ \begin{array}{c|c|c|c} 0 & j e^{j\psi} & \cdots & e^{j(N-1)\psi} \end{array} \right]^T, \quad (9.285)$$

---

<sup>15</sup>This example is taken from [SN91b].

and

$$\begin{aligned}
 \mathbf{d}^H \mathbf{U}_N \mathbf{U}_N^H \mathbf{d} &= \mathbf{d}^H (\mathbf{I} - \mathbf{v} (\mathbf{v}^H \mathbf{v}) \mathbf{v}^H) \mathbf{d} \\
 &= \mathbf{d}^H \mathbf{d} - \frac{|\mathbf{d}^H \mathbf{v}|^2}{\mathbf{v}^H \mathbf{v}} \\
 &= \frac{N(N-1)(2N-1)}{6} - \frac{N^2(N-1)^2}{4N} \\
 &= \frac{N(N^2-1)}{12}.
 \end{aligned} \tag{9.286}$$

Using (9.283) and (9.286) in (9.281),

$$\gamma = \frac{N(N+1)}{6(N-1)}. \tag{9.287}$$

Thus, for large values of  $N$ ,  $\gamma$  approaches  $N/6$ . Since MUSIC achieves the CRB for a single source, the variance of the ESPRIT estimator remains a fixed distance above the CRB bound in the asymptotic region.

#### Example 9.5.6

We consider a 10-element SLA with two equal-power sources separated by  $\Delta\psi_R$ . In Figure 9.43, the RMS error is plotted versus  $ASNR$ . We show the asymptotic results for TLS-ESPRIT and MUSIC, as well as the stochastic CRB. We also show the points from our simulations in Sections 9.4.1 and 9.4.3. We see that the threshold behavior of ESPRIT with  $d_s = 1$  is similar to root MUSIC, but its asymptotic variance is 1.0 dB higher. Note that ESPRIT with  $d_s = 5$  exhibits a more gradual threshold behavior. This is because we have used the *a priori* knowledge to limit the range of  $u$  (see (9.130)).

To improve the asymptotic performance for the  $d_s = 1$  case, we use the weighting discussed in (9.133). We illustrate this in the next example.

#### Example 9.5.7 (continuation)

Consider the same model as in Example 9.5.8. We let  $d_s = 1$  and analyze the performance for various  $m_s$ . The results are shown in Figure 9.44(a). In Figure 9.44(b) we show the difference between the normalized standard deviation and the normalized CRB. We see that, for  $m_s = 3, 4$ , and  $5$ , the variance is very close to the CRB and provides a factor of 5 improvement over the  $m_s = 1$  case.

A thorough asymptotic analysis of TLS-ESPRIT has been done by Ottersten et al. [OVK91] and Viberg and Ottersten [VO91]. The results are in a form that is suitable for numerical calculation, but is not conducive to an easy analytic summary. We refer the reader to the above reference for a detailed discussion.

Several examples are given in [OVK91] including correlated signals, different subarray choices, and constrained CRB results.

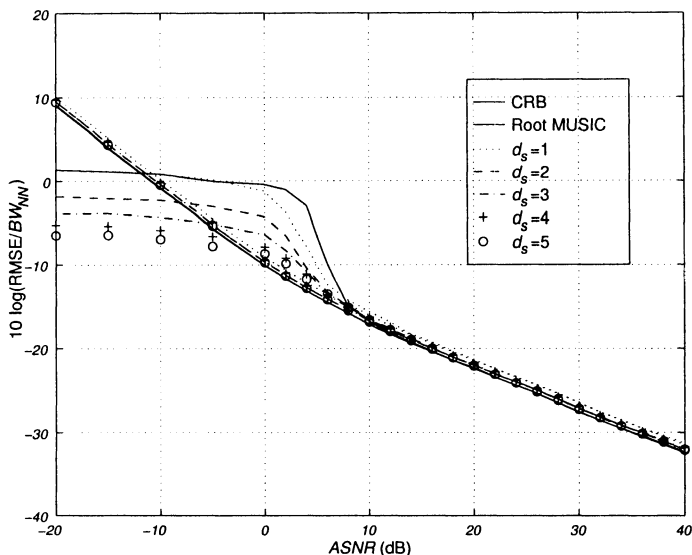


Figure 9.43 Analytic and simulated performance of TLS-ESPRIT and root MUSIC: normalized RMSE versus  $ASNR$ ,  $N = 10$ ,  $K = 100$ , various  $d_s$ , 500 trials.

#### 9.5.4 Summary

In this section we have derived a number of quantitative results to predict the probability of resolution and RMSE behavior of various algorithms. These results provide the theoretical basis for understanding the algorithms. In most cases, we must still simulate the algorithms to verify the assumptions in the analyses. Our theoretical results enable us to structure these simulations more efficiently.

## 9.6 Correlated and Coherent Signals

### 9.6.1 Introduction

In this section, we study the problem of correlated and coherent signals. Correlated signals are signals whose correlation coefficient  $\rho$  is non-zero. Coherent signals are signals where the magnitude of correlation coefficient,  $|\rho|$ , equals one. Signal correlation occurs in a multipath environment. In [Hay85], Chapter 3 discusses multipath models in the sonar environment and Chapter 4 discusses multipath models in the radar environment. Correlated

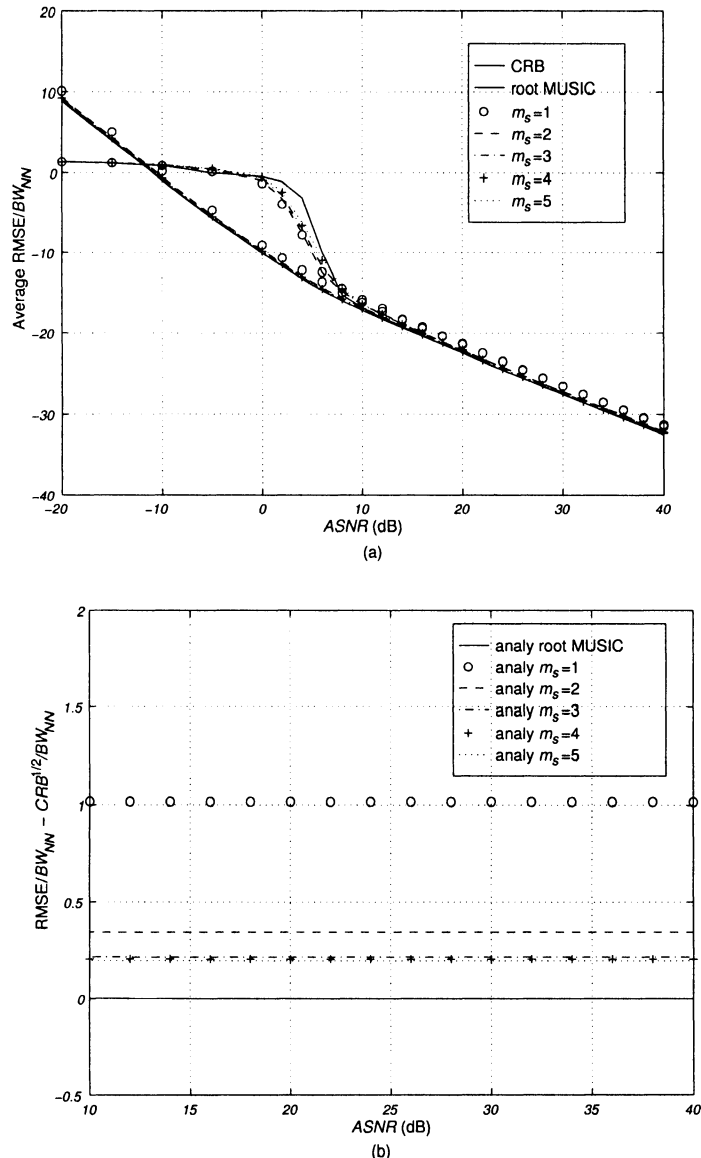


Figure 9.44 Performance of row-weighted TLS-ESPRIT and root MUSIC:  $N = 10, K = 100, d_s = 1$  various  $m_s$ , 500 trials: (a) analytic and simulated performances, normalized RMSE versus ASNR; (b) analytic asymptotic performance (normalized RMSE–normalized  $\text{CRB}^{1/2}$ ) versus ASNR.

signals can also arise in systems where smart jammers are utilized to interfere with radar or communication systems. In cellular communication systems, multipath is usually present (e.g., [ZO95] or [Win87]).

In Chapter 8, we derived the CRB for correlated and coherent signals. The algorithms that have been developed in Chapters 8 and 9 were adversely affected by correlation or coherence between the signals in the examples that we studied.

In some cases, the algorithm did not work when the signals were coherent. In other cases, the algorithm worked but the threshold occurred at a higher *ASNR* than in the uncorrelated signal case. In other cases, the RMSE did reach the CRB above threshold.

In this section, we develop algorithms to preprocess the data to remove the coherency. We focus our attention on a spatial smoothing algorithm that was invented by Evans, Johnson, and Sun ([EJS82], [EJS81]) in the context of angle of arrival estimation in air traffic control systems. Later Shan et al. [SWK85] and [SK85] studied a similar algorithm. Evans' algorithm was analyzed by William et al. [WPM88] and Pillai and Kwon [PK89a] and [PK89b] (see also [Pil89]). Rao and Hari [RH89b] obtain expression for the variance of the DOA estimate. Weiss and Friedlander [?] analyze the performance in the context of their work with interpolated arrays (e.g., [Fri90], [FW92], and [FW94]). We previously encountered spatial smoothing in the context of beamforming in Section 6.12.

A second approach to the problem is to remove the coherency by moving the array. This approach is discussed by Gabriel ([Gab80], [Gab81]) and is analyzed in detail by Haber and Zoltowski [HZ86].

A third approach utilizes constrained ML techniques (e.g., [Hay85]).

A fourth approach proposed by Cadzow [Cad80] uses a generalized eigenvector approach and obtains good results. However it requires the solution of a nonlinear programming problem. We do not discuss the last three approaches in the text.

In Section 9.6.2, we briefly review the spatial smoothing model. We then consider the three algorithms, FB-IMODE, unitary root MUSIC, and unitary TLS-ESPRIT, and compare their performance using forward–backward spatial smoothing (FBSS) to their performance using only FB averaging. In Section 9.6.3, we summarize our results.

### 9.6.2 Forward–Backward Spatial Smoothing

We previously encountered spatial smoothing in Chapter 6 in our discussion of optimum beamforming. The original use of spatial smoothing was in the

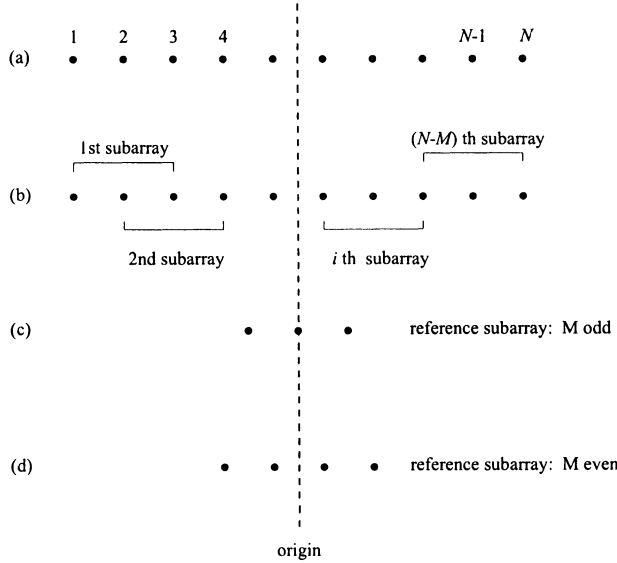


Figure 9.45 (a) Linear array; (b) subarrays; (c) reference subarray:  $M$  odd; (d) reference subarray:  $M$  even.

parameter estimation context and, although the basic model is the same as in the beamforming case, the performance issues are different.

The model of interest for forward-backward spatial smoothing was given in Section 6.12.4. The linear array of interest is shown in Figure 9.45(a). We construct a set of  $L$  subarrays of length  $M \geq D + 1$  as shown in Figure 9.45(b). Each subarray is shifted by one from the preceding subarray. The  $i$ th subarray has the  $i$ th element as its initial element. Typical reference subarrays are shown for  $M$  odd and  $M$  even.

For forward-only spatial smoothing, we compute

$$\hat{\mathbf{S}}_{SS} \triangleq \frac{1}{KL} \sum_{k=1}^K \sum_{i=1}^L \mathbf{X}_M^{(i)}(k) \left[ \mathbf{X}_M^{(i)}(k) \right]^H, \quad (9.288)$$

where  $\mathbf{X}_M^{(i)}(k)$  is the  $k$ th snapshot vector at the  $i$ th subarray.

For forward-backward spatial smoothing, we compute

$$\hat{\mathbf{S}}_{FBSS} = \frac{1}{2KL} \sum_{i=1}^L \sum_{k=1}^K \left\{ \mathbf{X}_M^{(i)}(k) \left[ \mathbf{X}_M^{(i)}(k) \right]^H + \mathbf{J} \left[ \mathbf{X}_M^{(i)}(k) \right]^* \left[ \mathbf{X}_M^{(i)}(k) \right]^T \mathbf{J} \right\}. \quad (9.289)$$

Note that the various subarrays have a large number of snapshots in common. This commonality should be exploited in the numerical calculation of (9.288) and (9.289).

We use the sample spectral matrix in either (9.288) or (9.289) in one of the algorithms that we have developed previously. We use a symmetric steering vector for a centered  $M$ -element array,

$$\mathbf{v}_S(\psi) = \left[ e^{-j\frac{N-1}{2}\psi} \ \dots \ e^{j\frac{N-1}{2}\psi} \right]^T. \quad (9.290)$$

The advantage of spatial smoothing is that the correlation between the signals will be reduced. For most algorithms, smaller correlation improves both the threshold behavior and the RMSE above threshold. The disadvantage of spatial smoothing is that the aperture of the subarray is smaller, which will degrade the performance. The trade-off between these two effects will depend on the algorithm that is used.

The spectral MUSIC algorithm provides a simple example of the behavior. To use MUSIC we perform an eigendecomposition of (9.288) and use the  $D$  eigenvectors corresponding to the  $D$  largest eigenvalues to construct a  $M \times D$  signal subspace matrix,  $\widehat{\mathbf{U}}_{FBSS,S}$ . We use the  $M - D$  remaining eigenvectors to form a noise subspace matrix  $\widehat{\mathbf{U}}_{FBSS,N}$ .

The spectral MUSIC algorithm using FBSS is

$$\hat{\psi} = \arg \min_{\psi} \left\{ \left| \mathbf{v}_S^H(\psi) \widehat{\mathbf{U}}_{FBSS,N} \right|^2 \right\}. \quad (9.291)$$

We consider a simple example using the MUSIC algorithm to illustrate a typical result. We need to consider a case where  $D \geq 3$  in order to study the effect of spatial smoothing.

#### Example 9.6.1<sup>16</sup>

In this example, we have a coherent source located at  $0^\circ$ . It undergoes multipath reflection, resulting in three additional coherent arrivals along  $-25^\circ$ ,  $45^\circ$ , and  $60^\circ$ . A standard 10-element linear array is used to receive these signals. The input SNR of the direct signal is 5 dB, and the attenuation coefficients of the three coherent sources are taken to be  $(0.4, 0.8)$ ,  $(-0.3, -0.7)$ , and  $(0.5, -0.6)$ , respectively. In the notation  $\alpha = (a, b)$ ,  $a$  and  $b$  represent the real and imaginary parts, respectively, of the complex attenuation coefficient  $\alpha$ . The result is shown in Figure 9.46. We use a FBSS scheme with two subarrays of nine sensors each, and then use the MUSIC algorithm. All four directions of arrival can be directly identified.

This example illustrates the ability of the FBSS-MUSIC algorithm to estimate the DOAs of four coherent sources that are separated by a moderate

---

<sup>16</sup>This example is similar to the example in Pillai and Kwon (p.12 of [PK89a]).

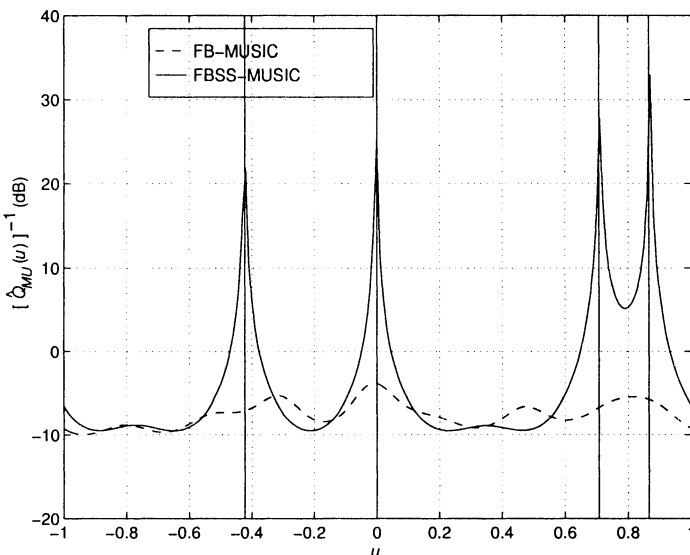


Figure 9.46 FB-MUSIC and FBSS-MUSIC: four coherent signals,  $N = 10$ ,  $M = 9$ ,  $K = 300$ ,  $SNR_1 = 5$  dB;  $(\hat{Q}_{MU}(u))^{-1}$  versus  $u$ .

amount in angle space. There are two effects that occur in FBSS. The first effect is the decorrelation that occurs because of the SS. For uniform weighting, the correlation coefficient after SS is given by (6.636) or (6.639). It is a function of the  $L \cdot \Delta\psi_{ij}$  product, where  $L$  is the number of subarrays and  $\Delta\psi_{ij}$  is the separation between the  $i$ th signal and the  $j$ th signal in  $\psi$ -space. The second effect is the FB averaging that reduces the correlation between the signals when  $(\phi_\rho)_{ij}$  is unequal to zero.

These effects indicate that FBSS will be most effective when the coherent signals are separated by a distance in  $\psi$ -space such that  $L$  can be chosen large enough to reduce the correlation significantly and the resulting subarray length will still allow the signals to be resolved. Thus, we anticipate that FBSS will be most useful when  $|\Delta\psi_{ij}| > BW_{NN}$ .

Spatial smoothing exploits the uniform spacing in a SLA. Several of the algorithms developed in Chapters 8 and 9 exploit the same characteristics. Therefore it is logical to compare the performance of some of these algorithms with spatial smoothing to their performance without spatial smoothing. In the next example, we consider the IMODE algorithm from Section 8.7.3, unitary root MUSIC from Section 9.3.2.3, and the unitary TLS-ESPRIT algorithm from Section 9.3.4.2.

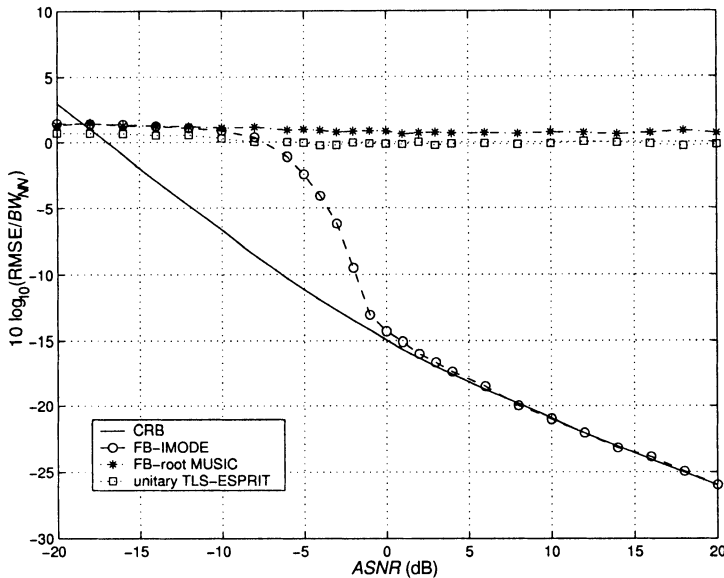


Figure 9.47 FB-root MUSIC, unitary TLS-ESPRIT with row weighting ( $m_s = 5$ ), FB-IMODE:  $N = 10$ ,  $\Delta u = 0.3$ ,  $|\rho| = 1$ ,  $\phi_\rho = 0$ ; normalized RMSE versus ASNR.

### Example 9.6.2

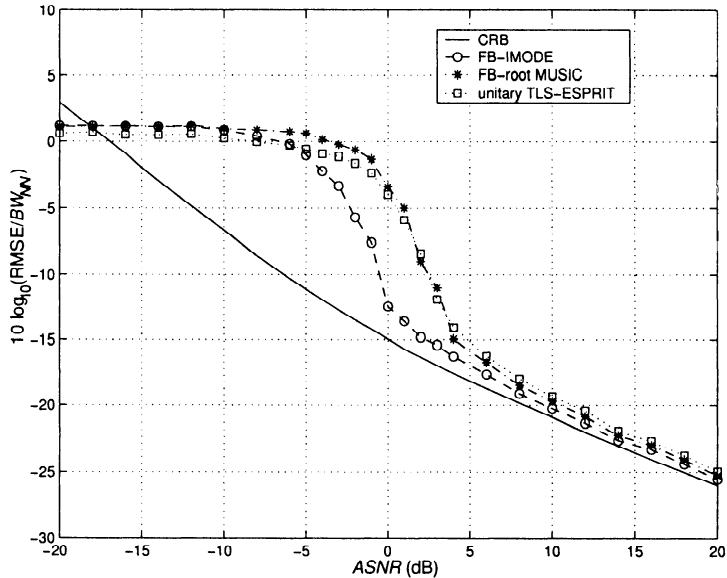
Consider a standard 10-element linear array. There are two equal-power coherent plane-wave signals impinging on the array. The magnitude of  $\rho$  equals one and  $\phi_\rho = 0$ .<sup>17</sup> We consider two values of signal separation,  $\Delta u = 0.3$  and  $\Delta u = 0.5$ .

In Figures 9.47 and 9.48,<sup>18</sup>  $\Delta u = 0.3$ . In Figure 9.47, no spatial smoothing is used. The normalized RMSE for IMODE with FB averaging and root MUSIC and unitary TLS-ESPRIT (with row weighting) with FB averaging are plotted versus ASNR. Because  $\phi_\rho = 0$ , FB averaging does not reduce the correlation and root MUSIC and unitary TLS-ESPRIT are not useful. For  $\phi_\rho = 0$ , FB-IMODE and FO-IMODE have the same performance. IMODE has a threshold at 0 dB and reaches the CRB for  $ASNR \geq 4$  dB. In Figure 9.48, FBSS is used. In Figure 9.48(a), the subarray length is 8 and  $L = 3$ . In Figure 9.48(b), the subarray length is 6 and  $L = 5$ . The normalized RMSE is plotted versus ASNR. The performance of the IMODE algorithm is poorer due to the decrease in aperture, so SS should not be used. The performance of root MUSIC and unitary TLS-ESPRIT is better with  $L = 5$  than with  $L = 3$ . The threshold is at  $ASNR = 2$  dB. However, the RMSE remains about 2 dB above the CRB because of the decreased aperture.

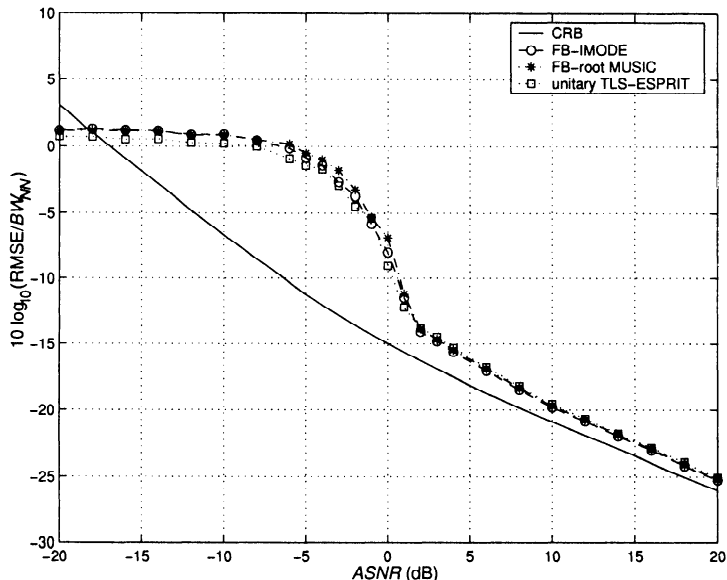
In Figures 9.49 and 9.50,  $\Delta u = 0.5$ . The same results are shown. As expected, the performance is improved but the same conclusions apply.

<sup>17</sup>We have used  $\phi_\rho = 0$  so that the comparison can focus on the smoothing issue.

<sup>18</sup>The results in Figures 9.47–9.50 are due to J. Hiemstra and D. Bray (private communication).



(a)



(b)

Figure 9.48 FB-root MUSIC, unitary TLS-ESPRIT with row weighting ( $m_s = 5$ ), FB-IMODE:  $N = 10$ ,  $\Delta u = 0.3$ ,  $|\rho| = 1$ ,  $\phi_\rho = 0$ ; FBSS; normalized RMSE versus ASNR: (a)  $L = 3$ ,  $M = 8$ ; (b)  $L = 5$ ,  $M = 6$ .

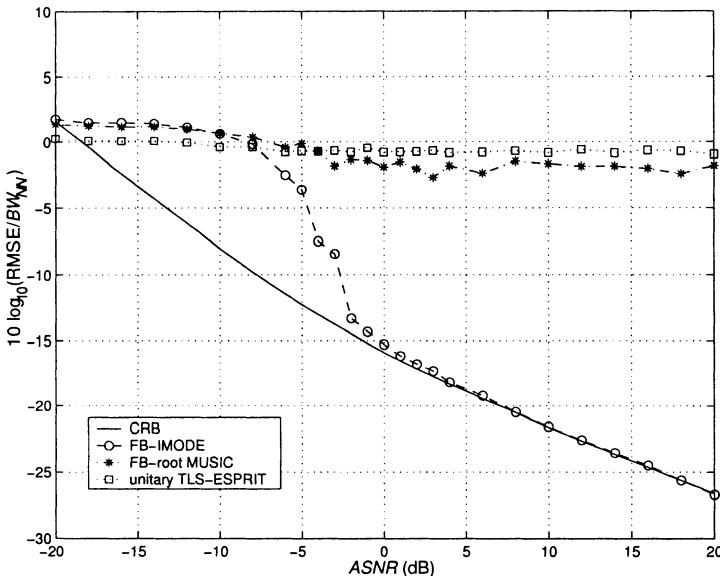


Figure 9.49 FB-root MUSIC, unitary TLS-ESPRIT with row weighting ( $m_s = 5$ ), FB-IMODE:  $N = 10$ ,  $\Delta u = 0.5$ ,  $|\rho| = 1$ ,  $\phi_\rho = 0$ ; normalized RMSE versus ASNR.

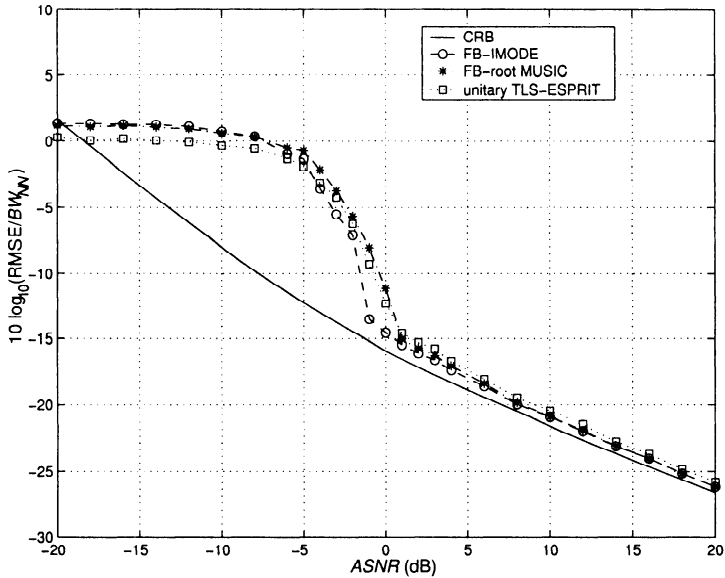
### 9.6.3 Summary

In this section, we have demonstrated how spatial smoothing provides a method for decorrelating coherent signals prior to implementing various DOA estimation algorithms.

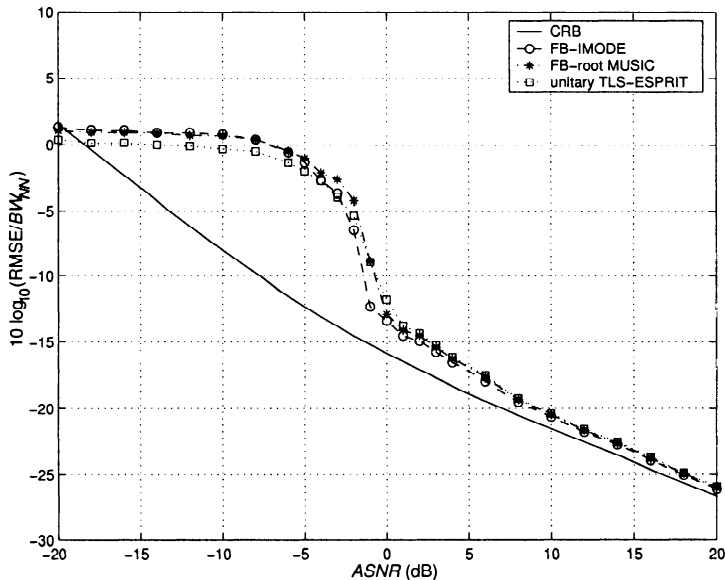
For algorithms, such as IMODE, that work well in the coherent signal environment the decrease in array length causes a performance degradation and SS and FBSS should not be used. For algorithms that do not perform well in a coherent environment, such as root MUSIC and unitary TLS-ESPRIT, FBSS is a useful technique.

There are several topics of interest that are addressed in the problems and in various references.

- (i) **Weighted spatial smoothing** In Section 6.12.4, we discussed weighted spatial smoothing in the beamforming context. One can use classical weights such as Dolph-Chebychev or the approach of Takao and Kikuma [TK87] to choose weights to Toeplitize the array (similar ideas are discussed in [RR92] and [PRK87]). One can adapt this approach to the DOA problem.



(a)



(b)

Figure 9.50 FB-root MUSIC, unitary TLS-ESPRIT with row weighting ( $m_s = 5$ ), FB-IMODE:  $N = 10$ ,  $\Delta u = 0.5$ ,  $|\rho| = 1$ ,  $\phi_\rho = 0$ ; FBSS; normalized RMSE versus ASNR: (a)  $L = 3$ ,  $M = 8$ ; (b)  $L = 5$ ,  $M = 6$ .

- (ii) **Detection of number of signals** Several of the detection algorithms discussed in Section 8.8 do not work in a coherent environment. Shan et al. [SPK87] describe a smoothed rank profile test for determining the rank and coherency structure of the incoming signals.
- (iii) **2-D spatial smoothing** Spatial smoothing is also applicable to planar arrays with a regular structure (e.g., Haardt et al. [HZMN95], Zoltowski et al. [ZHM96], or Fuhl et al. [FRB97]).
- (iv) **Interpolated arrays** When the array is not uniform, we can construct a virtual standard linear array by interpolating the snapshot vector. We can then use spatial smoothing on the interpolated array (e.g., Friedlander [Fri90], [Fri93] and Weiss and Friedlander [?] and Friedlander and Weiss [FW92]).

## 9.7 Beamspace Algorithms

In Section 8.10, we introduced parameter estimation using beamspace processing. We discussed the choice of beamspace matrices and computed the beamspace Cramér-Rao bound for several scenarios. We also derived the beamspace ML estimator and examined its performance. The reader should review that discussion.

In this section, we focus on two algorithms, beamspace MUSIC and beamspace unitary ESPRIT. In Section 9.7.1, we develop beamspace MUSIC and study its performance. In Section 9.7.2, we develop beamspace unitary ESPRIT and study its performance. In Section 9.7.3, we summarize our results.

### 9.7.1 Beamspace MUSIC

In this section, we discuss beamspace MUSIC. The beamspace snapshots are

$$\mathbf{X}_{bs}(k) = \mathbf{B}_{bs}^H \mathbf{X}(k). \quad (9.292)$$

The beamspace array manifold vector is

$$\mathbf{v}_{bs}(\psi) = \mathbf{B}_{bs}^H \mathbf{v}(\psi). \quad (9.293)$$

The beamspace spectral matrix is

$$\widehat{\mathbf{S}}_{\mathbf{x}_{bs}} = \mathbf{B}_{bs}^H \widehat{\mathbf{S}}_{\mathbf{x}} \mathbf{B}_{bs}. \quad (9.294)$$

If the columns of the beamspace matrix are conjugate symmetric, then the real part of  $\widehat{\mathbf{S}}_{\mathbf{x}_{bs}}$  can be used to achieve FB averaging.

An eigendecomposition of  $\widehat{\mathbf{S}}_{\mathbf{x}_{bs}}$  is performed. The  $D$  eigenvectors corresponding to the  $D$  largest eigenvalues are the columns of the  $N_{bs} \times D$  signal subspace matrix  $\widehat{\mathbf{U}}_{bs,S}$ . The remaining eigenvectors are the columns of the  $N_{bs} \times (N_{bs} - D)$  noise subspace  $\widehat{\mathbf{U}}_{bs,N}$ .

The beamspace null spectrum is

$$\widehat{Q}_{bs,MU}(\psi) = \left| \mathbf{v}_{bs}^H(\psi) \widehat{\mathbf{U}}_{bs,N} \right|^2. \quad (9.295)$$

We find the locations of the  $D$  minima of  $\widehat{Q}_{bs,MU}(\psi)$ . Those values are  $\widehat{\psi}_i$ ,  $i = 1, \dots, D$ .

We consider an example of a linear array to illustrate the behavior. We utilize a DFT beamspace matrix that was discussed in Sections 6.9 and 8.10.3.3 (e.g., Figure 6.80).

#### Example 9.7.1

We consider a 10-element SLA. Two equal-power uncorrelated signals are impinging on the array from  $\pm\Delta\psi/2$  where  $\Delta\psi$  corresponds to  $\Delta\psi_R$ . We use a DFT beamformer and consider a 3-beam case and a 5-beam case.

In Figure 9.51, we show the probability of resolution versus  $ASNR$  for  $N_{bs} = 3$  and 5. In Figure 9.52, we show the normalized RMSE versus  $ASNR$  for  $K = 100$ .

As expected, the threshold occurs at a lower  $ASNR$  than element-space MUSIC, and  $N_{bs} = 3$  is better than  $N_{bs} = 5$ . Above threshold, the beamspace algorithms are essentially on the CRB.

Asymptotic expressions for beamspace MUSIC covariance matrix are given by Stoica and Nehorai [SN91a], Xu and Buckley [XB93], and Weiss and Friedlander [WF94b]. Our discussion follows the latter reference.

From Section 9.5 (9.259), the asymptotic covariance matrix for element-space MUSIC is

$$\mathbf{C}_{MU} = \frac{\sigma_w^2}{2K} (\mathbf{H} \odot \mathbf{I})^{-1} \operatorname{Re} \left\{ \mathbf{H} \odot \mathbf{F}^T \right\} (\mathbf{H} \odot \mathbf{I})^{-1}, \quad (9.296)$$

where

$$\mathbf{H} \triangleq \mathbf{D}^H \mathbf{P}_V^\perp \mathbf{D}, \quad (9.297)$$

and

$$\mathbf{F} \triangleq \mathbf{S}_f^{-1} + \sigma_w^2 \mathbf{S}_f^{-1} \left( \mathbf{V}^H \mathbf{V} \right)^{-1} \mathbf{S}_f^{-1}. \quad (9.298)$$

The diagonal elements are given by

$$\mathbf{C}_{MU} \odot \mathbf{I} = \frac{\sigma_w^2}{2K} (\mathbf{F} \odot \mathbf{I}) (\mathbf{H} \odot \mathbf{I})^{-1}. \quad (9.299)$$

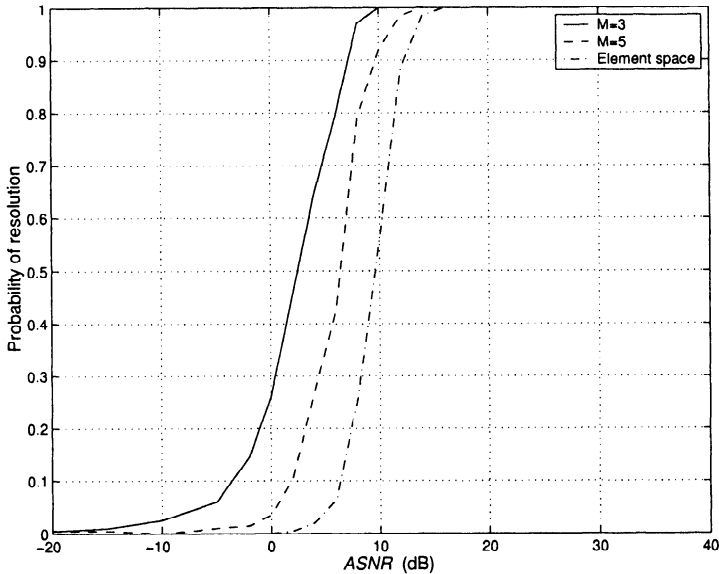


Figure 9.51 Beamspace spectral MUSIC, DFT beamspace matrix:  $N = 10$ ,  $N_{bs} = 3$  and 5, two equal-power uncorrelated plane-wave signals spaced at  $\Delta_R$ ,  $K = 100$ ; probability of resolution versus  $ASNR$ .

For beamspace MUSIC, the corresponding result is

$$\boxed{\mathbf{C}_{BMU} \odot \mathbf{I} = \frac{\sigma_w^2}{2K} (\mathbf{F}_{BS} \odot \mathbf{I}) (\mathbf{H}_{BS} \odot \mathbf{I})^{-1},} \quad (9.300)$$

where

$$\mathbf{H}_{BS} \triangleq \mathbf{D}^H \mathbf{B} \mathbf{P}_{\mathbf{V}_B}^\perp \mathbf{B}^H \mathbf{D}, \quad (9.301)$$

and

$$\mathbf{F}_{BS} \triangleq \mathbf{S}_f^{-1} + \sigma_w^2 \mathbf{S}_f^{-1} \left( \mathbf{V}^H \mathbf{P}_B \mathbf{V} \right)^{-1} \mathbf{S}_f^{-1}. \quad (9.302)$$

One can then show that, assuming  $\mathbf{S}_f$  is positive definite, that

$$\mathbf{C}_{MU} \odot \mathbf{I} \leq \mathbf{C}_{BMU} \odot \mathbf{I}. \quad (9.303)$$

For standard linear arrays using element-space processing, the root MUSIC algorithm has better threshold performance than spectral MUSIC and is computationally simpler. We would anticipate similar improvement in beamspace. Beamspace root MUSIC is discussed in several references.

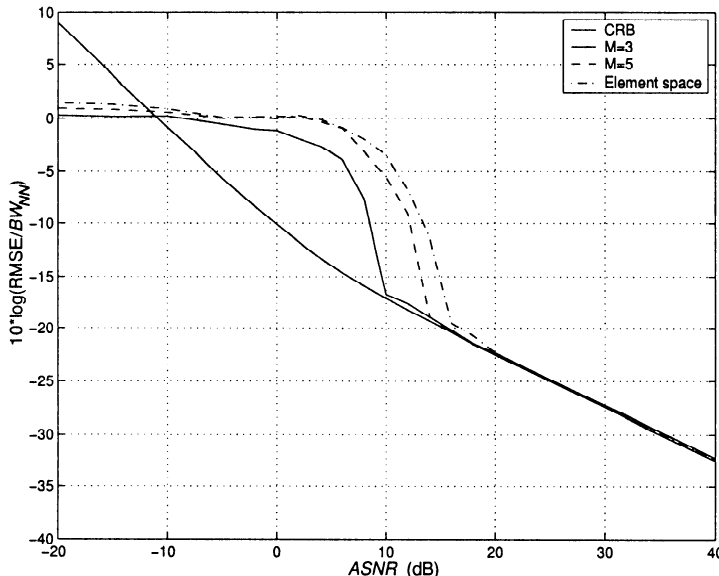


Figure 9.52 Beamspace spectral MUSIC, DFT beamspace matrix:  $N = 10$ ,  $N_{bs} = 3$  and 5, two equal-power uncorrelated plane-wave signals spaced at  $\Delta_R$ ,  $K = 100$ ; normalized RMSE versus ASNR.

The difficulty with beamspace root MUSIC is that the Vandermonde structure of the array manifold may not be preserved during the beamspace transformation. In addition, if we can obtain a polynomial to be rooted, we would like it to be  $(2N_{bs} - 2)$ -dimensional rather than  $(2N - 2)$ -dimensional.

Lee and Wengrovitz [LW88] approached the problem by using orthogonal matrix beamformers that can be factored. Their approach leads to a  $2N_{bs} - 2$  polynomial.

Zoltowski et al. [ZKS93] use a set of shifted DFT beams to construct  $\mathbf{B}_{bs}$ . They develop a  $2N - 2$  polynomial and reduce it to a  $2N_{bs} - 2$  polynomial. The construction of the  $\mathbf{C}$  matrix was discussed in Section 8.10.4.2 in the context of beamspace IQML. In a later paper, Kautz and Zoltowski [KZ96] (see Zoltowski et al. [ZKK94]) point out that the numerical instabilities in the beamspace root MUSIC algorithm limit its practical application. They develop a DOA algorithm that is based on telescoping the beamspace noise eigenvector into an element-space eigenvector. They refer to their algorithm as beamspace multirate eigenvector processing and show that it has good performance and is computationally stable. It also allows tapered beams in the beamspace matrix. The technique was extended to 2-D estimation using

URAs in Gansman et al. [GZK96]. We refer the reader to these references for further discussion.

In this section, we have developed beamspace spectral MUSIC and considered a simple example to illustrate its behavior. Although the example used a SLA, the algorithm can be used with arbitrary array geometries and beamspace matrices.

### 9.7.2 Beamspace Unitary ESPRIT

Several authors have proposed beamspace ESPRIT algorithms and analyzed various aspects of the algorithm's performance. Two references of interest are Li [Li92b] and Xu et al. [XSRK94].

Zoltowski et al. [ZHM96] developed a beamspace unitary ESPRIT algorithm using DFT beams that is computationally efficient and provides good performance.

The advantage of beamspace unitary ESPRIT is that, for many beamspace matrices of interest, the primary steps in ESPRIT can be done using real-valued calculations because the beamspace array manifold vector is real. In addition, the computational complexity is significantly reduced because of the reduced dimension of the beamspace. We develop the algorithm in this section. Our discussion follows Section IV of [ZHM96].

The beamspace matrix consists of  $N_{bs}$  orthogonal conventional beams whose MRAs are at  $2\pi m/N$  in  $\psi$ -space. The  $m$ th row of the beamspace matrix is

$$\mathbf{B}_{bs}^H = \frac{1}{N} \left[ e^{j(\frac{N-1}{2})m\frac{2\pi}{N}} \quad e^{j(\frac{N-3}{2})m\frac{2\pi}{N}}, \quad \dots, \quad e^{-j(\frac{N-1}{2})m\frac{2\pi}{N}} \right], m \in \sum_{N_{bs}} \quad (9.304)$$

where  $\sum_{N_{bs}}$  denotes the set of integers designating the beam locations.

This vector is just the Hermitian transpose of the steering vector for  $\psi_s = 2\pi m/N$ ,

$$[\mathbf{B}_{bs}^H]_m = \frac{1}{N} \mathbf{v}_s^H(\psi_s), \quad \psi_s = 2\pi m/N. \quad (9.305)$$

The values of  $m$  depend on the location of the center of the beamspace sector. For example, if the beamspace sector is centered at  $\psi = 0$  and  $N_{bs}$  is odd,

$$-(N_{bs} - 1)/2 \leq m \leq (N_{bs} - 1)/2. \quad (9.306)$$

To simplify the notation, it is convenient to denote the beam whose MRA is closest to  $\psi = -\pi$  as the left beam and use  $m_L$  for the value of  $m$  that

specifies its location. Then, the indexing on  $m$  is

$$m_L \leq m \leq m_L + N_{bs}. \quad (9.307)$$

Two points should be noticed:

- (i) If the center of the beamspace sector is near endfire, then  $m_L + N_{bs}$  may be greater than  $N$  and the beams wrap around in  $\psi$ -space.
- (ii) This notation assumes the MRAs are at  $m2\pi/N$ . The case for MRAs at  $(m - \alpha)2\pi/N$  is a straightforward modification.

The  $m$ th beam in  $\psi$ -space is

$$b_m(\psi) = [\mathbf{B}_{bs}^H]_m \mathbf{v}(\psi) = \frac{1}{N} \frac{\sin \left[ \frac{N}{2} \left( \psi - m \frac{2\pi}{N} \right) \right]}{\sin \left[ \frac{1}{2} \left( \psi - m \frac{2\pi}{N} \right) \right]}, \quad m = m_L, m_{L+1}, \dots, m_{L+N_{bs}}. \quad (9.308)$$

The total beamspace matrix is denoted by the  $N_{bs} \times N$  matrix,  $\mathbf{B}_{bs}^H$ .

The beamspace array manifold vector is a real vector,

$$\mathbf{v}_{bs}(\psi) = \mathbf{B}_{bs}^H \mathbf{v}(\psi) = [b_{m_L}(\psi) \ b_{m_{L+1}}(\psi) \ \dots \ b_{m_{L+N_{bs}}}(\psi)]^T, \quad (9.309)$$

where the rows of  $\mathbf{B}_{bs}^H$  are given by (9.304) and  $b_m(\psi)$  is given by (9.308).

Note that  $\mathbf{v}_{bs}$  is real. The key to beamspace ESPRIT is the observation that

$$b_{m+1}(\psi) = \frac{\sin \left[ \frac{N}{2} \left( \psi - (m+1) \frac{2\pi}{N} \right) \right]}{\sin \left[ \frac{1}{2} \left( \psi - (m+1) \frac{2\pi}{N} \right) \right]}, \quad (9.310)$$

and that the numerator in (9.310) is the negative of the numerator in (9.308). Therefore, the two successive components are related by

$$\begin{aligned} & \sin \left[ \frac{1}{2} \left( \psi - m \frac{2\pi}{N} \right) \right] b_m(\psi) + \\ & \sin \left[ \frac{1}{2} \left( \psi - (m+1) \frac{2\pi}{N} \right) \right] b_{m+1}(\psi) = 0. \end{aligned} \quad (9.311)$$

This equation can be manipulated into

$$\tan \left( \frac{\psi}{2} \right) \left\{ \cos \left( m \frac{\pi}{N} \right) b_m(\psi) + \cos \left( (m+1) \frac{\pi}{N} \right) b_{m+1}(\psi) \right\}$$

$$= \sin\left(m \frac{\pi}{N}\right) b_m(\psi) + \sin\left((m+1) \frac{\pi}{N}\right) b_{m+1}(\psi), \quad (9.312)$$

We want to define two  $(N_{bs} - 1) \times N_{bs}$  selection matrices relating successive beams,  $b_m(\psi)$  and  $b_{m+1}(\psi)$ .

Define

$$\Gamma_1 = \begin{bmatrix} \cos\left(m_L \frac{\pi}{N}\right) & \cos\left((m_L + 1) \frac{\pi}{N}\right) & 0 & \cdots & 0 \\ 0 & \cos\left((m_L + 1) \frac{\pi}{N}\right) & \cos\left((m_L + 2) \frac{\pi}{N}\right) & \cdots & 0 \\ 0 & 0 & \cos\left((m_L + 2) \frac{\pi}{N}\right) & \cdots & 0 \\ \vdots & \vdots & \vdots & \ddots & \vdots \\ 0 & 0 & 0 & \cdots & \cos\left((m_L + N_{bs}) \frac{\pi}{N}\right) \end{bmatrix}, \quad (9.313)$$

$$\Gamma_2 = \begin{bmatrix} \sin\left(m_L \frac{\pi}{N}\right) & \sin\left((m_L + 1) \frac{\pi}{N}\right) & 0 & \cdots & 0 \\ 0 & \sin\left((m_L + 1) \frac{\pi}{N}\right) & \sin\left((m_L + 2) \frac{\pi}{N}\right) & \cdots & 0 \\ 0 & 0 & \sin\left((m_L + 2) \frac{\pi}{N}\right) & \cdots & 0 \\ \vdots & \vdots & \vdots & \ddots & \vdots \\ 0 & 0 & 0 & \cdots & \sin\left((m_L + N_{bs}) \frac{\pi}{N}\right) \end{bmatrix}, \quad (9.314)$$

The relation in (9.312) can be written in matrix form as

$$\tan\left(\frac{\psi}{2}\right) \Gamma_1 \mathbf{v}_{bs}(\psi) = \Gamma_2 \mathbf{v}_{bs}(\psi). \quad (9.315)$$

For  $D$  sources, the beamspace array manifold matrix is

$$\mathbf{V}_{bs}(\psi) = \begin{bmatrix} \mathbf{v}_{bs}(\psi_1) & \mathbf{v}_{bs}(\psi_2) & \cdots & \mathbf{v}_{bs}(\psi_D) \end{bmatrix}. \quad (9.316)$$

Using (9.316) with (9.315) gives

$$\Gamma_1 \mathbf{V}_{bs}(\psi) \boldsymbol{\Omega}_\psi = \Gamma_2 \mathbf{V}_{bs}(\psi), \quad (9.317)$$

where

$$\boldsymbol{\Omega}_\psi = \text{diag}\left[\tan\left(\frac{\psi_1}{2}\right), \dots, \tan\left(\frac{\psi_D}{2}\right)\right]. \quad (9.318)$$

The signal eigenvectors are the eigenvectors corresponding to the  $D$  largest eigenvalues of

$$\text{Re} [\widehat{\mathbf{S}}_{\mathbf{x}, bs}] = \text{Re} [\mathbf{B}_{bs}^H \widehat{\mathbf{S}}_{\mathbf{x}} \mathbf{B}_{bs}]. \quad (9.319)$$

Then, the signal subspace is an  $N_{bs} \times D$  matrix,

$$\widehat{\mathbf{U}}_{bs,s} = \mathbf{V}_{bs} \mathbf{T}, \quad (9.320)$$

where  $\mathbf{T}$  is a non-singular  $D \times D$  matrix. Substituting

$$\mathbf{V}_{bs} = \widehat{\mathbf{U}}_{bs,s} \mathbf{T}^{-1}, \quad (9.321)$$

into (9.317) gives

$$\boldsymbol{\Gamma}_1 \widehat{\mathbf{U}}_{bs,s} \widehat{\boldsymbol{\Psi}} = \boldsymbol{\Gamma}_2 \widehat{\mathbf{U}}_{bs,s}, \quad (9.322)$$

where

$$\boldsymbol{\Psi} = \mathbf{T}^{-1} \boldsymbol{\Omega}_\psi \mathbf{T}. \quad (9.323)$$

Note that (9.322) has the same form as (9.119) with  $\widehat{\mathbf{U}}_{s1}$  replaced with  $\boldsymbol{\Gamma}_1 \widehat{\mathbf{U}}_{bs,s}$ , and  $\widehat{\mathbf{U}}_{s2}$  replaced with  $\boldsymbol{\Gamma}_2 \widehat{\mathbf{U}}_{bs,s}$ . The beamspace unitary LS-ESPRIT solution is

$$\widehat{\boldsymbol{\Psi}}_{bs,ULS} = \left[ \left[ \boldsymbol{\Gamma}_1 \widehat{\mathbf{U}}_{bs,s} \right]^T \left[ \boldsymbol{\Gamma}_1 \widehat{\mathbf{U}}_{bs,s} \right] \right]^{-1} \left[ \boldsymbol{\Gamma}_1 \widehat{\mathbf{U}}_{bs,s} \right]^T \left[ \boldsymbol{\Gamma}_2 \widehat{\mathbf{U}}_{bs,s} \right]. \quad (9.324)$$

The beamspace unitary TLS-ESPRIT solution is obtained by replacing  $\widehat{\mathbf{U}}_{s1}$  with  $\boldsymbol{\Gamma}_1 \widehat{\mathbf{U}}_{bs,s}$ , and  $\widehat{\mathbf{U}}_{s2}$  with  $\boldsymbol{\Gamma}_2 \widehat{\mathbf{U}}_{bs,s}$  in the formula for  $\tilde{\mathbf{C}}$  given in (9.123). Then,

$$\widehat{\boldsymbol{\Psi}}_{bs,UTLS} = -\mathbf{V}_{12} \mathbf{V}_{22}^{-1}. \quad (9.325)$$

The steps in beamspace ESPRIT can be summarized:

1. Find  $\widehat{\mathbf{U}}_{bs,s}$ , the  $N_{bs} \times D$  signal subspace matrix whose columns are the eigenvectors corresponding to the  $D$  largest eigenvalues of

$$Re \left[ \widehat{\mathbf{S}}_{\mathbf{x},bs} \right] = Re \left[ \mathbf{B}_{bs}^H \widehat{\mathbf{S}}_{\mathbf{x}} \mathbf{B}_{bs} \right].$$

- 2a. For unitary LS-ESPRIT,  $\widehat{\boldsymbol{\Psi}}_{bs,ULS}$  is given by (9.324).
- 2b. For unitary TLS-ESPRIT,  $\widehat{\boldsymbol{\Psi}}_{bs,UTLS}$  is given by (9.325), which is obtained by a  $2D \times 2D$  eigendecomposition of  $\tilde{\mathbf{C}}$ .
3. Find the  $D$  eigenvalues,  $\hat{w}_i$ , of the real-valued matrix in step 2; either  $\widehat{\boldsymbol{\Psi}}_{bs,ULS}$  or  $\widehat{\boldsymbol{\Psi}}_{bs,UTLS}$ .
4. Compute the estimated DOAs in  $\psi$ -space,

$$\hat{\psi}_i = 2\tan^{-1}(\hat{w}_i), i = 1, \dots, D.$$

We consider an example to illustrate the performance of beamspace unitary TLS-ESPRIT.

#### **Example 9.7.2**

Consider a standard 10-element linear array. Two equal-power uncorrelated plane-wave signals are impinging on the array from  $\pm\Delta\psi/2$  where  $\Delta\psi = \Delta\psi_R$ . We use the beamspace matrix described by (9.304) and implement the 3-beam and 5-beam case. The results are shown in Figure 9.53. Note that the three beams centered at  $\psi = 0$  correspond to  $m = -1, 0$ , and  $1$  in our indexing scheme. For five beams,  $m = -2, -1, 0, 1$ , and  $2$ .

We see that the resolution performance is slightly better than element-space TLS-ESPRIT. In the 3-beam case, the RMSE approaches the CRB above threshold. In the 5-beam case, the RMSE remains slightly above the CRB above threshold.

### **9.7.3 Beamspace Summary**

In this section, we have discussed beamspace processing. For the models considered, we have seen that beamspace processing can provide improvement in resolution and almost no loss in estimation accuracy. In addition, the computational complexity is reduced and the statistical stability for a given number of snapshots is increased.

For arbitrary array geometries and uncorrelated signals, beamspace spectral MUSIC can be used. For correlated signals, SS can be utilized.

For ULAs and a DFT beamspace matrix, beamspace IQML (or beamspace MODE) provides the best threshold performance and approaches the beamspace CRB above threshold. Beamspace unitary ESPRIT also provides good performance with less computation and is close to the CRB above threshold.

We discuss beamspace processing for planar arrays in Section 9.9.

## **9.8 Sensitivity and Robustness**

In Section 8.11, we developed models for array perturbations and environmental perturbations. We developed Cramér-Rao bounds for the case in which we jointly estimated the DOAs and the array parameters. We then developed joint estimation algorithms. In this section, we revisit the sensitivity problem in the context of the estimation algorithms that we have developed in this chapter.

The sensitivity discussion can be divided into three parts. In the first part, we assume that we use one of the estimation algorithms developed in this chapter and use the nominal array manifold in the calculation. We perturb the array using the perturbation model in Section 8.3.2 ((8.72)–(8.81)) and analyze (or simulate) the performance of the algorithm. We compare

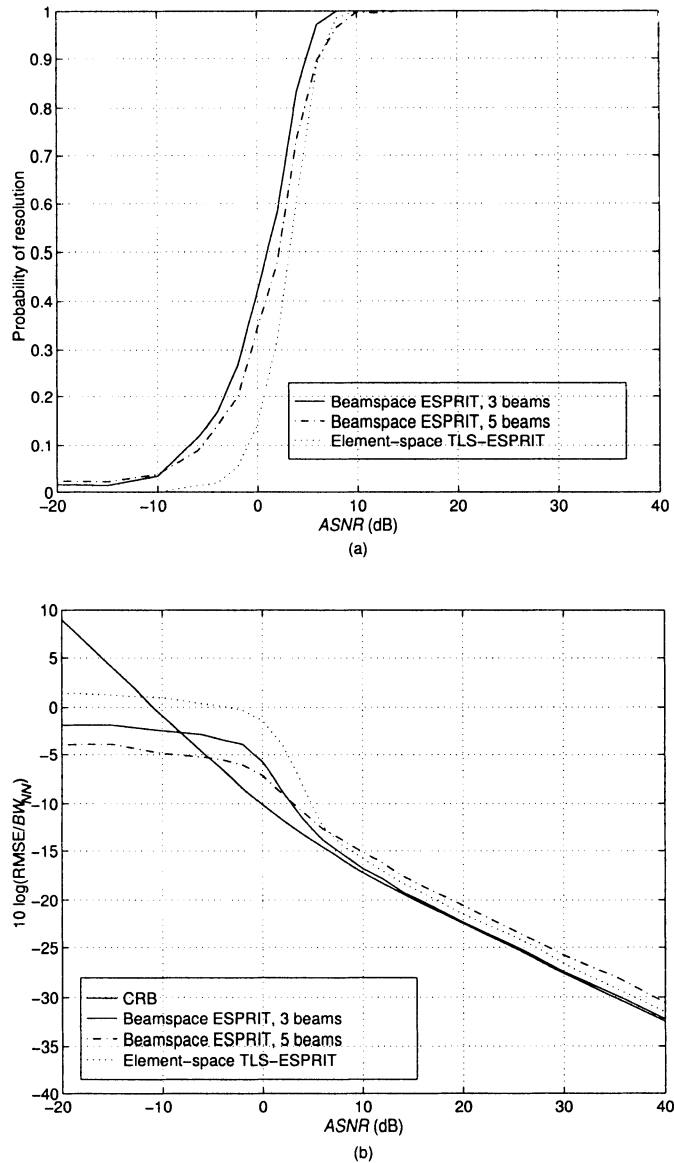


Figure 9.53 Performance of beamspace unitary TLS-ESPRIT using a DFT beamspace:  $N = 10$ ,  $N_{bs} = 3$  and  $5$ ,  $K = 100$ , 500 trials: (a) probability of resolution versus  $ASNR$ ; (b) normalized RMSE versus  $ASNR$ .

the resulting performance to the hybrid Cramér-Rao bounds derived in Section 8.11.2. In the second part, we modify the algorithms in some manner to make them more robust to the array perturbations. The robust algorithms in this second part do not explicitly estimate the perturbed array parameters. In the third part, we consider algorithms that treat the problem as a joint estimation problem and try to estimate both the DOAs and the perturbed array parameters.

Papers that focus on the first two parts of the problem include Swindlehurst and Kailath [SK92] (MUSIC), Swindlehurst and Kailath [SK93b] (multidimensional algorithms), Hamza and Buckley [HB95] (weighted eigenspace), Jansson et al. [JSO98] (WSF), Ng [Ng95], Ratnarajah [Rat98] (MUSIC), Viberg and Swindlehurst [VS94], Rockah et al. [RMS88], Rockah and Schultheiss [RS87], Weiss and Friedlander [WF94a] (resolution of MUSIC), Zhang and Zhu [ZZ95], Kuroc [Kur89] (lower bounds), and Friedlander and Weiss ([FW90], [FW93a]). We refer the reader to those references for a complete discussion. We consider a single example to illustrate the performance of root MUSIC and unitary TLS-ESPRIT.

**Example 9.8.1** (continuation, Example 8.11.1)

In this example, we consider the same perturbation model as in Example 8.11.1. The array is a 10-element SLA on the  $x$ -axis. There are two equal-power uncorrelated plane-wave sources at  $\pm\Delta\psi/2$ , where  $\Delta\psi = \Delta\psi_R$ . The perturbations of the each sensor in the  $x$ - and  $y$ -direction are independent zero-mean Gaussian random variables with standard deviation  $\sigma_p$ . We let  $\sigma_p = 0.05\lambda$ . This value corresponds to 10%, respectively, of the nominal interelement spacing.

In Figure 9.54(a), we plot  $P_R$  versus  $ASNR$  for  $\sigma_p = 0.05\lambda$ .<sup>19</sup> In Figure 9.54(b), we plot the normalized RMSE versus  $ASNR$  for root MUSIC and unitary TLS-ESPRIT. We also plot the hybrid CRB and the nominal CRB. There is very little degradation in the threshold behavior of root MUSIC and unitary TLS-ESPRIT. The RMSE for the two algorithms levels off above an  $ASNR = 20$  dB.

The gap between the RMSE of the algorithms and hybrid CRB suggests that there may be improved algorithms that provide better performance. Several of the above references suggest modifications to improve robustness.

In Section 8.11, we introduced two algorithms, the MAPprox algorithm and Weiss-Friedlander iterative algorithm that used joint (or alternating) estimation. The generalized WSF algorithm [JSO98] was also discussed. (This paper has an extensive list of references.) In that discussion either an ML or WSF algorithm was used for estimation. Modifications to incorporate MUSIC or ESPRIT can be derived. References that deal with the calibration problem or the joint estimation problem include Fuhrmann [Fuh94], Hung [Hun94], Huang and Williams [HW94], McCarthy et al. [MRP94], Soon et

---

<sup>19</sup>The results in Figure 9.54 are due to D. Bray (private communication).

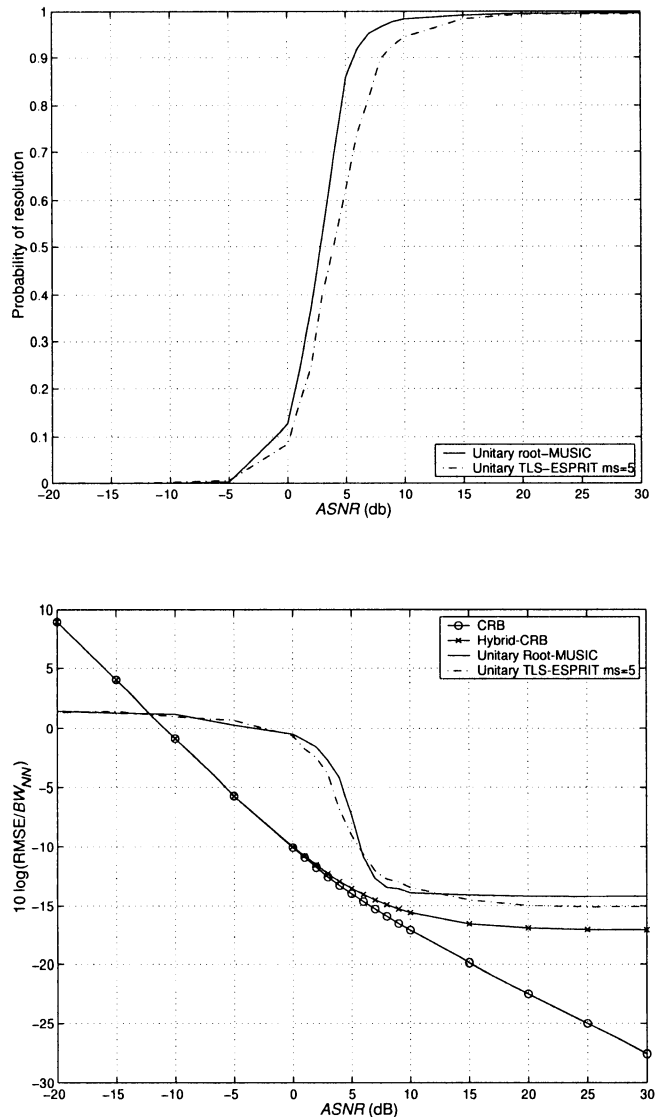


Figure 9.54 Unitary root MUSIC and unitary TLS-ESPRIT ( $d_s = 1$ ,  $m_s = 5$ ); SLA on  $x$ -axis,  $N = 10$ , two equal-power uncorrelated plane-wave signals,  $\Delta\psi = \Delta\psi_R$ , sensor position perturbations,  $\sigma_x = \sigma_y = 0.05\lambda$ , 100 trials: (a) probability of resolution versus ASNR; (b) normalized RMSE versus ASNR.

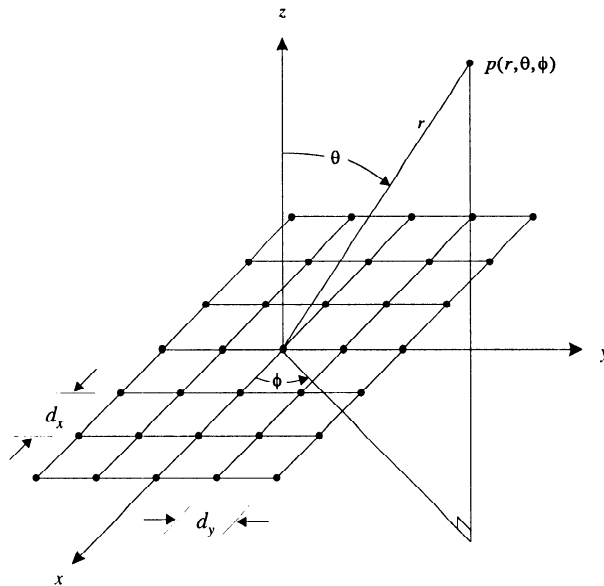


Figure 9.55 Geometry of a uniform rectangular array.

al. [STHL94], Talwar et al. [TPG93], Tseng et al. [TFG95], Weiss and Friedlander [WF91a], [WF91b], Wylie et al. [WRM94]. We refer the reader to these references for a discussion of these techniques. A recent dissertation by Flanagan ([Fla00]) studies the problem and contains an extensive list of references.

## 9.9 Planar Arrays

In this section, we extend some of the results in the earlier sections of the chapter to planar arrays. Some of the algorithms, such as spectral MUSIC, extend in an obvious manner. However, the extension to 2-D of algorithms such as root MUSIC that rely on a polynomial representation are less clear.

In Section 9.1, we study standard rectangular arrays and develop various 2-D algorithms. In Section 9.9.2, we discuss hexagonal arrays. In Section 9.9.3, we summarize our results.

### 9.9.1 Standard Rectangular Arrays

The geometry of a uniform rectangular array was shown in Figure 4.5 and is repeated in Figure 9.55 for convenience. In a standard rectangular array,

$$d_x = d_y = \frac{\lambda}{2}. \quad (9.326)$$

It is useful to define an array manifold matrix,

$$\begin{aligned} [\mathbf{V}(\psi)]_{nm} &= \mathbf{V}[\psi_x, \psi_y]_{nm} = e^{j(n-\frac{N-1}{2})\psi_x} e^{j(m-\frac{M-1}{2})\psi_y}, \\ n &= 0, \dots, N-1, \quad m = 0, \dots, M-1, \end{aligned} \quad (9.327)$$

where

$$\boldsymbol{\psi} = \begin{bmatrix} \psi_x & \psi_y \end{bmatrix}^T. \quad (9.328)$$

Note that the matrix descriptor is used in a different manner than in previous discussions.

The array manifold matrix can be written as a product of two vectors,

$$\mathbf{V}(\psi_x, \psi_y) = \mathbf{v}_x(\psi_x) \mathbf{v}_y^T(\psi_y), \quad (9.329)$$

where  $\mathbf{v}_x(\psi_x)$  and  $\mathbf{v}_y(\psi_y)$  are given by (2.72) or (2.73).

We can write  $\mathbf{V}(\psi_x, \psi_y)$  as an  $NM \times 1$  array manifold vector,

$$\text{vec}(\boldsymbol{\psi}) \triangleq \text{vec}(\mathbf{V}(\psi_x, \psi_y)). \quad (9.330)$$

Note that  $\text{vec}(\boldsymbol{\psi})$  is conjugate symmetric.

We can also write the  $k$ th snapshot of the input to the array as either an  $N \times M$  matrix  $\mathbf{X}_k$  or a  $NM \times 1$  vector  $\text{vec}(\mathbf{X}_k)$ . For notational simplicity we define

$$\mathbf{Z}_k \triangleq \text{vec}(\mathbf{X}_k). \quad (9.331)$$

We can write the sample spectral matrix of  $\mathbf{Z}_k$  as

$$\hat{\mathbf{S}}_{\mathbf{Z}} = \frac{1}{K} \sum_{k=1}^K \mathbf{Z}_k \mathbf{Z}_k^H. \quad (9.332)$$

Since  $\mathbf{Z}_k$  is conjugate symmetric, we can use FB averaging on  $\mathbf{Z}_k$  to obtain

$$\hat{\mathbf{S}}_{\mathbf{Z},fb} = \frac{1}{2K} \left\{ \sum_{k=1}^K \left( \mathbf{Z}_k \mathbf{Z}_k^H + \mathbf{J} \mathbf{Z}_k^* \mathbf{Z}_k^T \mathbf{J} \right) \right\}. \quad (9.333)$$

### 9.9.1.1 2-D spectral algorithms

The various spectral algorithms follow directly. For example, for spectral MUSIC, we find either the  $NM \times D$  signal subspace matrix,  $\widehat{\mathbf{U}}_S$ , or the  $NM \times (NM - D)$  noise subspace matrix,  $\widehat{\mathbf{U}}_N$ , and use either (9.44) or (9.45). The spectral MUSIC algorithm for SRAs is

$$\hat{\psi} = \arg \min_{\psi} \left\{ \text{vec}^H(\psi) \left[ \widehat{\mathbf{U}}_N \widehat{\mathbf{U}}_N^H \right] \text{vec}(\psi) \right\}, \quad (9.334)$$

or

$$\hat{\psi} = \arg \min_{\psi} \left\{ \text{vec}^H(\psi) \left[ \mathbf{I} - \widehat{\mathbf{U}}_S \widehat{\mathbf{U}}_S^H \right] \text{vec}(\psi) \right\}. \quad (9.335)$$

In almost all cases, the form in (9.335) will be used because normally  $D \ll NM$ . The disadvantage of using spectral MUSIC directly is that we must search over a 2-D surface.

A logical approach is to implement two 1-D algorithms such as root MUSIC or IMODE to generate preliminary estimates of  $\psi_x$  and  $\psi_y$ , and then use (9.335) to correctly pair the estimates. A scenario for two sources is shown in Figure 9.56. We substitute the four possible pairings of  $\hat{\psi}_{x_1}$ ,  $\hat{\psi}_{x_2}$ ,  $\hat{\psi}_{y_1}$ , and  $\hat{\psi}_{y_2}$  into the bracket expression on the right side of (9.335) and choose the two points with the smallest values.

In order to implement the 1-D algorithm, we compute the sample spectral matrix of each row, which we denote as  $\widehat{\mathbf{S}}_{x,n}$ . We then sum over the  $N$  rows to obtain

$$\widehat{\mathbf{S}}_x = \sum_{n=1}^N \widehat{\mathbf{S}}_{x,n}. \quad (9.336)$$

We use root MUSIC with  $\widehat{\mathbf{S}}_x$  to find a preliminary estimate of  $\psi_x$ , which we denote as  $\tilde{\psi}_x$ . Similarly, we compute the sample spectral matrix of each column, which we denote as  $\widehat{\mathbf{S}}_{y,m}$ . We then sum over the  $M$  columns to obtain

$$\widehat{\mathbf{S}}_y = \sum_{m=1}^M \widehat{\mathbf{S}}_{y,m}. \quad (9.337)$$

We use root MUSIC with  $\widehat{\mathbf{S}}_y$  to find a preliminary estimate of  $\psi_y$ , which we denote as  $\tilde{\psi}_y$ .<sup>20</sup> Because the rows and columns are standard linear arrays, FB averaging can be used. Any of the 1-D algorithms such as unitary TLS-ESPRIT or IMODE could be used to generate the 1-D estimates.

---

<sup>20</sup>A similar approach is used by Yeh et al. [YLC89] for spatial smoothing of coherent signals.

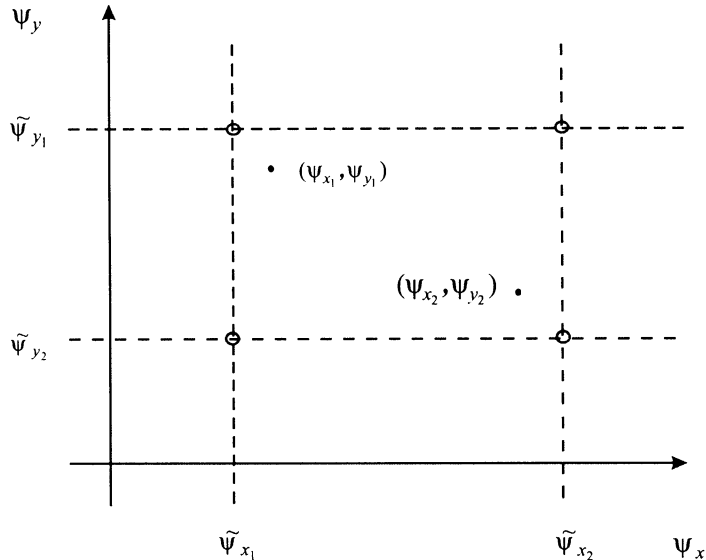


Figure 9.56 Pairing of 1-D estimates.

The next step is to pair the estimates. One approach is to evaluate (9.335) at the four locations in Figure 9.56:  $(\tilde{\psi}_{x1}, \tilde{\psi}_{y1})$ ,  $(\tilde{\psi}_{x1}, \tilde{\psi}_{y2})$ ,  $(\tilde{\psi}_{x2}, \tilde{\psi}_{y1})$ , and  $(\tilde{\psi}_{x2}, \tilde{\psi}_{y2})$ , and choose the two points with the smallest values.

If we stop at this point we have not exploited the coupling in the model. Thus, a second approach is to use the two points as the initial value for a localized gradient algorithm to find the minimum of (9.335). It turns out that in many cases, a coupled spectral approach has poorer resolution performance than the 1-D root algorithms, so the first approach is preferable.

We consider a simple example to illustrate the technique.

#### Example 9.9.1

Consider a standard  $10 \times 10$  rectangular array. Two equal-power uncorrelated plane-wave sources impinge on the array. The source locations are

$$(u_{x1}, u_{y1}) = (0, 0), (u_{x2}, u_{y2}) = (0, 0.0866).$$

The RMSE of  $i$ th source is,

$$RMSE_i = \left[ (\hat{u}_{xi} - u_{xi})^2 + (\hat{u}_{yi} - u_{yi})^2 \right]^{\frac{1}{2}}. \quad (9.338)$$

The first approach (paired 1-D roots) has better performance, so we have plotted its behavior. In Figure 9.57(a), we plot the probability of resolution versus  $SNR$ . In Figure 9.57(b), we plot the RMSE versus  $SNR$ . Note that the plot is not normalized and the horizontal axis is  $SNR$ .

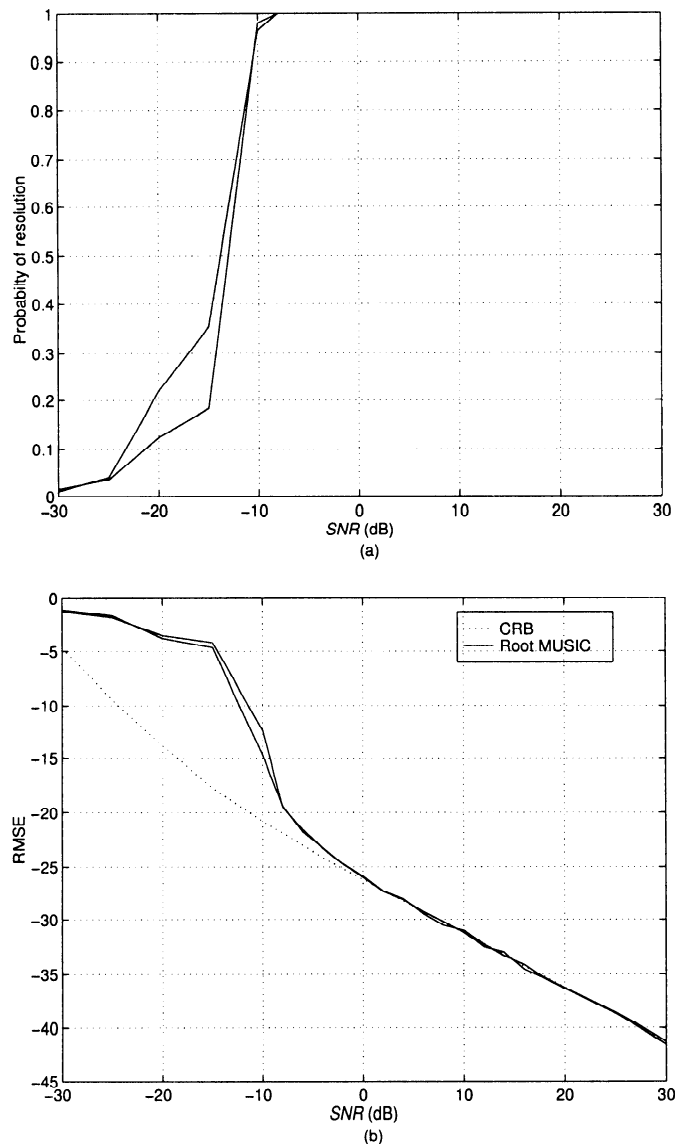


Figure 9.57 Performance of paired 1-D root MUSIC versus  $SNR$ ; standard rectangular array,  $N = 10$ ,  $M = 10$ ,  $u_1 = [0 \ 0]^T$ ,  $u_2 = [0 \ 0.0866]^T$ ,  $K = 100$ , 200 trials: (a) probability of resolution versus  $SNR$ ; (b) RMSE versus  $SNR$ .

For a larger number of signals this technique becomes cumbersome. In the next subsection, we develop a 2-D unitary ESPRIT algorithm that eliminates the pairing problem.

### 9.9.1.2 2-D unitary ESPRIT

In this section, we develop a 2-D extension of the unitary ESPRIT algorithm developed in Section 9.3.4.2. The extension is due to Zoltowski et al. [ZHM96] and our discussion follows that reference.

The array manifold of an  $N \times M$  rectangular array can be written as

$$\mathbf{V}(\psi) = \mathbf{V}(\psi_x, \psi_y) = \mathbf{v}_N(\psi_x)\mathbf{v}_M^T(\psi_y). \quad (9.339)$$

We have changed the subscripts of the vectors to emphasize their dimension. We pre-multiply  $\mathbf{V}(\psi)$  by  $\mathbf{Q}_N^H$  and post-multiply by  $\mathbf{Q}_M^*$  to obtain a real array manifold.

$$\begin{aligned} \mathbf{V}_R(\psi) &= \mathbf{Q}_N^H \mathbf{v}_N(\psi_x) \mathbf{v}_M^T(\psi_y) \mathbf{Q}_M^* \\ &= \mathbf{v}_{RN}(\psi_x) \mathbf{v}_{RM}^T(\psi_y). \end{aligned} \quad (9.340)$$

Now  $\mathbf{v}_{RN}(\psi_x)$  satisfies (9.151), where  $\mathbf{K}_1$  and  $\mathbf{K}_2$  are defined in (9.147) and (9.148). Therefore,

$$\left[ \tan\left(\frac{\psi_x}{2}\right) \mathbf{K}_1 \mathbf{v}_{RN}(\psi_x) \right] \mathbf{v}_{RM}^T(\psi_y) = [\mathbf{K}_2 \mathbf{v}_{RN}(\psi_x)] \mathbf{v}_{RM}^T(\psi_y), \quad (9.341)$$

or

$$\tan\left(\frac{\psi_x}{2}\right) \mathbf{K}_1 \mathbf{V}_R(\psi) = \mathbf{K}_2 \mathbf{V}_R(\psi). \quad (9.342)$$

We now rewrite (9.342) using  $vec(\cdot)$  notation and use (A.108),<sup>21</sup>

$$\tan\left(\frac{\psi_x}{2}\right) vec(\mathbf{K}_1 \mathbf{V}_R(\psi) \mathbf{I}_M) = vec(\mathbf{K}_2 \mathbf{V}_R(\psi) \mathbf{I}_M). \quad (9.343)$$

This can be rewritten as

$$\tan\left(\frac{\psi_x}{2}\right) \mathbf{K}_{x1} vec(\mathbf{V}_R(\psi)) = \mathbf{K}_{x2} vec(\mathbf{V}_R(\psi)), \quad (9.344)$$

where

$$\mathbf{K}_{x1} \triangleq \mathbf{I}_M \otimes \mathbf{K}_1, \quad (N-1)M \times MN, \quad (9.345)$$

$$\mathbf{K}_{x2} \triangleq \mathbf{I}_M \otimes \mathbf{K}_2, \quad (N-1)M \times MN. \quad (9.346)$$

---

<sup>21</sup>From (A.108),  $vec(\mathbf{ABC}) = (\mathbf{C}^T \otimes \mathbf{A})vec(\mathbf{B})$ .

Note that (9.344) defines  $(N - 1)M$  equations.

Similarly,

$$\tan\left(\frac{\psi_y}{2}\right) \text{vec}\left(\mathbf{I}_N \mathbf{V}_R(\psi) \mathbf{K}_3^T\right) = \text{vec}\left(\mathbf{I}_N \mathbf{V}_R(\psi) \mathbf{K}_4^T\right), \quad (9.347)$$

where

$$\mathbf{K}_3 = \text{Re} \left\{ \mathbf{Q}_{M-1}^H \mathbf{J}_{s2}^{(M)} \mathbf{Q}_M \right\}, \quad (9.348)$$

$$\mathbf{K}_4 = \text{Im} \left\{ \mathbf{Q}_{M-1}^H \mathbf{J}_{s2}^{(M)} \mathbf{Q}_M \right\}, \quad (9.349)$$

where  $\mathbf{J}_{s2}^{(M)}$  is given by (9.135) with  $N$  replaced by  $M$ . Then (9.347) can be rewritten as

$$\tan\left(\frac{\psi_y}{2}\right) \mathbf{K}_{y1} \text{vec}(\mathbf{V}_R(\psi)) = \mathbf{K}_{y2} \text{vec}(\mathbf{V}_R(\psi)), \quad (9.350)$$

where

$$\mathbf{K}_{y1} \triangleq \mathbf{K}_3 \otimes \mathbf{I}_N, \quad N(M-1) \times NM, \quad (9.351)$$

$$\mathbf{K}_{y2} \triangleq \mathbf{K}_4 \otimes \mathbf{I}_N, \quad N(M-1) \times NM. \quad (9.352)$$

Note that (9.350) represents  $N(M-1)$  equations.

The next step is to specify an  $NM \times D$  array manifold matrix,

$$\tilde{\mathbf{V}} \triangleq \begin{bmatrix} \text{vec}(\mathbf{V}_R(\psi_1)) & \text{vec}(\mathbf{V}_R(\psi_2)) & \cdots & \text{vec}(\mathbf{V}_R(\psi_D)) \end{bmatrix}. \quad (9.353)$$

Each column in  $\tilde{\mathbf{V}}$  satisfies (9.344). Therefore we can write

$$\mathbf{K}_{x1} \tilde{\mathbf{V}} \boldsymbol{\Omega}_x = \mathbf{K}_{x2} \tilde{\mathbf{V}}, \quad (9.354)$$

where

$$\boldsymbol{\Omega}_x \triangleq \text{diag} \left\{ \tan\left(\frac{\psi_{x1}}{2}\right), \tan\left(\frac{\psi_{x2}}{2}\right), \dots, \tan\left(\frac{\psi_{xD}}{2}\right) \right\}. \quad (9.355)$$

Similarly, each column in  $\tilde{\mathbf{V}}$  satisfies (9.350), so we can write

$$\mathbf{K}_{y1} \tilde{\mathbf{V}} \boldsymbol{\Omega}_y = \mathbf{K}_{y2} \tilde{\mathbf{V}}, \quad (9.356)$$

where

$$\boldsymbol{\Omega}_y \triangleq \text{diag} \left\{ \tan\left(\frac{\psi_{y1}}{2}\right), \tan\left(\frac{\psi_{y2}}{2}\right), \dots, \tan\left(\frac{\psi_{yD}}{2}\right) \right\}. \quad (9.357)$$

Just as in Section 9.9.2.1, we find  $\widehat{\mathbf{U}}_s$ , the  $NM \times D$  signal subspace estimate. Now

$$\mathbf{U}_s = \tilde{\mathbf{V}}\mathbf{T}, \quad (9.358)$$

where  $T$  is an unknown  $D \times D$  matrix. Replacing  $\mathbf{U}_s$  with  $\widehat{\mathbf{U}}_s$  gives

$$\widehat{\mathbf{U}}_s = \widehat{\tilde{\mathbf{V}}}\mathbf{T}, \quad (9.359)$$

or

$$\widehat{\tilde{\mathbf{V}}} = \widehat{\mathbf{U}}_s\mathbf{T}^{-1}. \quad (9.360)$$

Substituting (9.360) into (9.354) and (9.356) gives

$$\mathbf{K}_{x1}\widehat{\mathbf{U}}_s\widehat{\Psi}_x = \mathbf{K}_{x2}\widehat{\mathbf{U}}_s, \quad (N-1)M \times D, \quad (9.361)$$

where

$$\widehat{\Psi}_x \triangleq \mathbf{T}^{-1}\widehat{\Omega}_x\mathbf{T}, \quad (9.362)$$

and

$$\mathbf{K}_{y1}\widehat{\mathbf{U}}_s\widehat{\Psi}_y = \mathbf{K}_{y2}\widehat{\mathbf{U}}_s, \quad (N-1)M \times D, \quad (9.363)$$

where

$$\widehat{\Psi}_y \triangleq \mathbf{T}^{-1}\widehat{\Omega}_y\mathbf{T}. \quad (9.364)$$

After solving (9.361) and (9.363) for  $\widehat{\Psi}_x$  and  $\widehat{\Psi}_y$ , we find the eigenvalues of the  $D \times D$  complex matrix  $\widehat{\Psi}_x + j\widehat{\Psi}_y$ ,

$$\widehat{\Psi}_x + j\widehat{\Psi}_y = \mathbf{T}^{-1}(\widehat{\Omega}_x + j\widehat{\Omega}_y)\mathbf{T}. \quad (9.365)$$

From the resulting eigenvalues,  $\widehat{\lambda}_i, i = 1, 2, \dots, D$ , we can find  $\widehat{\psi}_{xi}$  and  $\widehat{\psi}_{yi}$ ,

$$\widehat{\psi}_{xi} = 2\tan^{-1}\left\{Re(\widehat{\lambda}_i)\right\}, \quad (9.366)$$

and

$$\widehat{\psi}_{yi} = 2\tan^{-1}\left\{Im(\widehat{\lambda}_i)\right\}. \quad (9.367)$$

In order to find  $\widehat{\mathbf{U}}_s$ , we use the  $N \times M$  data matrix at the  $k$ th snapshot,  $\mathbf{X}_k$ . Define the  $NM \times 1$  vector,

$$\mathbf{Y}(k) = \text{vec}\left(\mathbf{Q}_N^H \mathbf{X}_k \mathbf{Q}_M^*\right), \quad k = 1, \dots, K. \quad (9.368)$$

Using (A.108),

$$\mathbf{Y}(k) = \left( \mathbf{Q}_M^H \otimes \mathbf{Q}_N^H \right) \text{vec}(\mathbf{X}_k) = \left( \mathbf{Q}_M^H \otimes \mathbf{Q}_N^H \right) \tilde{\mathbf{X}}(k), \quad k = 1, \dots, K. \quad (9.369)$$

Now define an  $NM \times K$  matrix,

$$\mathbf{Y} = \begin{bmatrix} \mathbf{Y}(1) & \cdots & \mathbf{Y}(K) \end{bmatrix}. \quad (9.370)$$

The signal subspace is computed by an eigendecomposition of  $\text{Re}[\hat{\mathbf{S}}_y]$  or from an SVD of the  $ND \times 2K$  matrix  $[\text{Re} \mathbf{Y}, \text{Im} \mathbf{Y}]$ .

We summarize the 2-D unitary ESPRIT algorithm:

1. Compute  $\hat{\mathbf{U}}_s$ . The columns of  $\hat{\mathbf{U}}_s$  are the “largest” left singular vectors of  $[\text{Re} \mathbf{Y}, \text{Im} \mathbf{Y}]$  or the eigenvectors corresponding to the  $D$  largest eigenvalues of  $\text{Re}[\hat{\mathbf{S}}_y]$ .
2. Compute  $\hat{\Psi}_x$  and  $\hat{\Psi}_y$  as the solutions to (9.361) and (9.363). We use the TLS solution in all of our examples.
3. Compute the eigenvalues,  $\hat{\lambda}_i, i = 1, 2, \dots, D$  of  $\hat{\Psi}_x + j\hat{\Psi}_y$ .
4. Compute  $\hat{\psi}_{xi}$  and  $\hat{\psi}_{yi}$  using (9.366) and (9.367).

We consider an example with three sources to illustrate the performance of the 2-D unitary TLS-ESPRIT algorithm.

#### Example 9.9.2<sup>22</sup>

Consider an  $8 \times 8$  standard rectangular array. Three equal-power uncorrelated plane-wave signals impinge on the array from  $(u_{x1}, u_{y1}) = (0, 0)$ ,  $(u_{x2}, u_{y2}) = (0.125, 0)$ , and  $(u_{x3}, u_{y3}) = (0, 0.125)$ . The RMSE of the  $i$ th source is defined as

$$\text{RMSE}_i = \left[ (\hat{u}_{xi} - u_{xi})^2 + (\hat{u}_{yi} - u_{yi})^2 \right]^{\frac{1}{2}}. \quad (9.371)$$

In Figure 9.58, we plot the probability of resolution and normalized RMSE versus  $\text{SNR}$  for  $K = 100$  snapshots. We also show the CRB. As we would expect, the RMSE of the first signal is slightly higher.

We do not show the spectral MUSIC or paired root MUSIC result to keep the plot uncluttered. However, there is significant improvement in the threshold behavior compared to spectral MUSIC, and the above threshold RMSE is close to the CRB.

In the next example we show how we can use row weighting with unitary ESPRIT to achieve performance that essentially achieves the CRB.

---

<sup>22</sup>This example corresponds to the example on p. 326 of [ZHM96].

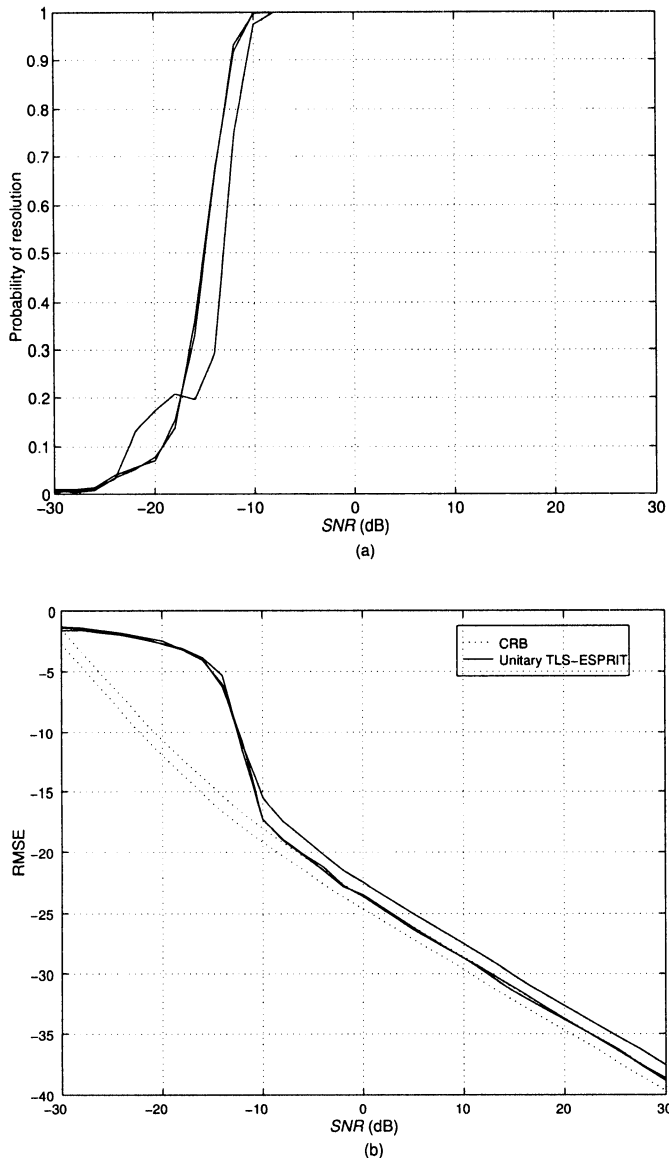


Figure 9.58 Performance of 2-D unitary TLS-ESPRIT;  $d_s = 1, m_s = 1$ , standard rectangular array,  $N=M=8$ ,  $\mathbf{u}_1 = [0 \ 0]^T$ ,  $\mathbf{u}_2 = [0.125 \ 0]^T$ ,  $\mathbf{u}_3 = [0 \ 0.125]^T$ ,  $K = 100$ , 500 trials: (a) probability of resolution versus  $SNR$ ; (b) RMSE versus  $SNR$ .

**Example 9.9.3** (continuation)

Consider the same model as in Example 9.9.2. We use weighted unitary TLS-ESPRIT with  $m_s = 3$ .

In Figure 9.59, we plot the probability of resolution and the normalized RMSE versus  $SNR$ . We also show the CRB.

We see that weighting improves the RMSE behavior and essentially achieves the CRB.

The performance of unitary TLS-ESPRIT is good. However, a disadvantage is the dimension of the problem for many arrays of practical interest. In the next section, we consider the beamspace implementation of ESPRIT.

### 9.9.1.3 2-D beamspace ESPRIT

In this section, we develop 2-D beamspace unitary ESPRIT. The algorithm is due to Zoltowski et al. [ZHM96] and our discussion follows that reference.

The beamspace array manifold matrix consists of  $N_{bs}M_{bs}$  orthogonal conventional beams whose MRAs are spaced at  $2\pi/N$  intervals in  $\psi_x$ -space and  $2\pi/M$  in  $\psi_y$ -space. The two matrices used to construct the beamspace are:

$$\left[ \mathbf{B}_{bsx}^H \right]_n = \frac{1}{N} \left[ e^{j(\frac{N-1}{2})n\frac{2\pi}{N}} \quad e^{j(\frac{N-3}{2})n\frac{2\pi}{N}} \quad \dots, \quad e^{-j(\frac{N-1}{2})n\frac{2\pi}{N}} \right], n \in \sum_{N_{bs}}. \quad (9.372)$$

where  $\sum_{N_{bs}}$  specifies the set of values on  $n$  used in the matrix. If the beamspace sector is centered at  $\psi_x = 0$  and  $N_{bs}$  is odd, then

$$-(N_b - 1)/2 \leq n \leq (N_b - 1)/2. \quad (9.373)$$

$\left[ \mathbf{B}_{bsx}^H \right]$  is an  $N_{bs} \times N$  matrix. Similarly,

$$\left[ \mathbf{B}_{bsy}^H \right]_m = \frac{1}{M} \left[ e^{j(\frac{M-1}{2})m\frac{2\pi}{M}} \quad e^{j(\frac{M-3}{2})m\frac{2\pi}{M}} \quad \dots, \quad e^{-j(\frac{M-1}{2})m\frac{2\pi}{M}} \right], m \in \sum_{M_{bs}}. \quad (9.374)$$

$\left[ \mathbf{B}_{bsy}^H \right]$  is an  $M_{bs} \times M$  matrix.

The beamspace array manifold matrix is an  $N_{bs} \times M_{bs}$  matrix,

$$\mathbf{V}_{bs}(\psi_x, \psi_y) = \mathbf{B}_{bsx}^H \mathbf{V}(\psi_x, \psi_y) \mathbf{B}_{bsy}^*, \quad (9.375)$$

where  $\mathbf{V}(\psi_x, \psi_y)$  is defined in (9.339).

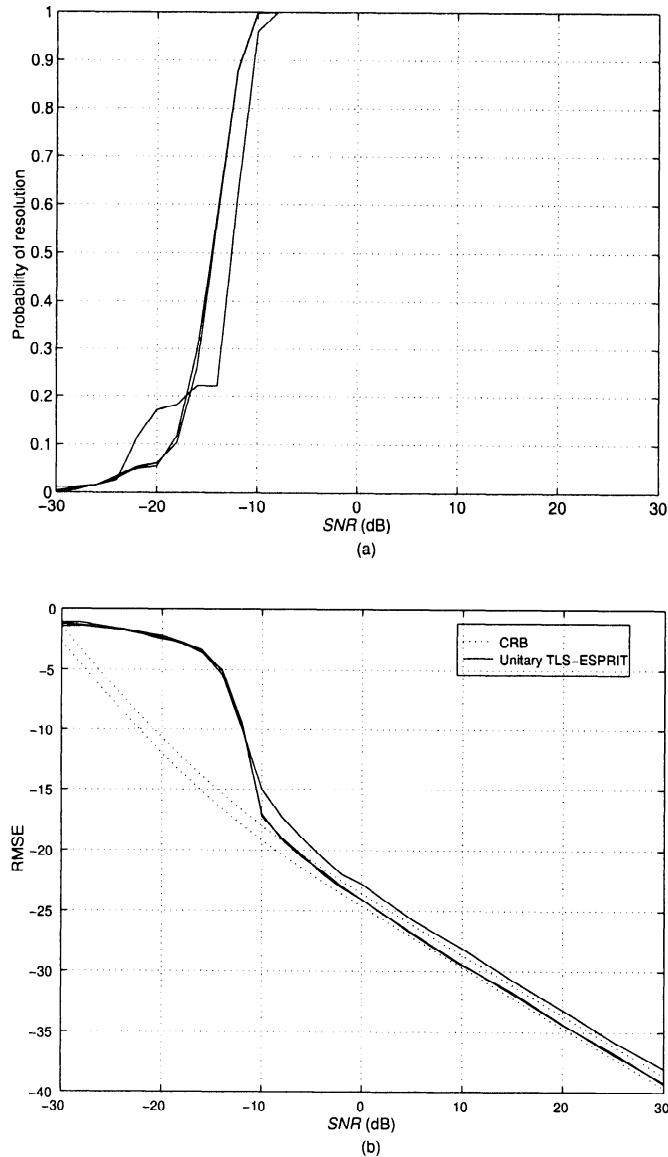


Figure 9.59 Performance of 2-D unitary TLS-ESPRIT with row weighting;  $d_s = 1, m_s = 3$ , standard rectangular array,  $N = M = 8$ ,  $\mathbf{u}_1 = [0 \ 0]^T$ ,  $\mathbf{u}_2 = [0.125 \ 0]^T$ ,  $\mathbf{u}_3 = [0 \ 0.125]^T$ ,  $K = 100$ , 500 trials: (a) Probability of resolution versus  $SNR$ ; (b) RMSE versus  $SNR$ .

The components of beamspace array manifold matrix are

$$b_{nm}(\psi_x, \psi_y) = \frac{1}{NM} \left\{ \frac{\sin \left[ \frac{N}{2} (\psi_x - n \frac{2\pi}{N}) \right]}{\sin \left[ \frac{1}{2} (\psi_x - n \frac{2\pi}{N}) \right]} \frac{\sin \left[ \frac{M}{2} (\psi_y - m \frac{2\pi}{M}) \right]}{\sin \left[ \frac{1}{2} (\psi_y - m \frac{2\pi}{M}) \right]} \right\}. \quad (9.376)$$

The beamspace array manifold matrix can be expressed as

$$\mathbf{V}_{bs}(\psi_x, \psi_y) = \mathbf{v}_{bsx}(\psi_x) \mathbf{v}_{bsy}^T(\psi_y), \quad (9.377)$$

where  $\mathbf{v}_{bsx}(\psi_x)$  is defined in (9.309) and  $\mathbf{v}_{bsy}(\psi_y)$  has the same form. Because  $\mathbf{v}_{bsx}(\psi_x)$  satisfies the invariance relationship in (9.315), we can write

$$\tan \left( \frac{\psi_x}{2} \right) \boldsymbol{\Gamma}_1 \mathbf{V}_{bs}(\psi_x, \psi_y) = \boldsymbol{\Gamma}_2 \mathbf{V}_{bs}(\psi_x, \psi_y), \quad (9.378)$$

where  $\boldsymbol{\Gamma}_1$  and  $\boldsymbol{\Gamma}_2$  are defined in (9.313) and (9.314).

We define an  $N_{bs} M_{bs} \times 1$  beamspace manifold vector,

$$\mathbf{v}_{bs}(\psi_x, \psi_y) = \text{vec} \{ \mathbf{V}_{bs}(\psi_x, \psi_y) \}. \quad (9.379)$$

Using (A.108), we can rewrite (9.378) as

$$\tan \left( \frac{\psi_x}{2} \right) \boldsymbol{\Gamma}_{\psi_x,1} \mathbf{v}_{bs}(\psi_x, \psi_y) = \boldsymbol{\Gamma}_{\psi_x,2} \mathbf{v}_{bs}(\psi_x, \psi_y), \quad (9.380)$$

where

$$\boldsymbol{\Gamma}_{\psi_x,1} = \mathbf{I}_{N_{bs}} \otimes \boldsymbol{\Gamma}_1, \quad (9.381)$$

and

$$\boldsymbol{\Gamma}_{\psi_x,2} = \mathbf{I}_{N_{bs}} \otimes \boldsymbol{\Gamma}_2, \quad (9.382)$$

are  $(N_{bs} - 1) M_{bs} \times N_{bs} M_{bs}$  matrices. We now repeat the process with the  $\psi_y$  component,

$$\tan \left( \frac{\psi_y}{2} \right) \boldsymbol{\Gamma}_3 \mathbf{v}_{bsy}(\psi_y) = \boldsymbol{\Gamma}_4 \mathbf{v}_{bsy}(\psi_y), \quad (9.383)$$

where  $\boldsymbol{\Gamma}_3$  and  $\boldsymbol{\Gamma}_4$  are defined as in (9.313) and (9.314) with  $N_{bs}$  replaced by  $M_{bs}$ . We can write

$$\tan \left( \frac{\psi_y}{2} \right) \mathbf{V}_{bs}(\psi_x, \psi_y) \boldsymbol{\Gamma}_3^T = \mathbf{V}_{bs}(\psi_x, \psi_y) \boldsymbol{\Gamma}_4^T. \quad (9.384)$$

Then, using (A.108),

$$\tan \left( \frac{\psi_y}{2} \right) \boldsymbol{\Gamma}_{\psi_y,1} \mathbf{v}_{bs}(\psi_x, \psi_y) = \boldsymbol{\Gamma}_{\psi_y,2} \mathbf{v}_{bs}(\psi_x, \psi_y), \quad (9.385)$$

where

$$\boldsymbol{\Gamma}_{\psi_y,1} = \boldsymbol{\Gamma}_3 \otimes \mathbf{I}_{M_{bs}}, \quad (9.386)$$

and

$$\boldsymbol{\Gamma}_{\psi_y,2} = \boldsymbol{\Gamma}_4 \otimes \mathbf{I}_{M_{bs}}, \quad (9.387)$$

are  $N_{bs}(M_{bs} - 1) \times N_{bs}M_{bs}$  matrices.

Now define the  $N_{bs}M_{bs} \times D$  real beamspace array manifold matrix,

$$\tilde{\mathbf{V}}_{bs} \triangleq \begin{bmatrix} \mathbf{v}_{bs}(\psi_{x1}, \psi_{y1}) & \cdots & \mathbf{v}_{bs}(\psi_{xD}, \psi_{yD}) \end{bmatrix}. \quad (9.388)$$

From (9.380),

$$\boldsymbol{\Gamma}_{\psi_x,1}\tilde{\mathbf{V}}_{bs}\boldsymbol{\Omega}_{\psi_x} = \boldsymbol{\Gamma}_{\psi_x,2}\tilde{\mathbf{V}}_{bs}, \quad (9.389)$$

where  $\boldsymbol{\Omega}_{\psi_x}$  is defined in (9.355). Similarly, from (9.385),

$$\boldsymbol{\Gamma}_{\psi_y,1}\tilde{\mathbf{V}}_{bs}\boldsymbol{\Omega}_{\psi_y} = \boldsymbol{\Gamma}_{\psi_y,2}\tilde{\mathbf{V}}_{bs}, \quad (9.390)$$

where  $\boldsymbol{\Omega}_{\psi_y}$  is defined in (9.357).

The signal subspace estimate,  $\hat{\mathbf{U}}_{bs,s}$ , is an  $N_{bs}M_{bs} \times D$  real matrix,

$$\mathbf{U}_{bs,s} = \tilde{\mathbf{V}}_{bs}\mathbf{T}, \quad (9.391)$$

where  $\mathbf{T}$  is a non-singular  $D \times D$  real matrix. Replacing  $\mathbf{U}_{bs,s}$  with  $\hat{\mathbf{U}}_{bs,s}$  gives

$$\hat{\mathbf{U}}_{bs,s} = \hat{\tilde{\mathbf{V}}}_{bs}\mathbf{T} \quad (9.392)$$

or

$$\hat{\tilde{\mathbf{V}}}_{bs} = \hat{\mathbf{U}}_{bs,s}\mathbf{T}^{-1}. \quad (9.393)$$

Then, (9.389) can be written as

$$\boldsymbol{\Gamma}_{\psi_x,1}\hat{\mathbf{U}}_{bs,s}\hat{\Psi}_{x,bs} = \boldsymbol{\Gamma}_{\psi_x,2}\hat{\mathbf{U}}_{bs,s}, \quad (9.394)$$

where

$$\hat{\Psi}_{x,bs} = \mathbf{T}^{-1}\boldsymbol{\Omega}_{\psi_x}\mathbf{T}. \quad (9.395)$$

Similarly, (9.390) can be written as

$$\boldsymbol{\Gamma}_{\psi_y,1}\hat{\mathbf{U}}_{bs,s}\hat{\Psi}_{y,bs} = \boldsymbol{\Gamma}_{\psi_y,2}\hat{\mathbf{U}}_{bs,s}, \quad (9.396)$$

where

$$\hat{\Psi}_{y,bs} = \mathbf{T}^{-1}\boldsymbol{\Omega}_{\psi_y}\mathbf{T}. \quad (9.397)$$

The next step is to construct the beamspace data matrix  $\mathbf{Y}_{bs}$ . The element-space data matrix for the  $k$ th snapshot is the  $N \times M$  matrix  $\mathbf{X}(k)$ . The beamspace data vector for the  $k$ th snapshot is

$$\mathbf{X}_{bs}(k) = \text{vec} \left( \mathbf{B}_{bsx}^H \mathbf{X}(k) \mathbf{B}_{bsy}^* \right). \quad (9.398)$$

Using (A.108), (9.398) can be written as

$$\mathbf{X}_{bs}(k) = \left[ \mathbf{B}_{bsy}^H \otimes \mathbf{B}_{bsx}^H \right] \text{vec}(\mathbf{X}(k)) = \left[ \mathbf{B}_{bsy}^H \otimes \mathbf{B}_{bsx}^H \right] \tilde{\mathbf{X}}(k). \quad (9.399)$$

The complete beamspace data matrix is the  $N_{bs}M_{bs} \times K$  matrix,

$$\mathbf{X}_{bs} = \begin{bmatrix} \mathbf{X}_{bs}(1) & \cdots & \mathbf{X}_{bs}(K) \end{bmatrix}. \quad (9.400)$$

We now proceed in an analogous manner to the 1-D beamspace and the 2-D element-space algorithms. We can summarize the beamspace unitary ESPRIT algorithm:

1. Compute

$$\mathbf{X}_{bs}(k) = \left( \mathbf{B}_{bsx}^H \otimes \mathbf{B}_{bsy}^H \right) \text{vec}(\mathbf{X}(k)) \mathbf{X}(k), \quad k = 1, \dots, K, \quad (9.401)$$

and construct  $\mathbf{X}_{bs}$ .

2. Construct  $\widehat{\mathbf{U}}_{bs,s}$  by finding the  $D$  largest left singular vectors of  $\widehat{\mathbf{X}}_{bs,E}$ , where

$$\widehat{\mathbf{X}}_{bs,E} \triangleq [\text{Re}[\mathbf{X}_{bs}], \text{Im}[\mathbf{X}_{bs}]], \quad (9.402)$$

or, by finding the eigenvectors corresponding to the  $D$  largest eigenvalues of

$$\text{Re} \left[ \widehat{\mathbf{S}}_{\mathbf{X}_{bs}} \right] = \text{Re} \left\{ \frac{1}{K} \sum_{k=1}^K \mathbf{X}_{bs}(k) \mathbf{X}_{bs}^H(k) \right\}. \quad (9.403)$$

3. Compute  $\widehat{\Psi}_{\psi_{x,bs}}$  as the solution to the  $(N_{bs} - 1)M_{bs} \times D$  matrix equation,

$$\boldsymbol{\Gamma}_{\psi_x,1} \widehat{\mathbf{U}}_{bs,s} \widehat{\Psi}_{\psi_{x,bs}} = \boldsymbol{\Gamma}_{\psi_x,2} \widehat{\mathbf{U}}_{bs,s}. \quad (9.404)$$

4. Compute  $\widehat{\Psi}_{\psi_{y,bs}}$  as the solution to the  $N_{bs}(M_{bs} - 1) \times D$  matrix equation,

$$\boldsymbol{\Gamma}_{\psi_y,1} \widehat{\mathbf{U}}_{bs,s} \widehat{\Psi}_{\psi_{y,bs}} = \boldsymbol{\Gamma}_{\psi_y,2} \widehat{\mathbf{U}}_{bs,s}. \quad (9.405)$$

We use either the LS or TLS solution in steps 3 and 4.

5. Compute  $\hat{\lambda}_i = 1, 2, \dots, D$  as the eigenvalues of the  $D \times D$  complex matrix,

$$\hat{\Psi}_{\psi_{x,bs}} + j\hat{\Psi}_{\psi_{y,bs}}. \quad (9.406)$$

6. Compute the estimates of the directional cosines as

$$\begin{cases} \hat{\psi}_{xi} = 2 \tan^{-1} \left\{ \operatorname{Re}(\hat{\lambda}_i) \right\}, & i = 1, \dots, D, \\ \hat{\psi}_{yi} = 2 \tan^{-1} \left\{ \operatorname{Im}(\hat{\lambda}_i) \right\}, & i = 1, \dots, D. \end{cases} \quad (9.407)$$

To illustrate the beamspace unitary ESPRIT algorithm, we use the same model as in Example 9.9.2.

**Example 9.9.4** (continuation, Example 9.9.2)

Consider an  $8 \times 8$  SRA. Three equal-power uncorrelated plane-wave signals impinge on the array from  $(0,0)$ ,  $(0.125, 0)$ , and  $(0, 0.125)$ .

A  $3 \times 3$  beamspace centered at  $(0, 0)$  is used. The indices are

$$\begin{aligned} n &= -1, 0, 1, \\ m &= -1, 0, 1. \end{aligned} \quad (9.408)$$

The RMSE and probability of resolution are plotted versus  $SNR$  in Figure 9.60. The performance is very similar to element-space unitary ESPRIT with  $d_s = 1$  and  $m_s = 1$ . This result is expected because the three signal DOAs are in the central area of the beamspace.

The 2-D beamspace unitary ESPRIT provides a computationally efficient solution to the 2-D estimation problem. It provides the 2-D estimates directly so the pairing problem is eliminated. Above threshold, its performance is close to the CRB.

#### 9.9.1.4 Summary: Rectangular arrays

In the preceding subsections, we have introduced the problem of parameter estimation using planar arrays. We discussed MUSIC, 2-D unitary ESPRIT, and beamspace ESPRIT. The ESPRIT algorithms have good threshold performance and the weighted versions approach the CRB above threshold.

There is a large number of papers in the literature concerning various aspects of the 2-D problem. Representative references include Rao and Kung [RK84], Swindlehurst and Kailath [SK89], Yeh et al. [YLC89], Zoltowski and Stavrinides [ZS89], Hua [Hua91], Clark [Cla92], Hua [Hua92], Sacchini [Sac92], van der Veen et al. [vdVOD92], Swindlehurst and Kailath [SK93a], Clark and Scharf [CS94], Hatke and Forsythe [HF96], Clark et al. [CES97], and Fuhl et al. [FRB97].

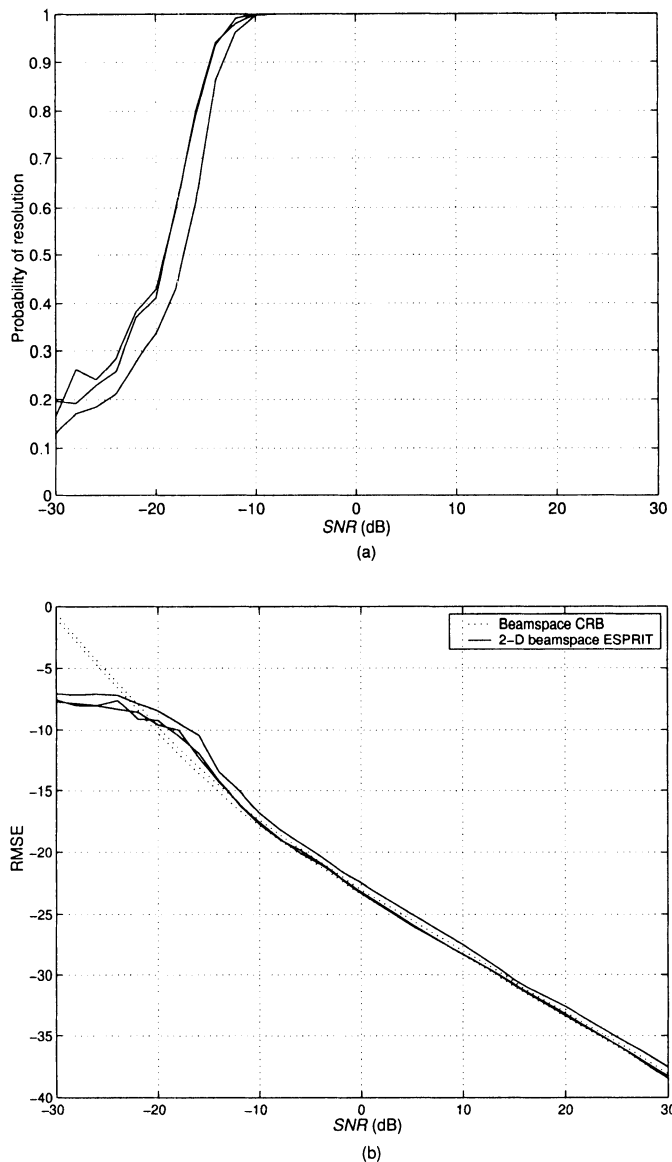


Figure 9.60 Performance of 2-D beamspace unitary ESPRIT;  $d_s = 1, m_s = 1$ , standard rectangular array,  $N=M=8$ ,  $\mathbf{u}_1 = [0 \ 0]^T$ ,  $\mathbf{u}_2 = [0.125 \ 0]^T$ ,  $\mathbf{u}_3 = [0 \ 0.125]^T$ ,  $3 \times 3$  beamspace centered at  $\mathbf{u} = [0 \ 0]^T$ ,  $K = 100$ , 500 trials: (a) probability of resolution versus  $SNR$ ; (b) RMSE versus  $SNR$ .

### 9.9.2 Hexagonal Arrays

In this section, we consider direction-of-arrival estimation using hexagonal arrays. In the text, we emphasize standard hexagonal arrays. Two examples lying in the  $xy$ -plane are shown in Figure 9.61. We use the symmetric indexing scheme shown in the figure (This is same technique as in Section 4.4.)

We identify the elements in a hexagonal array manifold as

$$v_{nm}(u_x, u_y) = \begin{cases} e^{j\pi[nu_x + m\frac{\sqrt{3}}{2}u_y]}, & m \text{ even}, \\ e^{j\pi[(n+\frac{1}{2})u_x + m\frac{\sqrt{3}}{2}u_y]}, & m \text{ odd}. \end{cases} \quad (9.409)$$

We can define an array manifold vector by stacking the transposes of the row vectors of the array. We denote this vector as  $\text{vec}_H(u_x, u_y)$  and note that it is conjugate symmetric.

For the 19-element array in Figure 9.61(b),

$$\text{vec}_H(u_x, u_y) = [\mathbf{v}_2^T \quad \mathbf{v}_1^T \quad \mathbf{v}_0^T \quad \mathbf{v}_{-1}^T \quad \mathbf{v}_{-2}^T]^T, \quad (9.410)$$

where

$$\mathbf{v}_2 = e^{j\pi\sqrt{3}u_y} [e^{-j\pi u_x} \quad 1 \quad e^{-j\pi u_x}]^T, \quad (9.411)$$

$$\mathbf{v}_1 = e^{j\pi\frac{\sqrt{3}}{2}u_y} [e^{-j\pi\frac{3u_x}{2}} \quad e^{-j\pi\frac{u_x}{2}} \quad e^{j\pi\frac{u_x}{2}} \quad e^{j\pi\frac{3u_x}{2}}]^T, \quad (9.412)$$

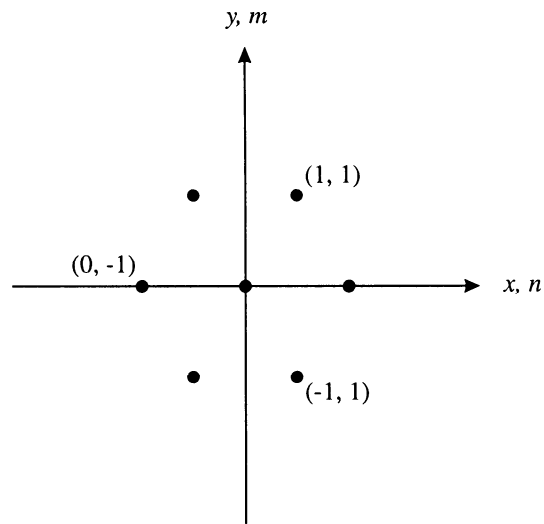
$$\mathbf{v}_0 = [e^{-j2\pi u_x} \quad e^{-j\pi u_x} \quad 1 \quad e^{-j\pi u_x} \quad e^{j2\pi u_x}]^T, \quad (9.413)$$

$$\mathbf{v}_{-1} = e^{-j\pi\frac{\sqrt{3}}{2}u_y} [e^{-j\pi\frac{3u_x}{2}} \quad e^{-j\pi\frac{u_x}{2}} \quad e^{j\pi\frac{u_x}{2}} \quad e^{j\pi\frac{3u_x}{2}}]^T, \quad (9.414)$$

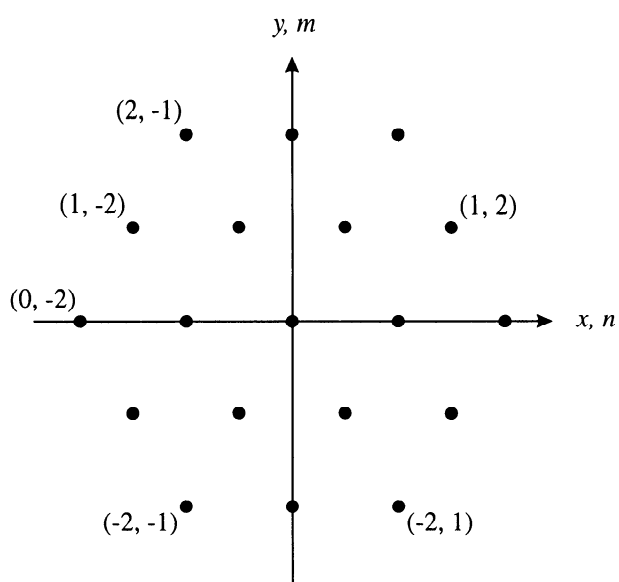
$$\mathbf{v}_{-2} = e^{-j\pi\sqrt{3}u_y} [e^{-j\pi u_x} \quad 1 \quad e^{-j\pi u_x}]^T. \quad (9.415)$$

We can use the spectral algorithms directly by defining a corresponding  $\text{vec}_H(\mathbf{X})$ , computing the sample covariance matrix, the noise subspace and applying the appropriate subspace algorithm.

However, in order to improve the threshold performance, a version of unitary ESPRIT is useful. In order to apply the rectangular results we transform the hexagonal array into an equivalent rectangular-grid array.



(a)



(b)

Figure 9.61 Standard hexagonal arrays: (a) 7 elements; (b) 19 elements.

### 9.9.2.1 Hexagonal-rectangular transformation

We use the transformation discussed in Section 4.4 and apply the unitary ESPRIT algorithms to the equivalent array. The algorithm estimates the signal DOAs in the  $(v_x, v_y)$  space and then finds the corresponding points in the  $(u_x, u_y)$  space. The transformation is shown in Figure 9.62 for the 19-element hexagonal array.

For the hexagonal-rectangular transformation,

$$v_x = u_x, \quad (9.416)$$

and

$$v_y = \frac{u_x}{2} + \frac{\sqrt{3}}{2}u_y, \quad (9.417)$$

or

$$\mathbf{v} = \begin{bmatrix} 1 & 0 \\ \frac{1}{2} & \frac{\sqrt{3}}{2} \end{bmatrix} \mathbf{u}, \quad (9.418)$$

and

$$\mathbf{u} = \begin{bmatrix} 1 & 0 \\ -\frac{1}{\sqrt{3}} & \frac{2}{\sqrt{3}} \end{bmatrix} \mathbf{v}. \quad (9.419)$$

The estimation algorithm is implemented on the rectangular grid array in Figure 9.62(a) to find  $\hat{\mathbf{v}}$  and then uses (9.419) to find  $\hat{\mathbf{u}}$ .

### 9.9.2.2 Unitary ESPRIT

In this section, the 2-D unitary ESPRIT discussed in Section 9.9.2 is adapted to the hexagonal array model.

In Figure 9.63, we show the subarrays that provide the necessary invariances. For  $u_x$ , we require

$$e^{ju_x} \mathbf{J}_{x1} \mathbf{v}(\psi) = \mathbf{J}_{x2} \mathbf{v}(\psi), \quad (9.420)$$

and

$$\mathbf{Q}_M^H \mathbf{J}_{x2} \mathbf{Q}_N = \mathbf{J}_{x1}. \quad (9.421)$$

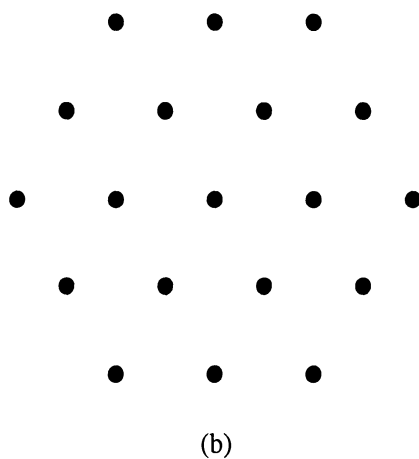
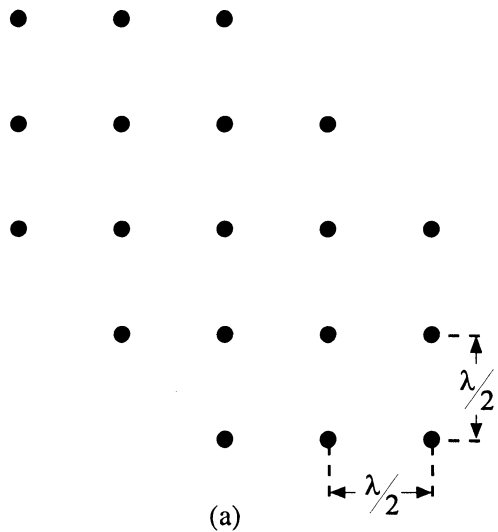


Figure 9.62 Hexagonal-rectangular transformation.

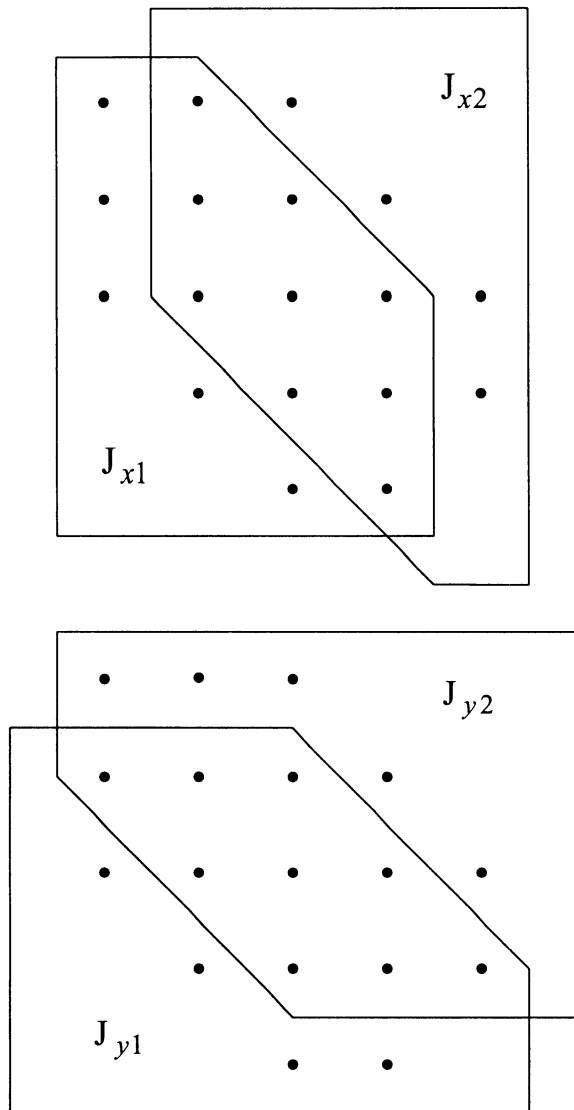


Figure 9.63 Subarrays for unitary ESPRIT.

The 14-element subarrays labeled  $\mathbf{J}_{x1}$  and  $\mathbf{J}_{x2}$  in Figure 9.63(a) provide the necessary invariance. The elements are

$$\begin{array}{cccc} 2 & 3 \\ 5 & 6 & 7 \\ 9 & 10 & 11 & 12 \\ 14 & 15 & 16 \\ 18 & 19 \end{array} \quad (9.422)$$

Similarly, for  $u_y$ , we require

$$e^{ju_y} \mathbf{J}_{y1} \mathbf{v}(\psi) = \mathbf{J}_{y2} \mathbf{v}(\psi). \quad (9.423)$$

The 14-element subarrays labeled  $\mathbf{J}_{y1}$  and  $\mathbf{J}_{y2}$  in Figure 9.63(b) provide the necessary invariance. The elements are

$$\begin{array}{cccc} 1 & 2 & 3 \\ 4 & 5 & 6 & 7 \\ 9 & 10 & 11 & 12 \\ 14 & 15 & 16 \end{array} \quad (9.424)$$

An example illustrates the performance.

### Example 9.9.5

Consider the 19-element hexagonal array in Figure 9.62(b) and the corresponding rectangular array in Figure 9.62(a). There are two equal-power uncorrelated signals impinging on the array from  $\mathbf{u}_1$  and  $\mathbf{u}_2$  where

$$\mathbf{u}_1 = [ \begin{array}{cc} 0 & 0 \end{array} ]^T, \quad (9.425)$$

and

$$\mathbf{u}_2 = [ \begin{array}{cc} 0 & 0.0866 \end{array} ]^T. \quad (9.426)$$

We use subarrays 1 and 2 in Figure 9.63 in the rectangular grid version of 2-D unitary ESPRIT. Unitary ESPRIT is implemented in  $\mathbf{v}$ -space to the transformed subarrays and the result is transformed to  $\mathbf{u}$ -space. In Figure 9.64, the probability of resolution and RMSE versus  $SNR$  are plotted.

The threshold occurs at  $SNR = 0$  dB. Above threshold, the RMSE is about 1 dB above the CRB. The use of row weighting will move the RMSE closer to the CRB.

One can also develop a 2-D unitary ESPRIT algorithm for the hexagonal array without going through the hexagonal-rectangular transformation. The subarrays and performance are identical.

#### 9.9.2.3 Summary: Hexagonal arrays

By using the transformation in Section 9.9.2.1, we can adapt most of the algorithms derived for rectangular grids to hexagonal grids. We discussed hexagonal unitary ESPRIT and showed that it provided good performance.

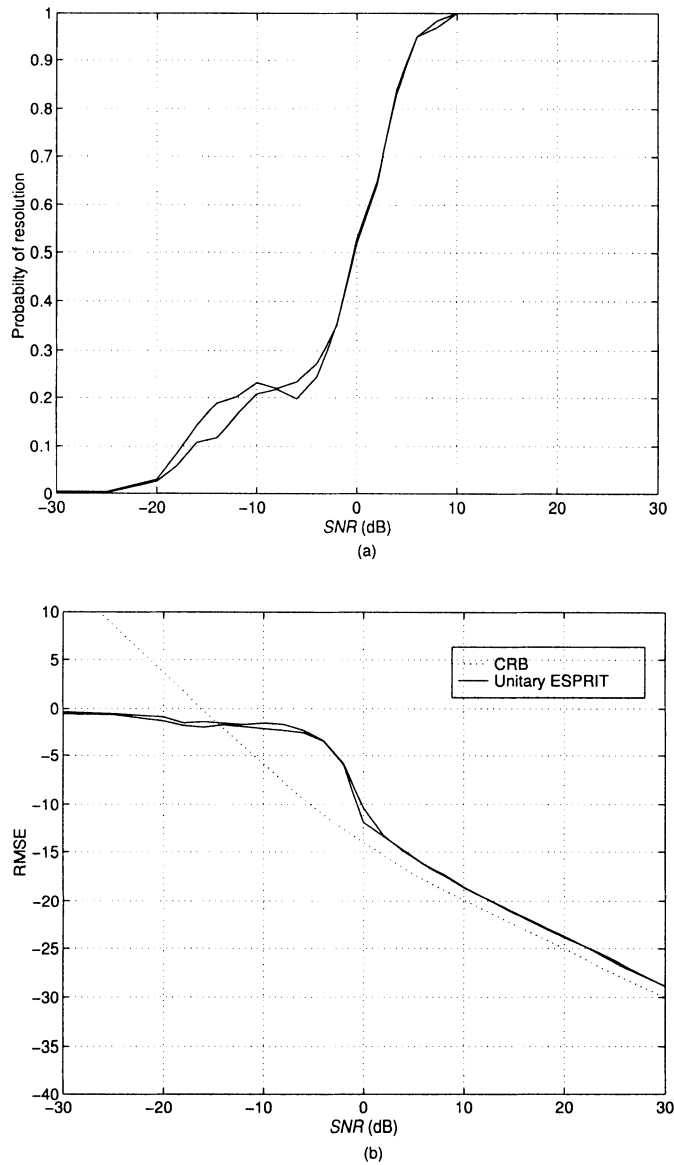


Figure 9.64 2-D unitary ESPRIT for a 19-element standard hexagonal array:  
 $\mathbf{u}_1 = [0 \ 0]^T$ ,  $\mathbf{u}_2 = [0 \ .0866]^T$ ,  $m_s = 1$ ,  $K = 100$ , 500 trials: (a) probability of resolution versus  $SNR$ ; (b) RMSE versus  $SNR$ .

### 9.9.3 Summary: Planar Arrays

In this section, we have discussed parameter estimation for planar arrays with either rectangular or hexagonal grids. We focused our attention on the 2-D unitary ESPRIT algorithm and the 2-D beamspace unitary ESPRIT algorithm. Both algorithms provided good performance with a reasonable amount of computation. Zoltowski et al. [ZHM96] also develop a version of beamspace ESPRIT that is applicable to cross arrays.

Uniform circular arrays are used in some applications. We can utilize the phase-mode excitation beamformer developed in Chapter 4 to provide an array manifold similar to a ULA. We then apply root MUSIC and ESPRIT to estimate the DOA. The principal references are Tewfik and Hong [TH92] and Mathews and Zoltowski [MZ94]. The ESPRIT technique has also been extended to filled circular arrays (FCA) whose sensors are located on rectangular, hexagonal, polar, or random lattices. Ramos et al. [RMZ99] have developed an FCA-ESPRIT algorithm that simultaneously estimates azimuth and elevation.

Wong and Zoltowski [WZ99] have developed a root MUSIC algorithm for azimuth and elevation estimation for an array of velocity hydrophones. The paper also contains a useful discussion of velocity hydrophones.

The reader is referred to these references for further discussion.

## 9.10 Summary

In Section 9.10.1, we summarize the major results in Chapter 9. In Section 9.10.2, we briefly discuss some related topics. In Section 9.10.3, we provide a brief introduction to Chapter 10.

### 9.10.1 Major Results

In Chapters 8 and 9, we discussed the parameter estimation problem. Chapter 8 focused on ML techniques and bounds. In Chapter 9, we developed algorithms that are computationally simpler. In many cases, some of these algorithms perform almost as well as the ML algorithms. We emphasized the performance of the algorithms for a moderate number of snapshots (generally  $K = 10N$ ) as a function of  $ASNR$ . Although we discussed asymptotic behavior ( $K \rightarrow \infty$ ), we did not emphasize it. Our examples focused on the case of plane waves whose DOAs were closely spaced ( $u < 0.5BW_{NN}$ ) because it stressed the algorithms. We evaluated the various algorithms using two criteria:

- (i) How close did the RMSE approach the CRB as the  $ASNR$  increased.
- (ii) At value of  $ASNR$  did the threshold behavior occur?

We also considered other cases, such as correlated or coherent signals, unequal signal powers, and low sample support, which stressed the algorithms.

In addition to the two criteria listed above, we must consider the behavior of the algorithms when the number of signals are unknown or the array is subject to perturbations. An important result from the discussion in Section 9.3.5 is that all estimation algorithms should be tested in conjunction with one or more detection algorithms and their robustness to overestimation of  $D$  should be measured. The discussion in Section 9.8 shows the importance of measuring the robustness of the algorithm to model perturbations.

Table 9.3: Parameter Estimation Algorithms for Standard Linear Arrays

Algorithm	Computation	Section
IQML-QC	Iterative	8.7.2
IMODE	EVD, iterative	8.7.3
Unitary IMODE	Real EVD, iterative	8.7.3
Two-step MODE	EVD	8.7.3
Root MUSIC	EVD, polynomial rooting	9.3.2
Unitary root MUSIC	EVD, polynomial rooting	9.3.2
Weighted LS & TLS ESPRIT	EVD	9.3.4.1
Weighted unitary LS & TLS ESPRIT	Real EVD	9.3.4.1

The majority of the discussion considered estimation in element space. Section 9.7 developed the corresponding algorithms in beamspace. The advantage of beamspace processing is a reduction in computational complexity.

Because of these issues the choice of the algorithm will depend on the particular application. We have provided the designer with an algorithm tool kit that can be utilized to choose the appropriate algorithm. Tables 9.3–9.6 list the algorithms with their computation and give a section reference.

Table 9.3 lists the algorithms that are most appropriate for standard linear arrays. For uncorrelated signals, all of the algorithms have similar

thresholds (within 2–3 dB) for the examples that we studied. Above threshold, all of the algorithms are close (1 or 2 dB) to the CRB. The unitary versions of the algorithms allow real computation and reduce computational complexity.

Table 9.4: Parameter Estimation Algorithms for Standard Rectangular and Hexagonal Arrays

Algorithm	Computation	Section
1-D root MUSIC with pairing	EVD, polynomial rooting	9.9.1.1
2-D unitary LS or TLS ESPRIT	Real EVD	9.9.1.2

Table 9.5: Parameter Estimation Algorithms for Arbitrary Arrays

Algorithm	Computation	Section
AML	D-dim. search	8.5.1
CML	D-dim. search	8.5.2
WSF(MODE)	EVD, D-dim. search	8.5.3
AML-AM	Successive 1-D searches	8.6.2
CML-AP	Successive 1-D searches	8.6.2
MODE-AP	Successive 1-D searches	8.6.2
CML-EM	Parallel 1-D	8.6.3
Bartlett	1-D search	9.2.2
MVDR (Capon)	1-D search	9.2.3
MUSIC	EVD, 1-D search	9.3.2
Min-Norm	EVD, 1-D search	9.3.3

In the case of correlated or coherent signals, the threshold performance is degraded for all of the algorithms. The IMODE algorithm reaches the CRB in the examples that we studied.

We have discussed more of the characteristics of the algorithms in the various sections. By running test scenarios that correspond to given applications and reviewing other constraints such as computational complexity and robustness, we can choose an appropriate algorithm. In the problem section, we provide a set of test scenarios to illustrate these ideas.

Our discussion of rectangular arrays was not as extensive as the SLA discussion. The 2-D unitary ESPRIT algorithm provided good performance with reasonable computational complexity in the examples studied.

For arbitrary arrays, and uncorrelated signals, either CML-AP or MODE-AP provided the best threshold behavior. Above threshold, CML-AP was close to the CRB and MODE-AP reached the CRB. An adequate initialization was essential to the satisfactory performance of the AP algorithms. The threshold of the MUSIC algorithm occurs at a higher value of  $ASNR$ . Above threshold, the RMSE of the MUSIC algorithm is close to the CRB for uncorrelated signals ( $ASNR_i^{-1}$  above it).

Both beamspace unitary ESPRIT and beamspace IQML required a DFT beamspace matrix. The algorithms provided good performance with reasonable computational complexity.

It is important to re-emphasize that the choice of the appropriate algorithm will depend on the scenarios that are encountered in a particular application. Our objective was to provide a collection of useful algorithms and study their behavior for a limited set of scenarios.

Table 9.6: Beamspace Algorithms

Algorithm	Computation	Section
BS-MUSIC	EVD	9.7.1
BS-unitary ESPRIT	EVD	9.7.2
BS-IQML	EVD	8.10.4

### 9.10.2 Related Topics

In Section 8.12.2, we discussed three related topics in the context of ML estimation; structured adaptive beamforming, nonlinear estimation, and correlated noise environments. All of the topics are also relevant to the parameter estimation algorithms discussed in this chapter. In this section, we briefly introduce several other related topics.

We have selected this particular set of topics because they provide interesting extensions of the discussion in the text. The topics are not of equal importance and the level of discussion varies among topics. We have tried to provide a very brief description of the problem and list several references that will enable the interested reader to get started.

### 9.10.2.1 Spatially spread sources

In Section 8.9, we introduced a parametric model for spatially spread sources and derived the Cramér-Rao bound. We formulated the ML problem but it appeared to be too complex to be practical. Various references have explored more techniques based on maximum likelihood or weighted subspace fitting techniques (e.g., Trump and Ottersten [TO96a], [TO96b], Swindlehurst and Stoica ([SS97],[SS98]), Bengtsson and Ottersten ([BO97],[BO01]), Besson and Stoica [BS99], Stoica et al. [SOR98], and Stoica and Besson [SB00]).

Several papers develop MUSIC-like algorithms. Jäntti [Jän92] models the spatially spread signal with a finite number of point sources and uses MUSIC and ESPRIT to estimate their location. Wu et al. [WWMR94] also use a discrete model and develop an algorithm called Vec-MUSIC. Valaee et al. [VCK95] use a continuous model for the distributed sources and develop a distributed-MUSIC which they call the distributed signal parameter estimation (DSPE) algorithm.

Meng et al. [MSW96] develop an improved algorithm called DISPARE (distributed signal parameter estimation). Bengtsson and Ottersten [BO00] developed a rank-two model which utilizes root MUSIC for estimation. Bengtsson and Ottersten [BO01] analyze the performance of weighted subspace fitting with full-rank models.

Other papers dealing with various aspects of spread signal estimation include Lee et al. [LCSL97], Messer et al. [MRG00], and Shahbazpanahi et al. [SVB01].

### 9.10.2.2 Broadband direction finding

Several papers address techniques for coherent subspace processing of broadband signals to estimate their DOA. Wang and Kaveh [WK85] develop a coherent signal subspace algorithm using focusing matrices. A number of refinements and extensions of this approach are described in Hung and Kaveh [HK88], Pierre and Kaveh [PK92], Bassias and Kaveh [BK91], and Doron and Weiss [DW92]. A discussion of focusing techniques is given by Krolik in Chapter 6 of [Hay91].

### 9.10.2.3 Sparse linear arrays

In many applications we use sparse linear arrays to obtain improved resolution with fewer sensors. The MRLAs that were discussed in Section 3.9.2 were examples of a sparse linear arrays. Chambers et al. [CTSD96] have considered various sparse geometries. They computed the CRB and simulated MUSIC. The results demonstrated improvements over ULAs. Fuchs [Fuc97] extended the Pisarenko method to sparse arrays. Abramovich et al. [AGSG96] [AGGS98] [ASG99] considered ambiguity issues and developed techniques for positive definite Toeplitz completion.

### 9.10.2.4 Non-Gaussian noise

Our discussion has assumed that the additive noise is a sample function of Gaussian random process. There are a number of references that extend some of the techniques to non-Gaussian environments.

Tsakalides and Nikias [TN96] considered a class of noise processes called alpha-stable processes that include Gaussian processes as a special case. A discussion of alpha-stable processes is given in Shao and Nikias [SN95]. Tsakalides and Nikias [TN96] develop a version of MUSIC and analyze its performance.

Other approaches utilize the higher order statistics of the non-Gaussian process. References include Porat and Friedlander [PF91], Forster and Nikias [FN91], Cardoso and Moulines [CM95].

### 9.10.2.5 Virtual Arrays

For standard linear arrays, we were able to find computationally efficient parameter estimation algorithms. Another approach is to create a virtual SLA by interpolating the outputs of the actual array. Friedlander, Weiss, and Stoica have published work using this idea (e.g., [Fri93], [WFS95], [FW92], [WF93b], or [FW93a]).

### 9.10.2.6 Near-field sources

For near-field sources, the curvature of the wavefront can be exploited to do range and bearing (DOA) estimation. There are a large number of references that discuss this problem. A representative list includes Hahn [Hah95], Swindlehurst and Kailath [SK88], Huang and Barkat [HB91], Weiss and Friedlander [WF93a], Starer and Nehorari [SN94], Chuberre et al. [CFF95], LeCadre [LeC95], Hung et al. [HCW96], Haardt et al. [HCS96], Yuen and

and Friedlander [YF96a], Haug and Jacyna [HJ96], Abed-Meraim and Hua [AH97], and Lee et al. [LYL01].

### 9.10.3 Discussion

This completes our two-chapter discussion of parameter estimation. In the next chapter we discuss optimum detection briefly and outline some related topics that are not covered in the book.

## 9.11 Problems

### P9.2 Quadratic Algorithms

#### Problem 9.2.1 (continuation, Example 9.2.3)

Consider a 10-element standard linear array and assume that there are two equal-power uncorrelated plane-wave signals impinging on the array from  $\pm\Delta\psi/2$  where  $\Delta\psi = \Delta\psi_R$ . Simulate the beamscan algorithm with FB averaging (9.10).

- (a) Plot the probability of resolution and the normalized RMSE versus  $ASNR$  for  $K = 100$ . Plot the CRB.
- (b) Plot the normalized RMSE versus  $K$  for  $ASNR = 20, 30$ , and  $40$  dB. Plot the CRB.

Discuss your results. Compare the results to those in Figures 9.2–9.4.

#### Problem 9.2.2 (continuation)

Consider the same model as in Problem 9.2.1 except  $\Delta\psi$  is varied. Simulate the beamscan algorithm. Plot the probability of resolution and the normalized RMSE versus  $\Delta\psi/BW_{NN}$  for  $ASNR = 10, 20$ , and  $30$  dB.

#### Problem 9.2.3

Read the paper by Zhang [Zha95b] on the resolution capability of the Bartlett beamformer. Simulate the beamscan for his parameter values. Discuss his results and their practical application.

#### Problem 9.2.4

Consider a 10-element standard linear array and assume that there are two equal-power uncorrelated plane waves impinging on the array from  $\pm\Delta u/2$  where  $\Delta u = 0.3$ . Simulate the MVDR and root MVDR algorithm using FB averaging.

- (a) Plot the normalized RMSE versus  $ASNR$  for  $K = 100$ . Include the CRB on the plot.
- (b) Plot the normalized RMSE versus  $K$  for  $ASNR = 10$  dB,  $20$  dB, and  $30$  dB.

Discuss your results.

#### Problem 9.2.5

Consider a standard 10-element linear array. The following uncorrelated plane-wave signals are impinging on it:

$$\text{Signal 1} \quad u_1 = 0 \quad SNR_1 = 10 \text{ dB}$$

$$\text{Signal 2} \quad u_2 = 0.3 \quad SNR_2 = 20 \text{ dB}$$

$$\text{Signal 3} \quad u_3 = 0.7 \quad SNR_3 = 5 \text{ dB}$$

$$\text{Signal 4} \quad u_3 = -0.5 \quad SNR_4 = 0 \text{ dB}$$

Simulate the MVDR algorithm for  $K = 20, 100$ , and  $500$ . Plot the MVDR spatial spectrum versus  $u$ . Estimate:  $\sigma_w^2, u_1, \dots, u_4$ , and  $\sigma_1^2, \dots, \sigma_4^2$ . Plot the normalized RMSE versus  $ASNR$ .

Compare your estimate of  $\sigma_w^2$  to that obtained from (8.324). Compare your estimate of  $u_i, i = 1, \dots, 4$  to the CRB.

**Problem 9.2.6: (Adaptive angular response (AAR) estimation)**

The component of the output of the MVDR algorithm due to the white noise input is

$$\hat{P}_{WN}(\psi) = |\mathbf{w}_{mvdr}(\psi)|^2, \quad (9.427)$$

and varies as a function of  $\psi$  in the MVDR estimator. Borgiottia and Kaplan [BK79] suggested maximizing

$$\begin{aligned} \hat{P}(\psi) &= \frac{1}{K} \sum_{k=1}^K \frac{1}{N} |\mathbf{w}^H \mathbf{X}_k|^2 \\ &= \mathbf{w}^H \mathbf{C}_x \mathbf{w}, \end{aligned} \quad (9.428)$$

subject to a constraint on the white noise gain,

$$\mathbf{w}^H \mathbf{w} = 1. \quad (9.429)$$

- (a) Carry out the constrained maximization and show that,

$$\hat{P}_{AAR}(\psi) = \frac{\mathbf{v}^H(\psi) \mathbf{C}_x^{-1} \mathbf{v}(\psi)}{\mathbf{v}^H(\psi) \mathbf{C}_x^{-2} \mathbf{v}(\psi)}. \quad (9.430)$$

The estimator in (9.430) is referred as the adapted angular response (AAR) estimator. The temporal version of this estimate is in [SM97](5.4.17).

- (b) Consider the same model as in Example 9.2.1. Plot the results for a typical trial.  
(c) Consider the same model as Example 9.2.2. Plot the probability of resolution and normalized RMSE versus  $ASNR$  for  $K = 100$ . Plot the normalized RMSE versus  $K$  for  $ASNR = 20, 30$ , and  $40$  dB. Discuss your results.

Note that  $\hat{P}_{AAR}(\psi)$  does not provide a spatial spectrum estimate.

**Problem 9.2.7 (Thermal noise algorithm (TNA) estimation)**

Haykin and Reilly [HR80] used a pole-zero argument to suggest that the denominator in (9.430) was the key element in locating the peaks of the spectra. They suggested an algorithm that is referred to as the thermal noise algorithm (TNA).

$$\hat{P}_{TNA}(\psi) = \frac{1}{\mathbf{v}^H(\psi) \mathbf{C}_x^{-2} \mathbf{v}(\psi)}, \quad (9.431)$$

and

$$\hat{Q}_{TNA}(\psi) = \mathbf{v}^H(\psi) \mathbf{C}_x^{-2} \mathbf{v}(\psi). \quad (9.432)$$

Gabriel [Gab80] [Kes86] independently approached this algorithm by considering the output of the MVDR filter

$$Y_o(\psi) = \mathbf{w}^H \mathbf{v}(\psi) = \Lambda [\mathbf{v}^H(\psi) \mathbf{C}_x^{-1} \mathbf{v}(\psi)], \quad (9.433)$$

and observing that in the asymptotic regime it approaches zero as  $\mathbf{v}(\psi)$  moves through a source location. It approaches zero because the weight vector  $\mathbf{w}$  approaches zero. Gabriel suggests using the reciprocal of the magnitude of  $\mathbf{w}$  squared as an estimator. (The constant  $\Lambda$  is omitted)

$$\widehat{P}_{TNA}(\psi) = \frac{1}{\mathbf{w}_o^H \mathbf{w}_o} = \frac{1}{\mathbf{v}^H(\psi) \mathbf{C}_x^{-2} \mathbf{v}(\psi)}. \quad (9.434)$$

The corresponding null spectrum is

$$\widehat{Q}_{TNA}(\psi) = \mathbf{v}^H(\psi) \mathbf{C}_x^{-2} \mathbf{v}(\psi). \quad (9.435)$$

A root version of TNA follows directly.

- (a) Repeat part (b) of Problem 9.2.6.
- (b) Repeat part (c) of Problem 9.2.6.

Note that the TNA algorithm is not a spatial spectral estimator.

### Problem 9.2.8

In the region of small sample support, we may be able to improve the performance by using diagonal loading. The various quadratic algorithms can be modified by replacing  $\mathbf{C}_x$  with  $\mathbf{C}_x + \sigma_L^2 \mathbf{I}$ .

Consider the same model as in Example 9.2.2. Plot the normalized RMSE versus  $K$  for  $ASNR = 20$  dB and 30 dB with

$$\sigma_L^2 / \sigma_w^2 = SNR \times 10^{-2}. \quad (9.436)$$

Discuss your results.

### Problem 9.2.9

An enhanced MVDR was proposed by Owsley (e.g., [Ows85], [Hay85]).<sup>23</sup> For simplicity, we assume that  $\mathbf{S}_x$  is available in order to derive the structure of the estimator. We then use  $\widehat{\mathbf{S}}_x$  to implement the estimator.

The enhanced MVDR starts with an eigenvector decomposition of the covariance matrix,

$$\mathbf{S}_x = \mathbf{U}_S \Lambda \mathbf{U}_S^H + \sigma_w^2 \mathbf{I}, \quad (9.437)$$

where  $\mathbf{U}_S$  is the  $N \times D$  matrix of eigenvectors corresponding to the signal subspace and  $\Lambda = \Lambda_S - \sigma_w^2$  is the diagonal matrix of the eigenvalues.

$$\mathbf{U}_S = [\Phi_1 \mid \Phi_2 \mid \cdots \mid \Phi_D]. \quad (9.438)$$

Owsley defines an enhanced data covariance matrix,

$$\mathbf{S}_x(e) \stackrel{\Delta}{=} e \mathbf{U}_S \Lambda \mathbf{U}_S^H + \sigma_w^2 \mathbf{I}, \quad (9.439)$$

where  $e$  is called the modal enhancement factor and has a range  $1 \leq e < \infty$ .

---

<sup>23</sup>Our discussion of the enhanced algorithm follows pp.168–177 of Owsley’s chapter in [Hay85]. He refers to it as the enhanced MV filter.

- (a) Find  $\mathbf{S}_x^{-1}(e)$ . Substitute  $\mathbf{S}_x^{-1}(e)$  in the MVDR algorithm and obtain,

$$P(\psi) = \frac{1}{\mathbf{v}^H(\psi) \mathbf{S}_x^{-1}(e) \mathbf{v}(\psi)}. \quad (9.440)$$

- (b) The enhanced MVDR (EMV) estimator is the limit of (9.440) as  $e \rightarrow \infty$ . Find  $P_{EMV}(\psi)$  and  $Q_{EMV}(\psi)$ .

- (c) In practice, we perform an eigendecomposition of  $\widehat{\mathbf{S}}_x$ ,

$$\widehat{\mathbf{S}}_x = \widehat{\mathbf{U}}_S \widehat{\mathbf{A}}_S \widehat{\mathbf{U}}_S^H + \widehat{\mathbf{U}}_N \widehat{\mathbf{A}}_N \widehat{\mathbf{U}}_N^H, \quad (9.441)$$

and use the estimated eigenvectors. Show that  $Q_{EMV}(\psi)$  can be written as

$$Q_{EMV}(\psi) \triangleq \mathbf{v}^H(\psi) \widehat{\mathbf{U}}_N \widehat{\mathbf{U}}_N^H \mathbf{v}(\psi) = \left| \mathbf{v}^H(\psi) \widehat{\mathbf{U}}_N \right|^2, \quad (9.442)$$

or

$$Q_{EMV}(\psi) \triangleq \mathbf{v}^H(\psi) \left[ \mathbf{I} - \widehat{\mathbf{U}}_S \widehat{\mathbf{U}}_S^H \right] \mathbf{v}(\psi). \quad (9.443)$$

The algorithm defined by (9.442) or (9.443) is identical to the MUSIC algorithm that we develop and analyze in Section 9.3.

- (d) Consider the array and signal model as Problem 9.2.1. Repeat Problem 9.2.1 for  $e = 10, 100$ , and  $\infty$ . Compare your results to Example 9.2.3. Discuss your results.

### P9.3 Subspace Algorithms

**Problem Note 9.3.1:** The first set of problems considers some of the test scenarios in Table 8.3 so that we can compare these results to the various ML results in Chapter 8. We also explore scenario excursions suggested by the results. We also use these test scenarios in problem Sections P.9.6, P.9.7, and P.9.8. Table 9.7 shows where the various test scenarios are used.

#### Problem 9.3.1

Consider a 10-element standard linear array. There are two equal-power uncorrelated plane-wave signals impinging on the array from  $\pm\Delta\psi/2$ , where  $\Delta\psi = 0.05BW_{NN}$ . Simulate the performance of MUSIC, root MUSIC, Min-Norm, and root Min-Norm. Assume  $K = 100$ .

- (a) Plot the normalized RMSE versus  $ASNR$ . Compare your results to the AML and CML results in Chapter 8.
- (b) Plot the probability of resolution. Discuss the behavior of the curve. Is the  $P_R$  definition useful for this scenario?

#### Problem 9.3.2 (continuation)

- (a) Repeat Problem 9.3.1 for the TLS-ESPRIT algorithm. Investigate appropriate row weightings.
- (b) Repeat part (a) for unitary TLS-ESPRIT.

Table 9.7

	TS1	TS2	TS3	TS4	TS5
9.3 Subspace	Ex.9.3.1	P.9.3.1 P.9.3.2	P.9.3.3 P.9.3.4	P.9.3.6 P.9.3.7 Ex.9.3.2	
9.6 Spatial Smoothing				P.9.6.1	
9.7 Beamspace	Ex.9.7.2 P.9.7.1 P.9.7.2	P.9.7.4	P.9.7.5	P.9.7.6 P.9.7.7	
9.8 Sensitivity	Ex.9.8.1 P.9.8.5 P.9.8.14	P.9.8.1 P.9.8.10	P.9.8.2 P.9.8.7 P.9.8.11 P.9.8.16	P.9.8.3 P.9.8.8 P.9.8.12 P.9.8.17	
	TS6	TS7	TS8	TS9	TS10
9.3 Subspace	P.9.3.8	P.9.3.10	P.9.3.11	P.9.3.12	P.9.3.13
9.6 Spatial Smoothing			P.9.6.3		
9.7 Beamspace	P.9.7.8	P.9.7.3	P.9.7.10	P.9.7.11	P.9.7.12
9.8 Sensitivity		P.9.8.4 P.9.8.6 P.9.8.13 P.9.8.15			

**Problem 9.3.3**

Consider a 10-element standard linear array. There are two uncorrelated plane-wave signals impinging on the array from  $\pm\Delta\psi/2$ , where  $\Delta\psi = \Delta\psi_R$ .  $SNR_1 = 100SNR_2$ . Simulate the performance of MUSIC, root MUSIC, Min-Norm, and root Min-Norm. Assume  $K = 100$ .

- (a) Plot the normalized RMSE for signal 1 versus  $ASNR_1$  and signal 2 versus  $ASNR_2$ .
- (b) Repeat for the case in which  $SNR_1 = 1000SNR_2$ .

**Problem 9.3.4 (continuation)**

- (a) Repeat Problem 9.3.3 for the TLS-ESPRIT algorithm. Investigate appropriate row weightings.
- (b) Repeat part (a) for unitary ESPRIT.

**Problem 9.3.5** (continuation, Problem 9.3.3)

Consider the same model as in Problem 9.3.3. Design a sequential MUSIC algorithm that estimates the DOA of signal 1 first. The algorithm then removes signal 1 from the data and estimates the DOA of signal 2. Simulate the performance of your algorithm and discuss its behavior.

**Problem 9.3.6** (continuation, Example 9.3.2)

Consider the same model as in Example 9.3.2, except the phase angle of  $\rho$  is not zero. In case 1,  $\rho = 0.95 \exp(j\pi/4)$ . In case 2,  $\rho = 0.95 \exp(j\pi/2)$ . We utilize FB averaging. Simulate the performance of MUSIC, root MUSIC, Min-Norm, and root Min-Norm.

- (a) Plot the normalized RMSE versus  $ASNR$ . Compare your results to the AML and CML results in Chapter 8.
- (b) Repeat part (a) with  $|\rho| = 0.99$ .

**Problem 9.3.7** (continuation)

Repeat Problem 9.3.6 for TLS-ESPRIT and unitary ESPRIT.

**Problem 9.3.8** (continuation, Example 9.3.1)

Repeat Example 9.3.1 for the low sample support case in which  $K = 20$ .

**Problem 9.3.9** (continuation, Example 9.3.4)

Consider the model as in Example 9.3.4 and assume  $d_s = 1$ . Simulate the performance of the LS-ESPRIT algorithm (9.121). Compare the results to the results using the TLS-ESPRIT algorithm. Discuss the computational difference.

**Problem 9.3.10**

Consider a 10-element standard linear array. There are three equal-power uncorrelated plane-wave signals impinging on the array from  $\psi_1 = -\Delta\psi$ ,  $\psi_2 = 0$ , and  $\psi_3 = \Delta\psi$ , where  $\Delta\psi = \Delta\psi_R$ . (Test scenario 7.)

- (a) Simulate the performance of MUSIC, root MUSIC, Min-Norm, and root Min-Norm. Plot the normalized RMSE versus  $ASNR$  for each of the three signals. Discuss your results.
- (b) Repeat part (a) for TLS-ESPRIT and unitary TLS-ESPRIT.

**Problem 9.3.11** (continuation)

Consider the same model as in Problem 9.3.10 except the signals are correlated with unequal power. (Test scenario 8.)

$$\begin{aligned} SNR_1 &= SNR_3 = 0.5SNR_2 \\ \rho_{12} &= 0.9, \quad \rho_{23} = 0.9, \quad \rho_{13} = 0.5 \exp(j\pi/2) \end{aligned}$$

Simulate the performance of MUSIC, root MUSIC, and ESPRIT. Plot the normalized RMSE versus  $ASNR$  for each of the three signals. Discuss your results.

**Problem 9.3.12** (continuation; Problem 9.3.10)

- (a) Repeat Problem 9.3.10 for the case in which the two plane waves at  $\pm\Delta\psi$  have an  $SNR$  that is 10 dB higher than the plane wave at  $\psi = 0$ . (Test scenario 9.)
- (b) Apply the algorithm derived in Problem 9.3.5 to this model.

**Problem 9.3.13** (continuation, Problem 9.3.10)

Consider the model in Problem 9.3.10. Repeat the problem for the case of five equal-power uncorrelated plane waves located at  $\psi = 0, \pm\Delta\psi, \pm 2\Delta\psi$ , where  $\Delta\psi = \Delta\psi_R$ . (Test Scenario 10)

**Problem 9.3.14**

Consider a standard 10-element array. There are two equal-power correlated signals impinging on the array from  $\pm\Delta\psi$ , where  $\Delta\psi = BW_{NN}$ . Let  $K = 100$ . Consider two phase angles for  $\rho$ ;  $\phi_\rho = 0$  and  $\phi_\rho = j\pi/2$ . Utilize FB averaging and implement MUSIC and root MUSIC. The  $ASNR = 10$  dB.

- (a) Plot the normalized RMSE versus  $|\rho|$  for the two phase angles.
- (b) Compute the CRB versus  $|\rho|$  for the two phase angles and plot the relative efficiency of the MUSIC estimator. In Example 9.5.1, we will show that

$$EFF_{MU} = 1 - |\rho|^2.$$

Compare your results to that formula.

**Problem Note 9.3.2:** The next set of problems consider a 32-element SLA. The problem with two and three signals are similar to the earlier problems. The larger array size allows us to consider more complicated scenarios.

**Problem 9.3.15**

Consider a standard 32-element linear array. There are two equal-power uncorrelated signals impinging on the array at  $\pm\Delta u/2$ , where  $\Delta u = 1/32$ . Consider  $K = 320$  and  $960$ .

- (a) Simulate MUSIC and root MUSIC. Plot the normalized RMSE versus  $ASNR$ .
- (b) Simulate TLS-ESPRIT. Plot the normalized RMSE versus  $ASNR$ .

**Problem 9.3.16** (continuation)

Repeat Problem 9.3.15 with  $\Delta u = 1/128$ .

**Problem 9.3.17** (continuation, Problem 9.3.15)

Repeat Problem 9.3.15 with  $\Delta u = 1/32$  and  $ASNR_1 = 100ASNR_2$ .

**Problem 9.3.18** (continuation, Problem 9.3.15)

Repeat Problem 9.3.15 with  $\Delta u = 1/32$  and  $\rho = 0.95$ ,  $\rho = 0.95 \exp(j\pi/4)$ , and  $\rho = 0.95 \exp(j\pi/2)$ .

**Problem 9.3.19** (continuation, Problem 9.3.15)

Repeat Problem 9.3.15 with  $\Delta u = 1/32$  and  $K = 64$ .

**Problem 9.3.20** (continuation, Problem 9.3.15)

- (a) Repeat Problem 9.3.15 with three equal-power uncorrelated signals located at  $-1/32, 0, 1/32$ .
- (b) Repeat part (a) with  $ASNR_1 = ASNR_3 = 100ASNR_2$ .

**Problem 9.3.21** (continuation, Problem 9.3.15)

Repeat Problem 9.3.15 for the following cases:

- (a) Five equal-power uncorrelated signals located at  $\pm 2/32, \pm 1/32, 0$ .
- (b) Seven equal-power uncorrelated signals located at  $\pm 3/32, \pm 2/32, \pm 1/32, 0$ .
- (c) Fifteen equal-power uncorrelated signals located at  $\pm m/32, m = 0, \dots, 7$ .

**Problem Note 9.3.3:** Our discussion and most of the discussion in the literature assumes that the number of signals,  $D$ , is known. In practice, we usually have to estimate  $D$ . The next three problems consider this issue.

**Problem 9.3.22** (continuation, Example 9.3.1)

Repeat Example 9.3.1 under the assumption that we do not know that there are two plane waves. Process the data using AIC-FB and MDL-FB to generate  $\hat{D}$ . Simulate MUSIC, root MUSIC, and TLS-ESPRIT assuming  $\hat{D}$  is correct. Plot the results. Discuss your results.

**Problem 9.3.23** (continuation)

Repeat Problem 9.3.22 for the signal model in Problem 9.3.6.

**Problem 9.3.24**

Repeat Problem 9.3.22 for the signal model in Problem 9.3.10.

**Problem Note 9.3.4:** The next several problems consider low redundancy arrays that were introduced in Section 3.9.2. We would expect that the larger aperture would improve resolution but would require a larger number of snapshots to achieve the same estimation accuracy.

**Problem 9.3.25**

Consider the 5-element linear array in Table 3.8. The sensor spacing is

$$1 \cdot 3 \cdot 3 \cdot 2$$

Two equal-power uncorrelated signals impinge on the array from  $\pm \Delta u/2$ , where  $\Delta u = 0.0866$ . Simulate the performance of the MUSIC algorithm for  $K = 100, 300$ , and  $500$ .

Plot the normalized RMSE versus ASNR for each value of  $K$ . Compare your results to those in Example 9.3.1 and the CRB derived in Chapter 8 (Problem 8.4.10). Discuss the trade-off between the number of elements and the number of snapshots.

**Problem 9.3.26** (continuation)

Repeat Problem 9.3.25 for the 7-element linear array in Table 3.8. The sensor spacing is

$$1 \cdot 3 \cdot 6 \cdot 2 \cdot 3 \cdot 2$$

Consider larger values of  $K$ , if necessary.

**Problem 9.3.27** (continuation, Problem 9.3.25)

Repeat Problem 9.3.25 for the 9-element linear array in Table 3.8. The sensor spacing is

$$1 \cdot 3 \cdot 6 \cdot 6 \cdot 6 \cdot 2 \cdot 3 \cdot 2$$

Consider larger values of  $K$ , if necessary.

**Problem 9.3.28** (continuation, Problem 9.3.25)

Repeat Problem 9.3.25 for the 10-element linear array in Table 3.8. The sensor spacing is

$$1 \cdot 2 \cdot 3 \cdot 7 \cdot 7 \cdot 7 \cdot 4 \cdot 4 \cdot 1$$

Consider larger values of  $K$ , if necessary.

**Problem 9.3.29**

The sensor spacing in a MRLA allows us to construct the  $\hat{\mathbf{S}}_x$  matrix corresponding to a uniform linear array on the same grid as the MRLA. Use this result to design a root MUSIC algorithm for the MRLA.

- (a) Simulate your algorithm for the MRLA in Problem 9.3.25. Compare your results to those in Problem 9.3.25.
- (b) Simulate your algorithm for the MRLA in Problem 9.3.26. Compare your results to those in Problem 9.3.26.
- (c) Simulate your algorithm for the MRLA in Problem 9.3.27. Compare your results to those in Problem 9.3.27.
- (d) Simulate your algorithm for the MRLA in Problem 9.3.28. Compare your results to those in Problem 9.3.28.

**Problem 9.3.30: Unitary IMODE ([GS99])**

The cost function for MODE is given in (8.524) as

$$J_{MODE}(\mathbf{b}) = \text{tr} [\mathbf{P}_B \hat{\mathbf{U}}_s \mathbf{W}_{ao} \hat{\mathbf{U}}_s^H], \quad (9.444)$$

where  $\mathbf{B}$  is given in (8.488) and satisfies

$$\mathbf{B}^H \mathbf{V} = 0. \quad (9.445)$$

The FB backward averaged spatial spectral matrix is given by (7.40) as

$$\mathbf{C}_{x,fb} = \frac{1}{2K} \sum_{k=1}^K (\mathbf{X}_k \mathbf{X}_k^H + \mathbf{J} \mathbf{X}_k^* \mathbf{X}_k^T \mathbf{J}) = \frac{1}{2} (\mathbf{C}_x + \mathbf{J} \mathbf{C}_x^* \mathbf{J}). \quad (9.446)$$

From (9.58)

$$\mathbf{C}_{x,Re} = \mathbf{Q}^H \mathbf{C}_{x,fb} \mathbf{Q} = \text{Re} [\mathbf{Q}^H \mathbf{C}_x \mathbf{Q}], \quad (9.447)$$

where  $\mathbf{Q}$  is given by (9.54) and (9.55). The eigendecomposition of  $\mathbf{C}_{x,Re}$  is given by (9.64) as

$$\mathbf{C}_{x,Re} = \hat{\mathbf{U}}_{S,Re} \hat{\mathbf{\Lambda}}_{S,Re} \hat{\mathbf{U}}_{S,Re}^H + \hat{\mathbf{U}}_{N,Re} \hat{\mathbf{\Lambda}}_{N,Re} \hat{\mathbf{U}}_{N,Re}^H. \quad (9.448)$$

- (a) Show that

$$(\mathbf{B}^H \mathbf{Q})(\mathbf{Q}^H \mathbf{V}) = (\mathbf{B}^H \mathbf{Q}) \tilde{\mathbf{V}} = \mathbf{0}, \quad (9.449)$$

where

$$\tilde{\mathbf{V}} \triangleq \mathbf{Q}^H \mathbf{V}. \quad (9.450)$$

- (b) Show that the unitary MODE cost function is

$$J_{UMODE}(\mathbf{b}) = \text{tr} [\mathbf{Q}^H \mathbf{P}_B \mathbf{Q} \hat{\mathbf{U}}_{S,Re} \mathbf{W}_{Re} \hat{\mathbf{U}}_{S,Re}^H], \quad (9.451)$$

where

$$\mathbf{W}_{Re} = \left( \hat{\Lambda}_{S,Re} - \hat{\sigma}_\omega \mathbf{I} \right)^2 \hat{\Lambda}_{S,Re}^{-1}. \quad (9.452)$$

- (c) Unitary IMODE uses (8.524)–(8.544) with the above cost function. Write out the appropriate equations.  
(d) Repeat Example 8.7.1 and 8.7.2 using unitary IMODE.

## P9.4 Linear Prediction

### Problem 9.4.1

Read Gabriel's [Gab80] development of linear prediction algorithms (see also Johnson and Degraaf [JD82]).

- (a) Show that the LP null spectrum can be written as

$$\hat{Q}_{LP}(\psi) = |B_{LP}(\psi)|^2 = \left| \mathbf{v}^H(\psi) \hat{\mathbf{S}}_x^{-1} \mathbf{e}_N \right|^2, \quad (9.453)$$

where

$$\mathbf{e}_N^T = [ \ 0 \ 0 \ \cdots \ 0 \ 1 \ ], \quad (9.454)$$

is a  $1 \times N$  matrix whose first  $N - 1$  elements are equal to zero. or

$$\hat{Q}_{FBLP}(\psi) = |B_{FBLP}(\psi)|^2 = \left| \mathbf{v}^H(\psi) \hat{\mathbf{S}}_{FB}^{-1} \mathbf{e}_N \right|^2, \quad (9.455)$$

if FB averaging is appropriate.

- (b) Consider the same model as in Example 9.2.2. . Plot the probability of resolution and normalized RMSE versus  $ASNR$  for  $K = 100$ . Compare your results to root MUSIC and the CRB.  
(c) Plot the normalized RMSE versus  $K$  for an  $ASNR = 20$  dB.

Discuss your results.

### Problem 9.4.2

Read Tufts and Kumaresan [TK82]. Develop the root version of the LP algorithm. Repeat parts (b) and (c) of Problem 9.4.1. Discuss your results.

### Problem 9.4.3

Read Kumaresan and Tufts [KT83] and show how they derive the Min-Norm algorithm from the linear prediction algorithm.

### Problem 9.4.4

There is also a family of algorithms that we refer to as the subarray linear prediction (SALP) family.

The basic algorithm is essentially the same as the maximum entropy algorithm developed by Burg (e.g.,[Bur67], [Bur75]) for spatial or temporal spectral estimation. Van den Bos [VDB71] showed that it could be interpreted as a linear predictor. In the spatial (or

temporal) estimation context, most discussions start with an underlying autoregressive or ARMA model for the spectra and assume a noiseless observation. Books by Kay [Kay83], Marple [Mar87], Haykin [Hay96], and Proakis et al. [PRLN92] contain extensive discussions. Although the emphasis is on temporal spectral estimation, most of the ideas map directly to the spatial problem in the case of SLA.

The algorithms are the multiple snapshot version of the frequency estimation algorithms contained in Tufts and Kumaresan [TK82].

- (a) Read [TK82] and derive the formula for the null spectra. Use the subarray model in Figure 6.102.
- (b) Repeat parts (b) and (c) of Problem 9.4.1. Discuss your results.

## P9.5 Asymptotic Performance

### Problem 9.5.1

Read Lee and Wengrovitz [LW91] and Zhang [Zha95a]. Reproduce the results in Figure 9.35.

### Problem 9.5.2

Read Krim et al. [KFP92]. Derive (9.199).

### Problem 9.5.3

Read Pillai and Kwon [PK89a]. Derive the appropriate equations for the FB averaging case.

### Problem 9.5.4

Consider the model in Example 9.5.1. Read the discussion in Section 9.6.3.2 of FBSS MUSIC. Plot the relative asymptotic efficiency of FBSS MUSIC for the same parameters as in Figure 9.38. Discuss your results.

### Problem 9.5.5

Read the bias analysis in Xu and Buckley [XB92]. Discuss the *ASNR* regions where the bias is a factor. Does their analysis reflect the bias behavior in the threshold region?

### Problem 9.5.6 (continuation, Problem 9.3.3)

Consider the model in Problem 9.3.3. Compute the asymptotic variance of MUSIC and ESPRIT (with row weighting). Discuss your results.

### Problem 9.5.7 (continuation, Problem 9.3.1)

Consider the model in Problem 9.3.1. Compute the asymptotic variance of MUSIC and ESPRIT (with row weighting). Discuss your results.

## P9.6 Correlated and Coherent Signals

### Problem 9.6.1

Consider a 10-element standard linear array with two equal-power correlated signals impinging on the array. The signal separation is  $\Delta u$ . Consider three cases of signal phase;  $\phi_\rho = 0, \pi/4$ , and  $\pi/2$  and two values of  $|\rho|$ ; 0.9 and 0.99. We use FBSS as a preliminary processor. Consider four values of  $M$ ; 3, 5, 7, and 9. (Test scenario 4.)

Simulate the MUSIC, root MUSIC, and ESPRIT algorithms on the output of FBSS processor.

- (a) Plot the normalized RMSE versus  $\Delta u$  for an  $ASNR = 20$  dB and 30 dB. Discuss your results.
- (b) Consider the parameter set in Example 9.3.2;  $\rho = 0.95$ ,  $\Delta u = 6\Delta\psi_R$ , and  $K = 100$ . Plot the normalized RMSE for the three algorithms and the four values of  $M$ . Compare your results to those in Figure 9.13 and 9.20(a).

**Problem 9.6.2** (continuation)

Consider the same model as in Problem 9.6.1 with  $\Delta u = 3BW_{NN}$ . Recall that the relative efficiency of MUSIC was essentially flat and equal to  $(1 - |\rho|^2)$  for  $\Delta u \geq BW_{NN}$ .

Simulate the MUSIC and root MUSIC algorithms and develop relative efficiency results for the FBSS algorithms with various  $M$ ,  $|\rho|$ , and  $\phi_\rho$ . Discuss your results.

**Problem 9.6.3** (continuation, Problem 9.3.11)

Consider the same model as in Problem 9.3.11. Use FBSS with various values of  $M$ . Simulate the performance of MUSIC, root MUSIC, and TLS-ESPRIT. Plot the normalized RMSE versus  $ASNR$  for each of the three signals. Compare your results to those in Problem 9.3.12. (Test scenario 8.)

## P9.7 Beamspace Algorithms

**Problem Note 9.7.1:** We consider many of the same problems as in Problem Section P.9.3 so we can compare the beamspace performance to the element-space performance.

**Problem 9.7.1** (continuation, Example 9.7.2)

Consider a 10-element standard linear array. Two equal-power uncorrelated plane-wave signals impinge on the array from  $\pm\Delta\psi/2$  where  $\Delta\psi = \Delta\psi_R$ . We use an  $N_{bs} \times N$  DFT beamspace matrix (9.304). We consider  $N_{bs} = 3$  and 5. Assume  $K = 100$ .

- (a) Simulate the beamspace MUSIC algorithm. Plot the normalized RMSE versus  $ASNR$ . Compare your results to the results in Example 9.7.1 and 9.7.2.
- (b) Assume that the two plane-wave signals are located at  $u_c - \Delta\psi/2$  and  $u_c + \Delta\psi/2$ . Simulate the beamspace unitary ESPRIT algorithm. Plot the normalized RMSE versus  $ASNR$  for representative  $u_c$  inside and outside the beam fan. Discuss your results.

**Problem 9.7.2** (continuation)

Consider the same model as in Problem 9.7.1 except we use  $N_{bs} = 4$  and 6 (see (3.322)). Assume  $K = 100$ . (Test scenario 1.)

Simulate the beamspace MUSIC algorithm and the beamspace unitary ESPRIT algorithm. Plot the normalized RMSE versus  $ASNR$ . Compare your results to Problem 9.7.1 and Example 9.7.2.

**Problem 9.7.3** (continuation)

Consider the same model as in Problem 9.7.1 except that there are three equal-power uncorrelated signals located at  $\psi = 0$  and  $\pm\Delta\psi$ , where  $\Delta\psi = \Delta\psi_R$ . We consider  $N_{bs} = 4$ , 5, and 6. (Test scenario 7.)

Simulate the beamspace MUSIC algorithm and beamspace unitary ESPRIT algorithm. Plot the normalized RMSE versus  $ASNR$ . Discuss your results.

**Problem 9.7.4** (continuation, Problem 9.3.1, Problem 9.7.1)

Consider the same beamspace matrix as Problem 9.7.1 and the same input signal model as Problem 9.3.1 ( $\Delta\psi = 0.05BW_{NN}$ ). Simulate beamspace MUSIC and beamspace unitary ESPRIT. Plot the normalized RMSE versus  $ASNR$ . Compare your results to the element-space results in Problems 9.3.1 and 9.3.2. (Test scenario 2.)

**Problem 9.7.5** (continuation, Problem 9.3.3, Problem 9.7.1)

Consider the same beamspace matrix as Problem 9.7.1 and the same input signal model as Problem 9.3.3 ( $SNR_1 = 100SNR_2$  and  $1000SNR_2$ ). Simulate beamspace MUSIC and beamspace unitary ESPRIT. Plot the normalized RMSE versus  $ASNR$ . Compare your results to the element-space results in Problems 9.3.3 and 9.3.4. (Test scenario 3.)

**Problem 9.7.6** (continuation, Problem 9.3.6, Problem 9.7.1)

Consider the same beamspace matrix as Problem 9.7.1 and the same input signal model as Problem 9.3.6 ( $\rho = 0.95$ ,  $0.95 \exp(j\pi/4)$ , and  $0.95 \exp(j\pi/2)$ ). Simulate beamspace MUSIC and beamspace unitary ESPRIT. Plot the normalized RMSE versus  $ASNR$ . Compare your results to the element-space results in Problems 9.3.6, 9.3.7, and Example 9.3.2. (Test scenario 4.)

**Problem 9.7.7**

Consider the same model as in Problem 9.7.6. Assume that a beamspace matrix with  $N_{bs} = 7$  is available. Design an algorithm which implements beamspace spatial smoothing. Plot the normalized RMSE versus  $ASNR$ . Compare your results to those in Problem 9.7.6. (Test scenario 4.)

**Problem 9.7.8** (continuation, Problem 9.3.8, Problem 9.7.1)

Consider the same beamspace matrix as Problem 9.7.1 and the same input signal model as Problem 9.3.8 ( $K = 20$ ). Simulate beamspace MUSIC and beamspace unitary ESPRIT. Plot the normalized RMSE versus  $ASNR$ . (Test scenario 6.)

(a) Compare your results to the element-space results in Problem 9.3.8.

(b) Repeat Problem 9.3.8 and part (a) for various values of  $K$ . Discuss your results.

**Problem 9.7.9** (continuation, Problem 9.7.2)

Consider the same beamspace matrix as Problem 9.7.2. The input is three equal-power uncorrelated plane-wave signals arriving from  $\psi = 0, \Delta\psi, 2\Delta\psi$ , where  $\Delta\psi = \Delta\psi_R$ . Simulate beamspace MUSIC and beamspace unitary ESPRIT. Plot the normalized RMSE versus  $ASNR$ . Compare your results to the element-space results in Problem 9.3.10.

**Problem 9.7.10** (continuation, Problem 9.7.9)

Repeat Problem 9.7.9 for the signal model in Problem 9.3.11. (Test scenario 8.)

**Problem 9.7.11** (continuation, Problem 9.7.10)

Repeat Problem 9.7.9 for the signal model in Problem 9.3.12. (Test scenario 9.)

**Problem 9.7.12** (continuation, Problem 9.7.2, Problem 9.3.13)

Consider the same beamspace matrix as Problem 9.7.2 and the same input signal model as Problem 9.3.13 (five signals at  $\psi = 0, \pm\Delta\psi, \pm2\Delta\psi$ ). Simulate beamspace MUSIC and

beamspace unitary ESPRIT. Plot the normalized RMSE versus  $ASNR$ . Compare your results to the element-space results in Problem 9.3.13. (Test scenario 10.)

#### Problem 9.7.13

All of the beamspace estimation algorithms have assumed that the number of signals are known. If we assume that all of our processing is done in beamspace then we need to implement either AIC-FB or MDL-FB in beamspace. We investigate the performance of the detection algorithms as a function of  $N_{bs}$  and  $ASNR$  in this problem.

Consider a 10-element SLA and an  $N_{bs} \times N$  DFT beamspace matrix. We utilize FB averaging of the data (see Section 8.10.2.5) and consider values of  $N_{bs} = 3, 4, 5, 6$ , and 7. In each part, we plot  $\hat{D}$  versus  $ASNR$  for various values of  $N_{bs}$ . The signals are plane-wave signals with the following characteristics (in all cases,  $\Delta u = \Delta\psi_R$ ):

- (a) two uncorrelated signals at  $u_1 = -\Delta u/2$ ,  $u_2 = \Delta u/2$ .
- (b) two uncorrelated signals at  $u_c - \Delta u/2$ ,  $u_c + \Delta u/2$ .

#### Problem 9.7.14

Consider the same beamspace and signal model as in Problem 9.7.1. Assume  $N_{bs} = 7$  and  $K = 100$ . We assume that the number of signals is unknown. Implement the following algorithm and simulate its performance:

- (a) Implement AIC-FB and MDL-FB in beamspace. Denote the estimate of the number of signals as  $\hat{D}$ .
- (b) Choose the  $(\hat{D} + 1)$  beams with the largest output.
- (c) Process these beams to estimate the DOAs.
- (d) Plot the RMSE versus  $ASNR$ .

#### Problem 9.7.15

Read the paper by Zoltowski et al. [ZKS93] on beamspace root MUSIC. Repeat Problem 9.7.1(a) using beamspace root MUSIC. Compare your results to those in Problem 9.7.1 and Example 9.7.2. Compare the computational complexity.

#### Problem 9.7.16 (continuation, Example 8.10.6 and Example 9.7.2)

Consider a standard 32-element linear array and a  $N_{bs} \times N$  DFT beamspace matrix. There are two equal-power uncorrelated plane-wave signals impinging on the array from  $u = \pm\Delta u/2$ , where  $\Delta u = 1/32$ ,  $K = 100$ .

- (a) Simulate the performance of beamspace MUSIC and beamspace unitary ESPRIT for the  $N_{bs} = 3$  and 5 cases. Plot the normalized RMSE versus  $ASNR$ . Discuss your results.
- (b) Repeat part(a) for  $\Delta u = 1/128$ . Discuss your results.
- (c) Repeat part(a) for  $\Delta u = 1/8$ . Discuss your results.

## P9.8 Sensitivity and Robustness

**Problem Note 9.8.1:** The first set of problems consider position perturbations using the perturbation model in Examples 8.11.1 and 9.8.1. We let  $\sigma_p = 0.05\lambda$ . All of the problems

have been simulated in an earlier section for the case of no perturbations. In each case, compare your result to the  $\sigma_p = 0$  case and the hybrid CRB from Section 8.11.

**Problem 9.8.1**

Repeat Problems 9.3.1 and 9.3.2 for the position perturbation case. (Test scenario 2.)

**Problem 9.8.2**

Repeat Problems 9.3.3 and 9.3.4 for the position perturbation case. (Test scenario 3.)

**Problem 9.8.3**

Repeat Problems 9.3.6 and 9.3.7 for the position perturbation case. (Test scenario 4.)

**Problem 9.8.4**

Repeat Problem 9.3.10 for the position perturbation case. (Test scenario 7.)

**Problem Note 9.8.2:** The next five problems consider beamspace processing and position perturbations. One objective is to compare the performance of beamspace processing and element-space processing for identical models.

**Problem 9.8.5**

Repeat Problem 9.7.1 for the position perturbation case. Compare your results to those in Example 9.8.1. (Test scenario 1.)

**Problem 9.8.6**

Repeat Problem 9.7.9 for the position perturbation case. Compare your results to those in Problem 9.8.4. (Test scenario 7.)

**Problem 9.8.7**

Repeat Problem 9.7.5 for the position perturbation case. Compare your results to those in Problem 9.8.2. (Test scenario 3.)

**Problem 9.8.8**

Repeat Problem 9.7.6 for the position perturbation case. Compare your results to those in Example 9.8.3. (Test scenario 4.)

**Problem 9.8.9**

Repeat Problem 9.7.3 for the position perturbation case.

**Problem Note 9.8.3:** The next set of problems consider sensor gain and phase perturbation. We use the model in Section 6.6.3 with no sensor perturbations. We let  $\sigma_g = 0.05$  and  $\sigma_\gamma = 2^\circ$ . In each case, compare your results to the  $\sigma_g = \sigma_\gamma = 0$  case and the hybrid CRB.

**Problem 9.8.10**

Repeat Problems 9.3.1 and 9.3.2 for sensor gain and phase perturbations. Compare your results to those in Problems 9.3.1 and 9.3.2. (Test scenario 2.)

**Problem 9.8.11**

Repeat Problems 9.3.3 and 9.3.4 for sensor gain and phase perturbations. Compare your results to those in Problems 9.3.3 and 9.3.4. (Test scenario 3.)

**Problem 9.8.12**

Repeat Problems 9.3.6 and 9.3.7 for sensor gain and phase perturbations. Compare your results to those in Problems 9.3.6 and 9.3.7. (Test scenario 4.)

**Problem 9.8.13**

Repeat Problem 9.3.10 for sensor gain and phase perturbations. Compare your results to those in Problem 9.3.10. (Test scenario 7.)

**Problem Note 9.8.4:**

The next several problems consider beamspace processing and sensor gain and phase perturbations.

**Problem 9.8.14**

Repeat Problem 9.7.1 for sensor gain and phase perturbations. Compare your results to those in Example 9.8.1. (Test scenario 1.)

**Problem 9.8.15**

Repeat Problem 9.7.3 for sensor gain and phase perturbations. Compare your results to those in Problem 9.8.13. (Test scenario 7.)

**Problem 9.8.16**

Repeat Problem 9.7.5 for sensor gain and phase perturbations. Compare your results to those in Problem 9.8.11. (Test scenario 3.)

**Problem 9.8.17**

Repeat Problem 9.7.6 for sensor gain and phase perturbations. Compare your results to those in Example 9.8.12. (Test scenario 4.)

## P9.9 Planar Arrays

**Problem 9.9.1**

Consider a standard  $10 \times 10$  rectangular array. There are two equal-power uncorrelated plane waves impinging on the array. Their  $(\theta, \phi)$  directions are  $(34^\circ, 45^\circ)$  and  $(26^\circ, 45^\circ)$ , respectively. Simulate the performance of 2-D spectral MUSIC and paired 1-D root MUSIC.

- Plot the RMSE (9.338) for each source versus  $SNR$  for  $K = 100$ . Discuss your results.
- Plot the RMSE (9.338) for each source versus  $K$  for an  $SNR = 20$  dB.
- Repeat part (a) for source locations of  $(34^\circ, 0^\circ)$  and  $(26^\circ, 0^\circ)$ .

**Problem 9.9.2**

Repeat Problem 9.9.1 for the case in which  $ASNR_1 = 100ASNR_2$ .

**Problem 9.9.3**

Repeat Problem 9.9.1 for the case in which the sources are correlated. Consider  $\rho = 0.95$  and  $0.95 \exp(j\pi/2)$ .

**Problem 9.9.4**

Consider a standard  $10 \times 10$  rectangular array. There are three equal-power uncorrelated plane waves impinging on the array. Their  $(\theta, \phi)$  directions are  $(45^\circ, 50^\circ)$ ,  $(45^\circ, 45^\circ)$ ,

( $45^\circ, 40^\circ$ ), respectively. Repeat parts (a) and (b) of Problem 9.9.1.

**Problem 9.9.5**

Repeat Example 9.9.1 for 2-D weighted unitary ESPRIT. Compare your results to those in Example 9.9.1.

**Problem 9.9.6**

Repeat Problem 9.9.1 for 2-D weighted unitary ESPRIT. Compare your results to those in Problem 9.9.1.

**Problem 9.9.7**

Repeat Problem 9.9.2 for 2-D weighted unitary ESPRIT. Compare your results to those in Problem 9.9.2.

**Problem 9.9.8**

Repeat Problem 9.9.3 for 2-D weighted unitary ESPRIT. Compare your results to those in Problem 9.9.3.

**Problem 9.9.9**

Repeat Problem 9.9.4 for 2-D weighted unitary ESPRIT. Compare your results to those in Problem 9.9.4.

**Problem Note 9.9.1:** The next four problems implement 2-D beamspace ESPRIT using nine beams. The advantage is a significant reduction in computational complexity.

**Problem 9.9.10**

Repeat Problem 9.9.1 for 2-D beamspace weighted unitary ESPRIT. Compare your results to those in Problem 9.9.1.

**Problem 9.9.11**

Repeat Problem 9.9.2 for 2-D beamspace weighted unitary ESPRIT. Compare your results to those in Problem 9.9.2.

**Problem 9.9.12**

Repeat Problem 9.9.3 for 2-D beamspace weighted unitary ESPRIT. Compare your results to those in Problem 9.9.3.

**Problem 9.9.13**

Repeat Problem 9.9.4 for 2-D beamspace weighted unitary ESPRIT. Compare your results to those in Problem 9.9.4.

**Problem Note 9.9.2:** The next several problems consider hexagonal arrays. In order to get some comparison with the  $10 \times 10$  rectangular array, we use the standard 91-element hexagonal array in Example 4.4.1.

**Problem 9.9.14**

Repeat Problem 9.9.1 for 2-D unitary ESPRIT. Compare your results to those in Problem 9.9.1.

**Problem 9.9.15**

Repeat Problem 9.9.2 for 2-D unitary ESPRIT. Compare your results to those in Problem 9.9.2.

**Problem 9.9.16**

Repeat Problem 9.9.3 for 2-D unitary ESPRIT. Compare your results to those in Problem 9.9.3.

**Problem 9.9.17**

Repeat Problem 9.9.4 for 2-D unitary ESPRIT. Compare your results to those in Problem 9.9.4.

**Problem 9.9.18**

Design a beamspace unitary ESPRIT algorithm for hexagonal arrays. Apply it to one or more of the models in Problems 9.9.14–9.9.18.

**Problem 9.9.19**

Read Tewfik and Hong [TH92] and Mathews and Zoltowski [MZ94]. Implement the algorithms for uniform circular array. Discuss your results.

## Bibliography

- [AGGS98] Y. I. Abramovich, D. A. Gray, A. Y. Gorokhov, and N. K. Spencer. Positive-definite Toeplitz completion in DOA estimation for nonuniform linear antenna arrays—part I: Fully augmentable arrays. *IEEE Trans. Signal Process.*, vol.SP-46, pp. 2458–2471, September 1998.
- [AGSG96] Y. I. Abramovich, D. A. Gray, N. K. Spencer, and A. Y. Gorokhov. Ambiguities in direction-of-arrival estimation for nonuniform linear antenna arrays. *Proc. ISSPA*, Gold Coast, Australia, pp. 631–634, 1996.
- [AI97] K. Abed-Meraim and Y. Hua. 3-D near-field source localization using second order statistics. *Proc. 31st Asilomar Conf. on Signals, Systems, and Computers*, vol.2, pp. 1307–1311, Pacific Grove, California, November 1997.
- [And63] T. W. Anderson. Asymptotic theory for principal component analysis. *Ann. Math. Stat.*, vol.34, pp. 122–148, February 1963.
- [And91] S. Anderson. On optimal dimension reduction for sensor array signal processing. Technical Report LiTH-ISY-I-1242, Department of Electrical Engineering, Linköping University, Linköping, Sweden, August 1991.
- [ASG99] Y. I. Abramovich, N. K. Spencer, and A. Y. Gorokhov. Positive-definite Toeplitz completion in DOA estimation for nonuniform linear antenna arrays—Part II: Partially augmentable arrays. *IEEE Trans. Signal Process.*, vol.SP-47, pp. 1502–1520, June 1999.
- [Bac95] R. Bachl. The forward-backward averaging technique applied to TLS-ESPRIT processing. *IEEE Trans. Signal Process.*, vol.SP-43, pp. 2691–2699, November 1995.
- [Bar83] A. J. Barabell. Improving the resolution performance of eigenstructure-based direction finding algorithms. *Proc. ICASSP*, Boston, Massachusetts, pp. 336–339, 1983.
- [BCD<sup>+</sup>84] A. J. Barabell, J. Capon, D. F. DeLong, J. R. Johnson, and K. D. Senne. Performance comparison of superresolution array processing algorithms. Technical Report Project Rep. TST-72, MIT Lincoln Laboratory, Lexington, Massachusetts, May 1984.

- [BK79] G. V. Borgiotti and L. J. Kaplan. Superresolution of uncorrelated interference sources by using adaptive array techniques. *IEEE Trans. Antennas Propag.*, vol.AP-27, pp. 842–845, November 1979.
- [BK80] G. Bienvenu and L. Kopp. Adaptivity to background noise spatial coherence for high resolution passive methods. *Proc. ICASSP*, vol.1, pp. 307–310, Denver, Colorado, April 1980.
- [BK83] G. Bienvenu and L. Kopp. Optimality of high resolution array processing using the eigensystem approach. *IEEE Trans. Acoust., Speech, Signal Process.*, vol.ASSP-31, pp. 1234–1248, October 1983.
- [BK84] G. Bienvenu and L. Kopp. Decreasing high resolution method sensitivity by conventional beamformer preprocessing. *Proc. ICASSP*, vol.5, pp. 33.2.1–33.2.4, San Diego, California, April 1984.
- [BK91] A. Bassias and M. Kaveh. Coherent signal-subspace processing in a sector. *IEEE Trans. Syst., Man, Cybern.*, vol.SMC-21, September/October 1991.
- [BO97] M. Bengtsson and B. Ottersten. Low complexity estimation for distributed sources. Signal Processing Technical Report IR-S3-SB-9721, Royal Institute of Technology, Department of Signals, Sensors, and Systems, October 1997.
- [BO00] M. Bengtsson and B. Ottersten. Low-complexity estimators for distributed sources. *IEEE Trans. Signal Process.*, vol.SP-48, pp. 2185–2194, August 2000.
- [BO01] M. Bengtsson and B. Ottersten. A generalization of weighted subspace fitting to full-rank models. *IEEE Trans. Signal Process.*, vol.SP-49, pp. 1002–1012, May 2001.
- [Böh83] J. F. Böhme. On parametric methods for array processing. *Proc. EUSIPCO-83*, September 1983.
- [Bri81] D. R. Brillinger, editor. *Time Series: Data Analysis and Theory*. Holden-Day, San Francisco, California, expanded edition, 1981.
- [BS87] C. Byrne and A. Steel. Sector-focused stability for high-resolution array processing. *Proc. ICASSP*, Dallas, Texas, pp. 54.11.1–54.11.4, 1987.
- [BS99] O. Besson and P. Stoica. Decoupled estimation of DOA and angular spread for a spatially distributed sources. *Conference Record of the 33rd Asilomar Conf. on Signals, Systems, and Computers*, vol.1, pp. 253–257, 1999.
- [BS00] O. Besson and P. Stoica. Decoupled estimation of DOA and angular spread for a spatially distributed sources. *IEEE Trans. Signal Process.*, vol.SP-48, pp. 1872–1882, July 2000.
- [Bur67] J. P. Burg. Maximum entropy spectral analysis. *Proc. 37th Annual Meeting of the Society of Exploration Geophysicists*, Oklahoma City, Oklahoma, October 1967.
- [Bur75] J. P. Burg. *Maximum Entropy Spectral Analysis*. Ph.D. Thesis, Stanford University, Stanford, California, 1975.
- [Cad80] J. A. Cadzow. High performance spectral estimation—a new ARMA method. *IEEE Trans. Acoust., Speech, Signal Process.*, vol.ASSP-28, pp. 524–529, October 1980.
- [Cap69] J. Capon. High-resolution frequency-wavenumber spectrum analysis. *Proc. IEEE*, vol.57, pp. 1408–1418, August 1969.

- [CES97] M. Clark, L. Elden, and P. Stoica. A computationally efficient implementation of 2-D IQML. *Proc. 31st ASILOMAR Conf. on Signals, Systems and Computers*, Pacific Grove, California, vol.2, pp. 1730–1734, 1997.
- [CFF95] H. Cheberre, T. Filleul, and J. J. Fuchs. Near-field sources localization: A model-fitting approach. *Proc. ICASSP*, vol.5, pp. 3555–3558, Detroit, Michigan, May 1995.
- [Cla92] M. P. Clark. *Estimation Techniques for Sensor Array Processing*. Ph.D. Thesis, University of Colorado, Boulder, Colorado, 1992.
- [CM95] J.-F. Cardoso and E. Moulines. Asymptotic performance analysis of direction-finding algorithms based on fourth-order cumulants. *IEEE Trans. Signal Process.*, vol.SP-43, pp. 214–224, January 1995.
- [Cox73] H. Cox. Resolving power and sensitivity to mismatch of optimum array processors. *J. Acoust. Soc. Am.*, vol.54, pp. 771–785, September 1973.
- [CS94] M. P. Clark and L. L. Scharf. Two-dimensional modal analysis based on maximum likelihood. *IEEE Trans. Signal Process.*, vol.SP-42, pp. 1443–1452, June 1994.
- [CTSD96] C. Chambers, T. C. Tozer, K. C. Sharman, and T. S. Durrani. Temporal and spatial sampling influence on the estimates of superimposed narrowband signals: When less can mean more. *IEEE Trans. Signal Process.*, vol.SP-44, pp. 3085–3098, December 1996.
- [CY91] L. Chang and C. Yeh. Resolution threshold for coherent sources using smoothed eigenstructure methods. *Proc. IEE*, vol.138, pp. 470–478, October 1991.
- [DJ85] S. R. DeGraaf and D. H. Johnson. Capability of array processing algorithms to estimating source bearings. *IEEE Trans. Acoust., Speech, Signal Process.*, vol.ASSP-33, pp. 1368–1379, December 1985.
- [DW92] M. A. Doron and A. J. Weiss. On focusing matrices for wide-band array processing. *IEEE Trans. Signal Process.*, vol.SP-40, p. 1295, June 1992.
- [Efr79] B. Efron. Bootstrap methods: Another look at the jackknife. *Ann. Stat.*, vol.7, pp. 1–26, 1979.
- [EJS81] J. E. Evans, J. R. Johnson, and D. F. Sun. High resolution angular spectrum estimation techniques for terrain scattering analysis and angle-of-arrival estimation. *Proc. 1st ASSP Workshop on Spectrum Estimation and Modeling*, Hamilton, Ontario, Canada, pp. 134–139, 1981.
- [EJS82] J.E. Evans, J.R. Johnson, and D.F. Sun. Application of advanced signal processing techniques to angle of arrival estimation in ATC navigation and surveillance systems. Technical report, M.I.T. Lincoln Laboratory, Lexington, Massachusetts, June 1982.
- [Fla00] B. P. Flanagan. *Self Calibration of Antenna Arrays with Large Perturbation Errors*. Ph.D. Thesis, George Mason University, Fairfax, Virginia, 2000.
- [FN91] P. Forster and M. Nikias. Bearing estimation in the bispectrum domain. *IEEE Trans. Signal Process.*, vol.SP-39, pp. 1994–2006, September 1991.
- [FRB97] J. Fuhl, J.-P. Rossi, and E. Bonek. High-resolution 3-D direction-of-arrival determination for urban mobile radio. *IEEE Trans. Antennas Propag.*, vol.AP-45, p. 672, April 1997.

- [Fri90] B. Friedlander. Direction finding with an interpolated array. *Proc. ICASSP*, Albuquerque, New Mexico, vol.5, pp. 2951–2954, April 1990.
- [Fri93] B. Friedlander. The interpolated root-MUSIC algorithm for direction finding. *Eur. J. Signal Process.*, vol.30, pp. 15–29, January 1993.
- [Fuh94] D. Fuhrmann. Estimation of sensor gain and phase. *IEEE Trans. Signal Process.*, vol.SP-42, pp. 77–87, January 1994.
- [Fuc97] J. Fuchs. Extension of the Pisarenko method to sparse linear arrays. *IEEE Trans. Signal Process.*, vol.SP-45, pp. 2413–2421, October 1997.
- [FV87] P. Forster and G. Vezzosi. Application of spheroidal sequences to array processing. *Proc. ICASSP*, vol.4, pp. 2268–2271, Dallas, Texas, April 1987.
- [FW88] B. Friedlander and A. J. Weiss. Eigenstructure methods for direction finding with sensor gain and phase uncertainties. *Proc. ICASSP*, vol.4, pp. 2681–2684, New York, New York, April 1988.
- [FW90] B. Friedlander and A. J. Weiss. Eigenstructure methods for direction finding with sensor gain and phase uncertainties. *Circuits, Syst. Signal Process.*, vol.9, pp. 271–300, 1990.
- [FW92] B. Friedlander and A. J. Weiss. Direction finding using spatial smoothing with interpolated arrays. *IEEE Trans. Aerospace Electron. Syst.*, vol.AES-28, pp. 574–587, April 1992.
- [FW93a] B. Friedlander and A. J. Weiss. Direction finding for wideband signals using an interpolated array. *IEEE Trans. Signal Process.*, pp. 1618–1634, April 1993.
- [FW93b] B. Friedlander and A. J. Weiss. Performance of direction finding systems with sensor gain and phase uncertainties. *Comput., Syst. Signal Proces.*, vol.12, pp. 3–35, 1993.
- [FW94] B. Friedlander and A. J. Weiss. Effects of model errors on waveform estimation using the MUSIC algorithm. *IEEE Trans. Signal Process.*, vol.SP-42, pp. 147–155, January 1994.
- [Gab80] W. F. Gabriel. Spectral analysis and adaptive array superresolution techniques. *Proc. IEEE*, vol.68, pp. 654–666, June 1980.
- [Gab81] W. F. Gabriel. Adaptive superresolution of coherent RF spatial sources. *Proc. 1st ASSP Workshop on Spectrum Estimation and Modeling*, Hamilton, Ontario, Canada, August 1981.
- [GB97] A. B. Gershman and J. F. Böhme. Improved DOA estimation via pseudo-random resampling of spatial spectrum. *IEEE Signal Process. Lett.*, vol.4, pp. 54–57, February 1997.
- [GB98] A. B. Gershman and J. F. Böhme. A pseudo-noise approach to direction finding. *Signal Process.*, vol.71, pp. 1–13, November 1998.
- [Ger98] A. B. Gershman. Pseudo-randomly generated estimator banks: A new tool for improving the threshold performance of direction finding. *IEEE Trans. Signal Process.*, vol.SP-46, pp. 1351–1364, May 1998.
- [GH99] A. B. Gershman and M. Haardt. Improving the performance of unitary ESPRIT via pseudo-noise resampling. *IEEE Trans. Signal Process.*, vol.SP-47, pp. 2305–2308, August 1999.

- [GS99] A. B. Gershman and P. Stoica. On unitary and forward-backward MODE. *Digital Signal Process.*, vol.9, pp. 67–75, April 1999.
- [Gup65] R. P. Gupta. Asymptotic theory for principal component analysis in the complex case. *J. Indian Stat. Assoc.*, vol.3, pp. 97–106, 1965.
- [GVL80] G. H. Golub and C. F. Van Loan. An analysis of the total least squares problem. *SIAM J. Numer. Anal.*, vol.17, pp. 883–893, 1980.
- [GVL83] G. H. Golub and C. F. Van Loan. *Matrix Computations*. The Johns Hopkins University Press, Baltimore, Maryland, 1983.
- [GW93] M. Gavish and A. J. Weiss. Performance analysis of the VIA-ESPRIT algorithm. *Proc. IEE (Radar Signal Process.)*, vol.140, pp. 123–128, April 1993.
- [GZK96] J. A. Gansman, M. D. Zoltowski, and J. V. Krogmeier. Multidimensional multirate DOA estimation in beampspace. *IEEE Trans. Signal Process.*, vol.SP-44, pp. 2780–2792, November 1996.
- [HAH94] M. Haardt and M. E. Ali-Hackl. Unitary ESPRIT: How to exploit additional information inherent in the rotational invariance structure. *Proc. ICASSP*, Adelaide, Australia, vol.IV, pp. 229–232, April 1994.
- [Hah95] W. R. Hahn. Optimum signal processing for passive sonar range and bearing estimation. *J. Acoust. Soc. Am.*, vol.58, no.1, pp. 201–207, July 1975.
- [Hay85] S. Haykin. *Array Signal Processing*. Prentice-Hall, Englewood Cliffs, New Jersey, 1985.
- [Hay91] S. Haykin, editor. *Advances in Spectrum Analysis and Array Processing*, vol.2, Prentice-Hall, Englewood Cliffs, New Jersey, 1991.
- [Hay96] S. Haykin. *Adaptive Filter Theory*. Prentice-Hall, Upper Saddle River, New Jersey, 3rd edition, 1996.
- [HB91] Y. D. Huang and M. Barkat. Near-field multiple source localization by passive sensor array. *IEEE Trans. Antennas Propag.*, vol.AP-69, pp. 968–975, July 1991.
- [HB95] R. M. Hamza and K. M. Buckley. An analysis of weighted eigenspace methods in the presence of sensor errors. *IEEE Trans. Signal Process.*, vol.SP-43, pp. 1140–1150, May 1995.
- [HCS96] M. Haardt, R. N. Challa, and S. Shamsunder. Improved bearing and range estimation via high-order subspace based unitary ESPRIT. *Proc. 30th Asilomar Conf. on Signals, Systems, and Computers*, vol.1, pp. 380–384, Pacific Grove, California, November 1996.
- [HCW96] H. S. Hung, S. H. Chang, and C. H. Wu. 3-D MUSIC with polynomial rooting for near-field source localization. *Proc. ICASSP*, vol.6, pp. 3065–3068, Atlanta, Georgia, May 1996.
- [HF96] G. F. Hatke and K. W. Forsythe. A class of polynomial rooting algorithms for joint azimuth/elevation estimation using multidimensional arrays. *Proc. 30th Asilomar Conf. on Signals, Systems, and Computers*, Pacific Grove, California, 1996.
- [HJ96] A. J. Haug and G. M. Jacyna. Comparison of the theoretical performance bounds for two wavefront curvature ranging techniques. *Proc. ICASSP*, vol.4, pp. 2445–2448, Atlanta, Georgia, May 1996.

- [HK87] H. Hung and M. Kaveh. On the statistical sufficiency of the coherently averaged covariance matrix for the estimation of the parameters of wideband sources. *Proc. ICASSP*, vol.1, pp. 33–36, Dallas, Texas, April 1987.
- [HK88] H. Hung and M. Kaveh. Focusing matrices for coherent signal subspace processing. *IEEE Trans. Acoust., Speech, Signal Process.*, vol.ASSP-36, pp. 1272–1281, August 1988.
- [HN95] M. Haardt and J. A. Nossek. Unitary ESPRIT: How to obtain increased estimation accuracy with a reduced computational burden. *IEEE Trans. Signal Process.*, vol.SP-43, pp. 1232–1242, May 1995.
- [HR80] S. Haykin and J. Reilly. Mixed autoregressive-moving average modeling of response of a linear array antenna to incident plane waves. *Proc. IEEE*, vol.68, pp. 622–630, 1980.
- [Hua91] Y. Hua. Estimating two-dimensional frequencies by matrix enhancement and matrix pencil. *Proc. ICASSP*, vol.5, pp. 3073–3076, Toronto, Canada, April 1991.
- [Hua92] Y. Hua. Estimating 2-D frequencies by matrix enhancement and matrix pencil. *IEEE Trans. Signal Process.*, vol.40, pp. 2257–2280, September 1992.
- [Hun94] E. Hung. A critical study of a self-calibrating direction-finding method for arrays. *IEEE Trans. Signal Process.*, vol.SP-42, pp. 471–474, February 1994.
- [HW94] S. Hwang and D. Williams. A constrained total least squares approach for sensor position calibration and direction finding. *Proc. IEEE National Radar Conference*, pp. 155–159, 1994.
- [HY91] K. C. Huarng and C. C. Yeh. A unitary transformation method for angle of arrival estimation. *IEEE Trans. Acoust., Speech, Signal Process.*, vol.ASP-39, pp. 975–977, April 1991.
- [HZ86] F. Haber and M. D. Zoltowski. Spatial spectrum estimation in a coherent signal environment using an array in motion. *IEEE Trans. Antennas Propag.*, vol.AP-34, pp. 301–310, March 1986.
- [HZMN95] M. Haardt, M. D. Zoltowski, C. P. Mathews, and J. A. Nossek. 2-D unitary ESPRIT for efficient 2-D parameter estimation. *Proc. ICASSP*, vol.4, pp. 2096–2099, Detroit, Michigan, May 1995.
- [Jän92] T. P. Jäntti. The influence of extended sources on the theoretical performance of the MUSIC and ESPRIT methods: Narrow-band sources. *Proc. ICASSP*, vol.II, pp. II-429-II-432, San Francisco, California, March 1992,
- [JD82] D. H. Johnson and S. R. Degraaf. Improving the resolution of bearing in passive sonar arrays by eigenvalue analysis. *IEEE Trans. Acoust., Speech, Signal Process.*, vol.ASSP-30, pp. 638–647, April 1982.
- [JF85] D. J. Jeffries and D. R. Farrier. Asymptotic results for eigenvector methods. *Proc. IEE*, pt. F, vol.132, pp. 589–594, June 1985.
- [JSO98] M. Jansson, A. L. Swindlehurst, and B. Ottersten. Weighted subspace fitting for general array error models. *IEEE Trans. Signal Process.*, vol.SP-46, pp. 2484–2498, September 1998.
- [Kay83] S. M. Kay. Recursive maximum likelihood estimation of autoregressive processes. *IEEE Trans. Acoust., Speech, Signal Process.*, vol.ASSP-31, pp. 56–65, February 1983.

- [Kay88] S. M. Kay. *Modern Spectral Estimation: Theory and Application*. Prentice-Hall, Englewood Cliffs, New Jersey, 1988.
- [KB86] M. Kaveh and A. J. Barabell. The statistical performance of the MUSIC and the Minimum-Norm algorithms in resolving plane waves in noise. *IEEE Trans. Acoust., Speech, Signal Process.*, vol.ASSP-34, pp. 331–341, April 1986.
- [KB90] M. Kaveh and A. Bassias. Threshold extension based on a new paradigm for MUSIC-type estimation. *Proc. ICASSP*, Albuquerque, New Mexico, vol.5, pp. 2535–2538, 1990.
- [Kes86] S. B. Kesler, editor. *Modern Spectrum Analysis, II*. IEEE Press, New York, 1986.
- [KFP92] H. Krim, P. Forster, and G. Proakis. Operator approach to performance analysis of root-MUSIC and root-Min-Norm. *IEEE Trans. Signal Process.*, vol.SP-40, pp. 1687–1696, July 1992.
- [KLF86] S. Y. Kung, S. C. Lo, and R. Foka. A Toeplitz approximation approach to coherent source direction finding. *Proc. ICASSP*, Tokyo, Japan, 1986.
- [KT83] R. Kumaresan and D. W. Tufts. Estimating the angles of arrival of multiple plane waves. *IEEE Trans. Aerospace Electron. Syst.*, vol.AES-19, pp. 134–139, January 1983.
- [Kum83] R. Kumaresan. On the zeros of the linear prediction-error filter for deterministic signals. *IEEE Trans. Aerospace Electron. Syst.*, vol.AES-19, January 1983.
- [Kur89] A. R. Kuruc. Lower bounds on multiple-source direction finding in the presence of direction-dependent antenna-array-calibration errors. Technical Report, M.I.T. Lincoln Laboratory, Lexington, Massachusetts, 1989.
- [KV96] H. Krim and M. Viberg. Two decades of array signal processing research. *IEEE Signal Process. Mag.*, pp. 67–94, 1996.
- [KZ95] G. M. Kautz and M. D. Zoltowski. Performance analysis of MUSIC employing conjugate symmetric beamformers. *IEEE Trans. Signal Process.*, vol.SP-43, pp. 737–748, March 1995.
- [KZ96] G. M. Kautz and M. D. Zoltowski. Beamspace DOA estimation featuring multirate eigenvector processing. *IEEE Trans. Signal Process.*, vol.SP-44, pp. 1765–1778, July 1996.
- [Lac71] R. T. Lacoss. Data adaptive spectral analysis methods. *Geophysics*, vol.36, p. 661, 1971.
- [LCSL97] Y. U. Lee, J. Choi, I. Song, and S. R. Lee. Distributed source modeling and direction-of-arrival estimation techniques. *IEEE Trans. Signal Process.*, vol.SP-45, pp. 960–969, April 1997.
- [LDD94] D. A. Linebarger, R. D. DeGroat, and E. M. Dowling. Efficient direction-finding methods employing forward/backward averaging. *IEEE Trans. Signal Process.*, vol.SP-42, pp. 2136–2145, August 1994.
- [LeC95] J. P. Le Cadre. Performance analysis of wavefront curvature methods for range estimation of a moving source. *IEEE Trans. Aerospace Electron. Syst.*, vol.AES-31, pp. 1082–1103, July 1995.

- [LF94] M. Lang and B. C. Frenzel. Polynomial root finding. *IEEE Signal Process. Lett.*, vol.SPL-1, pp. 141–143, October 1994.
- [Li92a] J. Li. Improving angular resolution for spatial smoothing techniques. *IEEE Trans. Signal Process.*, vol.SP-40, pp. 3078–3081, December 1992.
- [Li92b] J. Li. Improving ESPRIT via beamforming. *IEEE Trans. Aerospace Electron. Syst.*, vol.AES-28, pp. 520–527, April 1992.
- [LVT91] F. Li, R. J. Vaccaro, and D. W. Tufts. Performance analysis of the state-space realization (TAM) and ESPRIT algorithms for DOA estimation. *IEEE Trans. Antennas Propag.*, vol.AP-39, pp. 418–423, March 1991.
- [LW88] H. B. Lee and M. S. Wengrovitz. Improved high-resolution direction-finding through use of homogeneous constraints. *Proc. ASSP Workshop on Spectrum Estimation and Modeling*, Minneapolis, Minnesota, pp. 152–157, August 1988.
- [LW90] H. B. Lee and M. Wengrovitz. Resolution threshold of beamspace MUSIC for two closely spaced emitters. *IEEE Trans. Acoust., Speech, Signal Process.*, vol.ASSP-38, pp. 1545–1559, September 1990.
- [LW91] H. B. Lee and M. S. Wengrovitz. Statistical characterization of the MUSIC null spectrum. *IEEE Trans. Acoust., Speech, Signal Process.*, vol.ASSP-39, pp. 1333–1347, June 1991.
- [LYL01] C. M. Lee, K. S. Yoon, and K. K. Lee. Efficient algorithm for localizing 3-D narrowband multiple sources. *IEE Proc. Radar, Sonar, Navig.*, vol.148, pp. 23–26, February 2001.
- [Mak75] J. Makhoul. Linear prediction: A tutorial review. *Proc. IEEE*, vol.63, pp. 561–580, April 1975.
- [Mar77] L. Marple. Resolution of conventional Fourier, autoregressive, and special ARMA methods of spectrum analysis. *Proc. ICASSP*, Hartford, Connecticut, 1977.
- [Mar87] S. L. Marple, Jr . *Digital Spectral Analysis*. Prentice-Hall, Englewood Cliffs, New Jersey, 1987.
- [May87] J. T. Mayhan. Spatial spectral estimation using multiple beam antennas. *IEEE Trans. Antennas Propag.*, vol.AP-35, pp. 897–905, August 1987.
- [May88] S. Mayrague. On the common structure of several well-known methods for harmonic analysis and direction-of-arrival estimation induced by a new version of ESPRIT. *Proc. 4th ASSP Workshop on Spectrum Estimation and Modeling*, Minneapolis, Minnesota, pp. 307–311, August 1988.
- [MRG00] J. Messer, H. Raich, and R. Goldberg. Bearing estimation for a distributed source: modeling, inherent accuracy limitations and algorithms. *IEEE Trans. Signal Process.*, vol.SP-48, pp. 429–441, February 2000.
- [MRP94] F. McCarthy, R. Ridgway, and A. Paulraj. Fast techniques for sensor array calibration. *Proc. 28th Asilomar Conf. on Signals, Systems, and Computers*, vol.1, pp. 688–693, 1994.
- [MSW96] Y. Meng, P. Stoica, and K. Wong. Estimation of the directions of arrival of spatially dispersed signals in arrays processing. *Proc. Inst. Elect. Eng., Radar, Sonar, Navigat.*, vol.143, no.1, pp. 1–9, February 1996.

- [MZ91] Z. J. Mou and H. M. Zhang. Fast SVD for angle of arrival estimation. In E. F. Deprettere and A.-J. van der Veen, editors, *Algorithms and Parallel VLSI Architectures, Vol. B—Proceedings*, Elsevier, Amsterdam, The Netherlands, 1991.
- [MZ94] C. P. Mathews and M. D. Zoltowski. Eigenstructure techniques for 2-D angle estimation with uniform circular arrays. *IEEE Trans. Signal Process.*, vol.SP-42, pp. 2395–2407, September 1994.
- [Ng95] A. Ng. Direction-of-arrival estimation in the presence of wavelength, gain, and phase errors. *IEEE Trans. Signal Process.*, vol.SP-43, pp. 225–232, January 1995.
- [Nutt76] A. Nuttall. Spectral analysis of a univariate process with bad data points, via maximum entropy and linear predictive techniques. Technical Report 5303, Naval Underwater Systems Center, New London, Connecticut, March 1976.
- [OK90] B. Ottersten and T. Kailath. Direction-of-arrival estimation for wide-band signals using the ESPRIT algorithm. *IEEE Trans. Acoust., Speech, Signal Process.*, vol.ASSP-38, pp. 317–327, February 1990.
- [OVK91] B. Ottersten, M. Viberg, and T. Kailath. Performance analysis of the total least squares ESPRIT algorithm. *IEEE Trans. Signal Process.*, vol.SP-39, pp. 1122–1135, May 1991.
- [Ows85] N. L. Owsley. Signal subspace based minimum-variance spatial array processing. *Proc. 19th Asilomar Conf. Signal, Systems, and Computers*, pp. 94–97, November 1985.
- [PF88] B. Porat and B. Friedlander. Analysis of the asymptotic relative efficiency of the MUSIC algorithm. *IEEE Trans. Acoust., Speech, Signal Process.*, vol.ASSP-36, pp. 532–544, April 1988.
- [PF91] B. Porat and B. Friedlander. Direction finding algorithms based on high-order statistics. *IEEE Trans. Signal Process.*, vol.SP-39, pp. 2016–2025, January 1991.
- [PGH00] M. Pesavento, A. B. Gershman, and M. Haardt. Unitary root-MUSIC with a real-valued eigendecomposition: A theoretical and experimental performance study. *IEEE Trans. Signal Process.*, vol.48, pp. 1306–1314, May 2000.
- [Pil89] S. U. Pillai. *Array Signal Processing*. Springer-Verlag, New York, 1989.
- [Pis72] V. F. Pisarenko. On the estimation of spectra by means of non-linear functions of the covariance matrix. *Geophys. J. R. Astron. Soc.*, vol.28, pp. 511–531, 1972.
- [Pis73] V. F. Pisarenko. The retrieval of harmonics from a covariance function. *Geophys. J. R. Astron. Soc.*, pp. 347–366, 1973.
- [PK89a] S. U. Pillai and B. H. Kwon. Forward/backward spatial smoothing techniques for coherent signal identification. *IEEE Trans. Acoust., Speech, Signal Process.*, vol.ASSP-37, pp. 8–15, January 1989.
- [PK89b] S. U. Pillai and B. H. Kwon. Performance analysis of MUSIC-type high resolution estimators for direction finding in correlated and coherent scenes. *IEEE Trans. Acoust., Speech, Signal Process.*, vol.ASSP-37, pp. 1176–1189, August 1989.

- [PK92] J. W. Pierre and M. Kaveh. Wideband sensor array processing using a laboratory array testbed. *Proc. 35th Midwest Symp. on Circuits and Systems*, vol.2, pp. 945–948, August 1992.
- [Pra82] S. Prasad. On an index for array optimization and the discrete prolate spheroidal functions. *IEEE Trans. Antennas Propag.*, vol.AP-30, pp. 1021–1023, September 1982.
- [PRK86] A. Paulraj, R. Roy, and T. Kailath. A subspace rotation approach to signal parameter estimation. *Proc. IEEE*, vol.74, no.7, pp. 1044–1045, July 1986.
- [PRK87] A. Paulraj, V. U. Reddy, and T. Kailath. Analysis of signal cancellation due to multipath in optimum beamformers for moving arrays. *IEEE J. Oceanogr. Eng.*, vol.OE-12, pp. 163–172, January 1987.
- [PRLN92] J. G. Proakis, C. M. Rader, F. Ling, and C. L. Nikias. *Advanced Digital Signal Processing*. Macmillan, New York, 1992.
- [Rat98] T. Ratnarajah. Mitigating the effects of array uncertainties on the performance of the Music algorithm. *Proc. 9<sup>th</sup> IEEE SP Workshop on Statistical Signal and Array Processing*, pp. 236–239, Corfu, Greece, June 1998.
- [Red79] S. S. Reddi. Multiple source location: A digital approach. *IEEE Trans. Aerospace Electron. Syst.*, vol.AES-15, pp. 95–105, January 1979.
- [RH89a] B. D. Rao and K. V. S. Hari. Performance analysis of ESPRIT and TAM in determining the direction of arrival of plane waves in noise. *IEEE Trans. Acoust., Speech, Signal Process.*, vol.ASSP-37, pp. 1990–1995, December 1989.
- [RH89b] B. D. Rao and K. V. S. Hari. Performance analysis of root-MUSIC. *IEEE Trans. Acoust., Speech, Signal Process.*, vol.ASSP-37, pp.1939–1949, December 1989.
- [RH90] B. D. Rao and K. V. S. Hari. Effect of spatial smoothing on the performance of MUSIC and the Minimum Norm method. *Proc. IEE, Pt. F*, vol.137, pp. 449–458, December 1990.
- [RH93] B. D. Rao and K. V. S. Hari. Weighted subspace methods and spatial smoothing: Analysis and comparison. *IEEE Trans. Signal Process.*, vol.SP-41, pp. 788–803, February 1993.
- [RK84] D. V. B. Rao and S. Y. Kung. A state space approach for the 2-D harmonic retrieval problem. *Proc. ICASSP*, vol.4, pp. 4.10.1–4.10.4, San Diego, California, April 1984.
- [RK87] R. Roy and T. Kailath. ESPRIT—Estimation of signal parameters via rotational invariance techniques. In E. F. Deprettere, editor, *Singular Value Decomposition and Signal Processing* North-Holland, Amsterdam, The Netherlands, September 1987.
- [RK89] R. Roy and T. Kailath. ESPRIT: Estimation of signal parameters via rotational invariance techniques. *IEEE Trans. Acoust., Speech, Signal Process.*, vol.ASSP-37, pp. 984–995, July 1989.
- [RMS88] Y. Rockah, H. Messer, and P. M. Schultheiss. Localization performance of arrays subject to phase errors. *IEEE Trans. Aerospace Electron. Syst.*, vol.AES-24, pp. 402–409, July 1988.

- [RMZ99] J. Ramos, C. P. Mathews, and M. D. Zoltowski. FCA-ESPRIT: A closed-form 2-D angle estimation algorithm for filled circular arrays with arbitrary sampling lattices. *IEEE Trans. Signal Process.*, vol.SP-47, pp. 213–217, January 1999.
- [Roy87] R. Roy. *ESPRIT: Estimation of Signal Parameters via Rotational Invariance Techniques*. Ph.D. Dissertation, Stanford University, Stanford, California, 1987.
- [RPK86] R. Roy, A. Paulraj, and T. Kailath. ESPRIT—A subspace rotation approach to estimation of parameters of cisoids in noise. *IEEE Trans. Acoust., Speech, Signal Process.*, vol.ASSP-34, pp. 1340–1342, October 1986.
- [RR92] K. J. Raghunath and V. U. Reddy. A note on spatially weighted subarray covariance averaging schemes. *IEEE Trans. Antennas Propag.*, vol.AP-40, pp. 720–723, June 1992.
- [RS87] Y. Rockah and P. M. Schultheiss. Array shape calibration using sources in unknown locations—Part I: Far-field sources. *IEEE Trans. Acoust., Speech, Signal Process.*, vol.ASSP-35, pp. 286–299, March 1987.
- [Sac92] J. J. Sacchini. *Development of 2-D Parametric Radar Signal Modeling and Estimation Techniques with Application to Target Identification*. Ph.D. Thesis, Ohio State University, Columbus, Ohio, 1992.
- [SB00] P. Stoica and O. Besson. Decoupled estimation of DOA and angular spread of a spatially distributed source. *IEEE Trans. Signal Process.*, vol.SP-48, pp. 1872–1882, July 2000.
- [Sch79] R. O. Schmidt. Multiple emitter location and signal parameter estimation. *Proc. RADC Spectrum Estimation Workshop*, Griffiths AFB, Rome, New York, pp. 243–258, 1979.
- [Sch81] R. O. Schmidt. *Multiple Emitter Location and Signal Parameter Estimation*. PhD Dissertation, Stanford University, Stanford, California, 1981.
- [Sch83] R. O. Schmidt. New mathematical tools in direction finding and spectral analysis. *Proc. SPIE 27th Ann. Symp.*, San Diego, California, August 1983.
- [Sch86] R. O. Schmidt. Multiple emitter location and signal parameter estimation. *IEEE Trans. Antennas Propag.*, vol.AP-34, pp. 276–280, March 1986.
- [SDWK83] K. C. Sharman, T. S. Durrani, M. Wax, and T. Kailath. Asymptotic performance of eigenstructure methods. *Proc. ICASSP*, pp. 45.5.1–45.5.4, April 1983.
- [SDWK84] K. C. Sharman, T. S. Durrani, M. Wax, and T. Kailath. Asymptotic performance of eigenstructure spectral analysis methods. *Proc. ICASSP*, San Diego, California, pp. 45.5.1–45.5.4, March 1984.
- [SF86] R. O. Schmidt and R. E. Frank. Multiple source DF signal processing: An experimental system. *IEEE Trans. Antennas Propag.*, vol.-34, pp. 276–280, March 1986.
- [SJ97] P. Stoica and M. Jansson. On forward-backward MODE for array signal processing. *Digital Signal Process.*, vol.7, pp. 239–252, October 1997.
- [SK85] T.-J. Shan and T. Kailath. Adaptive beamforming for coherent signals and interference. *IEEE Trans. Acoust., Speech, Signal Process.*, vol.ASSP-33, pp. 527–534, June 1985.

- [SK88] A. Swindlehurst and T. Kailath. Passive direction-of-arrival and range estimation for near-field sources. *4th ASSP Workshop on Spectrum Estimation and Modeling*, pp. 123–128, August 1988.
- [SK89] A. Swindlehurst and T. Kailath. 2-D parameter estimation using arrays with multidimensional invariance structure. *Proc. 23rd Asilomar Conf. Signals, Systems, and Computers*, Pacific Grove, California, pp. 950–954, November 1989.
- [SK92] A. Swindlehurst and T. Kailath. A performance analysis of subspace-based methods in the presence of model errors, Part I: The MUSIC algorithm. *IEEE Trans. Signal Process.*, vol.SP-40, pp. 1758–1774, July 1992.
- [SK93a] A. Swindlehurst and T. Kailath. Azimuth/elevation direction finding using regular array geometries. *IEEE Trans. Aerospace Electron. Syst.*, vol.AES-29, pp. 145–156, January 1993.
- [SK93b] A. Swindlehurst and T. Kailath. A performance analysis of subspace-based methods in the presence of model errors, Part II: Multidimensional algorithms. *IEEE Trans. Signal Process.*, vol.SP-41, pp. 2882–2890, September 1993.
- [Sle78] D. Slepian. Prolate spheroidal wave functions, Fourier analysis, and uncertainty, V: The discrete case. *Bell Syst. Tech. J.*, vol.57, pp. 1371–1430, May-June 1978.
- [SM97] P. Stoica and R. Moses. Introduction to Spectral Analysis. Prentice-Hall, Englewood Cliffs, New Jersey, 1997.
- [SMW96] P. Stoica, Y. Meng, and K. W. Wong. Estimation of the directions of arrival of spatially dispersed signals in array processing. *IEE Proc. Radar, Sonar Navigat.*, vol.143, no.1, pp. 1–9, February 1996.
- [SN89] P. Stoica and A. Nehorai. MUSIC, maximum likelihood, and Cramér-Rao bound. *IEEE Trans. Acoust., Speech, Signal Process.*, vol.ASSP-37, pp. 720–741, May 1989.
- [SN90] P. Stoica and A. Nehorai. MUSIC, maximum likelihood, and Cramér-Rao bound: Further results and comparisons. *IEEE Trans. Acoust., Speech, Signal Process.*, vol.38, pp. 2140–2150, December 1990.
- [SN91a] P. Stoica and A. Nehorai. Comparative performance study of element-space and beam-space MUSIC estimators. *Circuits, Syst. Signal Process.*, vol.10, pp. 285–292, November 1991.
- [SN91b] P. Stoica and A. Nehorai. Performance comparison of subspace rotation and MUSIC methods for direction estimation. *IEEE Trans. Signal Process.*, vol.SP-39, pp. 446–453, February 1991.
- [SN94] D. Starer and N. Nehorai. Passive localization of near-field sources by path following. *IEEE Trans. Signal Process.*, vol.SP-42, pp. 677–680, March 1994.
- [SN95] M. Shao and C. L. Nikias. *Signal Processing With Alpha-Stable Distributions and Applications*. Wiley, New York, 1995.
- [SOR98] P. Stoica, B. Ottersten, and R. Roy. Covariance matching estimation techniques for array signal processing applications. *Digital Signal Processing*, pp. 185–210, August 1998.

- [SPK87] T.-J. Shan, A. Paulraj, and T. Kailath. On smoothed rank profile tests in eigenstructure methods for directions-of-arrival estimation. *IEEE Trans. Acoust., Speech, Signal Process.*, vol.ASSP-35, pp. 1377–1385, October 1987.
- [SS97] A. L. Swindlehurst and P. Stoica. Radar array signal processing with antenna arrays via maximum likelihood. *The 31st Asilomar Conf. on Signals, Systems, and Computers*, Pacific Grove, California, vol.2, pp. 1219–1223, 1997.
- [SS98] A. L. Swindlehurst and P. Stoica. Maximum likelihood methods in radar array signal processing. *Proc. IEEE*, vol.86, no.2, pp. 421–441, 1998
- [STHL94] V. C. Soon, L. Tong, Y. F. Huang, and R. Liu. A subspace method for estimating sensor gains and phases. *IEEE Trans. Signal Process.*, vol.SP-42, pp. 973–976, April 1994.
- [Swi93] D. N. Swigler. Simple approximations to the Cramer-Rao lower bound on directions of arrival for closely spaced sources. *IEEE Trans. Signal Process.*, vol.SP-41, pp. 1668–1672, April 1993.
- [SV95] P. Stoica and M. Viberg. Weighted LS and TLS approaches yield asymptotically equivalent results. *Signal Process.*, vol.45, pp. 255–259, 1995.
- [SVB01] S. Shahbazpanahi, S. Valaee, and M. H. Bastani. Distributed source localization using ESPRIT algorithm. *IEEE Trans. Signal Process.*, vol.SP-49, pp. 2169–2178, October 2001.
- [SWK85] T-J. Shan, M. Wax, and T. Kailath. On spatial smoothing for direction-of-arrival estimation of coherent signals. *IEEE Trans. on Acoust., Speech, Signal Process.*, vol.ASSP-33, pp. 806–811, August 1985.
- [TFG95] C. Y. Tseng, D. D. Feldman, and L. J. Griffiths. Robust high-resolution direction of arrival estimation via signal eigenvector domain. *IEEE J. Oceanogr. Eng.*, vol.OE-18, pp. 491–499, October 1993.
- [TGM96] J. S. Thompson, P. M. Grant, and B. Mulgrew. Performance of spatial smoothing algorithm for correlated sources. *IEEE Trans. Signal Process.*, vol.SP-44, pp. 1040–1046, April 1996.
- [TH92] A. H. Tewfik and W. Hong. On the application of uniform linear array bearing estimation techniques to uniform circular arrays. *IEEE Trans. Signal Process.*, vol.SP-40, pp. 1008–1011, April 1992.
- [TK82] D. W. Tufts and R. Kumaresan. Estimation of frequencies of multiple sinusoids: Making linear prediction perform like maximum likelihood. *Proc. IEEE*, vol.70, pp. 975–989, September 1982.
- [TK87] K. Takao and N. Kikuma. An adaptive array utilising an adaptive spatial averaging technique for multipath environment. *IEEE Trans. Antennas Propag.*, vol.AP-35, pp. 1389–1396, December 1987.
- [TN96] P. Tsakalides and C. L. Nikias. The robust covariance-based MUSIC (ROC-MUSIC) algorithm for bearing estimation in impulsive noise environments. *IEEE Trans. Antennas Propag.*, vol.AP-44, pp.1623–1633, July 1996.
- [TO96a] T. Trump and B. Ottersten. Estimation of nominal direction of arrival and angular spread using an array of sensors. *Signal Process.*, vol.50, no.1-2, pp. 57–69, April 1996.

- [TO96b] T. Trump and B. Ottersten. Estimation of nominal direction of arrival and angular spread using an array of sensors. Signal Processing Technical Report IR-S3-SB-9607, Royal Institute of Technology, Department of Signals, Sensors, and Systems, April 1996.
- [TPG93] S. Talwar, A. Paulraj, and G. H. Golub. A robust numerical approach for array calibration. *Proc. ICASSP*, vol.4, pp. 316–319, Minneapolis, Minnesota, April 1993.
- [UC76] T. J. Ulrych and R. W. Clayton. Time series modelling and maximum entropy. *Phys. Earth Planet. Inter.*, vol.12, pp. 188–200, August 1976.
- [VB95] C. Vaidyanathan and K. M. Buckley. Performance analysis of the MVDR spatial spectrum estimator. *IEEE Trans. Signal Process.*, vol.SP-43, pp. 1427–1436, June 1995.
- [VCK95] S. Valaee, B. Champagne, and P. Kabal. Parametric localization of distributed sources. *IEEE Trans. Signal Process.*, vol.SP-43, pp. 2144–2153, September 1995.
- [VDB71] A. Van Den Bos. Alternative interpretation of maximum entropy spectral analysis. *IEEE Trans. Inf. Theory*, vol.17, no.7, pp. 493–494, July 1971.
- [vdVOD92] A. J. van der Veen, P. B. Ober, and E. D. Deprettere. Azimuth and elevation computation in high resolution DOA estimation. *IEEE Trans. Signal Process.*, vol.SP-40, pp. 1828–1832, July 1992.
- [VO91] M. Viberg and B. Ottersten. Sensor array processing based on sub-space fitting. *IEEE Trans. Signal Process.*, vol.SP-39, pp. 1110–1121, May 1991.
- [VS94] M. Viberg and A. Swindlehurst. Analysis of the combined effects of finite samples and model errors on array processing performance. *IEEE Trans. Signal Process.*, vol.SP-42, pp. 3073–3083, November 1994.
- [VWV88] B. Van Veen and B. Williams. Structured covariance matrices and dimensional reduction in array processing. *Proc. 4th ASSP Workshop on Spectrum Estimation and Modeling*, Minneapolis, Minnesota, pp. 168–171, August 1988.
- [WF91a] A. J. Weiss and B. Friedlander. Array shape calibration using eigenstructure methods. *Signal Process.*, vol.22, pp. 251–258, Elsevier Science Publishers, New York, 1991.
- [WF91b] A. J. Weiss and B. Friedlander. Self-calibration for high-resolution array processing. In S. Haykin, editor, *Advances in Spectrum and Array Processing*, Vol. II, chapter 10, Prentice-Hall, Englewood Cliffs, New Jersey, 1991.
- [WF93a] A. J. Weiss and B. Friedlander. Range and bearing estimation using polynomial rooting. *IEEE J. Oceanogr. Eng.*, vol.OE-18, pp. 130–137, April 1993.
- [WF93b] A. J. Weiss and B. Friedlander. Performance analysis of spatial smoothing with interpolated array. *IEEE Trans. Signal Process.*, vol.41, pp. 1881–1892, May 1993.
- [WF94a] A. J. Weiss and B. Friedlander. Effects of modeling errors on the resolution threshold of the MUSIC algorithm. *IEEE Trans. Signal Process.*, vol.SP-42, pp. 1519–1526, June 1994.
- [WF94b] A. J. Weiss and B. Friedlander. Preprocessing for direction finding with minimal variance degradation. *IEEE Trans. Signal Process.*, vol.SP-42, pp. 1478–1484, June 1994.

- [WFS95] A. J. Weiss, B. Friedlander, and P. Stoica. Direction-of-arrival estimation using MODE with interpolated array. *IEEE Trans. Signal Process.*, vol.SP-43, pp. 296–300, May 1995.
- [Wil65] J. H. Wilkinson. *The Algebraic Eigenvalue Problem*. Oxford University Press, New York, 1965.
- [Win87] J. H. Winters. On the capacity of radio communication systems with diversity in a Rayleigh fading environment. *IEEE Sel. Areas Commun.*, vol.SAC-5, pp. 871–878, June 1987.
- [WK85] H. Wang and M. Kaveh. Coherent signal subspace processing for the detection and estimation of angles of arrival of multiple wideband sources. *IEEE Trans. Acoust., Speech Signal Process.*, vol.33, no.8, pp. 823–831, August 1985.
- [WPMS88] R. T. Williams, S. Prasad, A. K. Mahalanabis, and L. H. Sibul. An improved spatial smoothing technique for bearing estimation in a multipath environment. *IEEE Trans. Acoust., Speech, Signal Process.*, vol.ASSP-36, pp. 425–431, April 1988.
- [WRM94] M. Wylie, S. Roy, and H. Messer. Joint DOA estimation and phase calibration of linear equispaced (LES) arrays. *IEEE Trans. Signal Process.*, vol.SP-42, pp. 3449–3459, December 1994.
- [WWMR94] Q. Wu, K. M. Wong, Y. Meng, and W. Read. DOA-estimation of point and scattered sources–Vec-MUSIC. *Proc. 7th SP Workshop Statistical Signal Array Processing*, Quebec City, Canada, pp. 365–368, June 1994.
- [WZ99] K. T. Wong and M. D. Zoltowski. Root-MUSIC-based azimuth-elevation angle-of-arrival estimation with uniformly spaced but arbitrarily oriented velocity hydrophones. *IEEE Trans. Signal Process.*, vol.SP-47, pp. 3250–3260, December 1999.
- [XB90] X. L. Xu and K. M. Buckley. A comparison of element and beamspace spatial-spectrum estimation for multiple source clusters. *Proc. ICASSP*, vol.5, pp. 2643–2646, Albuquerque, New Mexico, April 1990.
- [XB92] X. L. Xu and K. M. Buckley. Bias analysis of the MUSIC location estimator. *IEEE Trans. Acoust., Speech, Signal Process.*, vol.ASSP-40, pp. 2559–2569, October 1992.
- [XB93] X.-L. Xu and K. M. Buckley. An analysis of beam-space source localization. *IEEE Trans. Signal Process.*, vol.SP-41, pp. 501–504, January 1993.
- [XK96] W. Xu and M. Kaveh. Comparative study of the biases of MUSIC-like estimators. *Signal Process.*, vol.50, pp. 39–55, 1996.
- [XSRK94] G. Xu, S. D. Silverstein, R. H. Roy, and T. Kailath. Beamspace ESPRIT. *IEEE Trans. Signal Process.*, vol.SP-42, pp. 349–356, February 1994.
- [YF96a] N. Yuen and B. Friedlander. Higher-order ESPRIT for localization of near-field sources: an asymptotic performance analysis. *Proc. 8th IEEE SP Workshop on Statistical Signal and Array Processing*, pp. 538–541, Corfu, Greece, June 1996.
- [YF96b] N. Yuen and B. Friedlander. Asymptotic performance analysis of ESPRIT, higher order ESPRIT, and virtual ESPRIT algorithms. *IEEE Trans. Signal Process.*, vol.SP-44, pp. 2537–2550, October 1996.

- [YLC89] C. C. Yeh, J. H. Lee, and Y. M. Chen. Estimating two-dimensional angles of arrival in coherent source environment. *IEEE Trans. Acoust., Speech, Signal Process.*, vol.ASSP-37, p. 153, January 1989.
- [YS95] J. Yang and A. L. Swindlehurst. The effects of array calibration errors on DF-based signal copy performance. *IEEE Trans. Signal Process.*, vol.SP-43, pp. 2724–2732, November 1995.
- [Zha95a] Q. T. Zhang. Probability of resolution of the MUSIC algorithm. *IEEE Trans. Signal Process.*, vol.SP-43, pp. 978–987, April 1995.
- [Zha95b] Q. T. Zhang. A statistical resolution theory of the beamformer-based spatial spectrum for determining the directions of signals in white noise. *IEEE Trans. Signal Process.*, vol.SP-43, pp. 1867–1873, August 1995.
- [ZHJ91] C. Zhou, F. Haber, and D. L. Jaggard. A resolution measure for the MUSIC algorithm and its application to plane wave arrivals contaminated by coherent interference. *IEEE Trans. Acoust., Speech, Signal Process.*, vol.ASSP-39, pp. 454–463, February 1991.
- [ZHM96] M. D. Zoltowski, M Haardt, and C. P. Mathews. Closed-form 2-D angle estimation with rectangular arrays in element space or beamspace via unitary ESPRIT. *IEEE Trans. Signal Process.*, vol.SP-44, pp. 316–328, February 1996.
- [ZKK94] M. D. Zoltowski, J. V. Krogmeier, and G. M. Kautz. Novel multirate processing of beamspace noise eigenvectors. *IEEE Signal Process. Lett.*, vol.1, pp. 83–86, May 1994.
- [ZKS93] M. D. Zoltowski, G. M. Kautz, and S. D. Silverstein. Beamspace root-MUSIC. *IEEE Trans. Signal Process.*, vol.SP-41, pp. 344–364, January 1993.
- [ZL91] M. D. Zoltowski and T. S. Lee. Interference cancellation matrix beamforming for 3-D beamspace ML/MUSIC bearing estimation. *IEEE Trans. Signal Process.*, vol.SP-39, pp. 1858–1876, August 1991.
- [ZO95] P. Zetterberg and B. Ottersten. The spectrum efficiency of a base station antenna array system for spatially selective transmission. *IEEE Trans. Veh. Technol.*, vol.VT-44, pp. 651–659, August 1995.
- [ZS89] M. D. Zoltowski and D. Stavrinides. Sensor array signal processing via a Procrustes rotations-based Eigenanalysis of the ESPRIT data pencil. *IEEE Trans. Acoust., Speech, Signal Process.*, vol.ASSP-37, pp. 832–861, June 1989.
- [ZZ95] M. Zhang and Z. Zhu. A method for direction finding under sensor gain and phase uncertainties. *IEEE Trans. Antennas Propag.*, vol.AP-43, pp. 880–883, August 1995.

Copyright of Optimum Array Processing is the property of John Wiley & Sons, Inc. 2002 and its content may not be copied or emailed to multiple sites or posted to a listserv without the copyright holder's express written permission. However, users may print, download, or email articles for individual use.